Studies of Fluid Flow in Arterial Bypass Grafts by Magnetic Resonance Imaging

by

Yannis Papaharilaou

A thesis submitted for the degree
of Doctor of Philosophy
of the University of London

Department of Aeronautics
Imperial College of Science, Technology & Medicine
London SW7

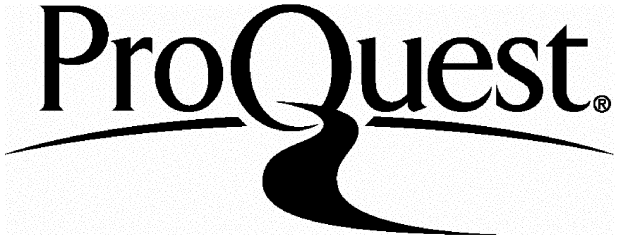

Abstract

This thesis is concerned primarily with the effects of graft geometry and flow pulsatility on the hemodynamics of arterial bypass grafts. Motivation for this work was the need of better understanding of the underlying flow related conditions that promote arterial bypass graft stenosis. The thesis describes techniques currently available for quantitative flow Magnetic Resonance Imaging (MRI). Methods to estimate and reduce measurement uncertainty in MRI phase contrast velocimetry are investigated. The MR phase-velocity mapping technique is calibrated in complex steady and transient flows by using highly resolved numerical computations as reference solutions. A novel splines based approximation method is introduced to model MRI velocity encoded phase. Applications of the proposed method to estimate wall shear stress and vorticity from MR phase velocity measurements are described and results from a series of validation studies are presented.

The influence of out-of-plane geometry on the flow field in arterial bypass grafts is assessed by comparing two idealised model geometries: a planar and a non-planar configuration under steady and time-varying flow. Procedures for the acquisition of three-dimensional bypass graft geometries by MRI and their transformation to a computer-aided-design (CAD) representation are described. Stereolithographic replicas of bypass graft geometries (an *in vivo* extracted femoro-tibial distal anastomosis and an *ex vivo* imaged aorto-coronary distal anastomosis) and silicon negative models were fabricated for use in MRI flow studies. The effect of flow pulsatility on the flow features in the realistic aorto-coronary distal anastomosis model is investigated by comparing the flow field generated by a sinusoidal (single harmonic) and a physiological (multi-harmonic) waveform. The influence of the distal-proximal graft outflow division on the distal anastomotic sinus flow field in the femoro-tibial bypass graft model is examined. Finally, an account of the results from the comparative studies is given, and the physiological implications of the flow features of note are discussed.

Acknowledgements

I would like first to thank my supervisor Dr Denis Doorly for his guidance and support throughout the project. I would also like to thank Drs Spencer Sherwin and Joaquim Peiro for their contributions on the numerical part of the project, Professor Colin Caro for making this investigation possible and Mr Nick Watkins for his skilful assistance in model making. I would like to thank the staff at the St' Mary's Hospital MRI Unit for access to their facilities and to Drs Mark Jackson and Vassileios Zervas of the Vascular Surgery Unit at St' Mary's Hospital for their assistance with the patient study. A thank you also goes to Dr Bal Sanghera for the stereolithography and to Mr Sergio Giordana for assistance with the surface reconstructions. A would also like to thank Ms Annie Papadaki for her friendship and her invaluable assistance with equipment and Dr Chuck Dumoulin for his help with the small bore MRI scanner.

I am very grateful to my family for their continued support and to Katerina for her understanding, patience and constant support.

Finally I would like to acknowledge the financial support by the University of London Academic Trust Funds, the Lilian Voudouri Foundation of Greece, the Garfield Weston Foundation, the Clothworkers' Foundation, the BUPA Foundation and the Henry Smith's Charity.

Table of Contents

Chapter 1.

Introduction

1.1 Fluid mechanics of the macrocirculation

The subject of arterial hemodynamics has been covered in detail in the standard texts by Pedley (1980), Caro et al. (1978), Milnor (1989) and McDonald (1990). An excellent introduction to the fluid mechanics of flow in the macrocirculation is given by Parker and Caro (1993). A good discussion on the physical interpretation of fluid dynamics can be found in Tritton (1977). Due to the complexity of the flow in large blood vessels, an understanding of the basic concepts of fluid mechanics associated with arterial blood flow is a very useful precursor to any experimental or numerical investigation of such flows. As there are only a small number of simple flows that have been analytically described, the understanding of complex flows relies mainly on results of experiments and in some cases of numerical computations.

Before introducing the equations of motion the concept of the fluid particle based on the continuum hypothesis is introduced. This states that if we can associate with any volume of fluid –no matter how small– those macroscopic properties associated with the fluid in bulk then at each point there is a fluid particle and therefore a large volume of fluid consists of a continuous aggregate of such particles, each having a certain velocity, temperature etc. These assumptions are valid if a fluid particle consists of a large number of molecules and these molecules strongly interact with one another.

An important concept in the motion of fluid particles and their interaction with a solid boundary is the non-slip condition. Viscous forces not only resist the motion between the neighbouring layers of a fluid, but also cause any fluid element in contact

with the solid boundary to adhere to it and thus have the same velocity as the boundary.

Equations of motion

The description of the equations of motion will be based on the Eulerian specification that uses a system of coordinates fixed in space rather than one that moves with the fluid particle as applied in the Lagrangian specification. The control volume is a primary feature in the Eulerian description of the flow and is defined as an arbitrary volume fixed in the Eulerian system of coordinates and entirely within the flow. The laws of mechanics are applied for the control volume to calculate the fluid motion. Fluid velocity is denoted by $\boldsymbol{u}$ with Cartesian components (υ, w, u) in directions (x, y, z) in agreement with the standard system of axis used in MRI scanners.

Continuity equation

The continuity equation is based on the principle of conservation of mass, which states that the rate of change of mass in the control volume is equal to the net rate of mass flux across the boundary of the control volume. The Eulerian description of the continuity equation can be expressed as follows:

$$\frac{\partial \rho}{\partial t} + \nabla \cdot (\rho \boldsymbol{u}) = 0, \tag{1.1}$$

where ρ is the fluid density and $\boldsymbol{u}$ the velocity.

For incompressible flows where the fluid density is constant the continuity equation reduces to:

$$\nabla \cdot \boldsymbol{u} = 0, \tag{1.2}$$

which in Cartesian coordinates is expressed as:

$$\frac{\partial \upsilon}{\partial x} + \frac{\partial w}{\partial y} + \frac{\partial u}{\partial z} = 0 \tag{1.3}$$

Navier-Stokes Equations

Application of the principle of conservation of momentum to the fluid in the control volume yields the Navier-Stokes equations:

$$\frac{\partial \boldsymbol{u}}{\partial t} + \boldsymbol{u} \cdot \nabla \boldsymbol{u} = -\frac{1}{\rho}\nabla p + \nu \nabla^2 \boldsymbol{u} + \frac{1}{\rho}\boldsymbol{F}, \tag{1.4}$$

where p is the pressure and ν the kinematic viscosity.

The term F represents body forces such as gravity or electromagnetic forces, which act on the whole of the fluid particle volume rather than over its surface. In Cartesian coordinates the Navier-Stokes equations can be written as:

$$\begin{aligned}
\rho\left[\frac{\partial \upsilon}{\partial t} + \upsilon\frac{\partial \upsilon}{\partial x} + w\frac{\partial \upsilon}{\partial y} + u\frac{\partial \upsilon}{\partial z}\right] &= -\frac{\partial p}{\partial x} + \mu\left[\frac{\partial^2 \upsilon}{\partial x^2} + \frac{\partial^2 \upsilon}{\partial y^2} + \frac{\partial^2 \upsilon}{\partial z^2}\right] + F_x \\
\rho\left[\frac{\partial w}{\partial t} + \upsilon\frac{\partial w}{\partial x} + w\frac{\partial w}{\partial y} + u\frac{\partial w}{\partial z}\right] &= -\frac{\partial p}{\partial y} + \mu\left[\frac{\partial^2 w}{\partial x^2} + \frac{\partial^2 w}{\partial y^2} + \frac{\partial^2 w}{\partial z^2}\right] + F_y \\
\rho\left[\frac{\partial u}{\partial t} + \upsilon\frac{\partial u}{\partial x} + w\frac{\partial u}{\partial y} + u\frac{\partial u}{\partial z}\right] &= -\frac{\partial p}{\partial z} + \mu\left[\frac{\partial^2 u}{\partial x^2} + \frac{\partial^2 u}{\partial y^2} + \frac{\partial^2 u}{\partial z^2}\right] + F_z
\end{aligned} \tag{1.5}$$

The above set of equations combined with the continuity equation form a set of four simultaneous equations that can be solved for one scalar variable (pressure) and one vector variable (velocity), effectively four unknown quantities.

The Bernoulli equation

The principle of conservation of energy for a flow system, where no external forces are applied, states that total energy of the system in the absence of nuclear reactions should remain constant. The Bernoulli equation is applied to the flow of an ideal frictionless fluid and relates the change in velocity, pressure, and the gravitational field along a streamline. In steady incompressible flow it is given by:

$$p + 1/2\,\rho u^2 + gz = \text{constant along a streamline}. \tag{1.6}$$

The three terms in the left hand side of equation (1.1) represent from left to right the pressure energy, the kinetic energy and the potential energy of the gravitational field respectively. If the effects of gravity are neglected (1.6) becomes:

$$p + 1/2\,\rho u^2 = \text{const} \tag{1.7}$$

In the presence of viscosity, the right hand side of equation (1.7) is no longer constant but depends on the pressure drop required to overcome viscous stress. Nevertheless, equation (1.7) is frequently used to estimate the pressure difference between two points closely spaced along a jet through a cardiac valve or an arterial stenosis, using measurements of velocity at these points and neglecting viscous effects over a short length.

Steady flow in a straight tube

A very important parameter in characterising flows is the Reynolds number (*Re*) given by the following expression:

$$Re = d\frac{U}{\nu} \tag{1.8}$$

U is the characteristic velocity and d the characteristic dimension of the flow. For steady flow in a pipe these parameters are the mean velocity and the tube diameter respectively. The Reynolds number can be considered as the ratio between inertial and viscous forces in a flow. In the human cardiovascular system it ranges from 0.0007 in the capillaries to 5800 in the ascending aorta for a blood viscosity of 3.5 cP, (although the flow in the capillaries cannot be described in terms of a homogenous fluid). For Reynolds numbers much higher than 1, inertial forces dominate the flow and viscous effects are significant only near the boundaries of the flow domain. The region in which viscous forces play an important role in determining the flow properties is called the boundary layer. In the entrance region of steady flow in a straight rigid pipe the boundary layer grows and gradually fills the cross section. Beyond this point the flow does not develop further and it is considered fully developed. It has been found that the entrance length (L) required for the development of a steady flow in a straight tube is given by the following expression (Tritton, 1977):

$$L \approx \frac{1}{30} d\,Re \tag{1.9}$$

Poiseuille in 1840 studied steady flow in a straight rigid pipe and derived an equation that describes the pressure flow relationship at a station far from the entrance:

$$Q = \frac{\pi \rho \Delta P a^4}{8 \mu L}, \tag{1.10}$$

where Q is the flow rate, $\Delta P / L$ is the pressure gradient driving the flow, μ the dynamic viscosity and a the pipe radius. This equation is valid only if the flow is fully developed, i.e. the wall shear stress just balances the driving pressure gradient force. The velocity at a radial position r is given by the following expression:

$$u(r) = u_0 \left(1 - \frac{r^2}{a^2} \right), \tag{1.11}$$

where u_0 is the centreline velocity. The shear rate is given by the following expression:

$$\frac{\partial u}{\partial r} = -\frac{2u_0 r}{a^2} = -\frac{4\bar{u}r}{a^2} = -\frac{4Qr}{\pi a^4}, \tag{1.12}$$

where $\bar{u}$ is the mean velocity.

Time-varying flow in a straight tube

Womersley (1955) derived a solution for axisymmetric fully developed flow in a straight rigid tube. The general form of the equation of motion for an incompressible viscous fluid in a straight rigid pipe is:

$$\frac{\partial^2 \boldsymbol{u}}{\partial r^2} + \frac{1}{r}\frac{\partial \boldsymbol{u}}{\partial r} + \frac{1}{\mu}\frac{\partial p}{\partial z} = \frac{1}{\nu}\frac{\partial \boldsymbol{u}}{\partial t} \tag{1.13}$$

For a flow driven by an oscillatory pressure gradient of magnitude $-\Delta P/L$ (where L is a small axial distance over which the pressure difference ΔP is taken) the solution of the equation of motion for velocity in a tube of radius a is:

$$u(r,t) = \frac{\rho a^2 \Delta P}{i^3 \alpha^2 \mu L}\left\{1 - \frac{J_0(i^{3/2}\alpha\, r/a)}{J_0(i^{3/2}\alpha)}\right\} e^{i\omega t}, \tag{1.14}$$

where J_0 is a Bessel function of the first kind of order zero and $i = \sqrt{-1}$. The parameter α which appears is non-dimensional and is often called the Womersley parameter. It characterises kinematic similarities in fluid motion and is given by the expression:

$$\alpha = a\sqrt{\frac{\omega}{\nu}} \tag{1.15}$$

where ω is the angular frequency of the oscillation. The Womersley parameter can be regarded as an indicator of the relative contribution to the flow field of the viscous and inertia terms in the time scale of the fundamental frequency of the pressure waveform. For low values of α (<1) viscous forces dominate and the flow can be considered quasi steady. The instantaneous velocity profile is fully determined by the instantaneous pressure gradient. For larger values of α inertia forces start to influence the flow and a phase lag develops between the pressure waveform and the flow waveform. For large values of α (>10) inertia forces dominate and viscous forces are restricted to a thin boundary layer. The Womersley solution for a single harmonic pressure pulse is particularly useful as it can be used to predict the time-varying velocity distribution in a straight rigid tube for any pressure waveform. This can be achieved by representing the waveform by its Fourier series, obtaining the Womersley solution for each Fourier mode, and taking the sum of the solutions for all modes. Velocity profiles for single-harmonic pulsatile flow in a straight rigid tube and for a range of oscillation frequencies are shown in Figure 1.1. It is clear from the figure that flow reversal first occurs near the wall and it increases with increasing waveform frequency. There is also a flattening on the central region of the velocity profile hence a reduction of flow amplitude with increasing frequency.

The solution for the flow rate is obtained by integrating equation (1.14) over the cross sectional area and is given by the following expression:

$$Q(t) = \frac{\rho \pi a^4 \Delta P}{i^3 \alpha^2 \mu L}\left\{1 - \frac{2J_1(i^{3/2}\alpha)}{i^{3/2}\alpha J_0(i^{3/2}\alpha)}\right\} e^{i\omega t} \tag{1.16}$$

The Womersley solution has been used (Frayne et al, 1995) to obtain an estimate of the accuracy of time-varying MR phase-velocity measurements.

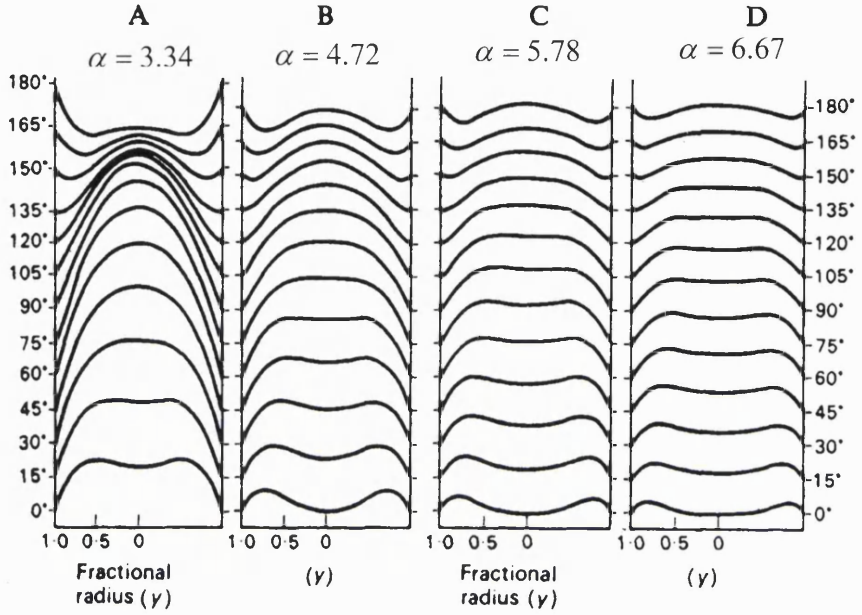

Figure 1.1 Velocity profiles at intervals of 15 degrees, of the flow resulting from a sinusoidal pressure gradient in a straight rigid tube for a range of Womersley parameter values representing the fundamental (A), the first (B), the second (C) and the third (D) harmonic of a physiologic flow waveform. Due to the waveform symmetry only half of the cycle is shown (From Nichols and O'Rourke 'Mc Donald's blood flow in arteries', 1990).

Flow in a curved pipe

For fluid particles travelling in a curved pipe, a radial component of acceleration is required. This lateral acceleration is caused by an in plane pressure gradient from the inner to the outer wall. This pressure gradient acts uniformly on all fluid particles and therefore the magnitude of the lateral acceleration u^2/R, where u is the velocity of the fluid particle and R is the radius of curvature of its path, should be equal for all particles. However, as the velocity of the particles near the wall is lower than those in the core of the flow due to the no-slip condition, the radius of curvature of the paths of particles in the core of the flow should be larger than those near the wall. This sets up a secondary circulation whereby fluid particles are swept from the core to the outer wall. Those near the wall are swept towards the inside of the bend. This secondary motion is characterised by a cross flow pattern with two symmetric counter rotating

vortices (Figure 1.2c). As high inertia fluid particles are swept towards the outer wall a skewed axial velocity profile develops (Figure 1.2a). This also results in higher levels of shear stress on the outer wall as compared to the inner wall. The rates of shear on the outer wall of the bend are higher than those in Poiseuille flow and result in an increased dissipation of kinetic energy from viscous effects. As a result, a higher pressure gradient is required to maintain the same flow rate through a curved pipe than that through a straight pipe.

A non dimensional parameter called the Dean number (*De*) has been used to characterise flows in curved tubes and can be calculated using the form proposed by Berger et al. (1983):

$$De = Re\sqrt{a/R}\,, \tag{1.17}$$

where a is the tube radius and R is the tube radius of curvature. In the circulation the Dean number varies between near zero in relatively straight sections of arteries to the order of hundreds in the aortic arch and in highly curved sections of the coronary arteries.

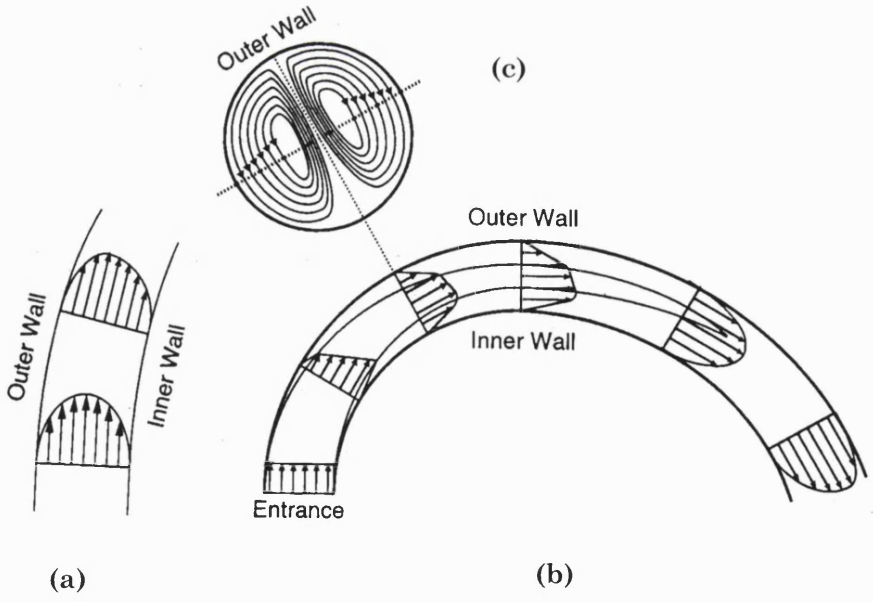

Figure 1.2 Velocity profiles in a curved pipe with a parabolic (a) and a flat (b) velocity profile specified at the inlet. Cross flow streamlines (c) show the two symmetric counter-rotating vortices (from Lefebvre et al., 1991).

Flow in a bifurcation

Bifurcations in the arterial system can be classified in two broad categories based on their geometric configuration: as Y-shaped where the trunk splits into two branches of comparable cross sectional areas, and as T-shaped where there is effectively a single side-branch growing from a fairly continuous trunk. Examples of Y-shaped bifurcations include the aortic, the carotid, the iliac and the coronary while examples of T-shaped bifurcations include the renal, the femoral and the celiac. In an idealised Y shaped arterial bifurcation (Figure 1.3a) the trunk vessel separates into two symmetric branch vessels with a lateral bifurcation angle θ and with a trunk-branch area (A) ratio (β) defined as:

$$\beta = \frac{\sum A_{branches}}{A_{trunk}}, \tag{1.18}$$

The area ratio β varies significantly throughout the vascular system, ranging from 0.52 to 1.39 in human arteries, and it changes with age (Caro et al., 1971). The mean area ratio of the adult human aortic bifurcation is 0.75. The trunk branch area ratio affects the reflection of the pressure wave at a bifurcation. It has been found that minimum pressure wave reflection at a bifurcation occurs for an area ratio of 1.15.

If a fully developed steady flow is present at the bifurcation inlet then as this flow enters a branch vessel, high inertia fluid particles from the core of the flow are found near the flow divider on the outer wall of the branch vessels. This leads to a skewed velocity profile with higher velocities at the outer wall and lower velocities on the inner wall (Figure 1.3a). The flow from the trunk to a branch is similar to that in a curved tube, where fluid particles experience a lateral component of acceleration necessary to negotiate the bend. Therefore a cross flow pattern, similar to that found in curved pipes and associated with the lateral pressure gradient, is expected to develop in the branches of a Y shaped bifurcation.

The configuration of the bifurcation and particularly parameters such as the bifurcation angles, the trunk-branch area ratio, the shape of the flow divider and the form of the corners (rounded or sharp) will strongly influence the flow field. A decrease in the lateral bifurcation angle θ (Figure 1.3b) will accentuate the separation of the boundary layer along the inner walls of the branching vessels, increase the skewness

of the velocity profile in the branches and hence the asymmetry in the distribution of wall shear stress. A branch-to-trunk area ratio of less than one is equivalent to a flow constriction and will cause flow acceleration that has a stabilising effect of the flow. A branch-to-trunk area ratio above one is equivalent to a flow expansion and will cause flow deceleration. Flow deceleration is achieved by a local adverse pressure gradient in the branch vessels, associated with the Bernoulli effect, that may cause low inertia fluid particles on the inner walls of the vessels to separate from the main stream and form regions of recirculating flow. Therefore, an expansion will typically have a destabilising effect on the flow.

In the human vascular system curvature torsion and branching of vessels may all occur with close proximity to each other hence their effects on the flow field cannot be easily separated. Therefore the notion of fully developed flow may only be applicable to small sections of the arterial tree. An excellent review of the fluid dynamics in arterial bifurcations is that by Lou and Yang (1992).

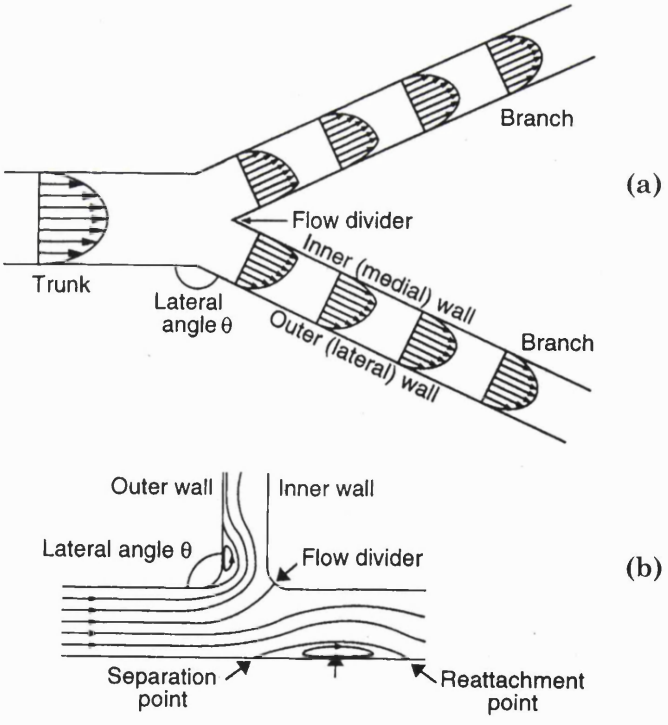

Figure 1.3 (a) Steady flow velocity profiles at various stations in a Y-shaped bifurcation. (b) Streamlines in a T-shaped bifurcation (from Lefebvre et al., 1991).

Vorticity

Vorticity is a kinematic property of the flow field and is a measure of the angular velocity of a fluid particle at each point. It is a vector quantity, having three scalar components. Denoted by the symbol ω, vorticity is defined in Cartesian and cylindrical coordinates by:

$$\begin{aligned}\omega &= \nabla \times \boldsymbol{u} \\ &= \boldsymbol{i}_x\left(\frac{\partial u}{\partial y}-\frac{\partial w}{\partial z}\right)+\boldsymbol{i}_y\left(\frac{\partial \upsilon}{\partial z}-\frac{\partial u}{\partial x}\right)+\boldsymbol{i}_z\left(\frac{\partial w}{\partial x}-\frac{\partial \upsilon}{\partial y}\right) \qquad (1.19)\end{aligned}$$

$$= \boldsymbol{i}_r\left(\frac{1}{r}\frac{\partial u_z}{\partial \theta}-\frac{\partial u_\theta}{\partial z}\right)+\boldsymbol{i}_\theta\left(\frac{\partial u_r}{\partial z}-\frac{\partial u_z}{\partial r}\right)+\boldsymbol{i}_z\left(\frac{1}{r}\frac{\partial}{\partial r}(ru_\theta)-\frac{1}{r}\frac{\partial u_r}{\partial \theta}\right) \qquad (1.20)$$

To elucidate the relationship between the vorticity and the angular velocity of a fluid element, the rigid-body rotation of a fluid about a fixed axis can be considered. Such rotation would occur if water was placed in a glass centred on a rotating turntable and sufficient time allowed for all the fluid to rotate at the same angular velocity Ω as the turntable. Using cylindrical coordinates fixed in the laboratory inertial reference frame, with the z-axis vertical, the velocity components are $u_r = 0$, $u_\theta = \Omega r$ and $u_z = 0$. Substituting these values in equation (1.20) to calculate the vorticity, only the axial component of vorticity is non zero:

$$\omega_z = \boldsymbol{i}_z\left(\frac{1}{r}\frac{\partial}{\partial r}(r^2\Omega)\right) = (2\Omega)\boldsymbol{i}_z . \qquad (1.21)$$

Because the fluid is in rigid-body rotation, the angular velocity is the same for each fluid element and so is the vorticity given by equation (1.21). Therefore, the vorticity is twice the angular velocity of a fluid element.

Flow without vorticity is called irrotational flow. Rotation, as specified by vorticity, corresponds to changing orientation in space of a fluid particle and not to motion of the particle on a closed path. For example in simple shear flow ($u = u(x), \quad \upsilon = w = 0$) although each fluid particle moves in a straight line it has a vorticity given by (1.19):

$$\omega_x = \omega_z = 0, \quad \omega_y = -\frac{\partial u}{\partial x} \tag{1.22}$$

On the other hand, in a flow where every fluid particle moves on a circular path about the z-axis with the following velocity distribution:

$$u_\theta = \frac{k}{r}, \quad u_r = u_z = 0 \tag{1.23}$$

where k is a constant, the vorticity is (1.20):

$$\omega_r = \omega_\theta = 0, \quad \omega_z = \frac{1}{r}\frac{\partial}{\partial r}(ru_\theta) = 0 \quad \text{for} \quad r \neq 0. \tag{1.24}$$

Turbulence

Turbulence can be defined as the flow condition in which velocity, pressure and other flow field variables vary randomly in space and time; in practice therefore the flow cannot be exactly determined in detail. Turbulent flows can however be described by their time and space average properties. An alternative short description of turbulence is that it is a state of continuous instability. Reynolds established experimentally that the transition from laminar to turbulent steady flow in a straight rigid pipe away from the entrance occurs for a value of a dimensionless parameter, now known as Reynolds number of about 2000. Turbulence has been reported to occur in the vicinity of the aortic valve, in the mid-ascending aorta (Nerem and Seed, 1972) and in diseased vessels distal to a stenosis (Hutchison and Karpinski, 1985). Turbulence increases energy dissipation but also enhances mixing of the fluid. Furthermore, turbulent flows have more plug-like velocity profiles and therefore thinner boundary layers and higher wall shear rates as compared to laminar flows. It should be noted that although very complex three-dimensional disturbed flow fields exist in the arterial system they are not necessarily turbulent.

1.2 Physiology and pathophysiology of arterial blood flow

Excellent reviews on the subject are given by Caro et al. (1979) and Dobrin (1997). Flow-mediated endothelial mechanotransduction is reviewed by Davies (1995) and intimal hyperplasia with respect to vascular grafts is reviewed by Dobrin (1994).

The structure of the arterial wall

The arterial wall is composed of three layers: the internal or tunica intima; the middle or tunica media; and the external layer or tunica adventitia (Figure 1.4). The intima is itself composed of two layers. The inner layer exposed to the blood stream is the endothelium and it is surrounded by the subendothelial layer. The endothelium is a single layer of endothelial cells that forms a continuous lining on all surfaces that are exposed to blood. The endothelial lining can be damaged by mechanical stress (e.g. high shear stress) but has a great capacity for regenerating itself. It can also form a lining in vein or synthetic bypass grafts inserted in the body surgically. The subendothelial layer contains fibroblasts and collagen fibres. The tunica media is composed of layers of elastic tissue separated by connective tissue, collagen fibres and smooth muscle cells. Between the media and the intima is the internal elastic lamina layer that is composed of branching elastic fibers. The adventitia forms the most external layer of the vessel wall and is composed of loose connective tissue containing elastin and collagen fibers. The tunica adventitia and tunica media layers of arteries larger than 1 mm in diameter are nourished through their own capillary blood supply network, the *vasa vasoroum*. The nourishment of the tunica intima relies on the transport of materials from the blood stream. The mechanical strength of the wall is primarily provided by the media layer. The stress and strain relation for the arterial wall is non-linear and viscoelastic. This is due to the layered configuration of the wall which is structured in such a way that as the wall is stretched it becomes stiffer.

The endothelium is the interface between the blood stream and the vascular wall. It plays an important role in the transduction of mechanical forces acting on the vessel wall as a result of the flow of blood. Therefore it has developed mechanisms to allow the transduction of hemodynamic information. The endothelium also plays an important role in the development of vascular wall disease, in particular with respect to the localisation of atherosclerotic lesions. The main functions of the endothelium are: the maintenance of anticoagulant properties; the physiological control of vascular tone and lumen diameter; and the regulation of vascular permeability. Endothelial function also has pathological implications associated with acute inflammation, wound healing and cardiovascular disorders such as the localisation of atherosclerosis. The

local hemodynamic conditions influence all these functions, either directly through mechanical forces or indirectly through mass transfer to the wall from the blood stream.

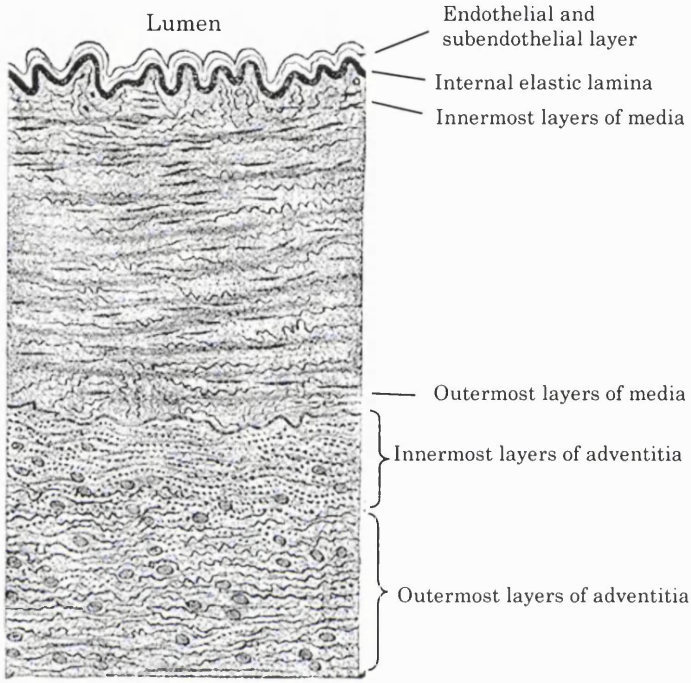

Figure 1.4 Schematic of a cross section of the wall of a middle sized artery showing the wall structure (from Grays Anatomy, 2000).

The mechanical force applied on the endothelial layer of the arterial wall due to the flow of blood can be divided into two components. One component acts normal to the wall and represents pressure and the other one acts tangential to the wall and represents shear stress. Although pressure affects all parts of the arterial wall, shear stress principally affects the endothelium. In large arteries and in uniform sections of the vessel away from bifurcations the mean wall shear stress typically ranges between 20 and 40 dyn/cm^2. However, in regions of disturbed and separated flow the shear stress will be negative or zero within the separation region and up to 40 and 50 dyn/cm^2 in its vicinity. These values vary both in magnitude and sign throughout the cardiac cycle. The morphology and orientation of endothelial cells often reflects the hemodynamic conditions that they have been exposed to. The alignment of the endothelial cells reflects the mean direction of the shear stress. In regions of axial laminar

flow shear stress is unidirectional and endothelial cells tend to align to the flow direction. However, in regions of disturbed flow where there is no prevailing mean shear stress direction, the endothelial cells show no preferred orientation.

Hemodynamic interactions between the endothelial cell and shear stress are mediated through the cell surface. *In vitro* studies (Tardy et al., 1997; White et al., 2001) have demonstrated that it is not only shear stress magnitude but also spatial and temporal gradients of shear that affect endothelial behaviour. In order to understand these complex interactions it is necessary to study the hemodynamic forces at a subcellular scale. It has been shown that endothelial cells are able to differentiate their response to flow environment conditions such as the frequency of the blood oscillatory motion.

One of the primary functions of the endothelium is vasoregulation. A number of vasoregulatory factors associated with the endothelium have been identified. Nitric oxide is the principal endothelial-derived relaxing factor with its release modulated by shear stress. Additional control of the vasoregulatory process is provided by prostacyclin, a vasodilator which is synthesised and released by the endothelial cells in the presence of high shear stress. Endothelin, a vasoconstrictor, is also synthesized and released by endothelial cells in response to changes in the shear stress exposure of the endothelium.

1.2.1 Atherosclerosis and Vascular Hemodynamics

Atherosclerosis alters the mechanical properties of arteries. The initial response of the vessel to the development of an atherosclerotic lesion is dilatation. This response allows the vessel to maintain a normal size lumen and continues until the lesion occupies approximately 40 percent of the vessel cross-sectional area. Studies in the coronary arteries have shown that further growth of the lesion cannot be accommodated by dilatation and inevitably leads to stenosis.

At an early stage atherosclerotic lesions are soft and have minimal impact on the wall stiffness. As the lesions enlarge, they cause a degradation of the load-bearing components of the wall that may lead to a reduction in wall stiffness. Eventually calcification of the atherosclerotic plaque leads to a significant stiffening of the artery.

It is well known that certain sites in the human circulation are more prone to the development of atherosclerotic lesions. Such sites are associated with disturbed and separated flow typically found in the vicinity of bifurcations and branches or regions of significant curvature or stenosis. Certain arteries are more susceptible to disease than others partly due to the differences in the structural properties of the wall but primarily due to the differences in the hemodynamic conditions. It has been demonstrated that atherosclerotic lesions are predominantly found in sites exposed to low mean wall shear stress (Caro et al., 1969) usually associated with flow separation and flow reversal. The exposure of the endothelium to low mean and oscillatory shear stress and separated flow triggers the secretion from endothelial cells of shear stress regulated factors that promote coagulation, leukocyte migration and smooth muscle proliferation hence promoting the development of atherosclerosis (Figure 1.5). These conditions also affect the survival of endothelial cells (Traub and Berk, 1998).

It has also been established that the flow environment can affect the mass transport characteristics of the arterial wall (Caro and Nerem, 1973, Caro, 1974; Deng et al., 1995). In the early studies by Caro and Nerem (1973) and Caro (1974) blood serum was mixed with ^{14}C-4 labelled cholesterol and the uptake of the label by an excised serum perfused canine common carotid artery was measured *ex vivo*. Two perfusion rigs were run simultaneously. Segments of the excised left and right carotid artery were mounted to the flow rigs and perfused with different rates of shear. The investigators found that a substantial increase in the uptake of the label from the wall occurred with increase of wall shear stress. A later study by Deng et al. (1995) showed that there is a higher accumulation of low-density lipoproteins in areas of the canine carotid wall surface exposed to low wall shear stress and where the permeability of the endothelium is enhanced. They also found that luminal lipid concentration affects the rate of infiltration of lipids into the wall.

A study by Friedman et al. (1981) of a time-varying flow in a realistic physical model of the aortic bifurcation of a subject with mild atherosclerosis indicated a negative correlation between intimal thickness and shear stress. The same study showed a positive correlation between oscillatory shear and intimal thickness. The authors concluded that the presence of low and oscillatory wall shear stress generates hemodynamic conditions that favour the development of atherosclerotic disease.

Atherosclerotic lesions may trigger a wall remodelling and adaptation process similar to that initiated by changes in flow rate (Zarins et al., 1987). It has also been postulated that atherosclerotic lesions may develop as a reaction to endothelial cell injury associated with greater wear and tear induced by high spatial gradients of wall shear stress. This has been supported by in vitro experiments which have shown a strong influence of spatial gradients of shear stress in the migration-proliferation behaviour of endothelial cells (Tardy et al., 1997). However in a recent *in vitro* model study by White et al. (2001) it was shown that temporal gradients of shear caused human endothelial cell proliferation whereas spatial gradients of shear had the same effect on cell proliferation as steady uniform shear stress. Although both studies used the sudden expansion flow chamber to generate high spatial shear gradients, White et al. (2001) introduced sudden onsets of flow to generate temporal gradients of shear.

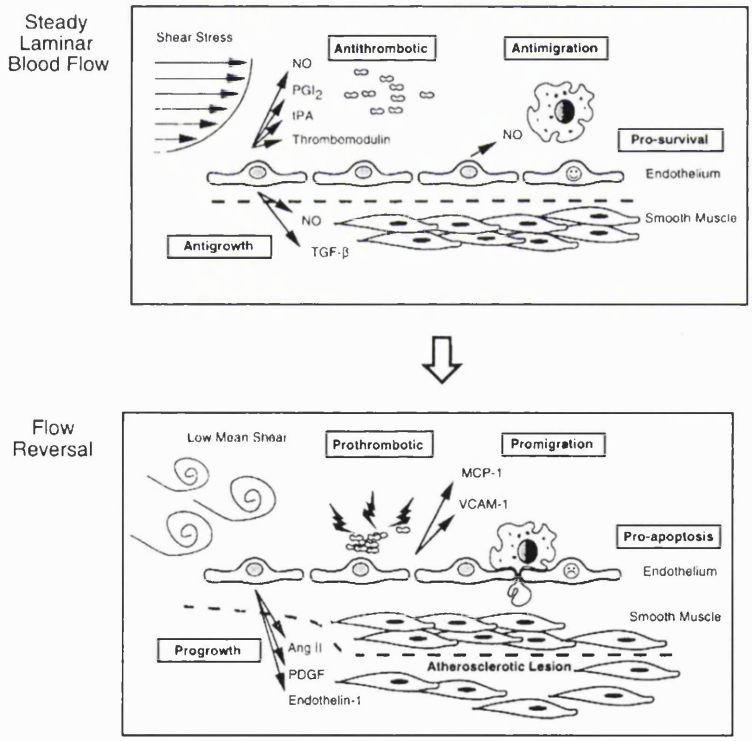

Figure 1.5 Endothelial cell biology and shear stress. The endothelium responds to steady laminar shear stress by releasing factors that inhibit coagulation, migration of leukocytes, and smooth muscle proliferation, and support endothelial cell survival. Conversely, the exposure of the endothelium to low mean shear stress and flow reversal triggers the release of factors that favours the opposite effects, hence promoting the development of atherosclerosis. PGI2 indicates prostacyclin; tPA, tissue plasminogen activator; TGF-beta, transforming growth factor-beta; Ang II, angiotensin II; PDGF, platelet-derived growth factor; VCAM-1, vascular cell adhesion molecule 1; MCP-1, macrophage chemo attractant protein 1; and NO, nitric oxide.(From Traub and Berk, 1998).

1.2.2 Atherosclerosis in the Coronary Arteries

Sabbah et al. (1986) studied a group of patients without obstructive left anterior descending (LAD) coronary artery disease to establish whether a correlation between low shear stress and atherosclerosis does exist. They assessed blood velocity and shear stress distribution in the LAD qualitatively from the clearance rate of a contrast material injected in the left main coronary artery from selective arteriograms. Regions of rapid and slow clearance were considered sites exposed to high and low shear stress respectively. In all cases there was slower clearance of contrast material along the inner wall (in contact with the myocardium) as compared to the outer wall of the vessel suggesting a skewed velocity profile in the LAD associated with the curvature of the vessel. Pathologic studies of the LAD in a different group of patients who died of non-cardiac disease revealed an uneven distribution of atherosclerosis between the inner and outer wall of the LAD with a preferential concentration of disease on the inner wall supporting the argument that atherosclerosis preferentially develops at sites of the wall exposed to low shear stress. A similar pattern of atherosclerotic distribution was also found in the right coronary arteries (Sabbah et al., 1984).

An earlier study by Fox et al. (1982) attempted to correlate the distribution of atheromatic lesions in the coronary arteries with the geometry of the vessel. They histologically examined 41 sets of vessels from subjects under the age of 40 who had died from non-cardiac disease. Vessels affected from early fatty disease were only analysed. The LAD was shown to be affected earlier and more severely by both fatty and fibrous disease. It was found that in most cases plaques were proximally concentrated. A higher concentration of disease along the inner wall of the major curvature was identified in the right coronary artery. In the LAD a spiralling distribution of lesions was observed possibly attributed to the helical flow patterns associated with the highly three-dimensional geometry of the LAD. It was also observed that regions of the wall near the flow divider in the LAD and circumflex arteries were spared of disease suggesting a significant role of the local hemodynamics on the distribution of wall lesions.

Sabbah et al. (1984) visualised the steady and time-varying flow patterns in a mold of the left coronary artery of a pig using dye injections in the sinus of Valsava. Reynolds numbers in the range of 60 to 300 were used for the steady flow experiments.

A Womersley number of 2.8 and a peak Reynolds number of 131 in the LAD were used to simulate flow conditions at rest. A Womersley number of 3.7 and a peak Reynolds number of 340 were used to simulate reactive hyperemia. The primary flow feature identified was a helical flow pattern in the distal part of both the LAD and the circumflex arteries. This pattern was more pronounced at higher Reynolds numbers and was attributed to the secondary flow motion associated with the complex curvature of the epicardial coronary arteries as they coursed along the heart surface.

In a later study by Altobelli and Nerem (1985) the flow in perfused coronary arteries of preserved excised baboon and canine hearts was measured by pulsed Doppler velocimetry. A series of velocity measurements at the left main, the LAD and the circumflex coronary arteries were conducted in pulsatile flow with a range of mean Reynolds numbers between 50 and 500 and Womersley numbers between 2 and 3.5. Skewed velocity profiles towards the free surface of the vessel corresponding to the outer side of the curvature were observed near the bifurcation of the left main into the LAD and circumflex coronary arteries. This flow pattern would be expected for viscous curved tube flow. The pattern of velocity profile skewness observed appeared to be determined by the bifurcation angle between the daughter vessels and the out-of-plane curvature of the bifurcation.

Asakura and Karino (1990) also investigated the role of hemodynamics in the localisation of atherosclerosis in human coronary arteries. They used flow visualisation techniques to monitor the behaviour of suspended tracer particles under steady and pulsatile flow in their realistic rigid wall models of human coronary artery segments. Atherosclerotic lesions were found almost exclusively on the outer wall of the daughter vessels and the inner walls of curved arterial segments. These sites were exposed to secondary flow, separated flow and low wall shear stress. Helical flow patterns were also reported in the vicinity of the junction region of coronary bifurcations.

He and Ku (1996) used numerical methods to study the flow in a left coronary artery bifurcation model based on mean geometric parameters under pulsatile flow. A coronary waveform with a mean Reynolds number of 240 and a Womersley number of 2.8 was prescribed at the inlet. Skewed velocity profiles were found in both the LAD and circumflex arteries towards the inner walls of the bifurcation. Time averaged shear stress was significantly lower on the outer walls as compared to the inner walls

of both daughter vessels in the vicinity of the bifurcation. It was also found that oscillatory shear was higher on the outer walls as compared to the inner walls. According to He and Ku (1996) the localisation of sites exposed to low and oscillatory shear correlates well with the distribution of atherosclerotic lesions reported in literature.

1.2.3 Intimal Hyperplasia in Vascular Grafts

Intimal hyperplasia is the primary cause of restenosis and loss of patency in vascular reconstructions. Intimal hyperplasia consists of both cellular and extracelllular elements in a laminated form. Smooth muscle myoblasts, myofibroblasts and degenerating myocytes constitute the primary cellular components. Fibrous collagen, elastin and amorphous ground substance constitute the extracellular matrix. A study in dogs by Berguer et al. (1980) has indicated that intimal hyperplasia preferentially develops in regions of low volume flow rate and low flow velocity. It was also shown that media thickness was not affected by either the volume flow rate or the flow velocity. It was later identified by Zarins et al. (1987) that shear stress and not volume flow rate and flow velocity was the primary modulator of intimal thickening. Shear stress was also found to play an important role in vasoregulation. A mean value of 15 dynes cm^{-2} is found to be the target arteries strive to maintain by adapting their diameter to the flow forces (Zarins et al., 1988; Glagov et al., 1988; Giddens et al., 1990).

Intimal hyperplasia has been found to preferentially occur in regions of low wall shear stress, flow stagnation, and flow separation (Asakura and Karino, 1990; Ojha et al., 1994). These findings have been initially observed in models but have also been confirmed *in vivo*. It is postulated that the endothelium is histologically disturbed in regions of complex flow. These disturbances attract platelets monocytes and leukocytes which access the wall triggering the biological processes responsible for intimal hyperplasia.

Several factors associated with the hemodynamics of vascular grafts and their effects on intimal hyperplasia have been investigated. An acute anastomosis angle has been shown to cause greater intimal thickening as compared to milder angles (Crawshaw et al., 1986). This is partly explained by the sensitivity of the size of the separation region that develops distal to the anastomosis junction on the anastomosis angle (Ojha et al., 1994). Compliance mismatch has also been commonly cited as a mechani-

cal factor that influences the development of intimal hyperplasia. A study of iliofemoral bypass grafts in dogs by Bassiouny et al. (1992) showed that intimal thickening at the suture line level was associated with wound healing and they hypothesised with compliance mismatch. Considering however that the observed intimal thickening on the arterial floor of the recipient artery should not be affected by graft compliance; the authors suggested that it was associated with the exposure of the wall to low and oscillatory shear stress.

Further investigations on end-to-side anastomosis models have revealed the development of an oscillating stagnation point along the bed of the host artery (Ojha et al., 1994). Intimal hyperplasia is found to preferentially develop on the floor of the recipient artery at the sites exposed to the oscillating stagnation point. Flow stagnation increases the residence times of platelets, platelet derived growth factors and other cytokines that may interact with the endothelium and trigger the biological processes responsible for intimal thickening. Ojha et al. (1994) obtained a second set of measurements where a slight protrusion was introduced on the bed wall of the distal end-to-side anastomotic junction to simulate tissue overgrowth. Based on these results they postulated that the thickened intima in the lumen might not necessarily constitute a lesion, unless grown in excess, but rather an adaptive response of the intima to the hemodynamic conditions.

1.3 Flow MRI – Theory and Techniques

A brief overview of the physical principles of nuclear magnetic resonance (NMR) is presented in the following section. This will be followed by an introduction to spatially localised NMR, which is known as magnetic resonance imaging (MRI), including a section outlining the various sources of error affecting the quality of MR images. The basic MRI methods that utilise flow effects to generate image contrast are introduced. The phase-velocity mapping imaging technique is outlined and the sources of error affecting the accuracy of the velocity measurements are discussed.

1.3.1 NMR

Nuclear magnetic resonance started as an experiment in physics following its discovery almost simultaneously by two independent groups in 1946, by Bloch et al.

(1946) at Stanford, and Purcell et al. (1946) at Harvard. This discovery won both Bloch and Purcell the Nobel Prize in 1952. However, it was not until the seventies that NMR was first used in medical applications (Damadian, 1971; Lauterbur, 1973; Mansfield et al., 1976; Andrew et al. 1977). The first commercial clinical scanners came out in the early eighties.

One of the fundamental physical principles of NMR is that a charged particle in motion will have a weak magnetic field associated with it. Spinning, nuclear, charged particles possess angular momentum quantized in units of Planck's constant divided by 2π. A constant 'I referred as the nuclear spin quantum number or nuclear spin can be used to classify nuclei. Nuclei with zero spin cannot experience nuclear magnetic resonance. According to the quantum-mechanical description of NMR for a nucleus with spin angular momentum $\boldsymbol{I}$ exposed to a strong, external, static magnetic field $\boldsymbol{B_0}$ there are only $2I+1$ possible orientations with respect to the orientation of the external field and thus only $2I+1$ possible energy states. The hydrogen nucleus, which is abundant in the human body, consists of a single proton and has a nuclear spin $I = ½$. Therefore only two ($2\times½ +1$) energy states are possible for the hydrogen nucleus. In the presence of a strong external magnetic field these two energy states associate the relative orientation of the magnetic field of the spin with the orientation of the external field. The spin is in a high-energy state when it is oriented antiparallel to the external field. Similarly, it is in a low energy state when it is oriented parallel to the external field. The energy difference (ΔE_m) between these two energy states is given by:

$$\Delta E_m = \gamma \hbar B_0 , \tag{1.25}$$

where γ is the gyromagnetic ratio, a physical property of the nucleus ($\gamma/2\pi = 42.5759$ MHz/T for H^1), $\hbar$ is Planck's constant divided by 2π, and B_0 is the flux of the external magnetic field. Transitions between these two energy states occur with the absorption or emission of energy in the form of electromagnetic waves, therefore constituting the signal source measured in NMR. Transitions are induced when energy supplied in the form of an electromagnetic field is absorbed by the spin system. In order for energy to be absorbed by the spin system it must be supplied exactly at the resonance frequency, which is the angular frequency (ω_0) of the magnetic moment. A fundamental equation in NMR is the Larmor equation:

$$\omega_0 = -\gamma B_0, \tag{1.26}$$

which describes the relationship between the angular or precessional frequency of a nuclear moment and the applied external magnetic field B_0.

At equilibrium there is a small fractional excess spin population in the lower energy state which is governed by the Boltzmann distribution:

$$\frac{n^+}{n^-} = e^{-\frac{\Delta E_m}{kT}} = e^{-\frac{\gamma \hbar B_0}{kT}}, \tag{1.27}$$

where n^+ and n^- are the fractions of the spin population in the high and low energy state respectively, k is Boltzman's constant and T is the absolute temperature of the spin system which is equal to the lattice temperature at equilibrium. For hydrogen nuclei in a one Tesla field the excess population is only approximately three parts per million. In a macroscopic scale this excess population provides a net magnetic moment and is the source of signal in NMR. It is this property of NMR that makes it a technique with an inherently extremely low signal. This minute signal can be detected by a RF (Radio Frequency) coil following the excitation of the spin system by an oscillating electromagnetic field $\boldsymbol{B}_1$ oriented normal to the main, static, magnetic field $\boldsymbol{B}_0$. It is important to note that in even the smallest volume there will be a significant fraction of Avogadro's number of nuclei. Therefore, in NMR we are not concerned with single nuclei but rather with a net magnetic moment $\boldsymbol{M}$, which is the vector sum of a large number of individual magnetic moments and which at equilibrium is aligned with the static field. The net magnetic moment $\boldsymbol{M}$ of an excited volume of spins will undergo a nutation (a rotating process around the $\boldsymbol{B}_1$ axis) during the application of the oscillating RF field gradually achieving higher energy state orientations. After the cessation of the RF field, $\boldsymbol{M}$ will relax towards its equilibrium lower energy state parallel to the static main field at an exponential rate characterised by the spin-lattice relaxation constant T_1.

Figure 1.6 shows a schematic of this nutation process. Following the application of the 90 degrees RF pulse the net magnetic moment $\boldsymbol{M}$ of the spin system is tilted away from the direction of the external field B_0 by 90 degrees and into the transverse plane through a rotating process around the B_1 axis, termed nutation. After the cessation of the excitation pulse the spins will, due to the slight differences in their local magnetic environment and T_2 relaxation effects, start precessing at different frequen-

cies and therefore gradually become out of phase with each other. This loss of phase coherence results in the reduction of the net magnetic moment component in the transverse plane and consequently the strength of the detected NMR signal. This relaxation process is exponential in nature and is described mathematically by Equations (1.28) and (1.29). After a period approximately equal to 5 T_1 the spin system will return to its equilibrium state with its net magnetic moment aligned with the main static field.

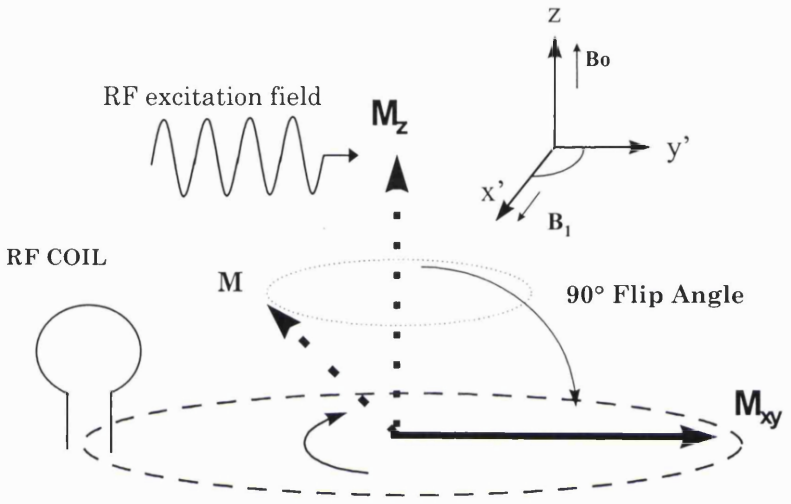

Figure 1.6 Schematic of the NMR signal generation process.

The net magnetisation vector has two components: the longitudinal and the transverse. The longitudinal is typically oriented along the Z-axis which is typically the long axis of the magnet bore (M_L or M_z) and the transverse typically lies on the XY plane (M_T or M_{xy}). The transverse component decays at an exponential rate with a constant T_2, termed the spin-spin relaxation constant. The equations that govern the relaxation of the longitudinal (M_z) and transverse (M_{xy}) components of the net magnetisation (M) follow:

$$M_z(t) = M(1 - e^{-t/T_1}) + M_z(0)e^{-t/T_1} \tag{1.28}$$

$$M_{xy}(t) = M_{xy}(0)e^{-t/T_2}. \tag{1.29}$$

where t is the time after excitation, $M_z(0)$ is the magnitude of the longitudinal component of the magnetisation immediately after excitation (t=0) and, M is the magnitude of the net magnetisation at equilibrium (when $\boldsymbol{M}$ is aligned with $\boldsymbol{B_0}$).

Bloch et al. (1946) successfully derived a set of equations which described the behaviour of the macroscopic magnetisation $\boldsymbol{M}$ in the presence of an RF field. The effect on the motion of an assembly of spins characterised by $\boldsymbol{M}$ from the presence of an applied field $\boldsymbol{B}$ can be described by the following equation:

$$dM / dt = \gamma \boldsymbol{M} \times \boldsymbol{B}, \tag{1.30}$$

which, after breaking the vector product into its components and adding magnetisation relaxation effects, can take the final form of the Bloch equations :

$$dM_x/dt = \gamma (M_y B_0 + M_z B_1 \sin\omega t) - M_x/T_2 \tag{1.31}$$

$$dM_y/dt = \gamma (M_z B_1 \cos\omega t - M_x B_0) - M_y/T_2 \tag{1.32}$$

$$dM_z/dt = -\gamma (M_x B_1 \sin\omega t + M_y B_1 \cos\omega t) - (M_z - M_0)/T_1, \tag{1.33}$$

where B_0 is the static magnetic field strength aligned with the Z axis and B_1 is the strength of the oscillating magnetic field in the XY plane. Bloch showed that the transverse component of the net magnetisation vector $\boldsymbol{M}_{xy}$ can be measured as a small signal induced in an RF coil and that B_1 could be provided by an RF coil on any axis normal to the Z axis.

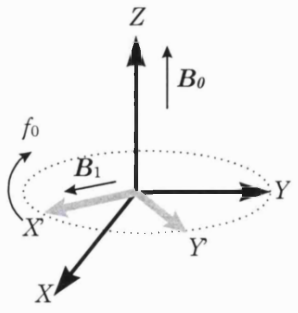

Figure 1.7 The frames of reference used to define the various planes in MRI. The laboratory frame XYZ is coupled with the rotating frame of reference $X'Y'Z$. The frequency of rotation (f_0) is the Larmor frequency of the spins.

In most cases it is more convenient to describe the motion of the magnetic moment $\boldsymbol{M}$ with respect to a frame of reference rotating with angular velocity $\omega_0 = 2\pi f_0$ in the transverse-XY plane, where f_0 is the Larmor frequency of the spin system (Figure 1.7).

1.3.1.1 Spatially localised NMR

The signal detected by the RF receiver coil is spatially encoded with the application of relatively small, linear perturbations of the main static magnetic field, termed magnetic field gradients. In the presence of these gradients the precessional frequency of spins contained in a small volume will be determined by their position in the linearly perturbed magnetic field according to the Larmor equation. Three sets of gradients in the X, Y and Z physical axes that are mapped to the logical axes termed by convention as readout, phase encoding and slice select respectively are part of an MRI system. By applying linear combinations of these gradients the NMR signal can be encoded to contain information from slices at any physical plane orientation. Typically, the NMR signal source is spatially encoded by an application of magnetic field gradients along both the X and Y directions defined by the imaging plane, resulting in a frequency and phase modulation of the NMR signal. The resulting frequency and phase information forms the Fourier or k-space image. To map information from Fourier space back to physical space and form the MRI image, a two dimensional inverse Fourier transform is applied.

The time sequence of events during an MRI experiment can be depicted in a pulse sequence diagram. A pulse sequence diagram of a typical spin-echo sequence is shown in Figure 1.8. A 90 degrees RF pulse excites the spin system which generates the free induction decay signal (FID), an NMR signal which is not spatially encoded. In order to rephase the excited spin system a 180 degrees refocusing RF pulse is applied. This inverts the phase of the spins which initiates a rephasing process. Phase coherence is achieved after the refocusing pulse with a time delay equal to the time interval between the centres of the excitation and refocusing RF pulses. At the centre or peak of the 'echoed' NMR signal spins are exactly rephased.

In order to selectively excite a volume of spins, a slice selection magnetic field gradient is applied in the slice select axis during the application of the excitation RF

In order to selectively excite a volume of spins, a slice selection magnetic field gradient is applied in the slice select axis during the application of the excitation RF pulse. The bandwidth of the excitation pulse and the strength of the slice select gradient determine the thickness of the excited volume of spins (slice thickness). To compensate for the dephasing effects of the slice select gradient a refocusing lobe (inverted lobe) is added on the slice select (GS) axis. In order to spatially encode the NMR signal detected by the receiver RF coil, two additional magnetic field gradients are applied along the *X* and *Y* physical axes. These magnetic field gradients encode the NMR signal in frequency and phase and hence termed frequency encoding or readout (GR) and phase encoding (GP) gradients respectively. The phase encoding gradient is applied before the application of the frequency encoding gradient and in steps of increasing strength. Each phase encoding step represents a line in the k-space image and provides spatial localisation in the *Y*-axis direction.

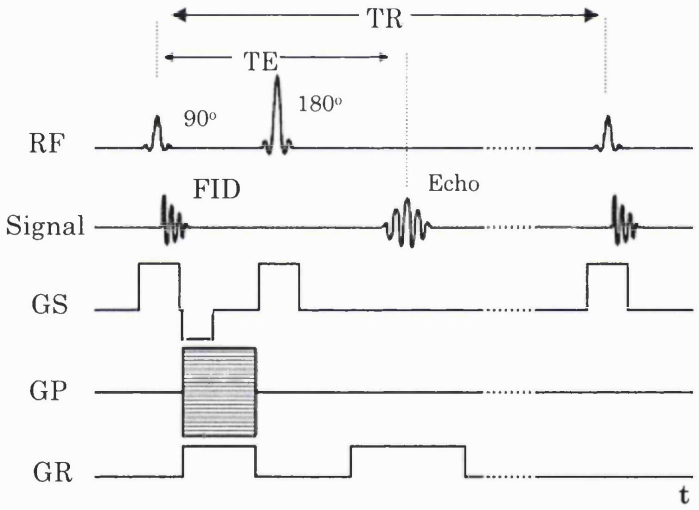

Figure 1.8 A pulse sequence diagram of the spin echo sequence. The evolution of the slice select (GS), phase encoding (GP) and readout (GR) or frequency encoding gradients with time is shown. The free induction decay signal, the Echo signal, the 90 degrees (excitation) and 180 degrees (refocusing) RF pulses, the echo time (TE) and repetition time (TR) intervals are also shown.

The frequency encoding gradient applied during the NMR signal collection period, is typically centred around the peak of the measured echo signal and provides spatial localisation in the X direction (forming the rows in k-space). Image data in k-

space are two-dimensional inverse Fourier transformed to form the image in physical space.

Another faster and widely used MR imaging technique is the field echo or gradient recalled echo or gradient echo (GRE) technique (Figure 1.9). The 180 degrees refocusing RF pulse is eliminated and the read-out gradient is modified to be bipolar. The inverted lobe in the read-out direction will dephase spins that will be subsequently refocused by the positive lobe. The elimination of the 180 degrees RF refocusing pulse reduces the echo and repetition times allowing for faster acquisitions thus reducing the sensitivity of the technique to motion effects and reducing the total amount of RF power applied to the patient. However, at the same time the static sources of proton dephasing, static magnetic field (B_0) inhomogeneities and magnetic susceptibility gradients, are not eliminated as in the spin echo sequence and therefore contribute to transverse magnetisation decay. This decay process occurs at a faster rate in a gradient echo sequence with a shorter relaxation time constant T_2^* as compared to the true T_2 relaxation time constant for a spin echo sequence ($1/T_2^* \geq 1/T_2$). The spoiler gradient on the slice select axis is applied to dephase spins completely and eliminate any residual transverse magnetisation before the application of the next RF excitation pulse.

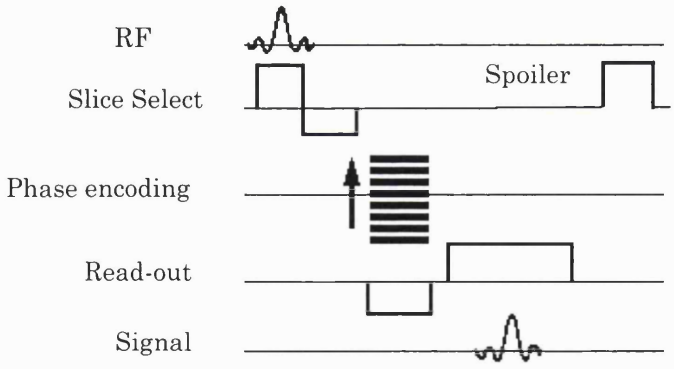

Figure 1.9 A typical field or gradient echo pulse sequence diagram with the addition of a spoiler gradient.

Sources of error in MRI

MRI is a highly complex experimental technique and is affected by a number of artifacts caused by both internal and external to the system sources. A short overview

of some of the most common artifacts affecting the quality of conventional magnetic resonance imaging results follows.

Chemical shift

This type of artifact is based on the principle that nuclei bound to different molecules resonate at slightly different frequencies when exposed to the same external magnetic field. The difference in precessional frequency originates from the principle that a nucleus bound to a molecule experiences a magnetic field which has been slightly altered by the shielding effect of the electron cloud of that molecule surrounding the nucleus. For molecules in rapid motion the coefficient which determines the field that the nucleus experiences, termed the shielding factor, can be treated as a simple number since its directional part averages out (Becker, 1980). If the simple case of hydrogen nuclei bound to two different molecules is considered, the presence of a chemical shift in the volume of interest has two effects. The first effect is a sinusoidal modulation of the NMR signal intensity versus echo time. The frequency of the modulation will be equal to the difference in chemical shift i.e. the precessional frequency difference between the spins bound to the two molecules. The amplitude of the modulation will be determined by the relative concentration of the molecules in the sampled volume. For example, if water is mixed with a molecule 'G' to which hydrogen nuclei are bound and a chemical shift between the precessional frequencies of protons bound to water and those bound to molecule 'G' exists (Figure 1.10), it is possible to ensure phase coherence at the centre of the echo by appropriate selection of the echo time.

The modulus of the NMR signal measured ($\boldsymbol{M}_{XY}$) is given by the modulus of the vector sum of $\boldsymbol{M}_G$ and $\boldsymbol{M}_{H_2O}$ according to following expression:

$$\left|\boldsymbol{M}_{xy}\right| = \left|\boldsymbol{M}_G + \boldsymbol{M}_{H_2O}\right| = \sqrt{\left|\boldsymbol{M}_G\right|^2 + \left|\boldsymbol{M}_{H_2O}\right|^2 + 2\left|\boldsymbol{M}_G\right|\left|\boldsymbol{M}_{H_2O}\right|\cos(\phi)}\,, \qquad (1.34)$$

where, ϕ is the angle between $\boldsymbol{M}_G$ and $\boldsymbol{M}_{H_2O}$. The above expression is maximised for $\phi =$ 0, i.e. when phase coherence has been restored. However reducing phase incoherence due to a chemical shift effect may require an increase in the minimum echo time. If this increase is significant the effects on image *SNR* due to the additional T_2

relaxation of the spin system before readout and the effects on the measurement uncertainty due to the accentuated echo time related artefacts should be considered.

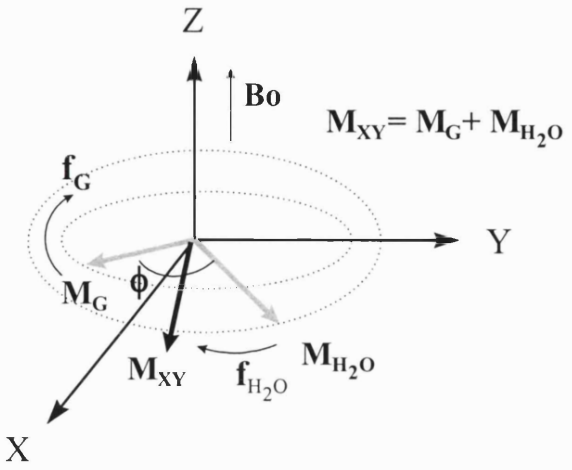

Figure 1.10 Chemical shift. Schematic of the relative contribution to the net transverse magnetisation vector ($\boldsymbol{M}_{XY}$) from each of its two major components. The magnetisation vector component of the protons bound to the molecule G ($\boldsymbol{M}_G$) and the magnetisation vector component of the protons bound to the water molecule ($\boldsymbol{M}_{H_2O}$). The difference between the precessional frequencies f_g and f_{H_2O} is determined by the chemical shift between the two molecules.

The second effect of chemical shift will be the presence of two overlapping representations of the object being imaged in the final MR image, shifted with respect to each other in the frequency encoding direction. The spatial extent of this shift in the frequency encoding direction will be determined by the chemical shift between the two molecules and the frequency resolution of the acquisition.

Magnetic field inhomogeneities

The homogeneity of the main external magnetic field varies in the MRI scanner magnet bore. Most magnets have a region of high magnetic field homogeneity (<10 ppm) in a volume termed 'sweet spot' at their isocenter. The magnetic field becomes less uniform according to a non-linear function of distance from the isocenter. Magnetic field inhomogeneity causes dephasing of spins in addition to that predicted by NMR theory (T_2). To account for this additional dephasing of spins, the dephasing caused by the application of magnetic field gradients and other sources, T_2^* the experimentally observable T_2, has been introduced. Gradient echo techniques are more susceptible to these types of artifacts compared to spin echo techniques due to the lack of an 180 degrees refocusing RF pulse. The use of a magnetic field gradient to refocus

spins and form the echo in GRE techniques does not compensate for magnetic field inhomogeneities as well as the 180 degrees RF refocusing pulse. This is because the 180 degrees RF refocusing pulse reverses the effects of magnetic field inhomogeneities on spin phase in order to refocus spins.

Magnetic field distortions can also be introduced by the presence of a patient in the magnet bore due to their non-uniform shape and tissue content. Main field distortions can also occur from the presence of metal objects such as metal clips in the bore. These local distortions of the magnetic filed will cause artifactual variations in the generated MR images. Artifacts can also result from non-uniformities in the oscillating field supplied by the transmit RF coil and from non-uniformities in the sensitivity of the receive RF coil. B_1 non-uniformity related artifacts appear as variations in the MR image intensity throughout the object.

Gradient non-linearities

Ideally the magnetic field gradients generated by the activation of the gradient coils should be linear within the boundaries of the maximum operating field of view specified by the manufacturer of the MRI scanner. Unfortunately this is not always true; linearity of the magnetic field gradients deteriorates usually outside the 'sweet spot' or isocenter of the scanner. NMR signal from regions of gradient non-linearity will be incorrectly encoded spatially and therefore objects or part of objects extending to these regions will appear geometrically distorted in the resulting MR image.

Flow encoding techniques will also be affected from gradient non-linearities since they rely on the application of gradients to encode spins in motion. Magnetic field non-linearites arise from a higher order magnetic field perturbation in addition to the linear imaging gradient (termed concomitant or Maxwell field) in agreement with the Maxwell equations $\nabla \cdot \boldsymbol{B} = 0$ and $\nabla \times \boldsymbol{B} \approx 0$. If the static field B_0 and the time-varying linear gradient fields in X, Y and Z directions (G_x, G_y, G_z) are active at the same time, then the total magnetic field B in a cylindrical gradient system is given by (Bernstein et al., 1998):

$$B = B_0 + G_x x + G_y y + G_z z + \frac{1}{8B_0} G_z^2 x^2 + \frac{1}{8B_0} G_z^2 y^2 +$$
$$\frac{1}{2B_0}\left[G_x^2 + G_y^2\right] z^2 - \frac{1}{2B_0} G_y G_z yz - \frac{1}{2B_0} G_x G_z yz + \qquad (1.35)$$
$$+(\text{terms with } 1/B_0^2 \text{ order dependence or higher})$$

The first four terms in the above equation represent the nominal magnetic field in the presence of the linear gradients. The following five terms represent higher order magnetic field perturbations which may cause significant phase errors in MRI.

Magnetic susceptibility gradients

Different substances possess different magnetic susceptibilities. Substances can be classified in three broad classes based on their magnetic susceptibility (χ): diamagnetic with no unpaired electrons ($\chi<0$) which are not attracted by a magnetic field as are most tissues in the human body; paramagnetic ($\chi>0$) which contain unpaired electrons and are weakly attracted by a magnetic field such as Gadolinium (Gd); and ferromagnetic ($\chi>>0$) which are strongly attracted by a magnetic field such as iron (Fe).

At interfaces between substances with significantly different magnetic field susceptibilities a magnetic field gradient develops. This gradient locally distorts the magnetic field, which results in signal loss and in a displacement type artifact in the MR image. A positive correlation exists between the level of magnetic field distortion and the strength of the magnetic susceptibility gradient that creates it.

Motion effects

The effects of spins in motion on the phase and magnitude of the NMR signal have been utilised to produce contrast between flowing and stationary spins in time-of-flight and phase contrast techniques. In conventional MRI however, motion effects are usually detrimental to the quality of the acquisition data and many techniques have been developed to suppress these effects. Even in flow imaging it is important to suppress certain motion effects on the NMR signal associated, for example, with the motion of the arteries and their supporting structures such as the motion of the heart wall. These types of motion effects are the main obstacle in high quality coronary artery imaging. Respiratory motion effects have been studied in detail by Axel et al.

(1986) using computer simulations of MRI and by imaging healthy volunteers. They demonstrated that in conventional 2DFT MRI with sequential phase encoding increments a maximum motion related ghost separation from the primary image could be achieved by selecting the product of the number of signal averages and TR equal to one-half the respiratory period. In contrast, minimum separation between ghost artifacts and primary image was achieved by selecting a phase encoding increment separation equal to the respiratory cycle. Furthermore the amplitude of the ghosts can be reduced by increasing the number of signal averages due to the smoothing of respiratory variation. It is therefore possible, to minimise respiratory artefacts, without respiratory gating, by careful selection of the imaging protocol parameters. It should be noted however that the application of this approach to reduce respiratory motion artifacts will be problematic in the presence of significant respiratory variability.

Another way to reduce motion effects is to use the navigator echo technique in which motion is measured during acquisition and data are modified accordingly (Wang et al., 1996). This method has found widespread use particularly in conjunction with MRI coronary flow imaging techniques. Breath-hold acquisition techniques have also been used to suppress artifacts associated with respiratory motion effects (Wang et al., 1995). Motion artifacts are also significant in MR flow acquisitions in vessels of the abdomen and the chest supported by tissues subjected to breathing and peristaltic motion. A study by Dumoulin et al. (1993) proposed a technique that suppresses these types of motion artifacts by applying complex data pair subtraction in adjacent views or echoes within the same cardiac cycle when imaging for example the aorta or the iliac arteries.

Spin saturation

A physical phenomenon that has been used to encode spin motion is that of magnetisation saturation. When a volume of spins is subjected to a series of very frequent RF pulses it gradually loses its ability to produce NMR signal. This effect is due to the change of the spin state distribution in the sample volume subjected to the RF pulses. There is a gradual decrease in the excess of spins in the low energy state and a subsequent decrease in the size of the signal generating spin pool. As a result there is

reduction in the net longitudinal magnetisation available for nutation by subsequent RF pulses. NMR signal loss due to spin saturation effects is proportional to the T_1 and T_2 relaxation rates, the square of the oscillating magnetic field strength (H_1^2) and the square of the gyromagnetic ratio of the substance (γ^2). The introduction of contrast agents, which reduce T_1, combined with the use of small flip angles (low H_1) are ways of reducing saturation induced signal loss.

Eddy currents

Eddy currents are small electrical currents induced in conducting material surrounding the gradient coils by the switching of the gradients. These eddy currents produce magnetic field gradients with exponential time constants that oppose the applied gradient hence distorting the temporal profile of the gradient pulses. Therefore they introduce errors in the spatial or flow encoding process. The effects of eddy currents can be corrected by either applying pre-emphasis on the prescribed gradient waveform or by using active shield gradient coils, an extra set of coils external to the main gradient coils designed to null the eddy current inducing magnetic fields before they reach the eddy current conducting material.

Radio frequency related artifacts

In MRI it is common practice to model a slice selective RF pulse after a sinc ($\sin(\pi x)/\pi x$) function. This is because a sinc function in the time domain is equivalent to a square function in the frequency domain or a band pass filter. Exactly this property is employed to selectively excite a volume of spins exposed to a magnetic field gradient.

For practical reasons a temporally constrained RF pulse in the time domain is applied that will result in an imperfect – not exactly square shape – excitation profile in the frequency domain (Figure 1.11). As a result spins external to the volume of interest will be excited by the RF pulse thus introducing artifacts to the resulting image.

Noise from radio frequency interference originating from sources external to the MRI scanner room can contaminate the weak NMR signal if the magnet room is insuf-

ficiently RF shielded. This type of noise is detected by the RF receiver coil and appears as bright signal in the MR image in a line extending in the phase encoding direction at a given frequency.

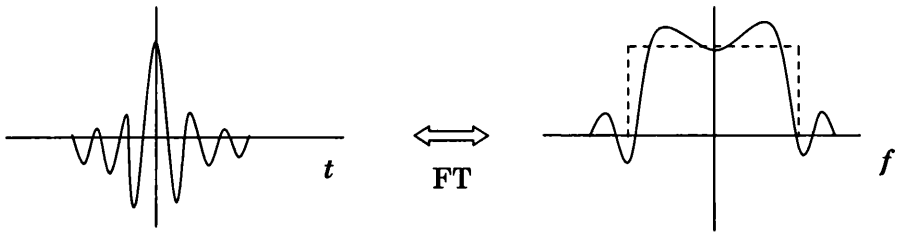

Figure 1.11 A sinc function RF pulse in the time domain (left) yields a square shape RF pulse in the frequency domain (solid line right). If the RF pulse is truncated in the time domain, deviations from the ideal square shape RF pulse in the frequency domain will occur (dashed line right).

Aliasing

Aliasing or wraparound results from sampling a periodic signal with a frequency below that specified by the Nyquist criterion, i.e. two samples per period. In MRI this happens when the selected field of view is smaller than the diameter of the object being imaged. During the application of the RF excitation pulse, which is spatially selective in a single direction only, spins external to the field of view (FOV) in the X and Y directions will be nutated and subjected to the same magnetic field gradient pulses as those within the region of interest. Therefore they will emit NMR signals at frequencies higher than the signal emitted from spins within the FOV boundaries. The sampling rate of the NMR signal during the digitisation process is determined by the FOV, the frequency resolution of the acquisition and, the Nyquist condition. As a result, signal from parts of the object external to the FOV is under-sampled and therefore appears wrapped around an axis defined by the FOV boundaries hence overlapping information in the region of interest. This problem can be eliminated or at least minimised by either selecting a larger FOV and then discard the information external to the region of interest, or alternatively by using a surface RF receive coil which will be sensitive only to signal sources from within a restricted volume encompassed by the coil conductor.

1.3.2 MRI Flow Measurement Techniques

There are two basic physical principles that govern the modulation of the NMR signal from spins in motion. One is the in flow or time of flight (TOF) effect and the other is the phase shift effect. A brief overview of these effects and the associated MRI flow techniques follows. An excellent review of the basic flow imaging techniques based on the effects of blood flow on the MRI signal is given by Axel (1984).

1.3.2.1 Time of flight

Time of flight effects refer to signal variations due to the motion of the nuclei that flow into or out of an imaging volume during a given pulse sequence. Early in the history of NMR and well before the introduction of MRI, blood flow effects on the NMR signal were identified. Suryan (1951) observed changes in the signal from spins in a fluid flowing through a coil. He found that by increasing the mean flow velocity the NMR signal initially increased but then decreased. As the mean velocity increased, partly saturated spins were replaced by fresh fully magnetised spins leading to signal enhancement. However, by further increasing the mean flow velocity the NMR signal was reduced as the spins entering the excitation region had not spent sufficient time in the main magnetic field to become fully magnetised.

Singer (1959) reported one of the earliest measurements of blood flow by NMR applying a spin-tagging technique. Unsaturated moving spins entering the excited volume generated a larger NMR signal compared to stationary spins, a phenomenon known as inflow enhancement. He applied this method for the measurement of venous flow in the human arm. Garroway (1974) offered an early description of an experimental technique to employ both inflow effects and phase effects to measure blood flow. Feinberg et al. (1984) reported one of the earliest true tagged time-of-flight techniques utilising a spatially selective 90 degrees RF pulse upstream of the volume of interest followed by a downstream, slice selective 180 degrees pulse to invert the spins and thereby produce an image of only those spins that where excited upstream.

In both spin echo and field echo or gradient echo sequences, inflow of nuclei between sequence repetitions results in increased signal (*in-flow enhancement*), while for the spin echo sequence, outflow may result in decreased signal due to flow out of the

slice between the 90 degrees and 180 degrees pulses. Enhancement of signal can be explained as follows: when stationary spins (e.g. in tissue) in the volume of interest are repeatedly subjected to RF pulses they become saturated. This results in a decrease of the potential NMR signal from tissue until the full recovery of the magnetisation. Spins that flow into the volume of excitation generate a stronger signal compared to stationary spins since they have not been subjected to previous RF pulses and are unsaturated. This signal enhancement is often observed at the inflow end of slices of a multi-slice acquisition. However, it can also be observed several slices deep into the volume of interest depending on the spin velocity normal to the slice; the 90 degrees RF pulse repetition rate; and the relaxation rates of the excited nuclei.

High velocity signal loss is observed in spin echo imaging in which a slice selective 180^0 refocusing pulse is used. It is a time-of-flight effect as well, in which spins flow out of the volume of interest before they are nutated by both RF pulses. If spins that only experience either a 90 degrees or a 180 degrees pulse, and hence do not contribute to the echo signal, dominate the spin population in the volume of interest, total signal loss occurs. High velocity signal loss can also occur in gradient echo procedures if a large fraction of the excited spins move out of the volume of interest before experiencing the refocusing gradient.

Axel et al. (1986) proposed a time-of-flight method to directly image blood velocities. The technique involved selective excitation of spins in orthogonal planes. Spins in a slice plane normal to the flow direction were selectively excited while spins in a slice plane parallel to and including the flow were selectively refocused by the 180 degrees RF pulse. In the resulting images, the displacement of the excited spins in the direction of the refocusing plane was equal to the product of the flow velocity and the echo time.

In his overview of time-of-flight effects Wehrli (1990) classifies spins in a time of flight experiment based on their excitation history and relaxation rates. Assuming at t=0 the application of a slice selective 90 degrees RF pulse on a volume of interest (slice) oriented perpendicular to the direction of flowing spins, he examines the population of spins in the slice at a time exactly after the application of a slice selective 180 degrees pulse following the second 90 degrees pulse (t = TR+½TE). Assuming that the

velocity of the spins (u) is sufficiently low to prevent complete washout of any population fraction i.e.:

$$u < \frac{L}{(TR + 1/2\,TE)}, \tag{1.36}$$

where L is the thickness of the volume of interest, a maximum of 4 populations of spins can be distinguished in the excited volume at t = TR+½TE based on the history of their prior excitations and relaxation time. These are: a population fraction with no transverse magnetisation, a fraction of fully relaxed spins, a fraction of inverted spins and a fraction of saturated spins. Depending on the magnitude and spatial distribution of the velocity of the spins, the distribution of spins in the above categories changes and with it changes the projected pixel intensities in the MR image.

Nishimura (1990) in his review of TOF angiography describes the three main methods of TOF techniques in angiography: bolus tracking, flow-related enhancement and selective tagging. With bolus tracking a bolus of blood is excited by a 90 degrees RF pulse upstream and then excited by an 180 degrees RF pulse downstream. Static tissue is suppressed since only blood receiving both pulses produces a spin echo. Flow-related enhancement is the term given when fully magnetised blood flows into the volume of interest producing an enhanced signal relative to that of the surrounding static tissue. This is achieved by applying repeated excitation pulses to the region of interest. Finally, in selective tagging two images are acquired; one image (with tagging off) has flow-related enhancement as described above, while for the second image, blood upstream to the volume of interest is tagged by a 180 degrees inversion pulse. Subtraction of these two images suppresses static tissue leaving a signal due only to flowing blood.

1.3.2.2 Phase contrast

The second category of MR angiography techniques are those relying on the flow induced phase shifts. Carr and Purcell (1954) were the first to report a motion induced phase effect and Hahn (1960) was the first to suggest a method of measuring slow seawater motion by detecting the phase shift of the signal due to flow in the direction of the gradient. A number of techniques based on flow induced phase effects have been

suggested since then, using different sequences (Moran, 1982; Bryant, 1984; O'Donnell, 1985).

Phase contrast phenomena are analogues to Doppler shift effects in ultrasound studies. Magnetic spins undergo a frequency shift when moving along a magnetic field gradient; this frequency shift is proportional to their velocity component parallel to the applied gradient direction. The product of this frequency shift and the magnetic field gradient pulse duration gives rise to the overall phase shift relative to stationary spins.

In the presence of a linear, constant in time, magnetic field gradient along the x-spatial co-ordinate, stationary spins at location x_0, resonate at a frequency $\omega = \gamma G x_0$. Spins moving with constant velocity u, in the direction of the gradient, gradually advance towards a higher magnetic field and their resonance frequency increases as (Bohning, 1991):

$$\omega = \gamma G(x_0 + ut) \tag{1.37}$$

Since $\omega = \mathrm{d}\phi/\mathrm{d}t$, the phase shift ($\phi$) of the nucleus can be written as:

$$\phi = \int \omega dt = \gamma \int Gx(t)dt = \gamma \int [Gx_0 + Gut]dt = \gamma [Gx_0 t + \tfrac{1}{2} Gut^2] \tag{1.38}$$

Equation (1.38) shows that the phase increase or phase shift is proportional to the velocity of the spin and the product of the strength and duration of the applied gradient. Generally, the phase shift of a nucleus placed in a time-varying magnetic field gradient G(t) is given by the following expression:

$$\phi = \gamma \int G(t)x(t)dt\,, \tag{1.39}$$

where $x(t)$, is the position of a moving spin at time t and can be described by its Taylor expansion around $t = 0$:

$$x(t) = x^{[0]}(0) + x^{[1]}(0)t + x^{[2]}(0)t^2 \frac{1}{2!} + \ldots + x^{[n]}(0)t^n \frac{1}{n!}, \tag{1.40}$$

where

$$x^{[n]}(0) = \frac{d^n x(0)}{dt^n} \tag{1.41}$$

is the n^{th} order temporal derivative of position x at time $t = 0$.

In blood flow studies in humans, higher than second order terms in the Taylor expansion are typically neglected since acceleration, if present, is approximately constant. However, higher order motion effects can be significant in diseased vessels and for example in the vicinity of an arterial stenosis.

There are essentially three types of flow quantification methods using velocity induced phase shifts. The first category comprises of phase-sensitive angiographic methods. One such method detects flow through a loss of phase coherence due to velocity dispersion within a volume element (voxel). Two images are acquired, one with flow compensation and one without flow compensation. Image subtraction suppresses the signal from stationary tissue leaving only that from flowing blood (Axel and Morton, 1987; Laub and Kaiser, 1988; Spritzer et al., 1990). A second phase sensitive angiographic method uses small flow encoding gradient pulses to produce discrete velocity induced phase shifts. Subtraction of echoes acquired from inverted and non-inverted flow encoding gradient pulses removes stationary tissue signal from the image (Dumoulin and Hart, 1986; Dumoulin et al., 1989). A typical pulse sequence diagram of the bipolar flow encoding gradient flow quantification method is shown in Figure 1.12. The first method relies on velocity induced phase shifts to provide an amplitude modulation of the flow signal, whereas the second method relies on discrete velocity induced phase shifts to produce a phase modulation of the flow signal.

The second category of flow quantification methods is the direct phase velocity mapping methods that use the flow induced phase shifts to measure velocity directly from the phase of the image voxel. Phase velocity mapping was first demonstrated by Van Dijk (1984) and Bryant et al. (1984). Improvements to the initial method were introduced by Young et al. (1986) and Nayler et al. (1986). The phase velocity measurement method has been extensively validated for flow measurement both *in vivo* and *in vitro* (Bryant et al., 1984; Firmin et al., 1987).

The Fourier velocity encoding methods are the third category of methods for flow quantification using velocity induced phase shifts to measure the intravoxel velocity distribution (Redpath et al., 1984; Feinberg et al., 1985; Hennig et al., 1988; Dumoulin et al., 1993). To achieve this, one spatially localising phase encoding gradient is replaced by a bipolar flow encoding gradient. As a result the reconstructed im-

age has one phase-encoded dimension along which signal displacement depends on spin velocity rather than on spin position.

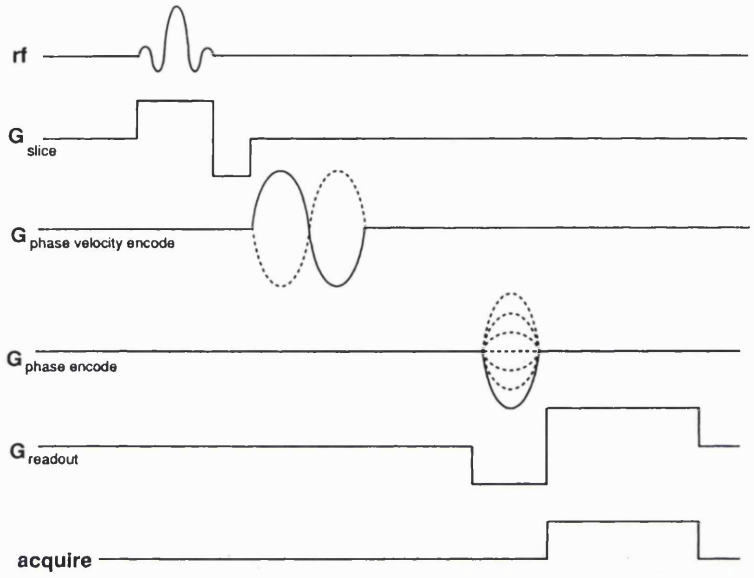

Figure 1.12 A basic pulse sequence diagram of the toggled bipolar phase velocity encoding technique. The flow encoding gradient can be applied on any axis, and the sign of each lobe is inverted on alternate excitations (adapted from Dumoulin et al., 1994).

Bernstein and Ikezaki (1991) compare the two main methods in wide use for subtraction of the two complex data sets obtained through toggled bipolar gradient acquisitions: the phase difference method and the complex difference method. In the phase difference method a phase map image is generated by subtracting the phase information in the two complex data sets acquired. Therefore, each pixel in the resulting image contains a signed phase value where its magnitude is directly proportional to the encoded spin velocity and its sign indicates the flow direction (Figure 1.13). In contrast, in the complex difference method, the magnitude of the complex difference of the complex data sets acquired by the pair of toggled bipolar flow encoding gradient acquisitions is computed. In the complex subtraction method flow direction information is lost; furthermore, the pixel intensity values in the final image are not directly proportional to velocity but rather are given by the following expression:

$$I = k\left|\sin(\gamma u T A)\right|, \tag{1.42}$$

where k is a constant of proportionality that includes spin density and instrument sensitivity, T is the time interval between the centre of the two lobes of the bipolar flow encoding gradient, A is the unsigned area under each lobe of the flow encoding gradient and u is the velocity of the spins in motion. However, if the aliasing velocity (V*enc*) is selected so that the phase shift (ϕ) caused by the highest encoded velocity is less than 1 radian, then the relationship between signal intensity and velocity becomes approximately linear. The main advantages of the complex difference method over the phase difference method are: its insensitivity in the presence of stationary spins together with flowing spins in the same voxel, making the technique more suitable in thick slab acquisitions; and its slightly higher SNR other things being equal.

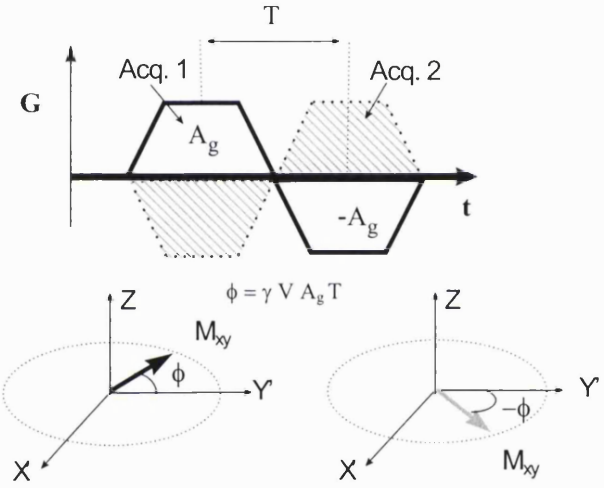

Figure 1.13 The toggled bipolar flow encoding gradient (top) and the phase difference subtraction method (bottom). The time course of the gradient strength (G) of the two bipolar gradient acquisitions (normal-unshaded and inverted-shaded areas) and the time (T) between the centre of the lobes are shown. The signed phase shift from each acquisition is also shown on a rotating frame of reference (X'Y'Z).

Phase contrast techniques have numerous clinical applications in MR angiography of the head and neck (Pernicone et al., 1990), the abdominal vessels (Steinberg et al., 1990; Vock et al., 1991) the peripheral vasculature (Steinberg et al., 1990; Caputo et al., 1992).

In an effort to reduce the echo time, hence reduce phase coherence related signal loss and echo time dependent artifacts in phase velocity mapping, several fast techniques have been developed. The FID acquired echo sequence (FACE) developed by Scheidegger et al. (1991) uses fractional echo acquisitions with sequential separate

sampling of the left and right k-space symmetry planes. Even faster flow and velocity quantification techniques are based on echo planar imaging methods with (Meier et al., 1992; Gatehouse et al., 1994) or without (Firmin et al., 1989; McKinnon et al., 1994) spiral k-space sampling. The application of multidimensional excitation pulses to achieve spatial localisation at excitation combined with time varying readout gradients has been proposed by Hu et al. (1993) to obtain real time single shot velocity measurements. Dougherty and Axel (1995) successfully applied this technique *in vivo* by measuring blood velocities in the portal vein of healthy volunteers in real time.

Sources of error in MR phase velocity measurement

Phase velocity mapping methods are typically based on the gradient echo imaging technique. Therefore they are more sensitive to artifacts such as magnetic field inhomogeneities and magnetic susceptibility gradients due to the absence of the 180 degrees RF refocusing pulse utilised in the standard spin echo technique. The effects of various imaging parameters and flow conditions on the accuracy of MR flow quantification have been reported by Firmin et al. (1990) and Buonocore and Bogren (1992). An overview of the factors that affect the quality of blood flow quantitative MR measurements is given below.

Spatial resolution

The effect of spatial resolution in the measurement error has been studied by various investigators. Poor spatial resolution (i.e. a small number of pixels covering the diameter of a vessel) has been shown to result in large errors from partial volume effects and incorrect lumen segmentation (Wolf et al., 1993; Tang et al., 1993; Hofman et al., 1995). Tang et al. (1993) found that a minimum requirement for accurate flow measurements is approximately 16 pixels across the diameter of the vessel imaged, in the case where the flow encoding direction is parallel to the flow direction. If this requirement is met, flow measurement accuracy within 10 % of the true value can be achieved. The presence of oblique flow will increase the minimum requirement for spatial resolution accordingly. This in turn raises the requirements in image signal-to-

noise ratio (SNR), as SNR can be traded for spatial resolution and vice-versa, rendering high quality flow quantification measurement very demanding in terms of SNR requirements. Polzin et al. (1995) have proposed a flow measurement method whereby information from both phase difference and complex difference processed phase-velocity encoded MR measurements is combined to produce a complex difference flow map that offers improved accuracy of flow quantification compared to the conventional phase-difference processing technique. The improved accuracy was achieved through the estimation of the fractional boundary voxel volume occupied by stationary spins and correcting the boundary voxel velocity for partial volume errors. This was possible due to the insensitivity of the complex difference technique to partial volume effects.

Higher orders of motion

Another potential source of error is the presence of orders of motion higher than velocity in the flow measured. In most cases flow encoding gradients are designed assuming constant velocity during the acquisition period which is typically 6-8 ms or less depending on the velocity encoding sensitivity that determines the area below the bipolar flow encoding gradient lobes. However, this assumption is not always valid. In pulsatile flow significant temporal acceleration may be present, or in steady stenotic flow convective or spatial acceleration is present. The effects of acceleration on the accuracy of MR phase-velocity mapping were investigated by Firmin et al. (1990). By measuring these effects for a physiologically realistic level of acceleration (10 m/s^2) they showed that a negative correlation between the echo time and the level of error introduced due to acceleration effects exists. For echo times of 6, 14 and 22 ms the error introduced was 1.7 %, 3.9 % and 7.9 % respectively. Oshinski et al. (1992) investigated the effect of convective acceleration in a 90 % stenosis on flow measurement error and reported a 37 % error in measurements of mean cross sectional velocity in the stenotic region, where convective acceleration was significant. They also demonstrated a strong negative correlation between echo time and error due to convective acceleration. Siegel et al. (1996) also studied the case of a 90 % area reduction stenotic flow and reported velocity measurement errors in the range of 20-100 % in various sites upstream and downstream of the stenosis. They attributed these large errors to sev-

eral factors including the presence of phase shifts due to convective (or spatial) acceleration, insufficient signal to noise ratio and flow induced spatial displacement artifacts. Acceleration compensated flow encoding gradients could be used to reduce or eliminate the additional phase shifts resulting from higher orders of motion. However, higher order motion compensation carries a penalty of increased gradient duration, leading to a longer minimum echo time that in turn accentuates phase errors. By the same principal it is possible to encode acceleration only and compensate for lower orders of motion.

Spatial misregistration

Flow-induced spatial displacement artifacts can introduce significant errors in cases were oblique flow is present. This is due to the temporal difference between spin phase encoding and frequency encoding (Frank & Buxton, 1993). In routine two-dimensional imaging, a pixel is spatially encoded by both phase and frequency. This process is not instantaneous and, in general, phase encoding precedes frequency encoding. The non-coincidence of phase and frequency encoding results in spatial misregistration of signal from flowing spins which is a frequently observed artifact. Assuming a straight vessel placed at some angle ϕ (Figure 1.14) relative to the frequency encoding axis and a mean delay Δt between the phase and frequency encodings, the spins will have travelled from location A at the time corresponding to the center of the phase encoding gradient to B at the echo time according to:

$$r(t_b) = r(t_a) + u\Delta t, \tag{1.43}$$

where u is the axial velocity of the spins, t_a is the time of the phase encoding and t_b is the time of the frequency encoding.

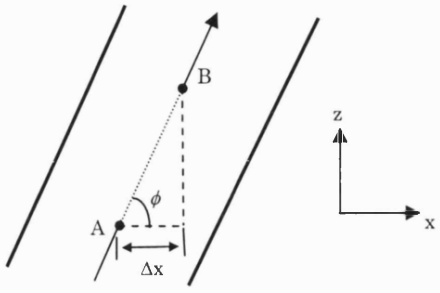

Figure 1.14 The spatial displacement effect.

The spins therefore will be mismapped in the x direction by a distance equal to:

$$\Delta x = u_x \Delta t = u\cos(\phi)\Delta t\,, \tag{1.44}$$

where u_x is the component of the velocity vector in the x direction. It is possible to predict the direction of flow when a flow misregistration artifact has been noted, since Δx is positive when $u_x < 0$ and negative when or $u_x > 0$. However, in complex flows where the in-plane velocity components are strong and not uniformly distributed, misregistration effects can be significant and equally non-uniformly distributed hence their prediction and correction is not straightforward (Steinman et al., 1997). Misregistration effects can be minimised by keeping the delay between phase and frequency encoding minimal. Conversely they will be accentuated if by increasing the echo time the delay between the phase and frequency encoding increases.

Aliasing

A mismatch between the dynamic range of the spin velocities encoded and the velocity sensitivity of the acquisition may introduce errors in flow measurements. Conturo and Smith (1990) applying propagation of error derived a relationship between the SNR of the phase image and the level of utilisation of the dynamic range of the signal sampling process, described by the velocity to noise ratio (VNR) on a voxel to voxel basis:

$$\text{VNR} = \frac{|\Delta\phi|}{\sqrt{2}} SNR_{mag} = \frac{|u|\pi}{\sqrt{2}\ V_{enc}} SNR_{mag}\,, \tag{1.45}$$

where SNR_{mag} is the SNR of the magnitude image, u is the mean velocity of the spins in the voxel and, V_{enc} is the aliasing velocity (i.e. the velocity sensitivity of the acquisition). Increasing the velocity sensitivity (i.e. reducing V_{enc}) of the acquisition by increasing the gradient first moment will, other factors being constant, increase the velocity to noise ratio. A mismatch between the velocity sensitivity and the encoded spin velocity dynamic range will affect the phase velocity image. If the velocity sensitivity is less than the spin velocity dynamic range, the motion induced phase shift is larger than π resulting in phase aliasing or phase wrapping (flow induced phase shifts larger

than π appear in the image wrapped back in the $(-\pi, +\pi)$ range e.g. $3\pi/2 \rightarrow -\pi/2$). If the velocity sensitivity is much higher than the spin velocity dynamic range the velocity to noise ratio of the result will be compromised.

Phase dispersion

One of the primary sources of signal loss in MR flow quantification techniques is intravoxel phase dispersion. This results, for example, from selecting a large voxel when measuring complex flows with high velocity encoding sensitivity. Turbulent flow, characterised by random motion of fluid particles, is another potential source of this type of artifact causing phase cancellation within a voxel and total signal loss. Phase dispersion effects can be reduced by decreasing the echo time thus allowing spins less time for phase accumulation thus a more uniform intravoxel phase distribution. Hence techniques with shorter echo times achieved for example by fractional RF excitations (Nishimura et al., 1988) are less sensitive to phase dispersion artefacts.

Eddy currents

Uncompensated, long time constant, eddy currents in phase contrast quantitative flow acquisitions will result in phase offset errors. These phase offsets will not be cancelled despite the subtraction of the phase components of the data sets acquired in the toggled, bipolar flow encoding gradient technique (Dumoulin, 1986). Peeters et al. (1995) modelled the effects of eddy currents in quantitative flow measurements and found that they will introduce a significant distortion in time resolved velocity measurements, a result that was also supported by appropriate experiments. They also reported that the phase offset error introduced by eddy currents could not be removed by applying background phase correction.

Flow encoding axis misalignment

In cases where a misalignment exists between the flow encoding axes and the bulk flow direction, an error will be introduced in the MR flow measurements. The

measured velocity at radial position r for a fully developed steady flow in a straight rigid pipe will be given by the following expression:

$$u_m(r) = u_t(r)\cos(\phi), \tag{1.46}$$

where u_m is the velocity measured, u_t is the true velocity and ϕ is the misalignment angle. Care should be taken when the flow contains significant in-plane velocity components as a coupling factor between components will contribute to the error of each measured velocity component.

Under sampling

Segmented k-space (or phase encode grouping) acquisitions offer reduced acquisition times but may introduce additional errors to the velocity measurements due to under-sampling and low pass filtering of the flow waveform, thus compromising measurement accuracy. Frayne and Rutt (1995a) found that there are three primary parameters that determine the frequency response for segmented k-space velocity measurements: the number of interleaved velocity encodings, the time between the encodings and the degree of balance between the first moments of the velocity encoding gradients. Li et al. (1995) established that sampling of a flow waveform below the Nyquist frequency due to inappropriate selection of the segment size was responsible for the underestimation of the spatiotemporal mean velocity. Polzin et al. (1996) showed that an increase in the number of views per segment will increase the smoothing or low pass filtering of the reconstructed flow waveform. However, by applying a moving segment window over contiguous views to reconstruct all intermediate flow phases, they found that the Nyquist sampling frequency becomes independent of the number of views. This only strictly applies to vessels that have a uniform *k*-space distribution. However the deviation between the predicted and the measured flow rate within a segment due to the non uniform weighting over the segment duration will be related to the view ordering scheme used. For segmented interleaved view ordering where all of *k*-space is traversed in each segment, the data are heavily weighted towards the point in the flow cycle in each segment where the central k_y-lines are acquired. This results in significant deviations between the measured and the mean flow

rate within the segment. This however is not a problem for segmented sequential view ordering (Foo et al., 1995) where neighbouring views are acquired in each segment and the weighting over the duration of the segment is uniform. Thus the difference between mean and measured flow rate within the segment is not expected to be significant and therefore the analysis of Polzin et al. (1996) applies.

1.4 Thesis Motivation and Aims

The work presented in this thesis is part of a wider study involving researchers from the departments of Aeronautics and Bioengineering of Imperial College and clinical collaborators from St' Mary's and Hammersmith hospitals of the NHS Trust. The study is aimed at better understanding the effects of the geometric configuration and inlet flow conditions on the local hemodynamics in the distal anastomosis of arterial bypass grafts. This thesis examines several aspects of the application of MRI in detailed investigations of the flow field in arterial bypass grafts. Although most of the experiments reported are in models, the techniques presented could be applied *in vivo*.

A large number of bypass grafts are implanted annually, worldwide, for the revascularisation of occluded arteries. However, failure rates of up to 25 % by 1 year for grafts in peripheral arteries (Cheshire and Wolfe, 1993) and up to 50 % by 10 years for grafts in coronary arteries (Bryan and Angelini, 1994) have been reported. The major cause of arterial bypass graft failure is stenosis resulting from intimal hyperplasia. As has been discussed previously in this chapter, although the underlying mechanism responsible for loss of graft patency is not fully understood, vascular hemodynamics is known to play an important role in the initiation and development of the disease processes responsible for the stenosis of the vessel.

Detailed investigations of the local bypass graft hemodynamics can facilitate the elucidation of the link between the disease processes and the flow environment in surgically revascularised vessels.

The role of bypass graft hemodynamics in the development of wall disease has been the subject of a number of experimental and computational investigations. The influence of geometric parameters such as the anastomosis angle, the graft to host artery area ratio, the size of the anastomotic junction, and other factors such as wall compliance, graft inlet flow waveform and graft outflow division on the flow field, have

been investigated both experimentally in animals and in models, and also numerically. Most studies, however, have ignored out-of-plane curvature which is common in human arterial bifurcations. Therefore, one of the primary aims of this thesis is to elucidate the influence of out-of-plane curvature on the distal anastomotic flow field in arterial bypass grafts and consider the pathophysiological implications of such a configuration.

MRI is the primary experimental modality employed in this investigation. It is a non invasive non ionising imaging modality that has been used successfully for *in vivo* velocity and geometry measurements in investigations of vascular pathophysiology. However, due to the lack of sufficient spatial and temporal resolution, it is currently not possible to obtain a detailed description of the distal anastomotic flow field in small calibre revascularised arteries *in vivo*. Small calibre arteries are of particular interest as they are more likely to develop wall disease and become occluded. It was therefore necessary to conduct the flow investigations in scaled idealised or realistic bypass graft models. MRI flow quantification techniques have been extensively calibrated for simple well defined steady and time-varying flows *in vitro* (Firmin et al., 1990; Frayne et al., 1995). However, an assessment of the accuracy of MR phase-velocity mapping of the complex highly three dimensional time-varying flows that are common near arterial bifurcations and in the distal anastomosis of bypass grafts, was lacking. This was problematic due to the absence of a reference data set of sufficiently high accuracy, as no analytical solution for such flows exists. To overcome this problem in this investigation, results obtained from highly accurate numerical computations of the same flows were used as reference. In an effort to improve the accuracy of the phase velocity mapping technique in both steady and time varying complex flows, certain measures were introduced both during data acquisition and post processing. Calibrations of the measurement method for well defined flows and estimates of the accuracy of MR phase-velocity mapping in steady and time-varying complex flows together with methods introduced to improve it are discussed in Chapter 2.

Bypass graft models, ranging from simple idealised ones consisting of rigid tubes to physiologically realistic compliant vascular replicas, have been used to investigate the influence of the various geometric and flow parameters on the local flow field. In this investigation, the influence of graft out-of-plane curvature, inlet flow waveform

and, graft outflow division are considered. For this, results obtained from both MR velocity measurements and numerical computations in both idealised and realistic rigid models of arterial bypass grafts will be discussed. Results from velocity field measurements in planar and non-planar idealised bypass graft models for steady and time-varying flow are discussed in the first half of Chapter 3. To elucidate the effects of the model geometry on the wall shear stress and oscillatory shear distribution, results from highly resolved numerical computations of the same flows are analysed in the second half of Chapter 3.

As has been discussed earlier in this chapter wall shear stress modulates endothelial cell function and has been associated with the development of vessel wall disease. Unfortunately wall shear stress cannot be measured directly by MR and is therefore typically calculated from near wall velocity measurements. Several methods have been proposed to extract wall shear stress from MR velocity measurements (Steinman, 1996; Oshinski, 1996; Oyre, 1998; Ringgaard, 1998). The accuracy of these methods however depends largely on the shape of the near wall velocity profile, the shape of the lumen boundary and the velocity to noise ratio of the near wall velocity measurements. Near wall velocity measurements typically contain a higher degree of uncertainty as compared to the mean uncertainty of the velocity measurement across the lumen. Furthermore calculating a derivative from noisy velocity samples may lead, due to propagation of error, to the accumulation of significant error in the result. To overcome these problems a novel data modelling method based on cubic spline functions is proposed. The method requires no assumptions in the shape of the lumen boundary or the underlying velocity distribution and can remove most of the random error from the data while the primary features in the velocity distribution are preserved. Wall shear stress and vorticity can be easily computed from the functional description of the velocity distribution. The proposed method and a series of validation results are presented in Chapter 4.

Idealised bypass graft models are very useful in understanding the effects of the gross geometric features on the distal anastomotic flow field. To assess the influence of the detail *in vivo* bypass graft geometry on the flow field, two geometrically realistic bypass graft models were fabricated through a process whereby the *in vivo* or *ex vivo* (from casts) extracted bypass graft geometry is reproduced at a scale convenient for

MR flow studies. Flow field measurements in an aorto-coronary and a femoro-tibial bypass graft model together with wall shear stress and vorticity estimates calculated from the splines based functional representation of the velocity field are discussed in Chapter 5.

Conclusions drawn from the thesis and suggestions for further work are presented in the Chapter 6.

Chapter 2.

Accuracy of MR Velocimetry of Complex Flows

2.1 *Introduction*

Complex flows are difficult to quantify *in vivo* with MRI and therefore are primarily assessed qualitatively in clinical practice. Although a number of studies of accuracy in MR quantitative flow measurement based on simple well-defined steady flows exist (Firmin et al., 1990; Ku et al., 1990; Maier et al., 1988; Tang et al., 1993). For flow in a straight tube positioned parallel to the magnet long axis an accuracy of +/- 5 % with respect to the mean velocity can be typically achieved. Ku et al. (1990) studied the accuracy of MR velocity measurements in steady flow using different geometries and flow rates to assess the technique for a range of flow conditions. Using laser Doppler anemometry (LDA) as their reference method, they found a very good agreement between the MRI and LDA results.

Few studies investigate accuracy based on more realistic flows (Steinman et al., 1996; Weston et al., 1998; Botnar et al., 2000). Steinman et al. (1996) used magnetic resonance phase contrast velocimetry and numerical simulations to measure and reproduce the flow field in a planar 45 degrees angle end-to-side anastomosis model with an occluded proximal host artery under steady flow. They demonstrated very good agreement between measurement and simulation and reported an rms error estimate of 15 % with respect to the mean velocity for both the two dimensional and three dimensional phase contrast techniques. A slight mismatch in the velocity profiles at the toe between measurements and computation was attributed to spatial displacement

artifacts due to the presence of oblique and convectively accelerating flow at the toe region. The level of measurement accuracy reported is significantly less than that reported in the literature for well defined steady flow acquisitions. They attributed this difference to the three dimensional character of the flow field due to the presence of strong secondary flow.

Several studies have investigated the effects of various parameters related to unsteady flow MRI measurement (Frayne and Rutt, 1993; Lauzon et al., 1994; Peeters et al., 1996). Some investigators (Van Tyen et al., 1994; Jou et al., 1996) have used numerical methods to solve both the flow and the magnetization evolution in models and have compared these results with those obtained using Magnetic Resonance Angiography (MRA). Other investigators (Napel et al., 1992; Buonocore et al., 1998) have proposed methods of offline processing of three-dimensional velocity encoded MR images, using streamlines and fluid particle paths, to improve visualization and quantification of complex flow patterns. Sun et al. (1992) investigated steady flow in a straight tube with a semi circular plate inserted normal to its axis and reported overall good agreement between results from numerical simulations of the flow and MRI phase contrast velocity measurements. Frayne et al. (1995) compared velocity measurements of transient flow in a straight rigid tube to the Womersley solution (Womersley, 1955) to validate the phase contrast (PC) technique for well-defined time-dependent flow. However, their approach provides only a basic estimate of accuracy and cannot be applied to the more clinically relevant complex flows.

The objective for this part of the investigation was to determine the accuracy of two-dimensional prospectively synchronised PC contrast enhanced MR velocity measurements of time dependent flow in a fully three dimensional bypass graft model (Figure 2.1). This is believed to be the first detailed attempt to estimate accuracy of MRI quantification of fully three-dimensional transient flows by quantitative comparison of velocity profiles from MRI and highly accurate numerical flow simulations.

The selection of the geometry was based on the following criteria: physiological significance, complex three-dimensional flow field, and feasibility of precise construction of the physical model. The selected geometry models a distal end-to-side anastomosis with the bypass vessel deformed out of the plane of symmetry of the host-vessel (Figure 2.1). The graft flow is of physiological interest since it has been postu-

lated that there is a correlation between the hemodynamics in bypass grafts and the development of intimal hyperplasia (Ojha et al., 1990; Sottiurai et al., 1989). The three-dimensional character of this geometry and its physiological relevance has been the focus of several investigations (Caro et al., 1996; Sherwin et al., 2000). In steady flow it has been shown by Sherwin et al. (2000) that this non-planar three-dimensional configuration notably alters the shear stress distribution at the bed of the anastomosis when compared to its planar version. The flow field in the host section also includes a combination of features such as steep velocity gradients, strong in-plane velocity components, significant asymmetry, and regions of recirculating flow.

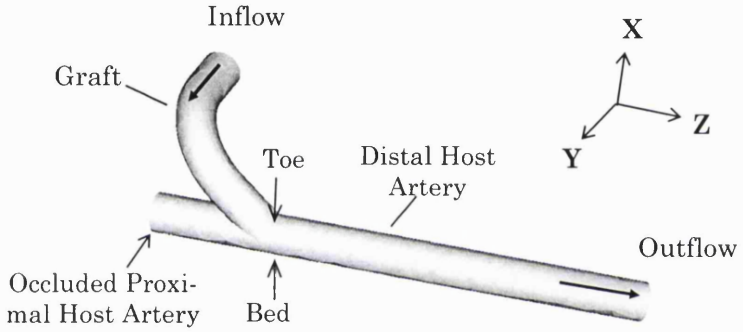

Figure 2.1 Model geometry of a distal end-to-side non-planar anastomosis.

In absence of an exact solution to this fluid flow problem, the results of a highly accurate numerical solution of the three-dimensional incompressible Navier-Stokes equations for unsteady flow were used as a reference solution. In this study, since the model geometry is precisely described and the flow is laminar and Newtonian, comparison of the MRI measurements with highly accurate computations provides an acceptable means of estimating experimental error. To validate the numerical method, its results were compared against analytical solutions such as the Hagen-Poiseuille solution for steady flow and the Womersley solution for unsteady flow. There was excellent agreement between the computational results and the analytical solutions with an accuracy well above that of the corresponding experimental.

The first part of this chapter reports the results from calibrations of the MR phase-velocity mapping technique obtained for simple steady (Hagen-Poiseuille) flow

and complex steady flow. In the latter case MR measurements and numerical computations of the flow in a planar bypass graft distal anastomosis model were compared. These results were included in the paper by Sherwin et al. (2000) and presented in the 1999 ISMRM flow and motion workshop (Papaharilaou and Doorly, 1999). The work presented in the second half of this chapter on the accuracy of complex time-varying flow measurements, formed the basis of an article published in the Journal of Magnetic Resonance Imaging (Papaharilaou et al., 2001).

2.2 *Steady Flow*

This part is concerned with the investigation of the accuracy of velocity measurements of complex steady flow in the 45 degree planar distal end-to-side anastomosis model (Figure 2.2). This model configuration has been used in a number of flow studies (Steinman et. al., 1996; Sherwin et al., 2000; Ethier et al. 2000). Results from the calibration of the MR velocity measurement technique in simple well defined steady flow are presented first and are followed by those obtained in complex steady flow.

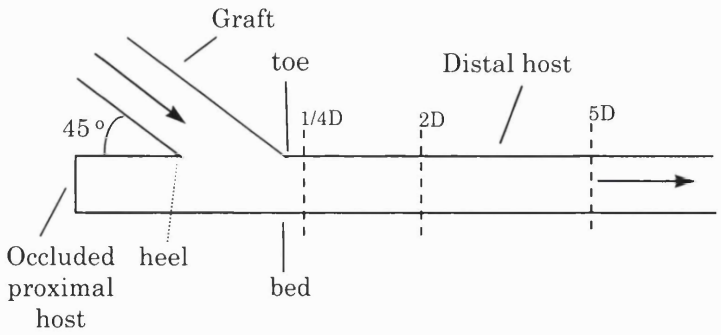

Figure 2.2 A cross section through the plane of symmetry of a planar bypass graft model. Arrows indicate direction of flow. The locations with respect to the toe of the centrelines of the MR slice extraction planes (dashed lines) are also shown.

2.2.1 Methods

Measurements were obtained using a 1.5 Tesla General Electric (GE) Signa small bore (30 cm diameter) scanner with a 58 mT/m peak gradient strength and a 150 T/m/s slew rate. A two dimensional phase contrast pulse sequence was used. A cali-

brated computer controlled flow pump (Quest Inc., London, Ontario) generated the required steady flow (Q=5.52 ± 0.05 ml/s; Re=250 ± 9.2). The circulating fluid was a 60-40 % water-glycerol solution (kinematic viscosity 3.4 ± 0.1 × 10^{-6} ms^{-2} at 20° C) doped with Gd-DTPA at a concentration of 0.75 mM/L (T_1 ~ 60 ms). The measurements were obtained with a 5×5 cm FOV on a 256 × 256 image matrix yielding an in-plane resolution of 0.195 mm and approximately 40 pixels across the tube inner diameter. A 2mm slice was excited with parameters TE = 5.6ms, TR = 14ms, flip-angle = 70 deg and NEX= 32. The aliasing velocity was set to 7 cm/s.

The baseline uncertainty for complex flow measurements was obtained by measurements of a simple well-defined fully developed flow in a straight tube (Poiseuille flow). An estimate of the velocity measurement accuracy of complex three dimensional flow downstream of the graft artery junction in the bypass graft model was obtained by comparing the MR measurements with highly accurate numerical computations of the same flow (Sherwin et al., 2000).

2.2.2 Results and Discussion

2.2.2.1 Poiseuille flow

Velocity measurements of steady flow through a straight rigid 8±0.2 mm internal diameter tube phantom oriented along the long axis of the magnet bore were obtained. For the error estimation process the scan parameters used in the model graft studies were also employed. The experiment was repeated for various flow rates yielding Reynolds numbers between 250 and 600 and at different stations along the straight tube. Fully developed laminar flow at the measurement station was ensured by scanning well beyond the entrance length (Equation (1.9)).

Both systematic (bias) and random error (precision) estimates were obtained by comparing the experimental cross sectional velocity profiles with the theoretical parabolic profiles for laminar flow (Figure 2.3). To obtain an estimate of the systematic error a two-step procedure was used. First a point to point comparison of the experimental velocity profile and the theoretical parabolic profile corresponding to the nominal flow rate yields an 'aggregate' root mean square (rms) error estimate. In the second step a least squares error parabolic profile fit to the experimental data points yields the

minimum rms error on a point to point profile comparison basis. The level of error calculated in the second step is used as an estimate of the precision of the experimental technique. The difference between the 'aggregate' error and the minimum error is used as an estimate of the systematic error or bias in the measurements. To avoid overestimation of the measurement error due to partial volume effects, boundary voxels were excluded from the calculations.

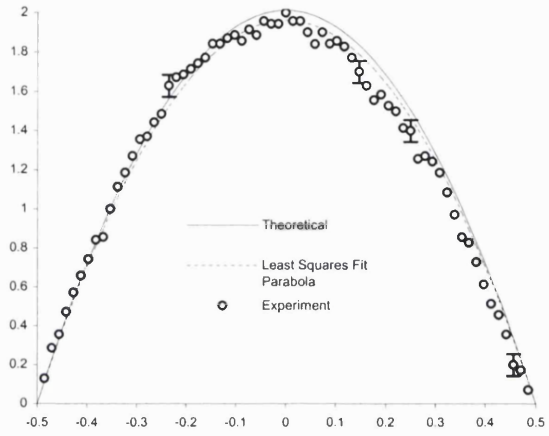

Figure 2.3 Comparison of the MR measured (symbols), theory predicted (solid line), and least squares error fit axial velocity profile (dotted line) of fully developed axisymmetric flow in a straight pipe (Re=560). Differences between theretical and least squares parabolic fit reveals bias in measurement. Error bars correspond to +/- 5.6 % U_{mean}.

A number of assumptions were necessary in the process of obtaining an estimate of experimental uncertainty. First the noise process present in the MR phase images was assumed normally distributed with zero mean. Second, the least squares error parabola fitted to the experimental data was assumed to be the 'true data' parabola for measurements with zero bias. Third, the difference between the theoretical parabola corresponding to the measured flow rate and the tube diameter and, the fitted parabola provides a valid estimate of the bias or systematic error in the experiment. Finally, the N velocity samples obtained at N stations along a tube cross section profile were assumed statistically equivalent to N velocity samples taken at a single station of the same profile.

To obtain an estimate of the level of uncertainty in the MRI velocity measurements an estimate of the precision and the bias levels is required. The measurement precision (S_x) can be calculated by the following expression:

$$S_x = \sqrt{\frac{1}{N-1}\sum_{i=1}^{N}(u_i - \bar{u})^2}\,, \tag{2.1}$$

where u_i and $\bar{u}$ are the measured and expected velocity at the i^{th} station or voxel along a tube cross sectional profile respectively and, N is the number of measurement stations or voxels along a profile included in the calculations. Since the sample mean (the least squares fit parabola corresponding value) of the velocity at each measurement station instead of the true value at that station is used, there are N-1 degrees of freedom, one degree of freedom less than if the true value was used. The uncertainty (U_x) can be calculated as the root-sum-square of the bias and precision:

$$U_x = \sqrt{S_x^{\,2} + B^2}\,. \tag{2.2}$$

Applying this procedure to the Poiseuille flow velocity measurements the following results were obtained: the precision level was 5 % with respect to the mean velocity, the bias was estimated at 2.5 % with respect to the mean velocity; and the uncertainty of the velocity measurements given by the geometric mean of the precision and bias limits was 5.6 % with respect to the mean velocity. Potential sources of systematic error were partial volume effects, intravoxel phase dispersion and phase averaging, uncompensated eddy currents, magnetic field gradient non-linearities, static field inhomogeneities, magnetic susceptibilities and, imperfections in the profile of the slice select RF excitation pulse. These effects were discussed in section 1.3.

The accuracy in the theoretical parabola estimate through the experimentally obtained volume flow rate was 3.6 % with respect to the mean velocity.

The effect of SNR on velocity measurement precision

By repeating a NMR experiment n times and reconstructing the mean signal we can improve the SNR of the modulus image by a factor of $\sqrt{n}$. According to the central limit theorem if random samples of size n are taken from a distribution with mean μ and standard deviation σ, the distribution of the sample mean will be approximately normal with mean m and standard deviation $\sigma/\sqrt{n}$. Therefore by reconstructing the

mean of n independent measurements of the NMR signal for each distinct encoded position, the signal (i.e the mean) remains the same but the noise (i.e the standard deviation) will be reduced by a factor of $\sqrt{n}$. The relationship between the SNR of the MRI modulus image and the number of signal averages can be expressed as follows:

$$SNR_1 = \frac{m(I)}{\sigma(I)} \tag{2.3}$$

$$SNR_n = \frac{m(I)}{\sigma(I)/\sqrt{n}} = \sqrt{n}\, SNR_1 \tag{2.4}$$

where SNR_1 and SNR_n are the signal to noise ratios in the modulus image obtained using no signal averaging (NEX=1) and n signal averages (NEX=n) respectively, $m(I)$ is the mean pixel intensity in the region of interest of the modulus image and $\sigma(I)$ is the standard deviation of the background noise. Furthermore as the velocity to noise ratio in the phase image of a phase contrast experiment is proportional to the signal to noise ratio of the modulus image (Equation (1.45)), the number of signal averages also affects the random component of the measurement error i.e. the measurement precision. This theoretical relationship was experimentally validated by obtaining an estimate of the modulus image SNR from a series of flow measurements for different values of the NEX parameter keeping other imaging parameters constant. For each value of the NEX parameter the experiment was repeated 3 times.

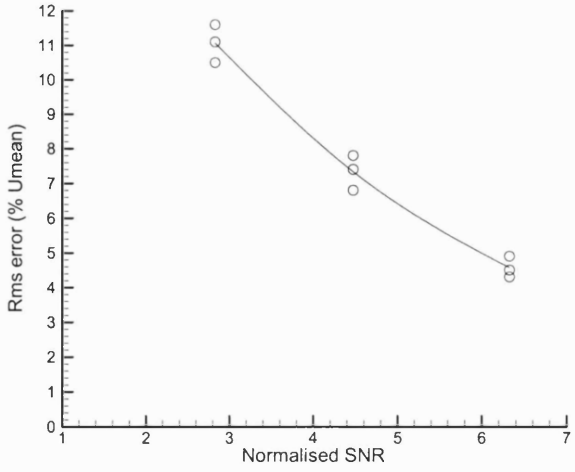

Figure 2.4 Estimate of the relationship between the precision of MR velocity measurements of axisymmetric steady flow (Re=290) and the relative SNR of the acquisition. Precision estimates (symbols) and a least squares cubic spline curve fit (solid line) to the points are shown. The SNR was normalised by the SNR obtained with no signal averaging.

The results from these measurements are shown in Figure 2.4. To show the trend in the relationship between the precision and the number of signals averaged, a least squares cubic spline curve was fit to the data samples.

2.2.2.2 Complex flow in a planar bypass graft model

Measurement of wall shear stress *in vivo* by MRI is difficult, mainly due to lack of sufficient spatial resolution required to capture large near-wall velocity gradients and to accurately determine the exact wall location. Partial volume, saturation, magnetic susceptibility and motion effects are additional sources of error. In phantom studies, however, acquisition protocol optimisation and longer acquisitions can allow for high spatial resolution flow measurements with reduced systematic error.

In this study the application of a 65 degrees flip angle combined with the use of a contrast agent, improved the magnitude image SNR and allowed for high spatial resolution acquisitions. In the presence of complex flow patterns such as large near wall velocity gradients, a skewed distribution of velocities and strong secondary flow, the spatial resolution requirements are high. Furthermore regions of flow separation may develop leading to long fluid particle residence times and NMR signal drop-out due to spin saturation.

A procedure similar to that used for steady axisymmetric flow was applied to estimate the error in the bypass graft velocity measurements. However in absence of an analytical solution to this flow, highly accurate numerical computations were used as a good approximation to the exact solution (Figure 2.5).

Strong cross flow of the order of magnitude of the axial flow was measured at the toe. This cross flow gradually dies out as the flow travels down the distal host artery. To assess the effect of secondary flow on the accuracy of the phase-velocity mapping technique, velocities were measured at three stations ¼ D, 2D and 5D downstream of the toe. Background phase correction was applied to reduce systematic error in the measurement. To minimise any mismatch between the numerical predictions and the experiments due to the finite slice thickness of the experiment, the numerical results used for the comparisons were linearly interpolated from a 2 mm thick section of the

numerical velocity field positioned around the centre of the corresponding MRI slice location.

Figure 2.6, Figure 2.7 and Figure 2.8 show comparisons of MRI measured and numerically computed axial y-centreline velocity profiles extracted at ¼ D, 2D and 5D distal to the toe respectively. The mean rms error was calculated using the formula:

$$\overline{E}_{\text{rms}} = \frac{1}{U_{\text{mean}}} \sqrt{\frac{1}{n} \sum_{i=1}^{n} (u_{\text{MRI}\,i} - u_{\text{CFD}\,i})^2} \tag{2.5}$$

where n denotes the number of experimental samples along a profile included in the calculation, $u_{\text{MRI}\,i}$ is the experimental value of the axial velocity and $u_{\text{CFD}\,i}$ is the corresponding numerically computed value for sample i.

The lumen centre coordinates were determined as the centroid of the set of all pixels in the magnitude image that had intensities above a user selected level. This level was chosen so that the area covered by the pixels equalled the nominal lumen area. To exclude errors associated with the exact location of the vessel axis in the estimation of measurement accuracy, the axis location that minimised the mismatch between the numerical and the experimental velocity profiles was selected at each measurement station.

Two error estimates were calculated: the rms error including all velocity samples along the profile except the boundary voxels, and the near wall rms error including only the first three intraluminal voxels. By this, differences between the near wall measurement error and the mean rms error could be identified. The error estimates obtained are summarised in Table 2.1. Overall there is a higher near wall error on the bed wall as compared to the toe wall primarily due to the difference in the respective velocity gradients. The mean rms error of complex flow velocity measurements for all three stations was 5.2 % of U_{mean}, very close to the value of 5 % of U_{mean} cited for well defined steady flows. The mean rms error of near wall velocity measurements for both toe and bed walls and for all measurement stations varied between 2.7 % and 8.4 % with a mean of 4.5 % of U_{mean}. This error is relatively low. However, although these measurements were obtained with a very high spatial resolution (~40 pixels/D) and a relatively high VNR, the accuracy achieved is close to that obtained for well defined flows for significantly lower spatial resolutions (~20 pixels/D) and VNR. It is therefore evident that the VNR and spatial resolution required to achieve the same level of

measurement accuracy in complex flows is significantly higher than that required in well-defined flows.

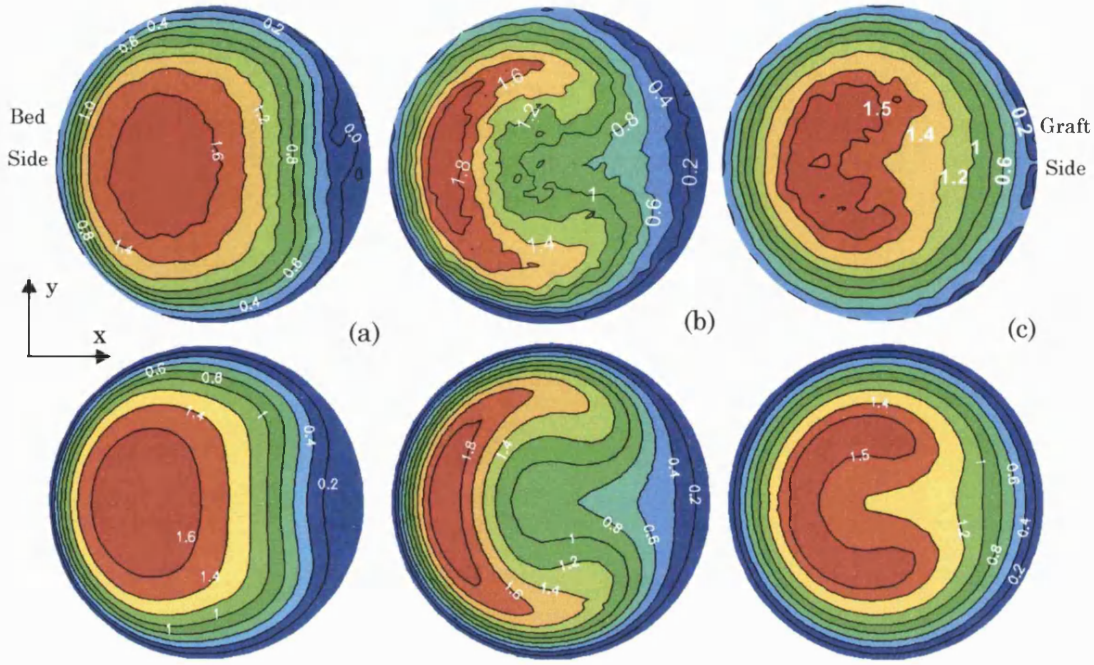

Figure 2.5 Comparison of MRI measured (top) and numerically computed (bottom) steady flow (Re=250) axial - u velocity component contour plots extracted from normal cross sections of the planar bypass graft model at the toe + ¼D (a) and, at 2D (b) and 5D (c) downstream of the toe. The nominal Reynolds number was 250.

		Rms Error (% U_{mean})		
		Near wall region only		Aggregate
		x/D=-0.5	x/D=0.5	
Scan Location	1/4D	8.4	3.7	6
	2D	4.7	3.4	5
	5D	3.2	2.7	4.5

Table 2.1 Accuracy estimates of MRI phase contrast steady flow velocity measurements at three stations along the distal host artery section of a distal end-to-side anastomosis model. Aggregate error estimates are calculated including near wall velocity measurements. The near wall region includes the first three intraluminal voxels.

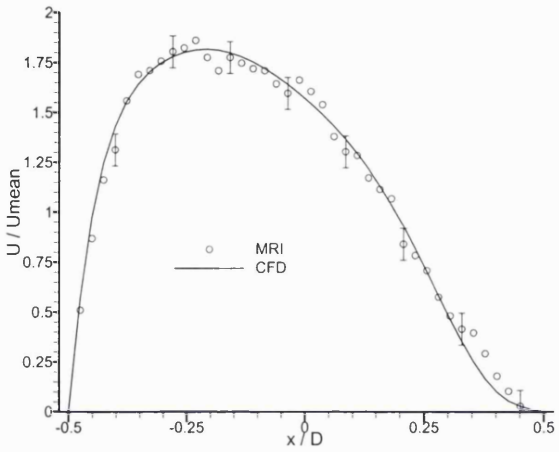

Figure 2.6 Comparison of MRI measured (symbols) and numerically computed (solid line) horizontal centreline (y=0) velocity profiles extracted from velocity maps at 1/4 D downstream of the toe of the planar bypass graft anastomosis model in steady flow. Error bars correspond to ± 8 % $U_{mean.}$

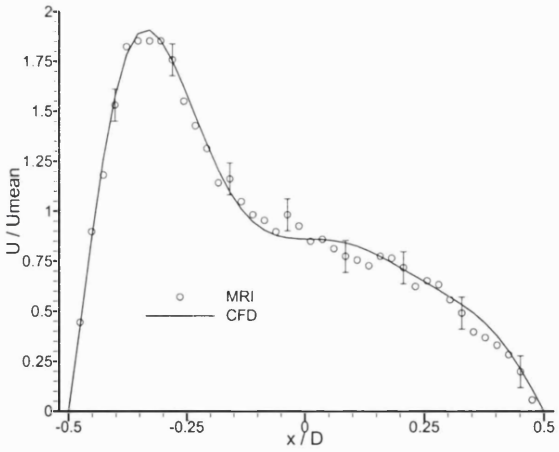

Figure 2.7 Comparison of MRI measured (symbols) and numerically computed (solid line) horizontal centreline (y=0) velocity profiles extracted from velocity maps at 2 D downstream of the toe of the planar bypass graft anastomosis model in steady flow. Error bars correspond to ± 8 % $U_{mean.}$

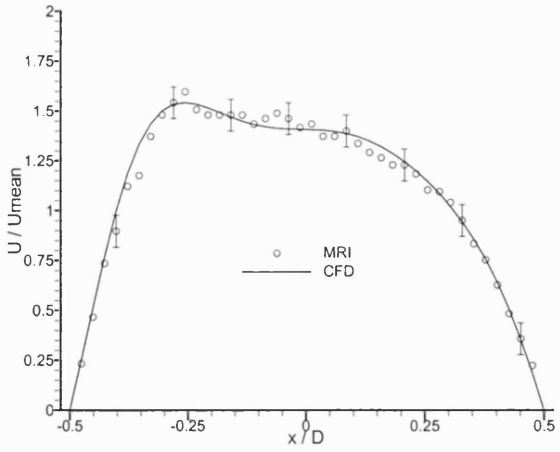

Figure 2.8 Comparison of MRI measured (symbols) and numerically computed (solid line) horizontal centreline (y=0) velocity profiles extracted from velocity maps at 5 D downstream of the toe of the planar bypass graft anastomosis model in steady flow. Error bars correspond to ± 8 % U_{mean}.

The results show a difference between the accuracy of near wall velocity measurements obtained at the toe wall and those obtained at the bed. This is primarily due to insufficient spatial resolution to eliminate intravoxel phase averaging effects. This finding demonstrates the influence of the flow field patterns on the accuracy of MR quantitative flow measurements and the subsequent difficulty in designing acquisition protocols ensuring a desired level of accuracy for various flow conditions.

It should be noted that the velocity measurements were not obtained under optimum conditions with respect to partial volume errors. This was associated with the lack of NMR signal from the type of material used (Perspex) to construct the flow model. As a result, the phase contribution of the wall material to the partially occupied boundary voxels was random within the phase dynamic range. If however the model had been constructed with an NMR signal generating material (e.g. Agarose gel), a zero phase contribution of the wall spins to the partially occupied boundary voxel would result. This would have allowed the estimation of the fractional voxel volume occupied by stationary material hence the calculation of the boundary voxel velocity corrected for partial volume error.

Calculations of wall shear stress based on MR phase-velocity measurements obtained even under the controlled conditions of an in vitro experiment are sensitive to noise. To demonstrate the significant errors that can occur, wall shear rates are calculated by fitting a least squares linear model to the near wall velocity measurements.

For this the three velocity measurements closest to the wall excluding the boundary voxel were used. Linear regression was applied to fit the linear models to the original data using a curve fitting software application (Curve Expert v1.3). The process of regression ensures that the 'merit function', which is an arbitrary function that measures the disagreement between the data and the model, is minimized. This is achieved by adjusting the model parameters until the merit function becomes as small as possible. Models which consist of a linear combination of a particular set of functions X_k are called linear models. The general form of a linear model is:

$$y(x) = \sum a_k X_k(x), \tag{2.6}$$

where $X_k(x)$ are fixed functions of x that are called the basis functions, and a_k are the free parameters. Linear refers only to dependence of the model on the parameters a_k; the basis functions $X_k(x)$ may be nonlinear. Minimization of the above linear model is performed with respect to the merit function:

$$S(a) = \sum_{i=1}^{n} \left[y_i - \sum_{k=1}^{nparam} a_k X_k(x_i) \right]^2 \tag{2.7}$$

The minimum of equation (2.7) occurs where the derivative of S with respect to the parameters a_k disappears. Substituting the linear model into this function, taking the first derivative, and setting this equal to zero gives the normal equations that are solved directly for the parameters a_k.

A comparison of numerically predicted and MRI extracted wall shear rates at the bed and toe wall at three stations along the distal host artery section of the bypass graft model are shown in Figure 2.9. The results show a higher shear rate at the bed wall as compared to the toe wall. This difference gradually diminishes as the flow travels down the host vessel, cross flow becomes weaker and, the velocity distribution becomes more uniform. The MR extracted wall shear rates at the toe and at 2D and 5D downstream for the bed wall consistently underestimate the numerical predictions. However this underestimation is reduced with decreasing wall shear rate. The result at the toe is noteworthy. The wall shear estimates calculated by the linear model are rather poor, especially for the bed wall. The numerically predicted velocity profile at

the toe (Figure 2.6) is highly non-linear near the toe wall. This feature however is not present in the experimental results. It should be noted that the numerical wall shear rate prediction at the toe and on the toe wall is almost zero. Accurately resolving velocities by MR in such regions, where VNR is compromised by spin saturation and phase dispersion induced signal drop out, can be problematic. In these regions high spatial resolution is also required to reduce intravoxel phase averaging and capture the non-linear velocity distribution.

The mean error for the linear wall shear rate estimation method is 36 % with respect to the inlet wall shear rate. This result shows that even under the controlled conditions of a model study the level of error in obtaining wall shear rates from near wall MR velocities can be large. As these errors are inversely dependent on the VNR of the measurement, it is necessary to apply some form of smoothing either in two or three spatial dimensions to the MRI measured velocity distribution before any estimates of wall shear are extracted. The smoothing process can assist in excluding outlier velocity samples that introduce significant error in shear rate calculations. A novel method whereby MR velocity data can be smoothed without significant loss of information will be introduced in Chapter 4.

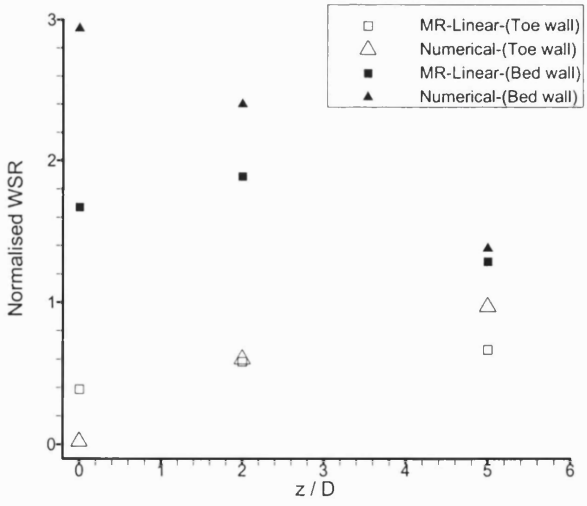

Figure 2.9 Comparison of normalised wall shear rates predicted numerically (triangle) and calculated from MR data using the least squares linear fit (square) method. Shear rates at the bed wall (solid symbols) and the toe wall (open symbols), extracted at three stations along the host artery section are shown. Wall shear rates were normalised by the inlet wall shear rate.

2.3 Time Varying Flow

2.3.1 Methods

Experimental method

The experiments were performed with a GE 1.5 T (Signa Horizon LX) MRI scanner with a 20 mT/m peak gradient strength. A GE standard clinical cardiac-gated fast two-dimensional PC pulse sequence was applied. The model was placed in the scanner with the axis of the host section aligned to the long axis of the magnet to avoid flow encoding misalignment errors. A dual 3-inch surface coil was used, and the flow phantom was placed in-between the two coil elements in a sandwich-like configuration. A field-of-view of 7 cm × 7 cm was selected with a 256 × 256 image acquisition matrix, yielding an in-plane resolution of 0.273 mm. Fractional echo sampling (60 %) was applied giving a minimum TE value of 5.5 ms which was used with a TR of 16.7 ms. Only the axial velocity component (u) was encoded.

The correct selection of the velocity encoding sensitivity is critical to the quality of MRI unsteady flow measurements: too low sensitivity compromises the velocity to noise ratio (VNR), too high sensitivity leads to velocity aliasing (Contouro and Robinson, 1992), in most cases to a longer minimum TE, and an accentuation of phase dispersion effects. Making the measurement more sensitive to velocity requires a larger velocity encoding pulse area that eventually leads to increased pulse duration and therefore to a longer TE. If the increase in TE is significant, then the penalty due to the reduced SNR and the accentuated TE related artifacts would outweigh the gain in VNR. The relationship between the phase image VNR and the magnitude image signal to noise ratio (SNR_{mag}) on a pixel-by-pixel basis is given by the following expressions assuming uncorrelated noise in the two receiver channels (Contouro and Smith, 1990; Contouro and Robinson, 1992)

$$\sigma(\phi) \simeq \frac{\sigma(I)}{I} \tag{2.8}$$

$$VNR \simeq \frac{|\Delta\phi|}{\sqrt{2}\sigma(\phi)} = \frac{|\Delta\phi|}{\sqrt{2}} \frac{I}{\sigma(I)} = \frac{|\Delta\phi|}{\sqrt{2}} SNR_{mag} = \frac{\pi |u|}{\sqrt{2} V_{enc}} SNR_{mag}, \tag{2.9}$$

where $|\Delta\phi|$ and $\sigma(\phi)$ are respectively the magnitude of the phase angle difference between the balanced flow encoding acquisitions and the standard deviation of the phase angle, and where I and $\sigma(I)$ are respectively the signal intensity and standard deviation of the magnitude reconstructed data. Since phase noise is independent of phase angle (Equation (2.8)), extending the phase dynamic range will improve the VNR of the phase-reconstructed images (Contouro and Smith, 1990) thus allowing greater precision in the measured data. Phase unfolding was used for all comparative results, i.e. an aliasing velocity (V_{enc}) of 9 cm/s was selected, which was significantly less than the numerically predicted peak velocity of 35.5 cm/s in the flow field. To avoid phase spillover an aliasing velocity of 36 cm/s would be selected. Therefore a factor of four gain in VNR is achieved (Equation (2.9)) by selecting a V_{enc} of 9 cm/s instead of 36 cm/s, assuming that the SNR_{mag} remains the same, and without increasing the total acquisition time significantly. However, in regions of high velocity gradients signal dropout associated with intravoxel phase dispersion may occur from the increase in velocity sensitivity. In this study, where the voxel size was small, the degradation of accuracy due to signal dropout from intravoxel phase dispersion was minor compared to the improvement in precision from the overall increase in VNR. Moreover the effect on SNR from a small (< 0.8ms) increase in the minimum TE was not significant. Increasing the VNR further, by reducing V_{enc} below 9 cm/s proved problematic, since the phase unwrapping method applied failed to unambiguously recover the original phase distribution from the aliased phase images.

To determine a suitable flip angle for the experiments T_1 was first estimated by applying an inversion recovery sequence on a stationary fluid sample with different inversion times. A T_1 of approximately 60 ms was calculated by fitting the experimental data to the following three parameter exponential expression:

$$I(\tau) = A - B\exp(-\tau/T_1), \tag{2.10}$$

where I is the pixel intensity at a time τ after the inversion pulse, and A, B are constants. The Ernst angle (θ_E) for our experiment calculated by the expression (Ernst and Anderson, 1966):

$$\theta_E = \cos^{-1}(e^{-TR/T_1}) \tag{2.11}$$

was 40 degrees. However, as the Ernst angle calculation does not take into account flow-related enhancement effects, it tends to underestimate the optimum flip angle in

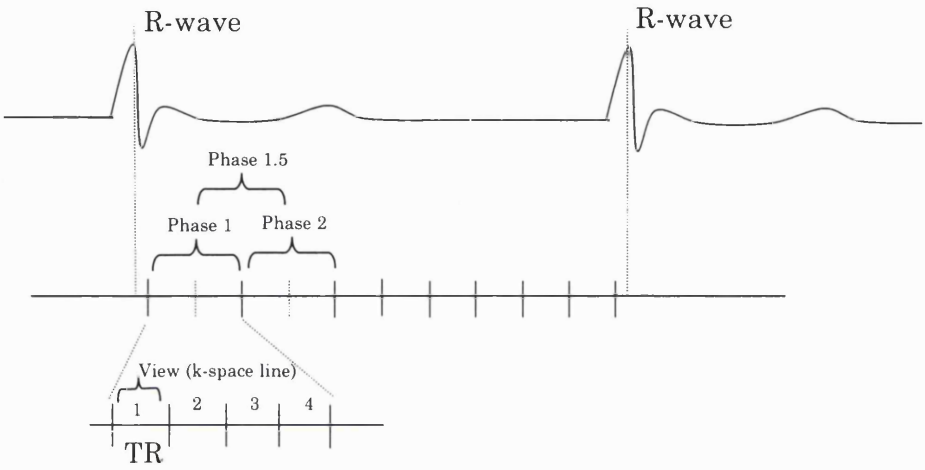

Figure 2.10 A schematic showing the fastcard segmented k-space view sharing technique employed to reduce total scan duration. The acquisition is triggered by the pseudo R wave. Each k-space segment is comprised of 4 k-space lines or views as determined by the vps parameter.

flow MRI experiments. To achieve a better estimate of the optimum excitation angle for the experiments, the spatially and temporally averaged SNR_{mag} was calculated from a series of MRI measurements of flow in a straight 8 mm inner diameter tube replicating the inflow conditions used in the anastomosis model. By varying the excitation angle between 40 degrees and 70 degrees in steps of 10 degrees it was found that most of the expected gain in SNR_{mag} (20 %) over the Ernst angle acquisition resulted for a flip angle of 50 degrees. Although a flip angle of up to 65 degrees would have further increased the spatial temporal mean SNR_{mag} by 10 % it was not selected to avoid excessive local saturation of spins in recirculation regions. A 2 mm slice was excited in order to reduce intravoxel phase dispersion and partial volume errors.

To compensate for the inherently low SNR of the measurements due to the thin slice selected, eight signal averages (NEX) were employed. To reduce scan duration, temporal averaging was applied in the form of view sharing (Foo et al., 1995). Segmented k-space acquisitions were employed to reduce scan duration. Four views (or k-space lines) per segment were acquired in a sequential manner. This reduces the tem-

poral resolution of the measurement by a factor of four. However, by sharing k-space lines of adjacent segments of k-space an extra phase was reconstructed for every two measured phases. This technique is termed view sharing and is part of GE's phase contrast pulse sequence. Part of the functionality of the pulse sequence used was designed for clinical applications; to account for heart rate variability in its cardiac gating option it includes a dead time of 10 % of the cardiac cycle were the scanner does not acquire data while waiting for the trigger. As a result, one true phase and one interpolated phase before the trigger were not reconstructed. Although view sharing may significantly reduce image acquisition time, it may also result in the appearance of ghost images of the object of interest spread along the phase encoding direction of the reconstructed image. Views are acquired at slightly different times in the flow cycle (TR apart) and therefore each view represents a different velocity distribution and hence contributes different phase content to the image. The number of ghosts is equal to the number of views per segment (vps) used to generate each image and their spacing depends on the properties of the flow waveform and the field of view. The temporal resolution of the scan was 66.8 ms which allowed for 25 phases to be reconstructed covering 90 % of the waveform cycle. The acquisition duration was 15 minutes per slice location.

A computer controlled flow simulator (Quest Imaging Inc., London, Ontario) was used to generate the flow waveform for the experiments. A 5V TTL pulse generated by the flow simulator at the start of each waveform cycle was used to trigger the MRI scanner. Frayne et al. (1992) investigated the accuracy of this flow simulator in MR flow studies and reported a 1 % uncertainty in steady flow mode and a good agreement between desired and measured time-averaged flow rates to within 0.2 ml/s in pulsatile mode with a 15 ml/s peak flow rate. They also reported good reproducibility of the generated waveforms with less than 0.2 ml/s cycle-to-cycle standard deviation in the time-averaged mean flow rate. Finally, they calculated the rms of the differences in the time-averaged flow rate among measurements taken at 30-minute intervals and found it to be less than 0.4 ml/s.

The circulating fluid was a 60-40 % by volume distilled water-glycerol solution. To improve the SNR a contrast agent (Gadolinium-DTPA, Omniscan, Nycomed) was introduced to the water-glycerol mixture to create a 0.75 mmol/L solution. The kine-

matic viscosity (ν) of the circulating fluid was measured using a capillary viscometer and was found to be ($3.4 \times 10^{-6} \pm 0.1$) $m^2 s^{-1}$ at 20 °C. The temperature sensitivity of the kinematic viscosity was measured and was found to be less than 0.03×10^{-6} $m^2 s^{-1}$ °C^{-1} in the range of (18-22) °C. The ambient temperature during the acquisitions was kept at (20 ± 1) °C.

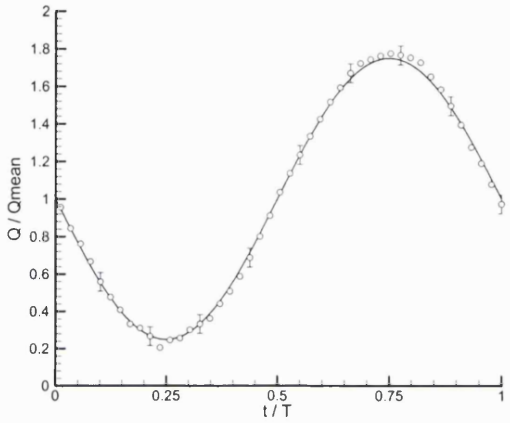

Figure 2.11. Comparison of the measured flow waveform (symbols) and the target flow waveform (solid line). Error bars correspond to ± 5 % of Q_{mean}.

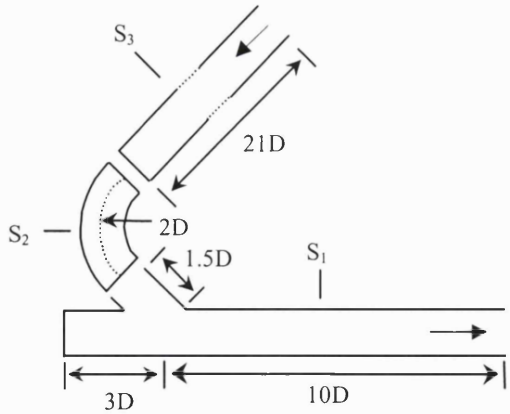

Figure 2.12 Schematic of the centreplane cross-section of the three components (S_1, S_2, S_3) assembled to form the physical model. All dimensions are normalised by the vessel diameter (D). Arrows in S3 and S1 indicate inflow and outflow locations respectively.

A sinusoidal flow waveform with a superimposed steady flow component was prescribed at the graft inlet. The Reynolds number varied in the range of 62 to 437 with a mean value of 250. The waveform period was T = 1.8 s and the Womersley pa-

rameter was equal to 4. A transit time flow meter (Transonic Systems Inc., Ithaca, New York) was used to calibrate the flow pump for unsteady flow and to assess the effects of the tubing connecting the phantom to the pump on the flow waveform measured in the phantom. A comparison of the target waveform and the measured sinusoidal waveform (Figure 2.11) indicated a very good agreement between the two with an rms difference of less than 2.5 % of Q_{mean}.

In order to compare experimental and computational results it was necessary to allow for the flow to become fully developed before entering section two of the model (Figure 2.12). For this study ($Re_{peak} = 437$, $\alpha = 4$) the definition of He and Ku (1994) of entrance length for time-dependent flow corresponds to 21 tube diameters. Flow conditioning was achieved by including a sufficiently long straight tube section upstream of the curved section of the model.

The physical model consisted of three sections (Figure 2.12). Section one (S_1) included the host artery and the graft-host vessel junction. Section two (S_2) is a 90 degrees bend with a centreline radius of two diameters, and section 3 (S_3) is a straight 8 mm internal diameter pipe used for upstream flow conditioning. S_1 and S_2 were precision milled as two symmetric halves from Perspex blocks. S_2 was mounted on S_1 so that the plane of symmetry of the 90 degrees bend was perpendicular to the plane of symmetry of S_1 (Figure 2.1). A flow straightener in the form of a 1 cm long tube bundle was placed at the entrance of S_3 to remove swirl and create rectilinear flow and S_3 was mounted on S_2. This assembly provided a continuous flow conduit with a circular cross section of 8 mm in diameter. An inspection of the model geometry indicated a less than 1 degree error in the angle of the anastomosis and less than 0.15 mm error in the conduit diameter.

Computational method

The computations were performed by Dr. Spencer Sherwin using a spectral/*hp* element algorithm (Sherwin and Karniadakis, 1996) to solve the three-dimensional time-dependent incompressible Navier-Stokes equations for unsteady flow. In this technique the solution domain is decomposed into tetrahedral subdomains or elements as is typical of standard finite element or finite volume discretisations. However,

unlike the standard techniques, each tetrahedral region is represented by a polynomial expansion.

Convergence of the numerical solution may be achieved either by reducing the characteristic size (h) of an element or increasing the order (p) of the polynomial within each element. For smooth solutions the advantage of a p-type approach is that high accuracy for a given amount of computational work can be obtained efficiently from the point of view of accuracy for a given amount of computational effort (Sherwin and Karniadakis, 1996). A further advantage of this method is that a refined simulation does not necessitate a redesign of the computational mesh since a higher order polynomial expansion may be used within each tetrahedral element of the existing mesh. Finally the complex curvature of the surface may be accurately represented by the high order polynomial expansion. The code has been validated extensively in steady and transient flows by comparisons with analytical and experimental results (Sherwin et al., 2000; Sherwin et al., 1997; Doorly et al., 1997).

The computations were performed using the domain shown in Figure 2.13 where the domain was subdivided into 1946 tetrahedral elemental subdomains. In constructing the computational domain a viscous layer of 0.1 D, based on the peak Reynolds number and the cycle period, was imposed adjacent to the vessel walls in order to capture the oscillating boundary layer. Simulations were performed at polynomial orders of p = 2, 4 & 6 which correspond to local degrees of freedom of 19 460, 68 110 and 163 464 respectively. By increasing the resolution in a hierarchical manner implicit to the spectral/*hp* element methodology it was ensured that the numerical error was well below the experimental error reported here. At the inflow boundary the exact Womersley solution was imposed, whilst at outflow a fully developed pipe flow was imposed with the conditions of constant pressure and zero normal derivatives of velocity enforced.

2.3.2 Data Analysis

Aliased velocities due to the low V_{enc} selected were corrected offline by applying an image processing algorithm that made use of a-priori knowledge of the general shape of the velocity distribution in the regions of interest (ROI) of the collected phase images. The phase unwrapping method applied was based on the assumption that lumen pixels can be classified in the following groups based on their velocity value

$$
\begin{aligned}
-V_{enc} < u_{i,j,t} \le V_{enc} \\
V_{enc} < u_{i,j,t} \le 3V_{enc} \\
3V_{enc} < u_{i,j,t} < 4V_{enc}
\end{aligned}
\tag{2.12}
$$

where $u_{i,j,t}$ is the axial velocity corresponding to pixel co-ordinates i, j at time t in the waveform cycle. Initially all phase images are magnitude masked and segmented to extract the lumen pixels. The image matrix is then scanned horizontally (x-direction) and $+V_{enc}/-V_{enc}$ transitions in the velocity values of neighbouring pixels are detected. Assuming that flow reversal occurs only near the wall we can correct the velocity aliased phase images by applying the following rules:

$$
\begin{aligned}
&\text{if} \quad V_{enc} < |u_{i+1,j,t} - u_{i,j,t}| \le 3V_{enc} \quad \text{then} \quad u_{i+1,j,t} = u_{i+1,j,t} + 2V_{enc} \\
&\text{if} \quad |u_{i+1,j,t} - u_{i,j,t}| > 3V_{enc} \quad \text{then} \quad u_{i+1,j,t} = u_{i+1,j,t} + 4V_{enc}
\end{aligned}
$$

The process is repeated for the y-direction. Figure 2.13 shows an example of the application of the phase unfolding method outlined. Errors in the process can occur when the magnitude of the velocity step is less than the aliasing velocity due to a combination of low pixel SNR and very high velocity gradients. Then the transition is not detected and pixel velocities along the same scan line are not corrected, as shown in Figure 2.13d. Nevertheless this error occurred rarely and was easily rectified manually. The lumen centre coordinates were determined as the centroid of the set of all pixels that had intensities above a user selected level. This level was chosen so that the area covered by the pixels equalled the nominal lumen area. The peak flow phase at each station was used to determine the lumen centre as it provided optimum SNR conditions.

A total of 32 CFD time slices covering the full waveform cycle were available and each slice was consistently interpolated at 6^{th} order accuracy into a circular mesh with 50 radial and 100 azimuthal points. Experimental results were linearly interpolated into a circular mesh of the same resolution. This operation did not smooth the MRI data since the inherent resolution of the experiment was less than that of the circular mesh selected. By using a common grid configuration to map the results from experiments and simulations, a one-to-one comparison between measured and computed velocities at each grid point was possible.

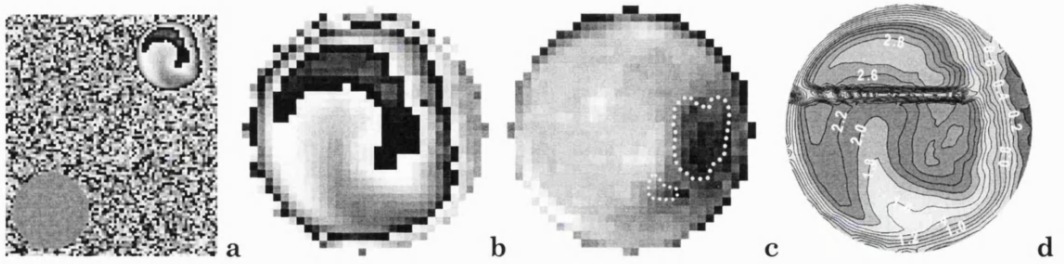

Figure 2.13 A raw MRI phase map image (a) including a stationary fluid region of interest (ROI) (lower left) used to calculate background phase statistics and the flow ROI (upper right) at the toe during late systolic acceleration. Also shown are a close-up on the extracted flow ROI (b), its corresponding magnitude image ROI with the low SNR regions highlighted (c) and, the corresponding axial velocity contour plot after partial phase unfolding (d).

The CFD results were first interpolated temporally to produce a more closely sampled data sequence through the cycle. Temporal matching of the MRI and CFD results was obtained as follows: the experimental velocity profile extracted from the first MRI phase in time was compared with each computed profile from the fine sequence of CFD results and each rms difference was calculated. The point in the computed sequence that minimised the rms difference was taken to correspond to the first MRI phase. Subsequent MRI phases were mapped to CFD time points according to the temporal spacing of the MRI time series. This process was necessary since the CFD and MRI results had a different sampling rate and the exact position in the cycle of each phase of the MRI measurement was very difficult to determine. This uncertainty was due to the combination of temporal averaging and interpolation applied during the measurement (Foo et al., 1995) and the presence of a small phase lag between the flow waveform generated at the pump and the flow waveform measured in the model.

Finally, background phase statistics, calculated from the stationary fluid region of the phase images (Figure 2.13a), indicated a normal distribution of phase noise with a negligible mean value ($<3\text{x}10^{-3}\pi$ rad) and a standard deviation of around 0.033π rad. In addition, no phase gradient could be detected.

2.3.3 Results

Error in MRI flow measurements can be classified as random or systematic. Sources of systematic error in triggered two-dimensional PC flow measurements in-

clude partial volume effects, intravoxel phase dispersion, flow encoding axis and bulk flow misalignment, velocity aliasing, flow induced spatial–displacement artifacts, phase offsets and higher orders of motion artifacts. To reduce the systematic component of error in the measurements a thin slice (2 mm) was selected and the shortest possible TE (5.5 ms) was used given the relatively low aliasing velocity and high spatial resolution of the acquisition. All MRI velocities are normalised with the spatio-temporal mean velocity (U_{mean}= 10.7 cm/s) calculated by:

$$U_{mean} = \frac{Q_m}{A}, \tag{2.13}$$

where Q_{m} is the nominal mean flow rate and A is the nominal flow conduit cross sectional area. The mean velocity was also calculated from the measurements by integrating the velocities over the vessel cross-sectional area, dividing by the number of samples, and averaging the spatial mean velocity from all time phases. The difference between the two results was less than 2 % of U_{mean} at all slice extraction locations. The computations were also suitably scaled to produce a unit spatio-temporal mean inlet velocity. The rms differences between the experimental and the corresponding computational velocities were used as an estimate of the random error of the measurement. The following expression derived from the definition of the standard deviation by replacing the expected with the numerically computed velocity was used to calculate the profile mean spatio-temporal rms differences ($\overline{E}_{\text{rms}}$):

$$\overline{E}_{\text{rms}} = \frac{1}{U_{\text{mean}}} \sqrt{\frac{1}{nk} \sum_{t=1}^{k} \sum_{i=1}^{n} (u_{\text{MRI}\,t,i} - u_{\text{CFD}\,t,i})^2}, \tag{2.14}$$

where n denotes the number of experimental samples along a profile included in the calculation as determined by the radial density of the circular interpolating grid (here n=98), k the number of temporal phases included in the calculation as determined by the MRI temporal resolution (here k=25), $u_{\text{MRI}\,t,i}$ is the experimental value of the axial velocity and $u_{\text{CFD}\,t,i}$ is the corresponding numerically computed value for radial coordinate i at time t in the cycle. To establish the accuracy of the technique in complex time-varying flow $\overline{E}_{\text{rms}}$ was calculated at three stations at the toe (0D), and at two and four diameters distal to the toe. At each station MRI and CFD axial velocity profiles extracted from both along the constant y and the constant x centrelines were com-

pared. This approach ensured that the resulting error estimate is neither profile nor direction specific.

Before discussing the results in detail, the effects of varying the FOV and V_{enc} parameters from those selected for the subsequent measurements on the velocity to noise ratio of the results are demonstrated. Figure 2.14 shows four axial velocity contour plots extracted at the toe in steady flow (Re = 437). Two FOV settings, 10 cm × 10 cm (Figure 2.14a & Figure 2.14b) and 7 cm × 7 cm (Figure 2.14c & Figure 2.14d) were used. A low velocity sensitivity setting (V_{enc}= 1.2 u_{peak}) was used for the results in Figure 2.14a and in Figure 2.14c and a high velocity sensitivity setting (V_{enc} = 0.3 u_{peak}) for the results in Figure 2.14b and Figure 2.14d. In all cases a NEX of 2, corresponding to a scan duration that is more clinically relevant, was selected. There is a factor of eight in VNR improvement (Equation (2.9)) between the result shown in Figure 2.14a and Figure 2.14d. This is caused partly by the twofold increase in the SNR from the increased FOV (i.e. larger voxel) and mainly by the fourfold increase in the velocity sensitivity.

Figure 2.15 shows a comparison of numerically computed and MRI measured axial velocity contour plots at the toe, and Figure 2.16 shows the corresponding profiles comparison. The spatially and temporally averaged rms error ($\overline{E}_{rms}$) calculated using equation (2.14) from the profile comparisons at the toe, was 1.2 cm/s or 11.5 % of U_{mean} for both the y-constant and x-constant centrelines. In the upper panel of Figure 2.16 an increased concentration of error in the near-wall region at the toe side (x/D = 0.5) is evident during the flow acceleration phases ($0<t/T<0.5$). In that region the computations exhibit a highly non-linear profile shape, a feature not well resolved in the experiment.

The presence near the toe of a recirculation zone, a region where reversing flow and stagnant or very slowly moving forward flow coexist in a relatively small volume, probably exhausts the spatial resolution of the measurement. In this region the values of both the first and the second spatial derivative of the velocity are high. Furthermore, from inspection of the corresponding magnitude images, one example of which is shown in Figure 2.13c, it was found that the SNR in the recirculation region was reduced by a factor of three compared to the SNR of adjacent image regions. This drop in SNR translates to a proportional drop in VNR, according to equation (2.9), and can be

attributed to a combination of primarily spin saturation due to long particle residence times and secondarily phase dispersion effects. Resolving velocities under these adverse flow conditions was only possible by using a contrast agent to reduce T_1 and by significantly extending the dynamic range of the velocity measurement.

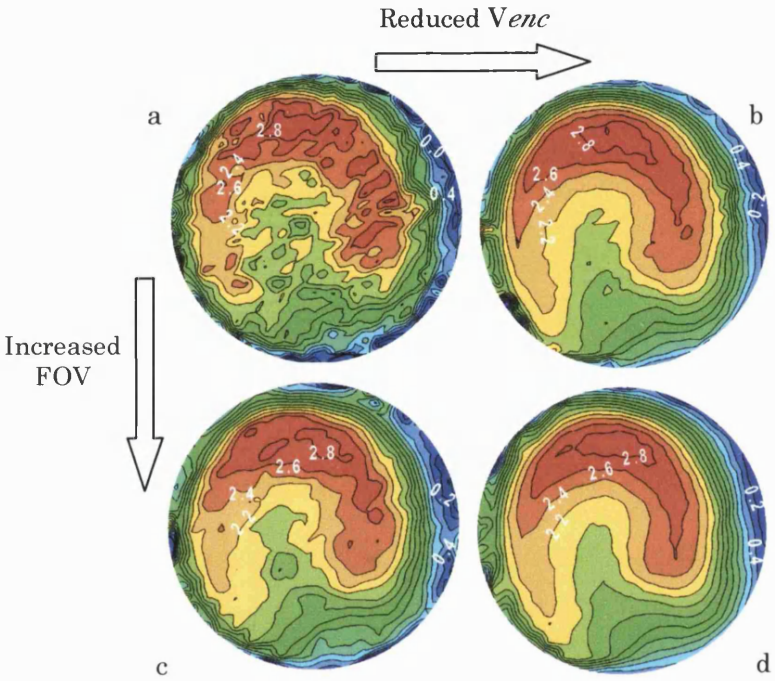

Figure 2.14 A comparison of MRI axial velocity contour plots extracted at the toe in steady flow (Re = 437) with a 7 cm × 7 cm (top) and a 10 cm × 10 cm (bottom) FOV. For a & c V_{enc}= 1.2 u_{peak} and V_{enc} = 0.3 u_{peak} for b & d. Measurements presented in b & d have been phase unfolded. All data are normalized by the Poiseuille mean velocity. Note the significant improvement in the velocity to noise ratio achieved by increasing the velocity sensitivity of the acquisition.

There is an apparent increased error during the late acceleration part of the cycle, which is most prominent in the central region of both the x-centreline and y-centreline profiles. This is most evident at the toe where the in-plane flow is strongest and the through-plane velocity gradients are steepest. Spatial displacement effects contribute to this error given the peak magnitude of the in-plane velocity (11.7 cm/s), the spatial resolution of the measurement, and the echo time (5.5 ms). The combination of temporal averaging and interpolation applied as part of the measurement (Foo et al., 1995) to reduce scan time is another source of error, which can act in conjunction with the former. Finally uncompensated non-zero higher order motion terms may also contribute to this error.

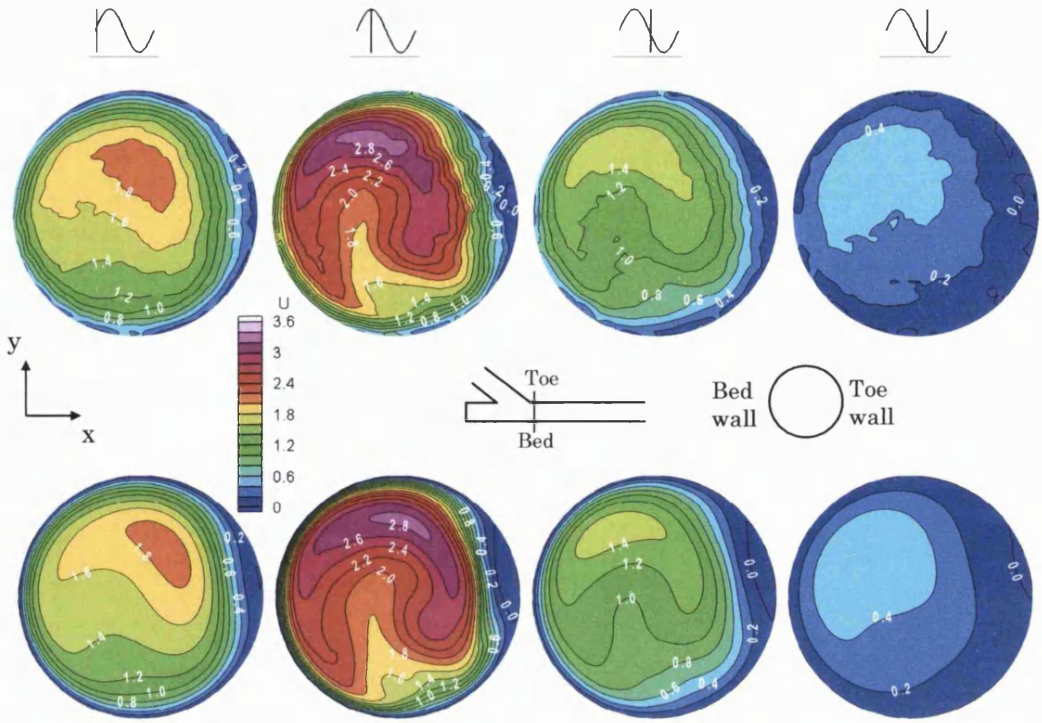

Figure 2.15 Comparison of MRI measured (top) and numerically computed (bottom) normalized axial velocity at the toe and (from left to right) at approximately mid acceleration, peak flow, mid deceleration and late deceleration respectively.

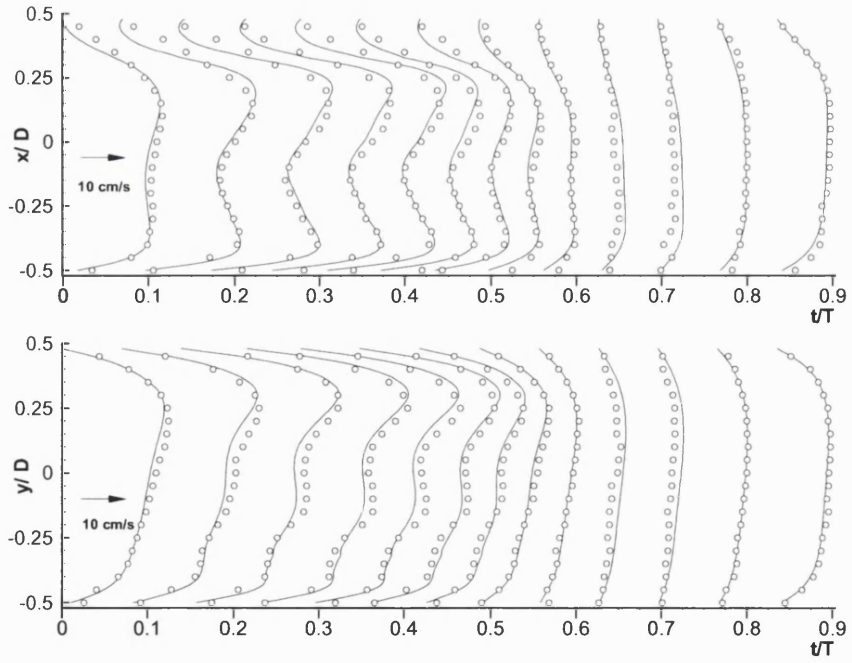

Figure 2.16 Comparison of the axial velocity profiles from MRI (symbols) and CFD (solid line) at the toe. Profiles are extracted along the constant y centreline (upper panel) and the constant x centreline (lower panel) and plotted against a dimensionless (t/T) time axis with 90 % of the waveform cycle shown. One in two of the acquired phases and two in three of the velocity samples per profile are shown. The centre of the cross section is at x = 0, y = 0 with the x and y axes orientation as in Figure 2.15. Peak flow corresponds to approximately $t/T = 0.25$.

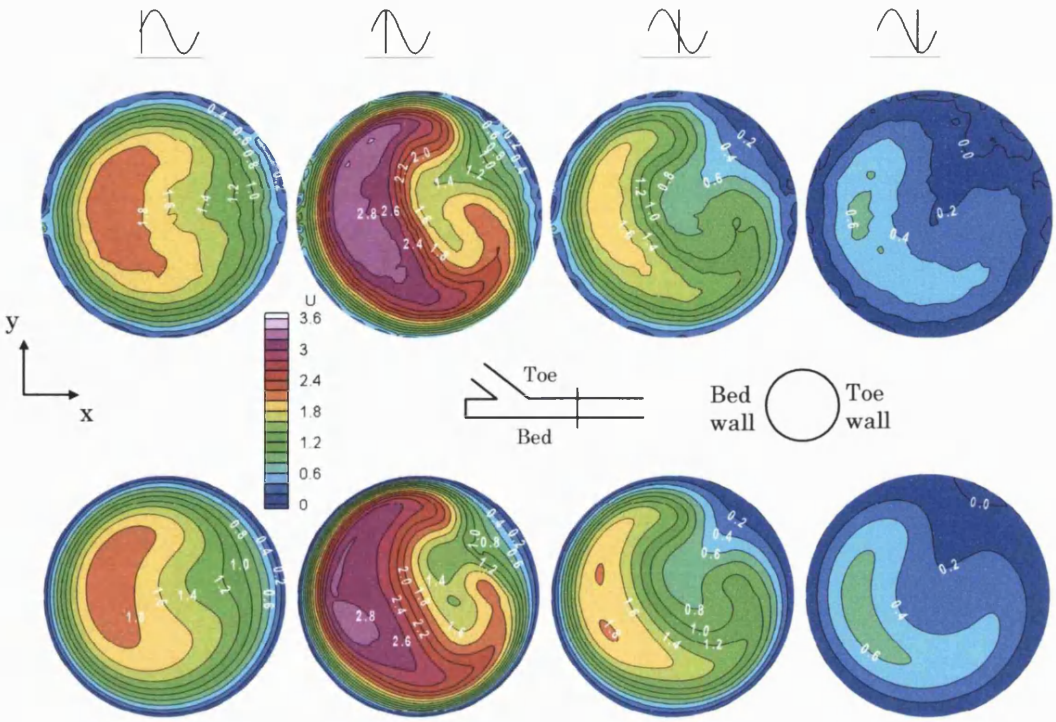

Figure 2.17 Comparison of MRI (top) and CFD (bottom) normalized axial velocity at 2D and (from left to right) at approximately mid acceleration, peak flow, mid deceleration and late deceleration respectively.

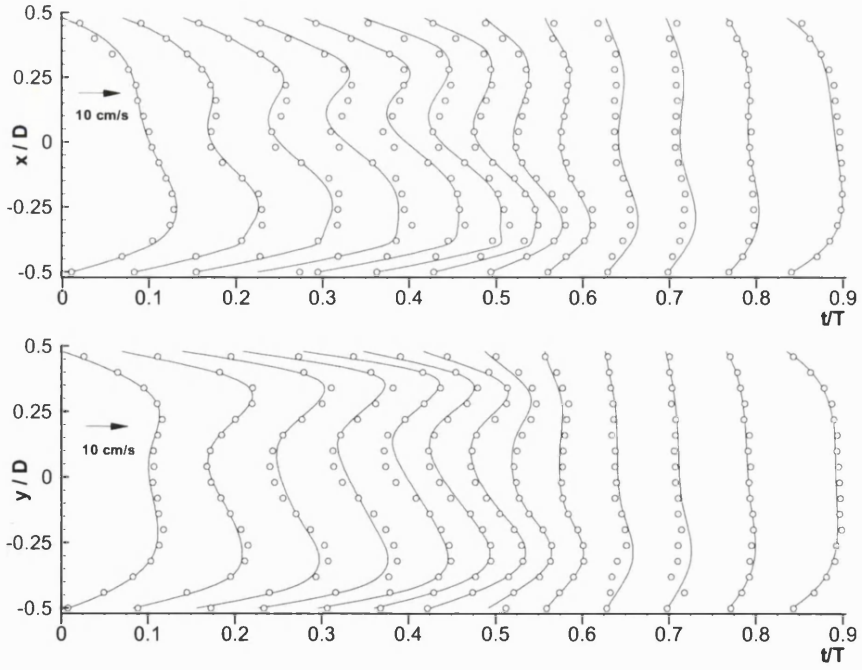

Figure 2.18 Comparison of the axial velocity profiles from MRI (symbols) and CFD (solid line) at 2 D downstream of the toe. Profiles are extracted along the constant y centreline (upper panel) and the constant x centreline (lower panel) and plotted against a dimensionless (t/T) time axis with 90 % of the waveform cycle shown. One in two of the acquired phases and two in three of the velocity samples per profile are shown. The centre of the cross section is at x = 0, y = 0 with the x and y axes orientation as in Figure 2.17. Peak flow corresponds to approximately $t/T = 0.25$.

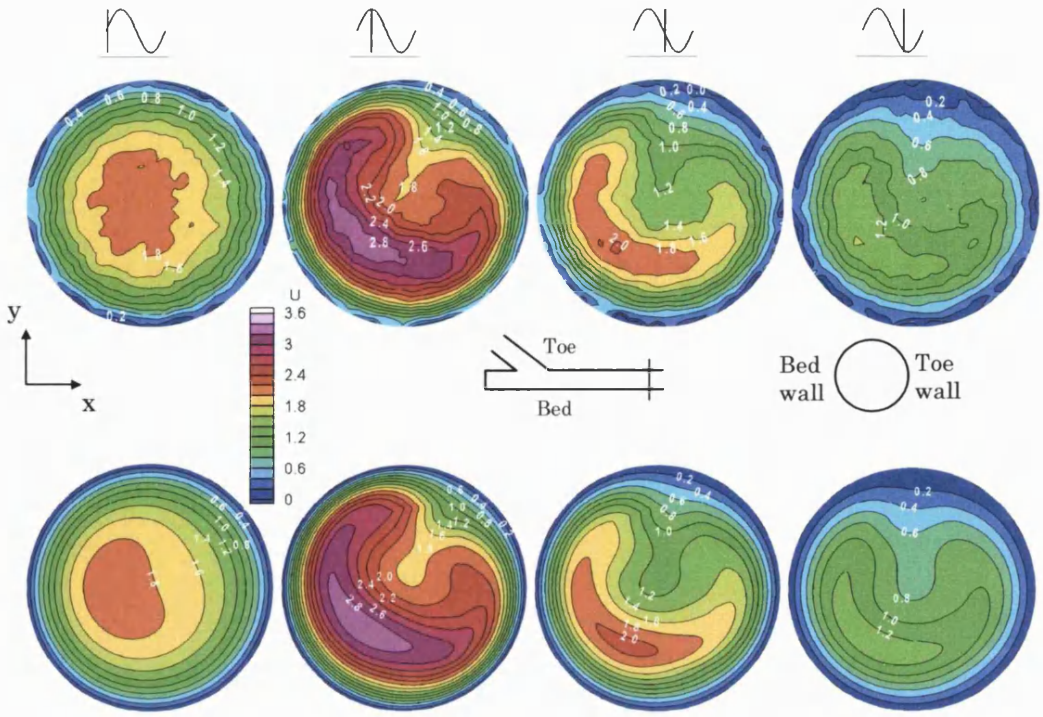

Figure 2.19. Comparison of MRI (top) and CFD (bottom) normalized axial velocity at 4D and (from left to right) at approximately mid acceleration, peak flow, mid deceleration and late deceleration respectively.

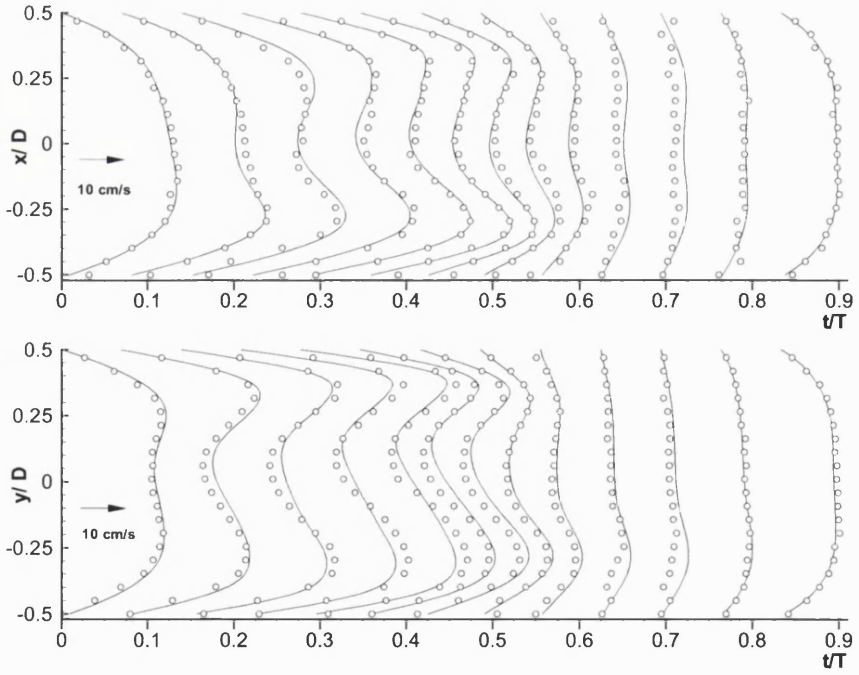

Figure 2.20 Comparison of the axial velocity profiles from MRI (symbols) and CFD (solid line) at 4D downstream of the toe. Profiles are extracted along the constant y centreline (upper panel) and the constant x centreline (lower panel) and plotted against a dimensionless (t/T) time axis with 90 % of the waveform cycle shown. One in two of the acquired phases and two in three of the velocity samples per profile are shown The centre of the cross section is at x = 0, y = 0 with the x and y axes orientation as in Figure 2.19. Peak flow corresponds to approximately $t/T = 0.25$.

Figure 2.17 shows the comparison of numerically computed and MRI measured axial velocity contour plots at 2D distal to the toe and Figure 2.18 the corresponding profile comparisons. The spatially and temporally averaged rms error calculated from the profile comparisons at 2D was 1.06 cm/s or 10 % of U_{mean} for the x-constant centreline and 0.91 cm/s or 8.6 % of U_{mean} for the y-constant centreline. Finally, at 4D (Figure 2.19) these values were 0.88 cm/s or 8.3 % of U_{mean} and 0.82 cm/s or 7.8 % of U_{mean} respectively. The mean rms error for all locations and profiles was 9.6 % of U_{mean}. The temporal variation of the calculated rms error in the flow cycle at the toe and at two and four diameters downstream of the toe is shown in Figure 2.21. The calculated error is clearly flow dependent and reaches its maximum at peak flow. There is also an increased error during the low flow part of the cycle ($0.65<t/T<0.75$) that is attributed partly to the reduced VNR of the measurements and partly to deviations of the measured flow waveform from that prescribed that were more pronounced at the low flow phases of the cycle.

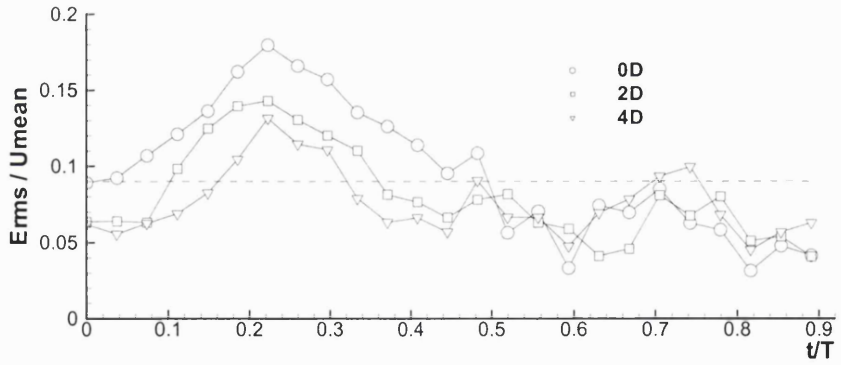

Figure 2.21 Plot of the temporal variation of the MRI velocity measurement rms error in the flow cycle calculated using the y-centreline profiles extracted at the toe (0D) and at two (2D) and four (4D) diameters downstream of the toe. The error is normalised by the spatial temporal mean velocity (U_{mean}). Time is normalised by the cycle period (T). Peak flow corresponds to approximately $t/T = 0.25$. Dotted line corresponds to the mean rms error averaged for all measurements stations (0-2D-4D).

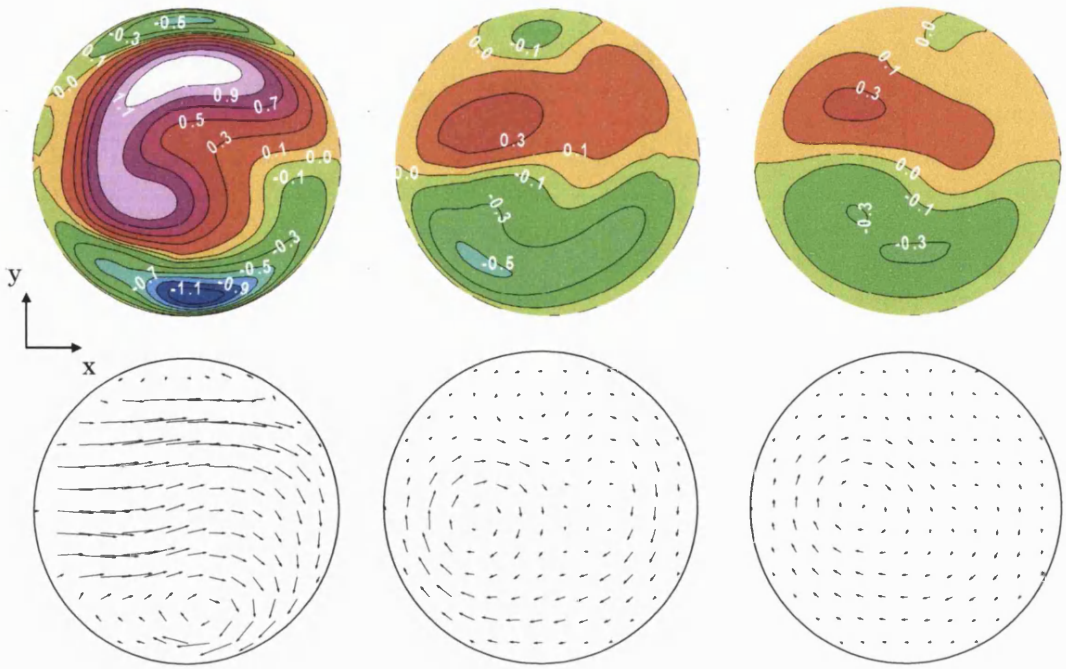

Figure 2.22 Numerically computed horizontal v-component cross flow velocity normalized by the axial mean velocity (U_{mean}). Slices extracted at the toe (a), 2D distal to the toe (b) and 4D distal to the toe (c) at peak systole.

2.3.4 Discussion

The aim of this study was to examine the use of the triggered two-dimensional PC technique for quantifying complex time dependent flows, to establish an estimate of the level of achievable accuracy, and to investigate techniques that can be applied to further improve accuracy and sensitivity of the measurements. The investigation focussed on the flow at a model junction representative of a distal anastomosis of a bypass graft; as such flows are both complex and have been the subject of a number of studies. However, a markedly three-dimensional graft geometry was considered, both since this produces strong secondary flow components, and because the flow patterns which result from breaking the symmetry of the graft geometry are of interest. The combination of out-of-plane curvature, which is common in arterial branching (Caro et al., 1996), and time-varying flow has a significant impact on the flow patterns in the model used. These patterns are likely to be more representative of the true *in vivo* flow conditions compared to those found in a two dimensional model. By restricting this study to a well-defined single harmonic sinusoidal flow in a model, it was possible to reduce errors associated with the characteristics of the waveform and its reproduc-

tion. Whilst overall the results show that the technique works well under complex flow conditions with most features in the flow field being well resolved, there are a number of points worth discussing after considering the results for the specific flow investigation.

Differences between the accuracy estimates presented here (7.8 % $U_{mean} < \bar{E}_{rms} <$ 11.5 % U_{mean}) and those cited for measurements of simple steady or time dependent flow were not large. The accuracy cited for axial unsteady flow in a straight rigid pipe is 7.5 % with respect to the spatially and temporally averaged velocity (Frayne et al., 1995). The accuracy commonly cited for steady Hagen-Poiseuille flow is in the region of 5 % of the mean velocity (Firmin et al., 1990; Ku et al., 1990; Maier et al., 1988). In this study it was found that the difference in error calculated at the toe and at 2D and 4D distal to the toe is related to the strength of the secondary flow at these locations. As the fluid moves in the straight host artery section it recovers from the effects of the upstream geometry and the cross-flow components gradually diminish.

Figure 2.22 shows, from the computations, the changes of the horizontal v-component distribution in the host artery. These results show that at the toe $|v_{peak}| = 1.1U_{mean}$ and that it diminishes as the flow moves distal to the toe to 0.6 U_{mean} at 2D and to 0.3 U_{mean} at 4D. The vertical w-velocity component was an order of magnitude weaker than v at the same locations. In spite of this significant change in the cross flow magnitude, the spatio-temporal mean rms error was not much altered. At the toe the error was 11.5 % of U_{mean}, at 2D distal to the toe it reduces to about 9.3 % of U_{mean}, and at 4D distal to the toe it is about 8 % of U_{mean}. A drop in the VNR in the recirculation region at the toe was attributed to signal dropout caused primarily by spin saturation effects and secondarily by intravoxel phase dispersion. This finding is in agreement with the results of Van Tyen et al. (1994) and Jou et al. (1996) for two-dimensional steady flow and three-dimensional transient flow respectively in the carotid bifurcation. They used numerical techniques to calculate both the flow and the magnetization evolution, and qualitatively compared, in the two-dimensional case, their predictions with MRA experiments. Both studies predicted a significant signal dropout in the carotid bulb in the flow separation region attributed to spin saturation primarily and to phase dispersion secondarily.

The degree of mismatch between experiments and computations was reduced as much as possible. The construction of the model was very precise, the inlet flow was appropriately conditioned and, the effects of MRI slice thickness were simulated in the computations by linearly interpolating a 2 mm thick section of the numerical velocity field positioned around the centre of the corresponding MRI slice location. However, as the slice excited was relatively thin, the effects of slice thickness were not significant. Even at the toe, where the strongest cross flow was found, the effect on error was less then 1 %. Finally, to improve the temporal matching of the results, CFD phases were interpolated temporally producing a more closely sampled data sequence through the cycle. However, especially at the toe, and during parts of the cycle error introduced by spatial displacement effects in conjunction with the combination of temporal averaging and interpolation applied during the measurement (Foo et al., 1995) was above the spatio-temporal mean rms error quoted. All sources of error have not been accounted for. To avoid overestimating error levels, near wall velocity measurements with very poor SNR were excluded from our error calculations. Near wall measurements suffer from partial volume effects, magnetic susceptibility artifacts and/or the presence of microbubbles on the wall surface.

A limitation of this study was that three phases immediately before mid acceleration were not reconstructed. This was due to a restriction in the clinical pulse sequence used that did not allow full coverage of the waveform cycle to reduce the effects of normal heart rate variations (*in vivo*) on the cardiac gating process. Nevertheless, the impact of this restriction on the temporally averaged error estimate was small, as the relative error contribution of low flow phases in the cycle to the spatially and temporally averaged error ($\bar{E}_{rms}$) was small.

The importance of considering the fine balance between the aliasing velocity, the echo time, and the spatial resolution in the design of a flow quantification MRI protocol was demonstrated. By careful selection of the aliasing velocity and by offline aliased velocity correction, an improvement in the VNR by a factor of four over the conventional no phase spill over approach has been achieved. Due to this gain in VNR, even velocities from phases during late deceleration were resolved. The dramatic improvement in the VNR that can be achieved by phase unfolding is shown in Figure 2.14. Several investigators (Axel and Morton, 1989; Conturo and Robinson, 1992; Ye-

ung and Kormos, 1986; Lee et al., 1995; Herment et al., 2000; Yang et al., 1996; Xiang, 1995) have demonstrated the significant benefits from applying dynamic range extension on clinical velocity measurements and have proposed various techniques to correct aliased velocities off line that if incorporated to clinical flow quantification protocols would improve measurement precision.

The results presented should be considered as an ideal case in comparison with *in vivo* studies, which are made under significantly less controlled conditions with additional sources of error. In a clinical setting the scan duration would most likely be reduced, by lowering the number of signal averages, typically by a factor of four (~ 4 min / slice) and a conservative velocity sensitivity setting ($V_{enc} \geq u_{peak}$) would probably be selected. These changes applied to the protocol used in this study could result in a reduction of the SNR by a factor of two and a reduction of the VNR (Equation (2.9)) by a factor of eight (a factor of four from the fourfold increase in V_{enc} and a factor of two from the twofold drop in SNR) without taking into account phase dispersion effects. This predicted drop in VNR would probably be even more pronounced in a typical clinical imaging situation considering the reduced proximity of the RF coil to the vessel of interest.

It is evident that the velocity measurement accuracy quoted here for complex unsteady flow can not be attained with the same spatial and temporal resolution in a clinical measurement and in a clinically acceptable time frame from a two-dimensional PC acquisition with the current typical MRI hardware. Nevertheless, as it was attempted to reduce systematic errors in the measurements, the results of this study provide a guideline to the inherent capabilities of MRI triggered phase contrast velocimetry in measuring complex unsteady flows. The combination of highly resolved numerical flow simulations with *in vivo* MRI flow measurements of the flow domain boundary conditions is an indirect method of obtaining estimates of near wall velocities and velocity gradients at the wall.

Chapter 3.

Flow in Idealised Bypass Graft Models

This chapter reports the results from experimental and numerical investigations of flow in model end-to-side anastomosis geometries. The first part examines the steady and time-varying velocity field obtained by MRI phase-velocity measurements. The second part presents an analysis of the results of accurate and detailed numerical computations of the time-varying flow field in the analytically described bypass graft geometries.

3.1 Introduction

The principal cause of arterial bypass graft failure is stenosis secondary to intimal hyperplasia. Surgical revascularization of arterial occlusive disease by autogenous or synthetic bypass grafts results in a flow conduit that differs significantly from that naturally occurring in the arterial system with significant physiological consequences. It is well known that a strong link between vessel wall biology and the local flow field exists with wall shear stress being one of the most influential flow features (Davies, 1995). Although the exact mechanisms associated with the development of vessel wall disease have not been fully understood, it has been demonstrated that intimal hyperplasia tends to occur preferentially in regions of low time averaged shear stress and long residence times (Sottiurai et al., 1983; Sottiuari et al., 1989; Ojha et al., 1990; Bassiouny et al., 1992). These studies have shown that in the distal anastomosis of end-to-side bypass grafts intimal hyperplasia occurs preferentially at the heel

and toe of the junction and on the bed of the host vessel opposite the toe (Figure 3.1). It has also been suggested that a link exists between spatial wall shear stress gradients or rapid temporal changes in wall shear stress and regions where intimal hyperplasia preferentially develops (Ojha et al., 1990; Ojha, 1993; Lei et al., 1997). Ojha et al. (1990) applied a physiological flow waveform at the graft inlet of a rigid, end-to-side, planar, anastomosis model and reported axial flow separation at the toe and low wall shear stress at the toe, the heel and the bed, sites commonly cited as preferential for intimal hyperplasia development. This result supports suggestions by Bassiouny et al. (1992) that intimal hyperplasia related arterial wall lesions in the region of the bed of the host artery could not be attributed to graft host artery compliance mismatch alone but should also relate to the presence of oscillatory flow and regions of low shear. In a different experiment Ojha (1993) studied planar end-to-side anastomosis models under pulsatile flow conditions and reported a region of flow stagnation on the bed of the host artery.

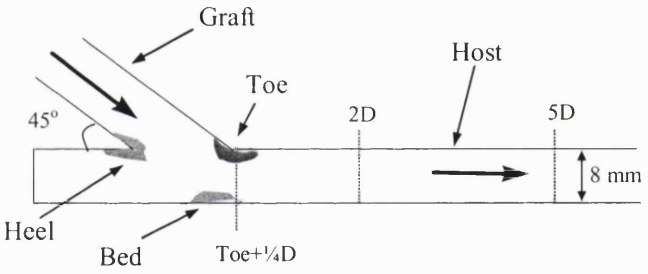

Figure 3.1 A schematic of a centre plane cross-section of a distal end-to-side anastomotic bypass graft showing the preferential sites of intimal hyperplasia development. The MRI scan plane orientation and locations are also shown.

Local flow features such as low time averaged shear, flow separation and shear oscillation have been found to promote the development of atherosclerotic lesions (Ku and Giddens, 1983; Friedman et al., 1987; Yamamoto et al., 1992). Jones et al. (1997) using pulse Doppler velocimetry obtained *in vivo* blood flow velocity profiles from canine ilio-femoral bypass grafts and observed separation zones at the hood and toe and an oscillating stagnation region on the bed of the host artery. They also noted a strong effect of out-of-plane curvature on the flow field.

Although there has been extensive research on the effect of hemodynamics on vessel pathogenesis (Lei et al., 2001; Steinman et al., 1996; Hofer et al., 1996; Henry et

al., 1996; White et al., 1993; Sottiurai et al., 1989; Ojha et al., 1990; Ojha, 1993), little work has been done to investigate the effects of the three-dimensional nature of the geometry of the vessels (Caro et al., 1996; Sherwin et al., 1997; Ding and Friedman, 1997); such geometry would be found in a physiologically correct anastomosis. The focal nature of intimal hyperplasia in bypass grafts can be attributed to the local hemodynamics in the perianastomotic region which are strongly influenced by the non-physiological configuration of the anastomosis. Caro et al. (1996) have suggested that arterial bifurcations are commonly 'non-planar', with non-planarity characterised by the presence of both curvature and torsion as in a helix. They also suggested that the introduction of non-planarity is expected to induce a swirling pattern to the flow, resulting in improved mixing of blood and in a circumferentially more uniform distribution of wall shear stress. These suggestions were supported by evidence of circumferentially more uniform, near-wall, velocity gradients in the non-planar configuration compared to the planar case.

So far most investigations whether in vitro experimental or numerical simulations have been restricted to geometries where the bypass and host vessel centrelines lie in a plane and can be termed planar. A few studies (Doorly et al., 1997; Sherwin et al., 2000; Xu et al., 1999; Moore et al., 1999) investigated model geometries with out-of-plane curvature. Doorly et al. (1997) used a combination of computational and MRI techniques to assess the effect of curvature and torsion on the flow field in the anastomotic region of a distal end-to-side anastomosis model. They compared the flow field in a planar and a non-planar distal anastomosis in steady flow and showed that the introduction of a small degree of torsion, rendering the proximal portion of the graft quasi-helical, would strongly affect the flow field downstream introducing a clockwise swirl type flow. Moore et al. (1999) removed geometrical features from an anatomically faithful finite element model of a human end-to-side arterial anastomosis to produce a series of simplified models. They reported that removal of out-of-plane curvature substantially changed the secondary flow field and particle residence times, but did not markedly alter the distribution of wall shear stress. However, they considered only models with a hood, which by expanding graft cross-sectional area and reducing mean velocity, would potentially lessen the effect of out-of-plane curvature on the flow field.

In an experimentally validated numerical investigation Sherwin et al. (2000) compared steady flow features from two distal anastomosis geometries, one planar and one non-planar. In the non-planar configuration the bypass vessel lies perpendicular to the original planar geometry as shown in Figure 3.2. The planar geometry used includes a 45 degrees anastomosis and the host vessel is fully occluded proximal to the anastomotic junction similar to previous investigations (Steinman et al., 1996; Hofer et al., 1996; Henry et al., 1996; Ethier et al., 2000). Sherwin et al. (2000) reported a 10 % reduction in the peak shear stress at the bed region of the host artery in the anastomosis region in the non-planar model as compared to the planar configuration. They also found an 80 % increase in the absolute flux of velocity in the occluded section proximal to the anastomosis, comparing their non-planar versus their planar model geometry. The significance of the effects of flow pulsatility on the flow patterns and the wall shear stress distribution in the planar end-to-side anastomosis was demonstrated in a study by Ethier et al. (1998).

The aim of this investigation is to achieve fundamental understanding of the influence of out-of-plane curvature in the graft in a controlled and well-studied steady and transient flow environment. This objective would not have been met as part of a patient specific study. The experimentally validated numerical investigations of Sherwin et al. (2000) are furthered by introducing flow pulsatility and using the same model geometries. Rigid wall models are used and blood is assumed to be Newtonian. Although these conditions are not true *in vivo* it appears that the influence of wall compliance on the local hemodynamics is secondary compared to the effects of the overall geometry, inflow and outflow conditions and the transient behaviour of the flow. Liepsch and Moravec (1984) reported a reduction in wall shear stress magnitude and a damping of retrograde flow as a result of introducing wall compliance to their rigid wall arterial model. However Friedman et al. (1992) found no significant changes in the correlation of vascular disease to normalised wall shear by introducing wall compliance or a non-Newtonian fluid in their model. A study by Moore et al. (1994) comparing results from an in vitro glass model study and an *in vivo* study of the flow in the abdominal aorta, showed that the most important flow features present *in vivo*, such as skewed velocity profiles and flow reversal, where also present in the rigid wall model. In a later numerical investigation of flow in a compliant carotid artery model,

Perktold and Rappitsch (1995) demonstrated that the global flow and shear stress patterns remain largely unchanged from the introduction of wall compliance.

This investigation was also limited to a single harmonic sinusoidal flow waveform. Although this is also a deviation from the true physiological flow conditions it nevertheless allows the dissociation of the fundamental effects of transient flow from the effects of patient or site-specific flow waveform characteristics on distal anastomotic hemodynamics. Although current blood flow investigations in models are moving towards more patient specific geometries and flow conditions (Perktold et al., 1998; Hughes et al., 1998; Milner et al., 1998; Moore et al., 1999), simplified model geometries can still help in better understanding the evolution and interaction of the complex flow structures that develop in bypass grafts and their relationship to various geometric parameters. In this investigation a combination of magnetic resonance imaging (MRI) experiments and numerical flow simulations are used to discuss the major features of the flow field. Wall shear stress direction maps and particle paths are used to illustrate the oscillatory motion of the stagnation point and the dynamic behaviour of the flow separation regions.

3.2 *Experimental Investigation*

In this part of the chapter results from an investigation on the effects of the bypass graft configuration on the perianastomotic steady and time-varying velocity field measured by MRI phase-velocity mapping will be discussed. Part of the steady flow results presented here has been incorporated in the paper by Sherwin et al. (2000) published in the Journal of Biomechanical Engineering.

3.2.1 Methods

Bypass graft model configurations

For the purposes of this investigation three distal end-to-side anastomosis model configurations were considered. One termed planar where the host and graft centrelines lie in a plane (Figure 3.2 a). A second termed non-planar (Figure 3.2 b) where a 90 degree bend originating approximately 4 diameters upstream of the graft-host cen-

treline anastomotic junction was introduced taking the upstream part of the graft out of the graft-artery junction plane and into a plane perpendicular to that defined by the centrelines of the graft host junction. Finally, to assess the effects of the angle of the out-of-plane curvature on the flow field, a third bypass graft configuration was considered where the curved graft section of the non-planar model was rotated clockwise so that the graft inlet and the graft-host artery junction symmetry plane were at a 30 degree angle. Although the physical model was designed to accommodate a range of out-of-plane curvature angles between 0 degrees and 90 degrees, due to practical limitations only the 90 and 30 degree configurations were investigated. The model which was constructed however allows effortless variation of the out of plane angle parameter. Given more time, results could have been obtained for any other intermediate value of the out of plane angle very conveniently, which is the advantage of the experimental method over the numerical simulations.

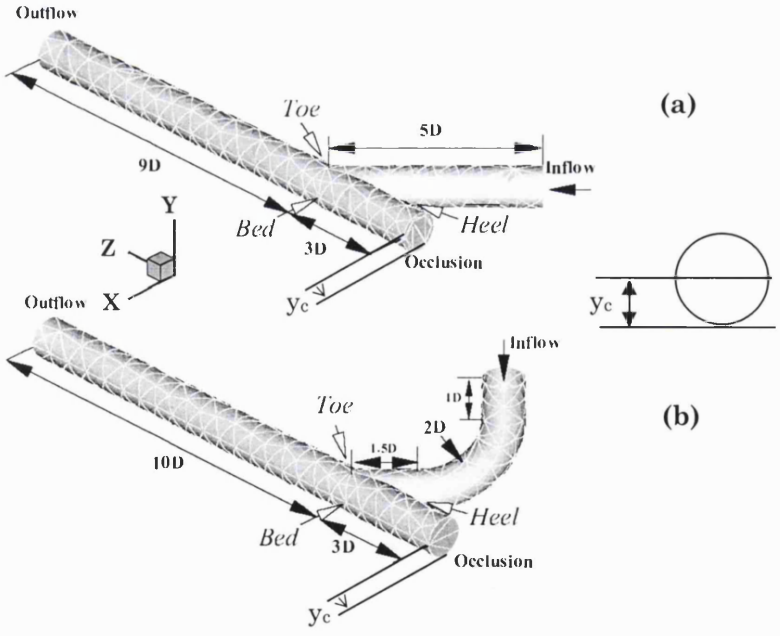

Figure 3.2 Model geometries of a distal 45 deg end-to-side anastomosis: planar (top) and 90 degrees non-planar (bottom). Dimensions shown are scaled by the vessel diameter.

MRI protocol

A two dimensional phase contrast pulse sequence on a GE Signa 1.5 Tesla whole body scanner was used for the steady flow acquisitions. The FOV was 12 cm × 12 cm and a 512 × 512 image matrix was used yielding a 0.234 mm in-plane resolution. This value corresponds to approximately 34 pixels across the vessel diameter, a value much higher than the minimum requirement of 15 proposed by Tang et al. (1993) to ensure a flow measurement error of less than 10 % of the true value. A 60 degrees flip angle (FA) was used and a slice thickness of 2 mm (equivalent to ¼ of the tube radius) was selected. The minimum (fractional) TE and TR of 8.2 ms and 22 ms respectively were selected with a 32 KHz receive bandwidth. An 11 cm/s aliasing velocity (V_{enc}) was selected and all velocity components i.e. axial (u), horizontal in plane (v) and vertical in plane (w) were encoded. Ten averages were applied to compensate for the inherently low signal-to-noise ratio due to the thin slices selected which resulted in a seven minute per slice location acquisition time.

The MRI protocol applied in the time-varying flow acquisitions for the non-planar model configurations was described in detail in section 2.3.1. The velocity measurement protocol was slightly different for the velocity measurements in the planar model. The aliasing velocity was 30 cm/s and thus no phase wrapping occurred. Due to the reduced velocity sensitivity of the measurement however, the results obtained are not as well resolved as those in the non-planar case, especially at the low flow phases of the cycle. Practical reasons prevented the repetition of the measurements with the lower aliasing velocity for the planar configuration. A computer controlled flow pump was used to provide both the constant flow (Re=250) and the sinusoidal flow waveform with a Reynolds number varying in the range between 62 and 437 with a mean Reynolds number of 250.

3.2.2 Results and Discussion

3.2.2.1 Steady flow

The velocity field in the host artery distal to the toe in the three distal end-to-side bypass graft models described in section 3.2.1 was investigated. A comparison of the axial velocity distributions, for the planar and the two non-planar models (30 degrees and 90 degrees out-of-plane curvature) is shown in Figure 3.3. The results are compared for slices just downstream of the toe, and at one diameter and at two diameters distal to the toe. The results clearly show a rotation of the crescent shaped contours of the velocity field as the flow travels distally in the host artery section. This clockwise rotation of the 'velocity crescent' is indicative of a swirling pattern imposed on the flow by the out-of-plane curvature of the graft. As the flow travels down the host artery the effects of the upstream curvature diminish with increasing distance from the toe. The cross flow gradually weakens and the fully developed parabolic velocity profile imposed at the graft inlet is gradually restored. The distribution of the in-plane velocity components (v, w) extracted just distal to the toe (~¼D) of the planar anastomosis is shown in Figure 3.4.

The difference in the level of flow asymmetry introduced by the varying degree of out-of-plane graft curvature is clearly demonstrated by these results. There is a reduced rotation of the velocity crescent in the thirty degrees case as compared to the 90 degrees out-of-plane graft curvature configuration. Differences in the shape of the velocity profile are more pronounced near the toe of the anastomosis where cross flow (Figure 3.5 and Figure 3.6) is strongest and the effects of the upstream out-of-plane graft curvature on the flow have not been influenced by the straight host section. By inspection of the contour level density near the wall a qualitative assesment of the wall shear stress distribution can be obtained. It is evident that overall there is a higher shear stress magnitude on the bed wall as compared to the toe wall. Axial flow separation appears to occur only in the planar model just distal to the toe on the toe wall. However as the velocity to noise ratio in this region of the vessel lumen is significanlty lower than elsewhere and as a result there is an increased level of uncertainty in the velocity measurement in that region, the possibility that what

appears as retrograde flow might actually be stagnant or slow forward flow cannot be excluded.

The overall flow structure provided by the various graft geometries, as revealed by the velocity field measurements, can be compared. Some discussion of the condition of the flow achieved by the various graft geometries is warranted. In the planar case a fully developed laminar flow enters the junction of the anastomosis and negotiates the angle of the anstomosis in a manner similar to that in a pipe with a fairly sharp bend. The in-plane pressure gradient that develops as a result of the centrifugal force acting on the fluid particles negotiating the junction sets up a cross flow pattern comprising a pair of counterrotating vortices similar to that of a Dean type flow in a curved vessel (Figure 3.7 a).

In the non-planar anastomosis the flow entering the graft-host junction is conditioned by a sharp 90 degrees bend with a radius of curvature equal to 2 vessel diameters. Therefore the flow enters the graft-vessel junction with a skewed velocity profile with higher velocities on the outer wall as compared to the inner wall. Thus the flow stream from the graft into the artery is not symmetrically disposed about the centre plane of the artery, which corresponds to the plane at $y=y_c$ in Figure 3.2. Instead proportionately more of the flow enters below $y=y_c$ and this results in the dominance of a vortex that has clockwise rotation in the distal outflow host section. A vortex dynamics model of the flow which relates the vortical structure which develops to the tilting and stretching of vortex rings is discussed in Doorly et al. (2001). Alternatively one may relate the graft geometry to that of a helix, given that as the flow travels first in the 90 degree bend in one plane, and that the 45 degree junction lies in another plane, the mean flow path is approximately helical. Steady flow in helical pipes has been theoretically investigated in a number of studies (Germano, 1982; Kao, 1987; Zabielski and Mestel, 1998). Kao (1987) found that although cross flow in fully developed helical flow consists of two vortices, these appear asymmetrically distributed with one dominating the pipe cross section. Helical-type flows have been reported in non-planar vessels such as the aortic arch (Kilner et al., 1993) and the left coronary artery (Sabbah et al., 1984).

The effects of the graft out-of-plane geometry on the cross flow pattern are shown in Figure 3.7. The cross flow streamlines in the planar case show two counter-

rotating symmetric vortices. This vortical flow symmetry however is broken in the non-planar configurations, a feature more pronounced in the ninety degrees out-of-plane graft curvature case. An estimate of the mean♦ pitch of the helical flow in the portion of the artery just downstrem of the junction bypass graft can be obtained from the change in the rotation angle of the velocity crescent as the flow travels down the host vessel. Figure 3.8 shows a comparison of the axial velocity distribution obtained at five diamaters distal to the toe in the three graft configurations. Due to the symmetry of the geometry no bulk velocity crescent rotation occurs in the planar model. However comparing the results at the toe and at five diameters downstream there is an approximately 90 degrees bulk velocity crescent rotation for the thirty degrees out-of-plane curvature graft and an approximately 180 degrees bulk velocity crescent rotation for the ninety degrees out-of-plane graft curvature configuration. This result suggests that even by introducing a mild angle of out-of-plane curvature in the graft, significant flow swirl can be induced.

The crescent shape of the velocity distribution suggests that the bed wall of the host artery is exposed to higher levels of shear stress than the toe wall opposite. It is also evident that whereas the shear stress distribution is symmetric about the plane of symmetry in the planar anastomosis, the asymmetry in the axial velocity distribution in the non-planar models will lead to an asymmetric shear stress distribution. Although quantitative estimates of the absolute magnitude of wall shear stress could be calculated from these measurements it would be difficult to quantify the differences in the distribution of shear stress magnitude in the host vessel between the three bypass graft model configurations. Relative differences in the wall shear stress distribution between the three configurations would be more valuable as there are no conclusive results regarding the range of wall shear stress that provides a favourable force environment for the vessel wall thus preventing the development of intimal hyperplasia and vessel restenosis. Highly accurate numerical computations of the steady flow field in the planar and non-planar (90 degree) models have been used by Sherwin et al. (2000) to assess the influence of the upstream graft geometry on the distribution of wall shear stress in the host artery.

♦ Due to viscosity the swirl in velocity decays so the pitch is constantly lengthening

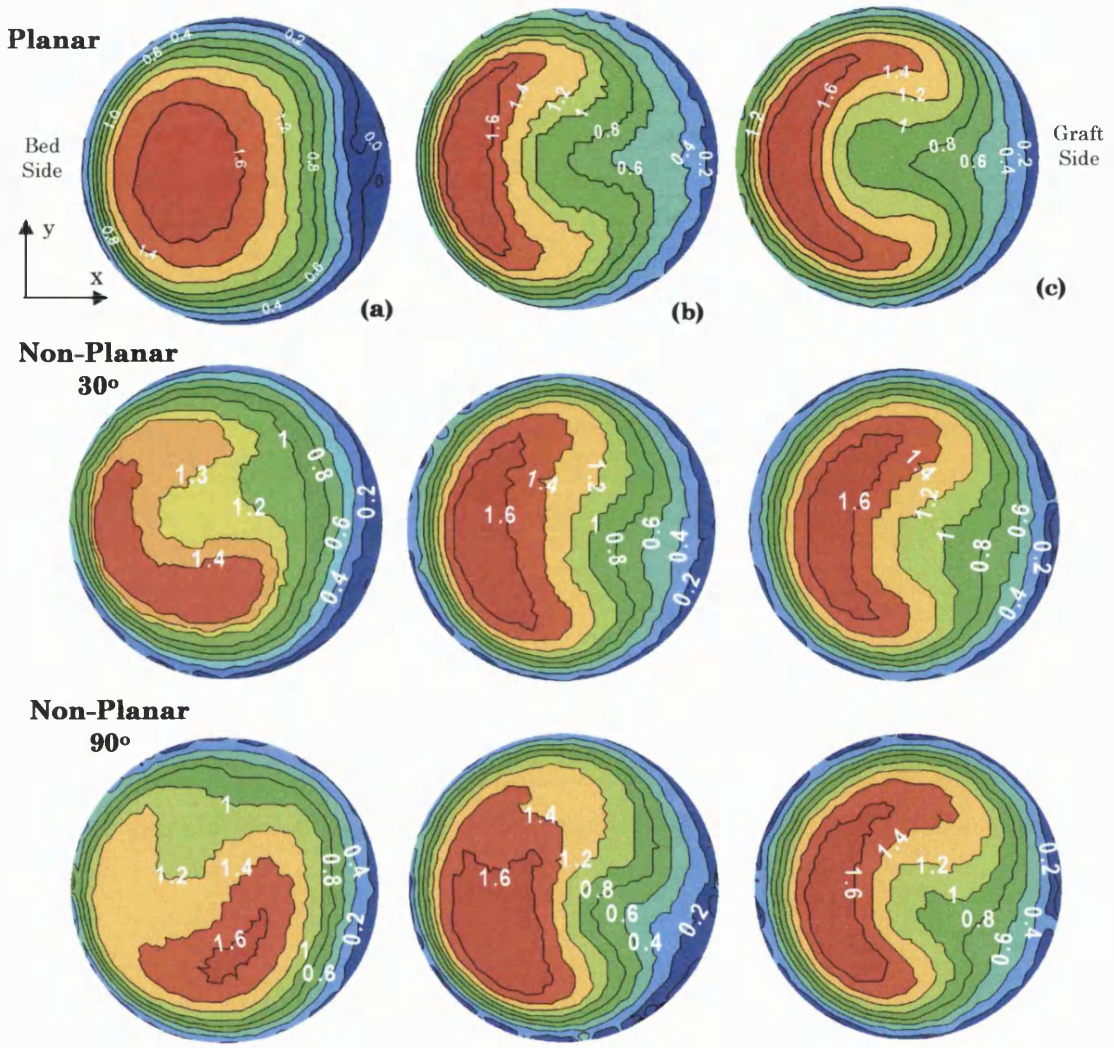

Figure 3.3 Comparison of axial velocity component extracted at 1/4D (a) 1D (b) and 2D (c) distal to the toe of the planar (top) and the non-planar anastomosis models with a 30 degrees (middle) and 90 degrees (bottom) upstream out-of-plane curvature.

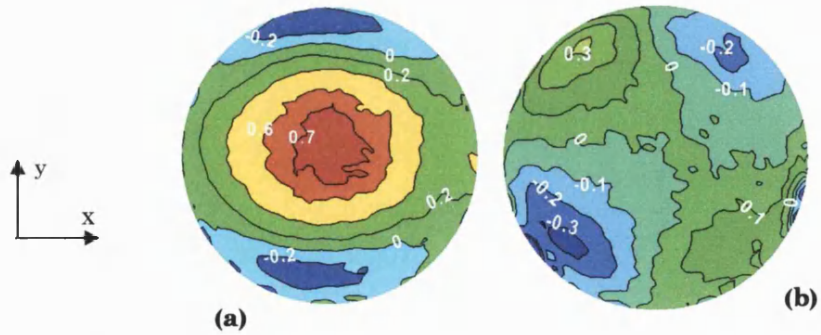

Figure 3.4 In–plane velocity components *v*-horizontal (a) and *w*-vertical (b) measured at ¼ diameter downstream of the toe in the planar end-to-side anastomosis model.

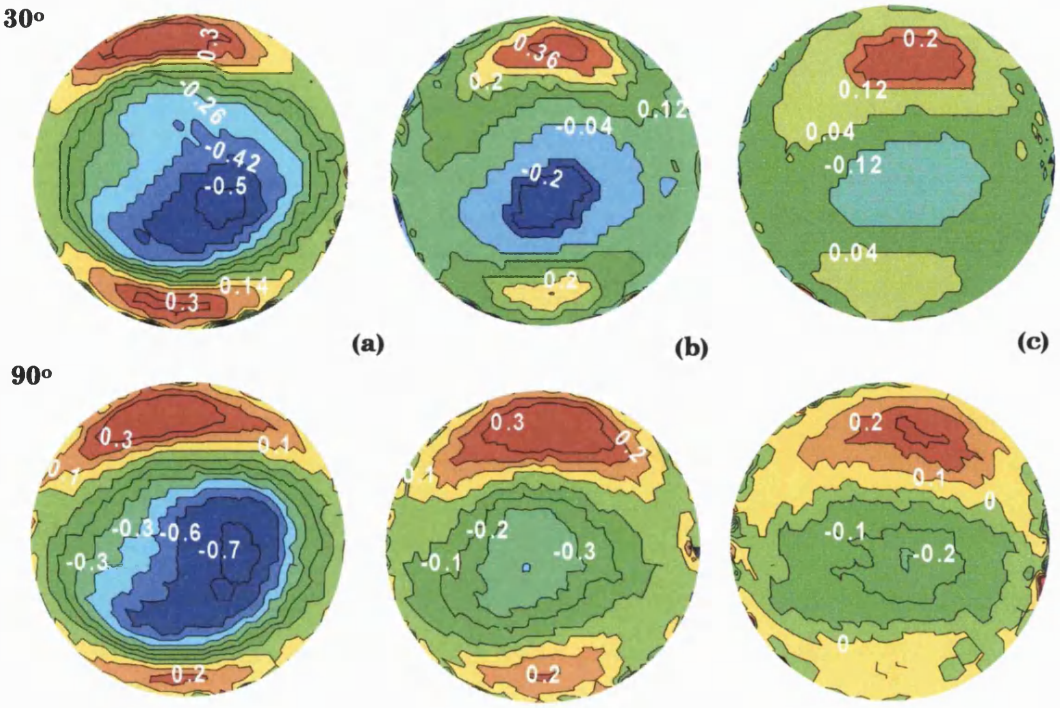

Figure 3.5 Comparison of horizontal-v velocity component extracted at 1/4D (a) 1D (b) and 2D (c) distal to the toe of the non-planar anastomosis model with a 30 degrees (top) and 90 degrees (bottom) upstream out-of-plane curvature.

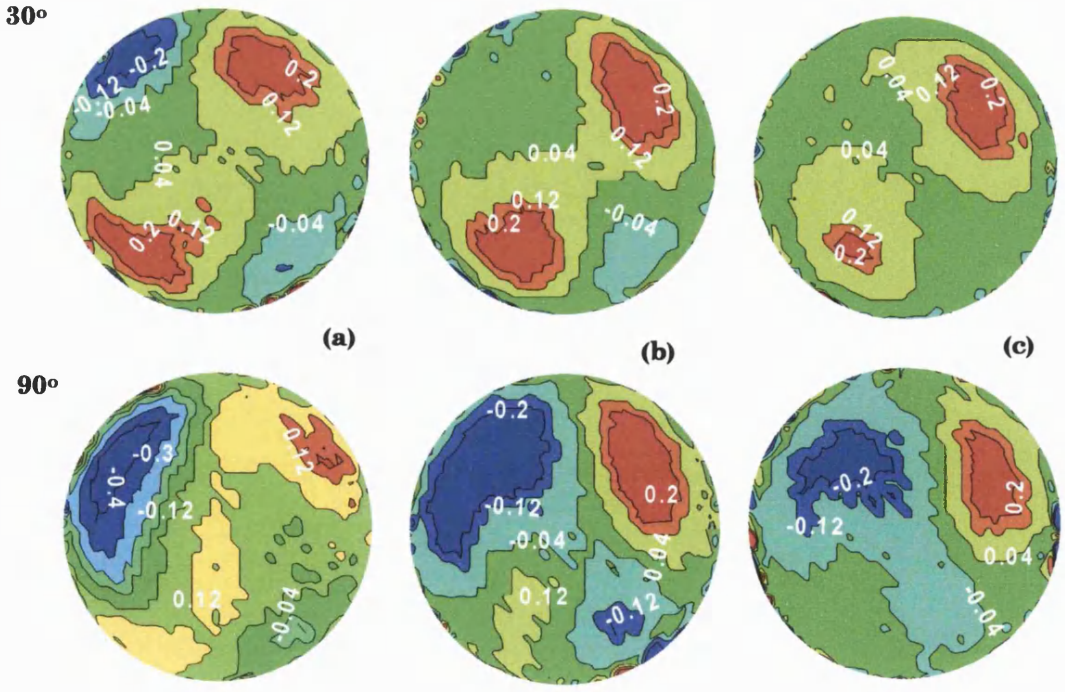

Figure 3.6 Comparison of vertical-w velocity component extracted at 1/4D (a) 1D (b) and 2D (c) distal to the toe of the non-planar anastomosis model with a 30 degrees (top) and 90 degrees (bottom) upstream out-of-plane curvature.

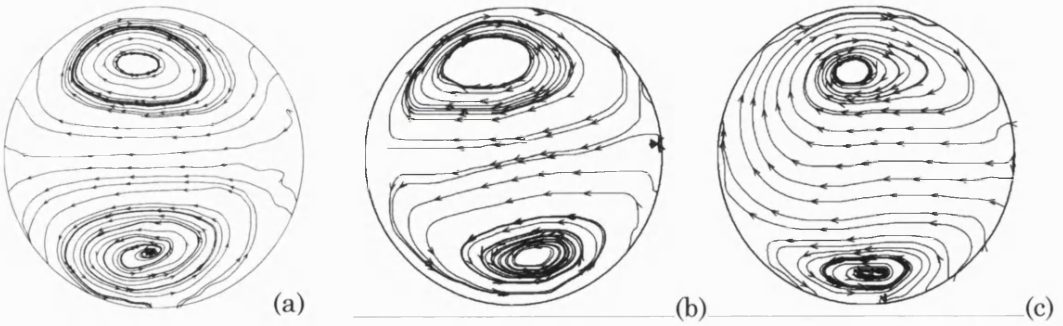

Figure 3.7 Comparison of cross flow streamlines extracted at ¼ diameter distal to the toe of the planar (a) and the non-planar anastomosis model with a 30 degrees (b) and 90 degrees (c) upstream out-of-plane curvature.

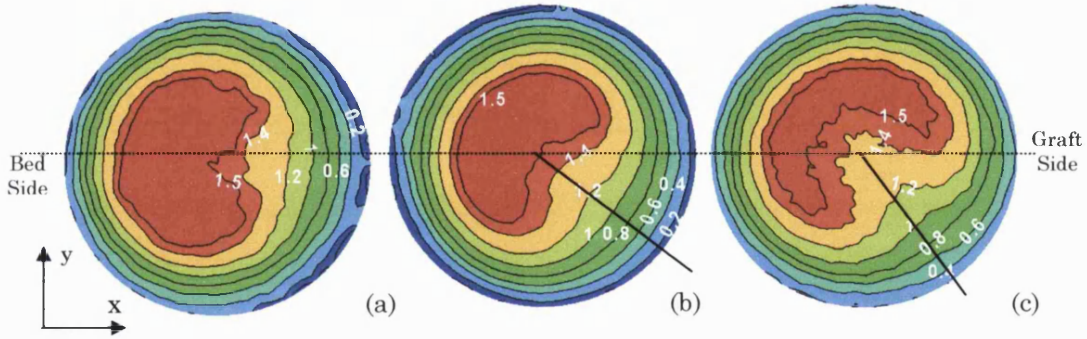

Figure 3.8 MRI normalised axial-u velocity component contour map extracted at a normal cross section of the planar (a) and the non-planar anastomosis model with a 30 degrees (b) and 90 degrees (c) upstream out-of-plane curvature at 5 diameters downstream of the toe. The Reynolds number was Re = 250. Lines indicate angle of velocity crescent rotation.

3.2.2.2 Time-varying flow

The steady flow measurements in the three bypass graft models showed a swirling flow pattern introduced by the out-of-plane curvature in the graft. To examine the dynamics of the flow field and the significance of the geometry induced flow features, a single harmonic sinusoidal flow waveform was applied at the graft inlet of the planar and the 30 and 90 degree non-planar bypass graft models. The axial velocity distribution was measured at four locations within the host artery section, at the toe and at one, two, and five diameters downstream of the toe in all bypass graft configurations.

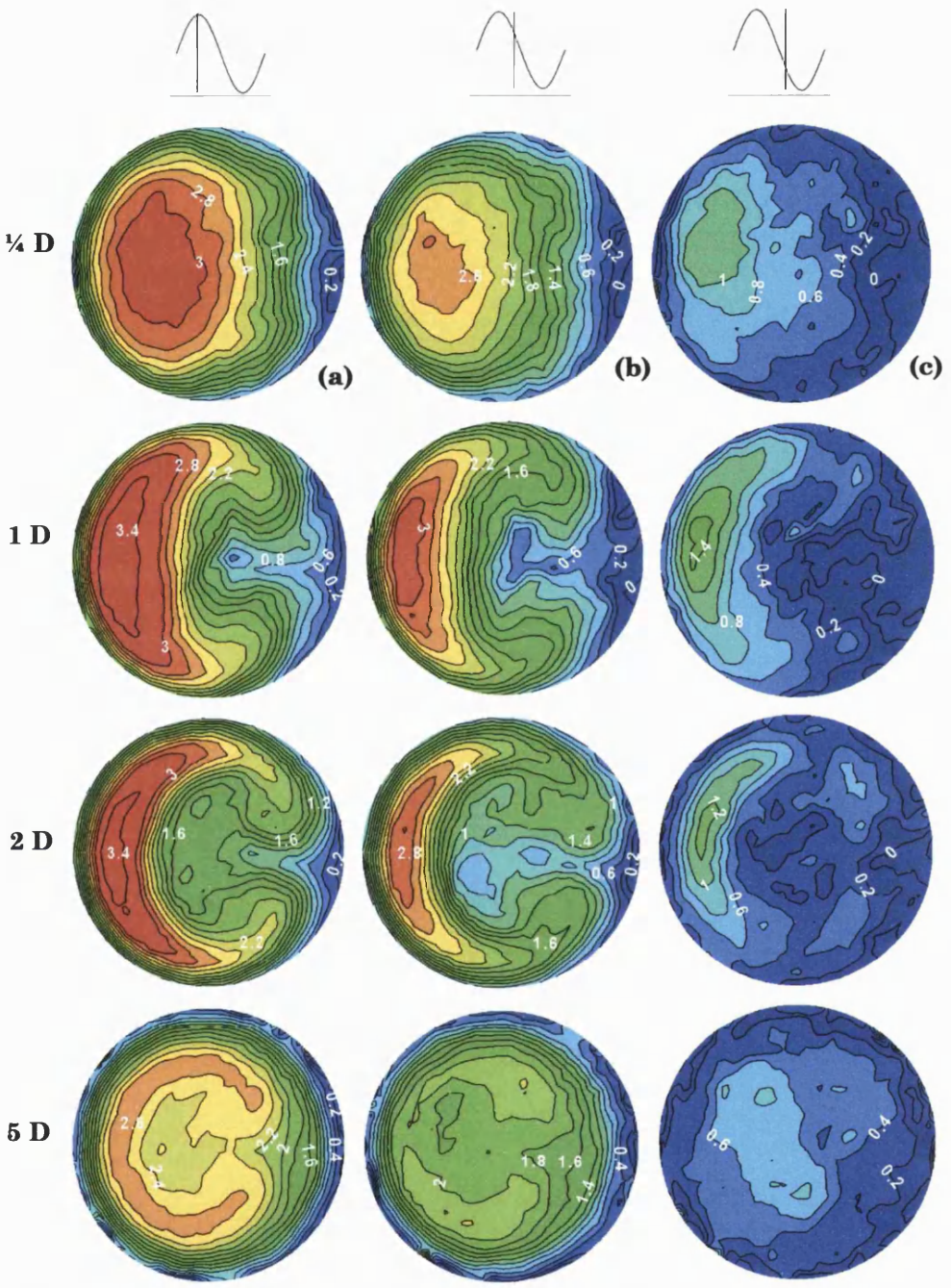

Figure 3.9 Axial velocity contour plots from the **planar** anastomosis model extracted at (top to bottom) the toe + ¼ D and at 1 diameter, 2 D and 5 D distal to the toe in sinusoidal flow. Views of the velocity distribution at peak flow (a), during early deceleration (b) and late deceleration (c) as indicated by the corresponding panels at the top are shown. Velocities have been normalised by the mean Poiseuille velocity at the inlet.

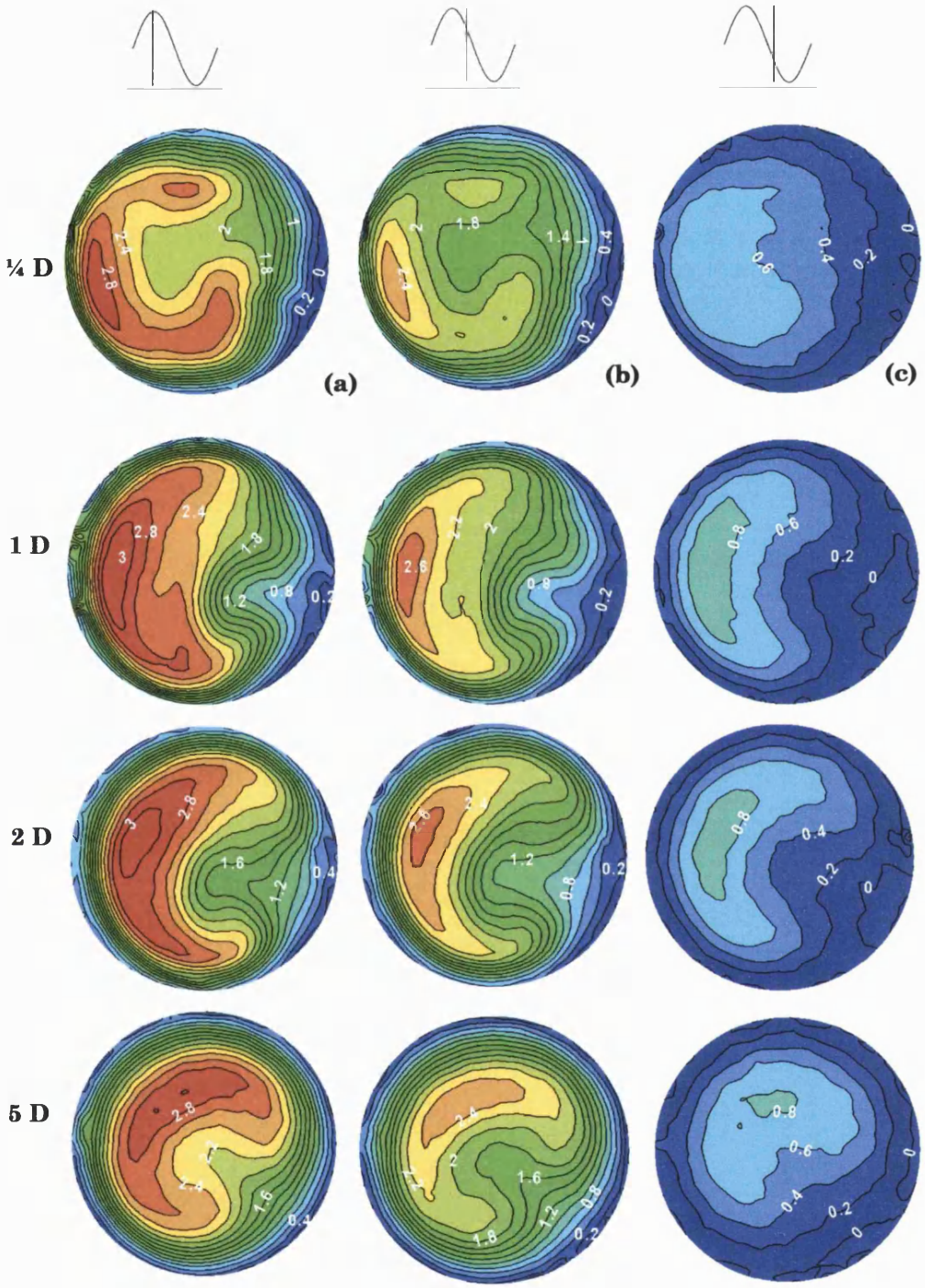

Figure 3.10 Axial velocity contour plots from the non-planar anastomosis model with a **30 degrees** upstream out-of-plane curvature extracted at (top to bottom) the toe + ¼ D and at 1 D, 2 D and 5 D distal to the toe in sinusoidal flow. Views of the velocity distribution at peak flow (a), during early deceleration (b) and late deceleration (c) as indicated by the corresponding panels at the top are shown. Velocities have been normalised by the mean Poiseuille velocity at the inlet.

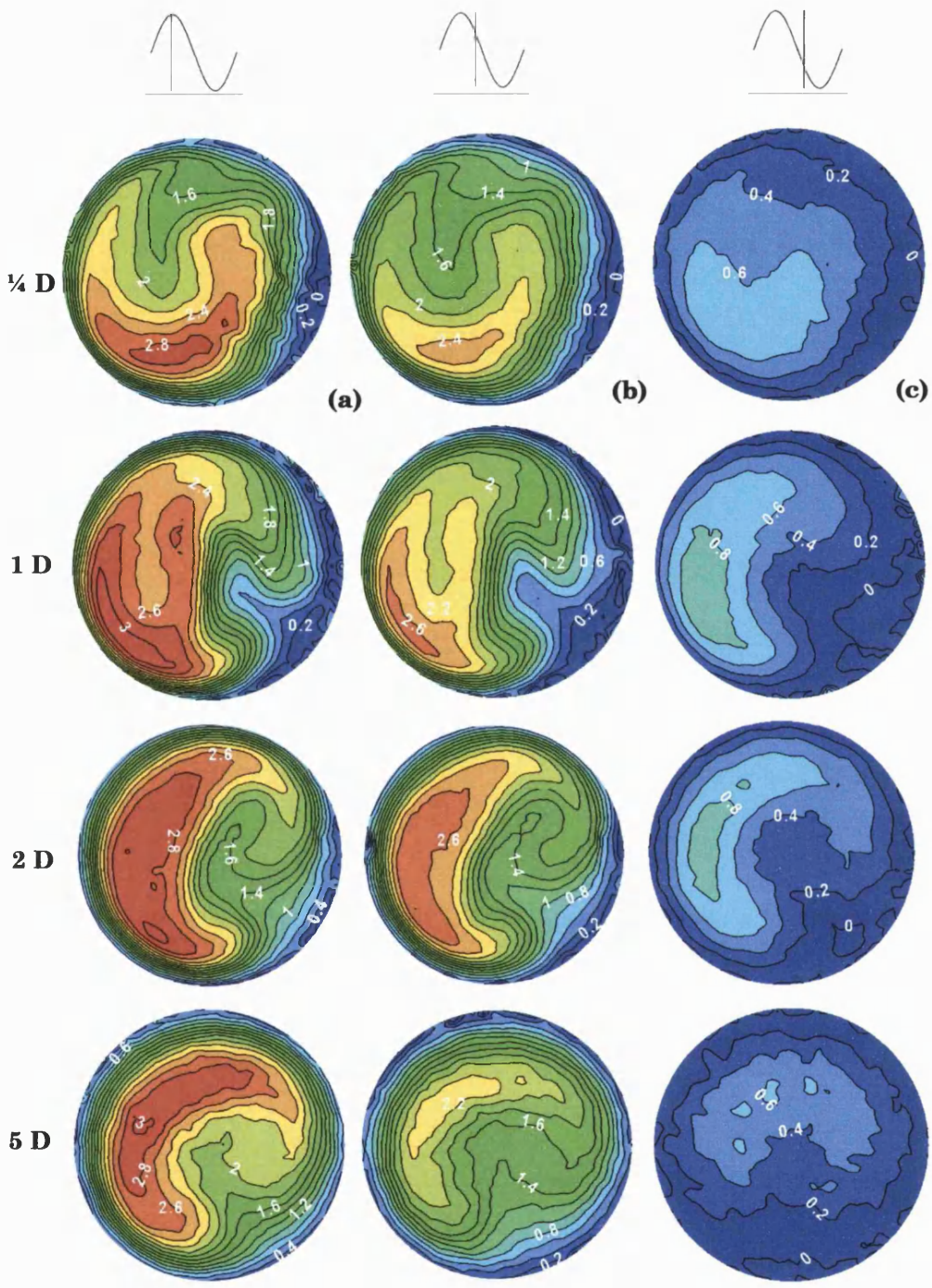

Figure 3.11 Axial velocity contour plots from the non-planar anastomosis model with a **90 degrees** upstream out-of-plane curvature extracted at (top to bottom) the toe + ¼ D and at 1 D, 2 D and 5 D distal to the toe in sinusoidal flow. Views of the velocity distribution at peak flow (a), during early deceleration (b) and late deceleration (c) as indicated by the corresponding panels at the top are shown. Velocities have been normalised by the mean Poiseuille velocity at the inlet.

Figure 3.9 shows the axial velocity distribution during peak flow, early acceleration and late acceleration acquired at the toe and at one, two and five diameters distal to the toe in the planar anastomosis. The first flow feature that clearly differentiates the time-varying from the steady flow field is the presence of a region of axial flow separation in the former case. The flow separates during the deceleration phase of the cycle as a result of the adverse pressure gradient acting on the low momentum fluid particles near the toe wall. The region of flow separation extends between the toe and two diameters distal to the toe and is centred at one diameter distal to the toe were it is most spatially extensive. It should be noted that the time-varying flow measurements in the planar model were obtained with a higher aliasing velocity of 30 cm/s compared to 9 cm/s used for the non-planar model results. This reduced the velocity to noise ratio of the velocity measurements by more than a factor of three but it was not possible to repeat the measurements with the lower aliasing velocity due to practical limitations. As a result phase-velocity maps obtained from low flow phases in the cycle are not very well resolved. There is also some asymmetry in the axial velocity distribution which is probably associated with slight imperfections in the fabrication of the model. Overall and apart from the axial flow separation occurring near the toe wall the shape of the velocity distribution is similar to that found in the planar geometry for steady flow.

The axial velocity distribution extracted from four locations in the host section of the 30 degrees non-planar bypass graft model is shown in Figure 3.10. These results show that the region of axial flow separation on the toe wall although minimal at the level of the toe appears axially expanded as compared to the planar case as it extends up to 5 diameters downstream of the toe. The footprint of the flow separation region follows the bulk flow rotation and therefore follows a path that is oblique to the vessel axis. A further spatial reduction in the region of axial flow separation is found in the velocity distribution in the 90 degrees non-planar bypass graft shown in Figure 3.11. In this case there is practically no axial flow separation at the toe and the separation region extends axially up to 5 diameters downstream of the toe with its core at approximately one diameter downstream of the toe. It should be noted that since the flow field is only sampled at four stations along the distal host artery section of the bypass graft it cannot be established whether the regions of retrograde flow shown belong to a

single axial flow separation cell or secondary separation cells have been established. It should be noted that velocities in flow separation regions are difficult to resolve with MRI phase-velocity mapping due to signal drop-out from spin saturation and intravoxel phase-dispersion effects. It is therefore necessary to partly compensate for these errors by introducing a contrast agent to the fluid and reduce its spin-lattice relaxation rate, reduce the voxel size, and increase the overall SNR by for example extending the acquisition time.

Comparing the axial velocity distribution in the planar and non-planar (both thirty and ninety degrees) bypass graft models it is evident that there is reduction in the peak velocities of approximately 10 percent in the non-planar case as compared to the planar case. This difference suggests a more uniform velocity distribution introduced as a result of the upstream out-of-plane curvature in the graft.

For the measurements reported a simple sinusoidal, single harmonic flow waveform was applied at the inlet. Typically flow waveforms in large arteries include a number of significant Fourier modes (harmonics) leading to phases of steep flow acceleration and deceleration. Although the inlet flow conditions prescribed are thus not physiologically realistic, however by selecting a simple inlet waveform the uncertainty of the phase-velocity measurements due to errors associated with its physical reproduction is reduced and the influence of the bypass graft geometric configuration can be assessed.

Spatial resolution strongly influences the accuracy of MR phase-velocity mapping measurements. Although the spatial resolution of the current acquisition is relatively high compared to typical clinical MRI protocols, the effects of partial volume and intravoxel phase averaging on the accuracy of near wall velocity measurements cannot be neglected. These effects will be accentuated in regions were the boundary layer is thin hence the velocity gradients near the wall are high. It is widely accepted that wall shear stress plays an important role in the development of vascular wall disease. Extremes of wall shear stress may prove detrimental to the health of the vessel wall. It would therefore be extremely valuable if wall shear stress could be either measured directly or estimated with acceptable accuracy from *in vivo* MRI phase-velocity measurements. For steady flow in a pipe wall shear stress (τ) can be calculated by the following expression:

$$\tau = -\mu \left. \frac{\partial u}{\partial r} \right|_{r=R}, \tag{3.1}$$

where μ is the fluid dynamic viscosity and u is the axial velocity component, r is the radial distance from the axis, and R the tube radius. If shear stress is calculated by extrapolation of near wall velocity measurements, the uncertainty in the shear estimate will be a multiple of that of the velocity measurement. Due to the sensitivity of wall shear estimates to the uncertainty of the velocity measurement and the uncertainty of the exact wall location, acceptably accurate results from such techniques can only be obtained from phase velocity measurements in a highly controlled relatively simple flow environment *in vitro*.

3.3 Numerical Investigation

3.3.1 Introduction

In the first part of this chapter the influence of out-of-plane geometry on the gross features of distal anastomotic flow has been investigated experimentally by magnetic resonance velocimetry. However the assessment of the physiological significance of these effects on the biology of the vessel wall would be assisted by knowledge of the wall shear stress distribution, the oscillatory shear index distribution and the presence and dynamic behaviour of axial or cross flow stagnation points. The use of analytically described idealised model bypasses graft geometries, although simplifying, allows for a very accurate numerical calculation of the flow field. Sherwin et al. (2000) investigated the effects of out-of-plane graft curvature in distal end-to-side anastomosis for steady flow. As part of the continuing effort of the biomedical flow group in the Aeronautics department towards improving the understanding of arterial bypass graft hemodynamics, numerical calculations of the time-varying flow field in the planar and non-planar models have been carried out. The raw time-varying flow field data set was numerically computed by Dr Spencer Sherwin and was processed and analysed by the author forming the material for a paper due to appear in the Journal of Biomechanics (Papaharilaou et al., 2002). Parts of this paper are presented in the following sections.

3.3.2 Methods

The experimental and numerical methods applied to produce the results presented in this chapter have been detailed in section 2.3.1.

3.3.2.1 Modified oscillatory shear index

To obtain a measure of the oscillatory motion of the wall shear stress vector a modified oscillatory shear index was calculated (OSI) based on the definition of Ku et al. (1985) and the formulation introduced by Moore et al. (1999). As both shear vector magnitude and direction change with time in a continuous fashion the OSI is defined as follows:

$$OSI = \frac{\int_0^T w\left|\boldsymbol{\tau} \cdot \boldsymbol{n}_{mean}\right| dt}{\int_0^T \left|\boldsymbol{\tau} \cdot \boldsymbol{n}_{mean}\right| dt}, \tag{3.2}$$

where $\boldsymbol{\tau}$ is the instantaneous wall shear stress, $\boldsymbol{n}_{mean}$ is the mean shear direction defined as:

$$\boldsymbol{n}_{mean} = \int_0^T (\boldsymbol{\tau} / \|\boldsymbol{\tau}\|) dt, \tag{3.3}$$

where T is the period of the flow waveform and w is a weighting factor defined as:

$$w = 0.5(1 - \cos a), \tag{3.4}$$

where a is the angle between $\boldsymbol{\tau}$ and $\boldsymbol{n}_{mean}$. This definition of the oscillatory shear index allows for the inclusion in the calculation of a continuous range of instantaneous shear vector angles with respect to the mean shear direction. The range of values for the modified index is 0<OSI<0.5 where 0 corresponds to unidirectional shear flow and 0.5 to the purely oscillatory shear case.

3.3.3 Results

3.3.3.1 Axial velocity

Figure 3.12 shows a comparison of the spatial distribution of the axial velocity component at mid deceleration and at four stations along the host vessel in the two

models. The out-of-plane inflow geometry breaks flow symmetry and establishes a bulk rotation of the velocity crescent that sets-up a Dean type flow in the graft vessel (Doorly et al., 1997). This rotation is evident in the host vessel and is dependent on the axial downstream distance from the toe. At the level of the toe on the bed wall the absence of retrograde flow in the non-planar model in contrast to the planar configuration is noted. This is not separated flow and is caused by the oscillatory motion of the stagnation point discussed further in section 3.3.4. In the non-planar configuration there is a distal 0.25 D migration of the separation point as compared with the planar model. The separation region in the non-planar model reaches its full extent along the bed wall during late deceleration spanning a region between 0.25 D and 2 D distal to the toe. Furthermore in the non-planar model the peak axial velocity in the host vessel distal to the toe is reduced by 10 % on average as compared to the planar configuration. The effects of flow unsteadiness on the transient perianastomotic flow patterns although evident in both model configurations are more pronounced in the non-planar configuration.

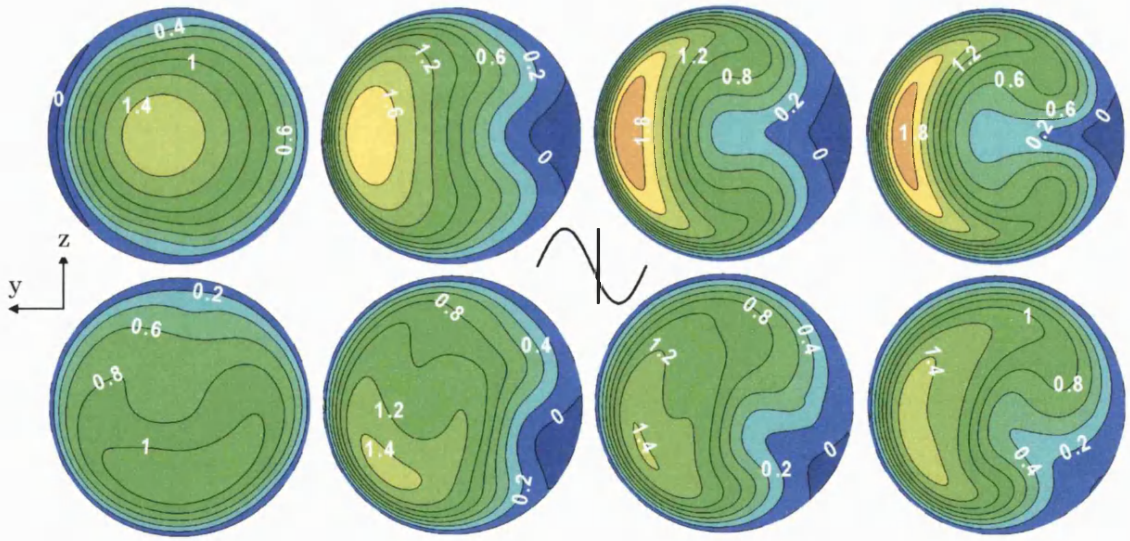

Figure 3.12 Numerically computed normalised axial velocity contour plots extracted (from left to right) at toe, 0.5D, 1D and 1.5D downstream of the toe from the planar (top) and non-planar (bottom) models just after mid-deceleration.

Both models exhibit regions of flow separation with their temporal and spatial evolution dependent on the downstream distance from the toe. Flow separation first

occurs during mid-acceleration with the separation point oscillating between the toe and 0.5 D distal to the toe in phase with the bulk flow. Apart from the distinctive clockwise displacement, looking down the vessel, of the separation zone in the non-planar model, its evolution is similar to the planar case. In the planar model the separation zone extents between the toe and approximately 1.7 D distal to the toe whereas in the non-planar model it extends between 0.25 D and 2 D distal to the toe. The size of the separation zone in both models is time dependent and peaks during late deceleration. Retrograde flow on the toe wall first appears at 0.5 D distal to the toe at mid-acceleration and gradually extends both distally and proximally during early deceleration until late deceleration. At end deceleration the adverse pressure gradient that causes flow separation has sufficiently weakened to allow full recovery of forward flow within the host vessel. Overall the introduction of out-of-plane curvature in the graft of the distal anastomosis causes a distal shift of the most proximal location of the separation point and a change in the spatial distribution of the separation region along the toe wall of the host artery as compared to the planar configuration.

3.3.3.2 Secondary flow

A comparison of the computed normalized horizontal–v velocity and the cross-flow streamlines in the two model geometries is shown in Figure 3.13. Flow symmetry is preserved in the planar model although not explicitly prescribed in the solution. The magnitude of the strongest (horizontal v-velocity) cross flow component is inversely related to the downstream distance from the toe. It drops steeply in the region between 0 D and 2 D downstream of the toe and more gradually further downstream. In the planar model the presence of two symmetric counter-rotating vortices in the transverse plane is noted. These Dean type vortices account for the clockwise and counter clockwise motion of fluid particles in the upper and lower recirculation regions respectively. On the toe wall at 4 D downstream of the toe two weak vortices rotating against the main vortices appear. These vortices are probably caused by the delayed response of viscous effects on the axial separated flow just downstream of the toe.

The out-of-plane curvature introduced in the non-planar configuration breaks flow symmetry and causes a 10 % reduction in the peak cross flow magnitude at the toe as compared to the planar configuration. Although two counter-rotating cells can

still be identified at the toe as in the planar case, the upper cell is significantly stronger than the lower one. As a result a strong clockwise vortex with its core at the top of the cross section dominates and the weaker secondary counter clockwise vortex is constrained spatially at the lower part of the cross section. At 2 D downstream of the toe the core of the dominant vortex has rotated clockwise by 90 degrees and has generated a weak secondary co-rotating vortex in the process. The core of the weaker vortex appears displaced towards the vessel axis. By 4 D distal to the toe the weaker vortices have dissipated and a single vortex remains.

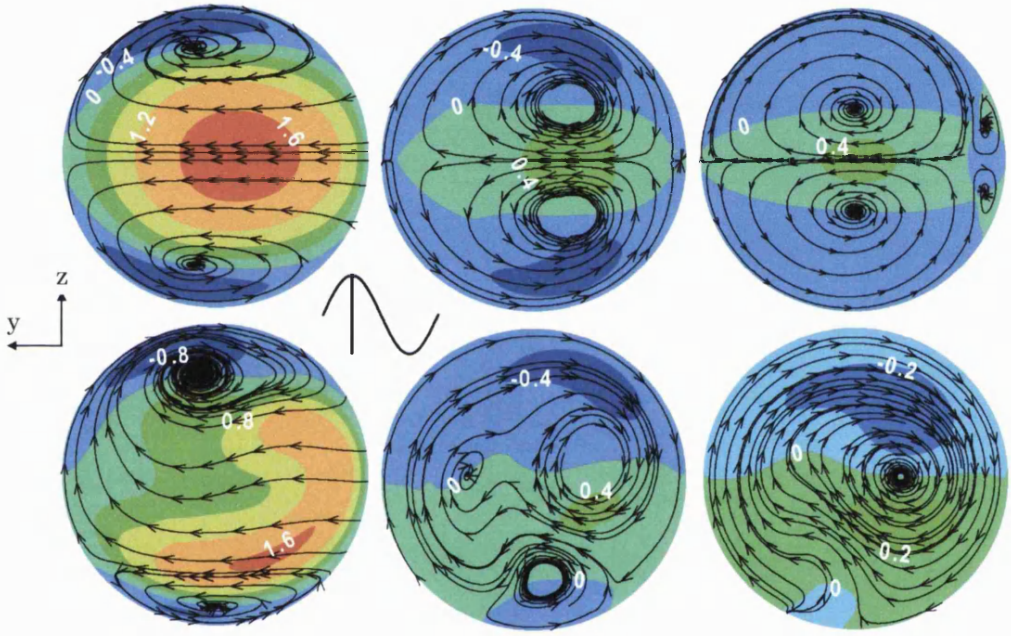

Figure 3.13 Comparison of numerically computed normalised horizontal v-cross flow velocity and cross flow streamlines in the planar (top) and non-planar (bottom) geometries at peak flow. Velocities extracted and streamlines calculated at the toe (left), 2D distal to the toe (centre) and 4D distal to the 'toe' (right).

3.3.3.3 Wall shear stress

The wall shear stress maps shown in Figure 3.14 and Figure 3.15 should be interpreted so that the horizontal axis represents distance along the host vessel and the vertical axis represents the circumferential distance along the wall of the host vessel. The orientation of the map has been selected so that the bed region appears at the centre. Wall shear stress magnitude has been normalized with respect to the wall shear stress of the Hagen-Poiseuille flow within a straight pipe of the same diameter and

and with Re = 250. Irregularities seen in the shape of the wall shear stress contour lines along the horizontal centerline in the non-planar model are due to velocity gradient discontinuities across mesh element boundaries.

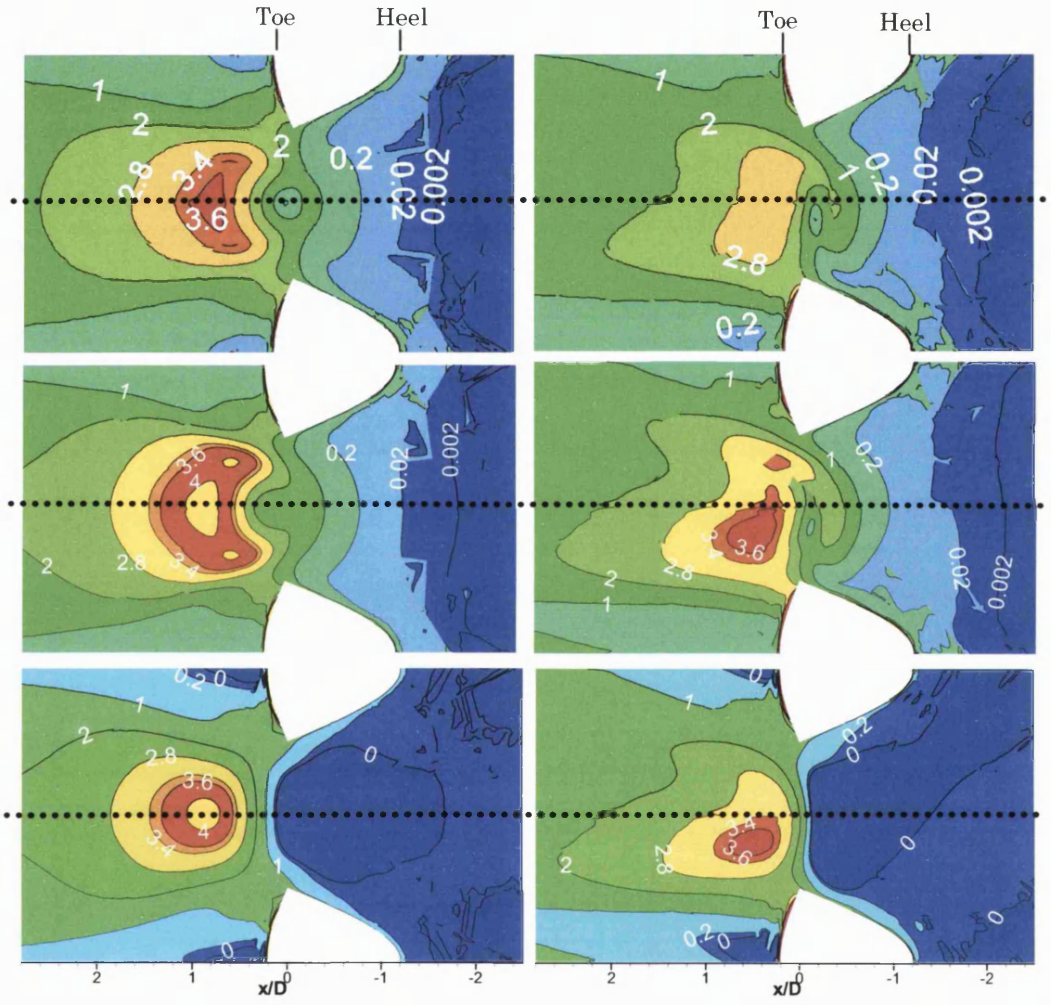

Figure 3.14 Comparison of numerically computed steady flow wall shear stress magnitude (top), mean pulsatile flow wall shear stress magnitude (middle) and mean pulsatile flow axial wall shear stress (bottom), normalized with the mean Poiseuille flow wall shear stress, in the unfolded planar (left) and non-planar (right) models. Dotted line plotted along the bed of the host vessel.

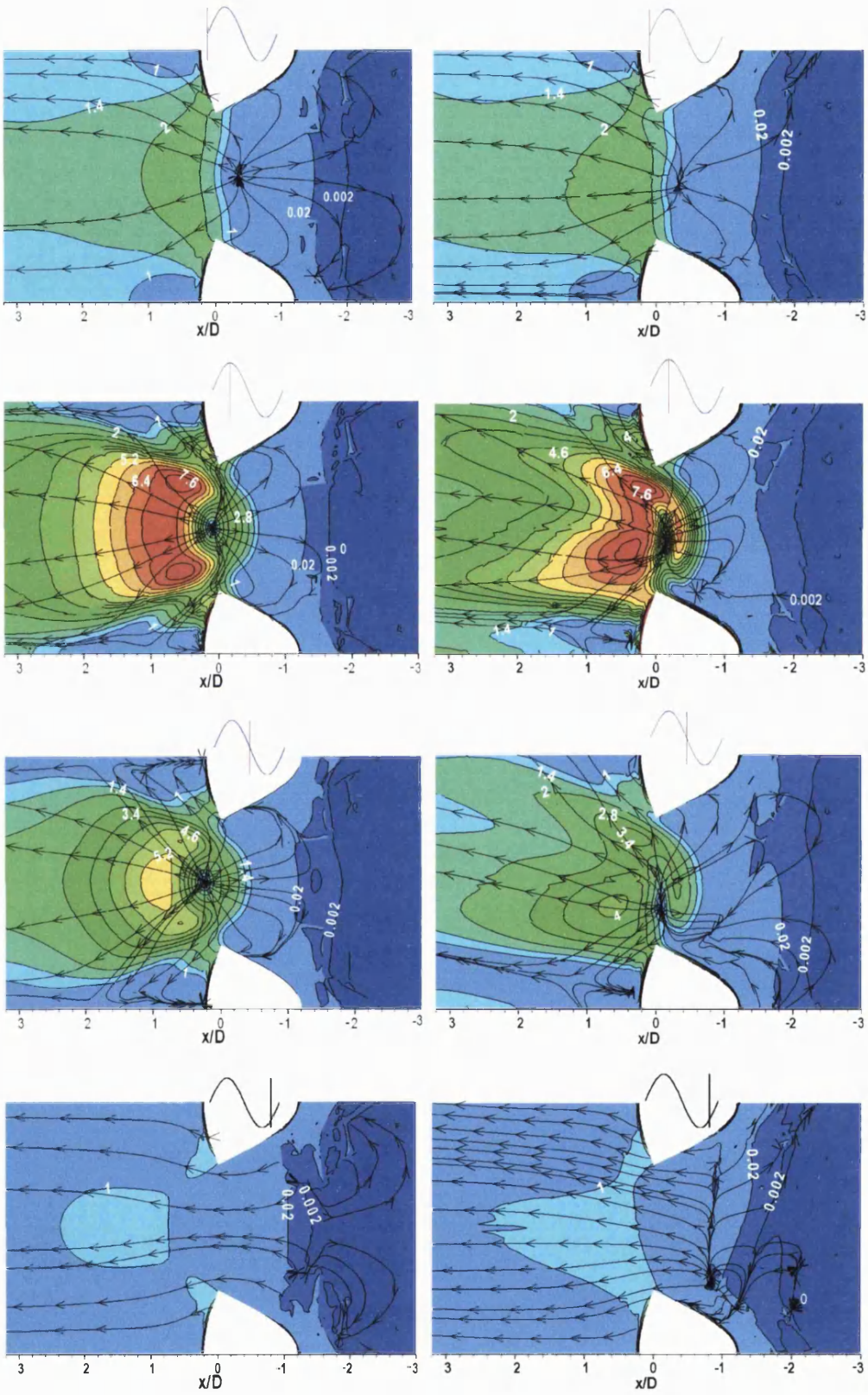

Figure 3.15 A comparison of numerically computed normalized wall shear stress magnitude, in the unfolded planar (left) and non-planar (right) models. Shear stress maps are shown at mid acceleration (top), at peak flow and mid deceleration (middle) and early acceleration (bottom). Stream traces of the wall shear vector are also shown.

Figure 3.14 shows a comparison of the numerically computed steady and pulsatile mean wall shear stress magnitude distribution in the planar and non-planar models. Also shown is a comparison of the numerically computed pulsatile mean axial component of wall shear stress in the two models where regions of negative shear are clearly marked by zero axial shear contours. There is a 10 % increase in the temporally averaged peak wall shear stress in pulsatile flow as compared to steady flow. The asymmetry of the flow in the non-planar model leads to an increased concentration of high shear levels at the lower half of the shear map. The location of the peak wall shear stress magnitude has been displaced proximally and away from the bed centerline in the non-planar model at 0.5 D as compared to 0.8 D downstream of the toe in the planar case. There is also a 10 % reduction in the peak wall shear stress magnitude in the non-planar model as compared to the planar configuration. Overall, a more uniform distribution of wall shear stress results from the introduction of the upstream out-of-plane curvature.

Figure 3.15 shows a comparison of the numerically computed normalized wall shear stress magnitude in the planar and non-planar models at four points in the flow cycle with wall shear vector surface streamlines superimposed. Points where shear streamlines converge to or diverge from are of particular interest as they indicate separation and reattachment (stagnation) points respectively. A characteristic feature in both wall shear stress maps is a region of low shear at the toe level on the bed wall of the anastomosis associated with a stagnation point. The proximity of this low shear zone to a high shear region creates steep spatial gradients of shear that are accentuated in the non-planar model by the presence of an additional high shear cell proximal to the low shear area.

The magnitude of wall shear stress in the region proximal to the heel is one to three orders of magnitude less than the temporal mean shear stress at the graft inlet. This is due to the limited mass flux through the heel in the occluded host section. Note the proximal displacement of the minimum wall shear stress contour (0.002) in the non-planar model indicating elevated shear stress levels in the occluded host vessel region as compared to the planar configuration. In terms of the dynamic behavior of the wall shear stress distribution a 30 % drop in the peak wall shear stress magnitude in the non-planar model at mid deceleration as compared to the planar configuration

is noted, with subsequent effects on the magnitude of the associated spatial gradients of shear. Although these differences between the two geometries are less pronounced during other points in the flow cycle, overall there is a more uniform temporal distribution of wall shear stress in the non-planar configuration.

An important difference between the two geometries is related to the location and motion of the stagnation point. By tracking the excursion of the stagnation point throughout the flow cycle, significant differences in both amplitude and direction of its oscillatory motion between the two models (Figure 3.15) were identified. In the planar configuration the stagnation point oscillates along the symmetry line on the bed and between 0.7 D proximal to the toe at early acceleration and 0.1D distal to the toe at mid deceleration. In the non-planar case the stagnation point oscillates about a center that is located off the symmetry plane intersection with the host artery bed wall, and following a parabolic path with a 0.7 D longitudinal and 0.5 D transverse excursion. It should be noted that in both configurations the stagnation point disappears between end acceleration and early acceleration. In the non-planar model during early acceleration a reattachment line initially forms (Figure 3.15) becoming a point during the following phase in the cycle.

On the wall shear streamline maps points of shear direction reversal are of particular interest as they highlight flow separation zones. The location of the reattachment point can be readily identified at the top and bottom of the shear direction map of the planar model at mid deceleration. In the non-planar configuration and at mid deceleration the separation zone is shifted away from the toe wall towards the bed wall and extends along a line that is oblique to the vessel axis. This behavior is associated with the bulk flow rotation forced by the upstream curvature in the graft.

3.3.3.4 Oscillatory shear index

Figure 3.16 shows a comparison of the oscillatory shear index distribution in the planar and non-planar configurations calculated applying the OSI definition introduced in section 3.3.2.1 and the definition of Moore et. al (1999). The OSI calculations were performed at a post processing stage using the computed shear distribution in the unfolded host vessel. A threshold of 5 % of the mean Poiseuille flow wall shear stress magnitude was applied to exclude very low signal to noise shear data (primarily

from the occluded proximal host region) from the oscillatory shear index calculation. The irregularities in some of the contours in Figure 3.16 are indicative of the difficulty in resolving this flow index. Distinct regions of elevated oscillatory shear can be identified in both models. One such region encapsulates the spatial temporal mean location of the stagnation point on the bed of the planar anastomosis. Another region of elevated oscillatory shear located on the toe wall of the host vessel exhibits a peak at 0.8 D downstream of the toe and extends between the toe and 2D downstream of the toe. This region is spatially associated with the flow separation zone on the toe wall depicted in Figure 3.12 and Figure 3.15.

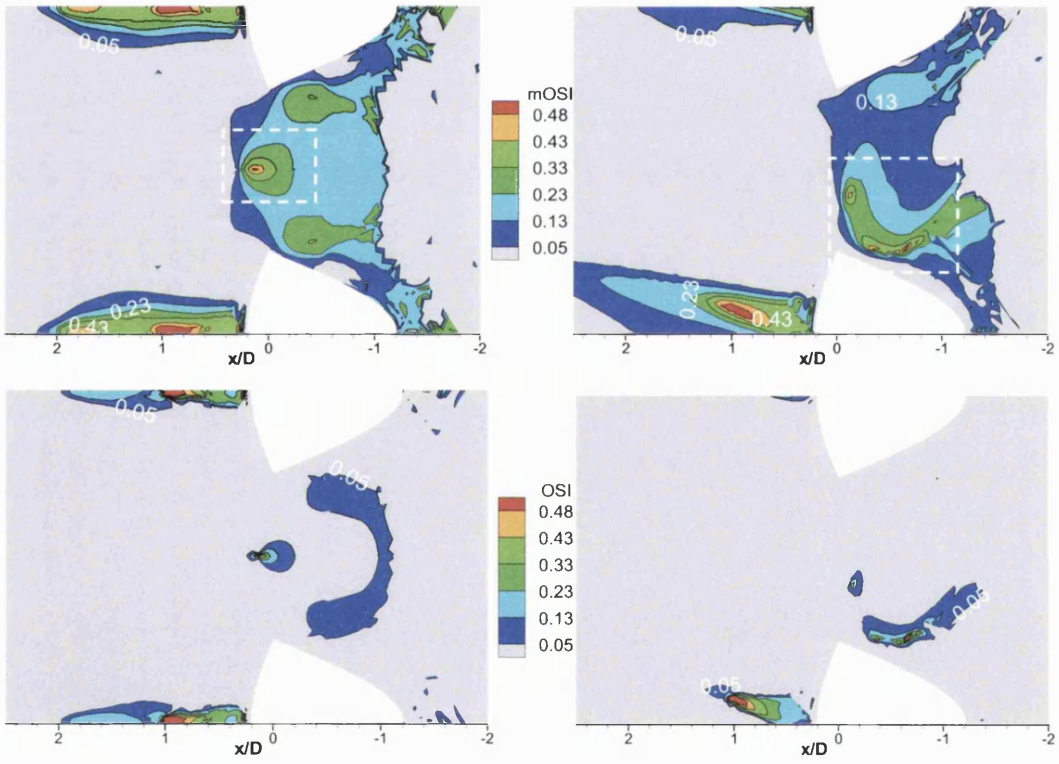

Figure 3.16 Comparison of the numerically computed modified (top) and original (bottom) oscillatory shear index in the unfolded planar (left) and non-planar (right) models. Regions enclosed by dashed lines are shown in close-up view in Figure 3.17.

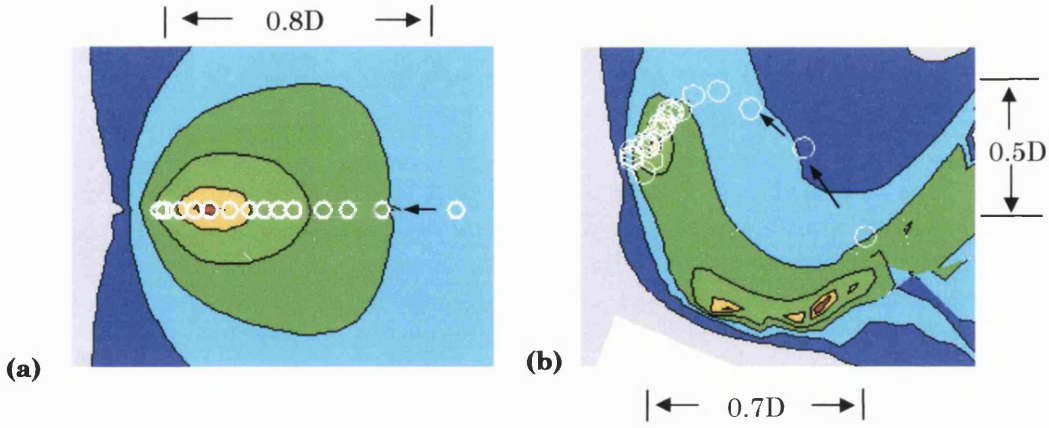

Figure 3.17 Comparison of the stagnation point excursion on the wall of the unfolded host vessel in the planar (left) and non-planar (right) anastomosis. Symbols are superimposed on close-up of the corresponding oscillatory shear index map region and are equally spaced in time. Right most symbols correspond to early acceleration and arrows indicate the direction of motion of the stagnation point.

In the non-planar model regions of elevated oscillatory shear are also spatially associated with the separation zone and the stagnation point. It should be noted however that the region of elevated oscillatory shear does not stretch along the path followed by the stagnation point. This can be explained by the spatio-temporal concentration of the motion of the stagnation point that accounts for the filtering effect exhibited by the oscillatory shear index localisation. Regions of elevated shear not accounted for by the stagnation point dynamics are associated with a secondary flow separation proximal to the toe on the bed of the anastomotic wall. This flow separation can be identified on the shear direction maps (Figure 3.15) during peak flow and mid deceleration as a point of shear vector streamtrace convergence. This secondary separation is associated with the complex flow vortices that develop in the anastomotic junction. The spatial extent of the elevated oscillatory shear regions is reduced in the non-planar model and as compared to the planar configuration. Moreover, in the non-planar model, and for OSI values above 0.1 the mean oscillatory shear was reduced by 22 % as compared to the planar configuration.

Figure 3.17 shows a close-up of the oscillatory shear distribution in both model configurations in the vicinity of the stagnation point trace also shown. Several points are worth noting. There is significant temporal concentration of the stagnation point excursion in both models although more pronounced in the non-planar configuration.

This region of concentrated stagnation point movement corresponds spatially with a peak in the oscillatory shear magnitude. Most of this motion occurs during early acceleration with the stagnation point positioned most proximally during the first acceleration phase.

The comparison of the oscillatory shear distribution obtained by the definition of Moore et al. (1999) and the modified definition proposed here shows, as expected, a very similar distribution pattern in both cases. However, a reduced spatial extent and less uniform distribution oscillatory shear is evident in the existing definition as compared to the modified OSI definition proposed.

3.3.3.5 Flow in the proximal non-planar host vessel

Figure 3.18 shows the flow behaviour at the anastomotic junction. Figure 3.18 a and b show an axial velocity contour map extracted along the z=-0.3D plane at mid acceleration (a) and early deceleration (b). Vectors and streamtraces of the in-plane velocity components are also plotted. Note the formation of a recirculation region, which varies in spatial extent and topology throughout the cycle. In the x-y plane, the recirculation appears as a vortex, and the streamlines in this plane show fluid particles that enter the occluded part of the host vessel are swept back into the main flow stream by the vortex and are convected downstream in the host vessel. However the vortical structure is three-dimensional, and varies both in strength and topological form. Turning to Figure 3.18 c and d, at mid-acceleration two almost symmetrical vortex cores are found which transport flow out of the proximal portion, whereas at mid deceleration, a single strong vortex is generated by the decelerating flow and draws flow out of the recirculation region limiting the spatial extent of the flow reversal. The instantaneous Reynolds number is (Re=200) for plots (a) and (c) and (Re=250) for plots (b) and (d); so although these do differ to some extent, the flow features are radically altered indicating the profound effect of the flow unsteadiness.

The structure of the vortex is complex but some insight can be had from examining the paths of particles released into the flow frozen in the cycle at the mid-deceleration point (Figure 3.18 e-h). At x/D =-1.2 on the bed wall fluid particles arriving from both directions converge and are pulled swiftly off the wall to join the strong clockwise vortex forming at the centre of the lumen.

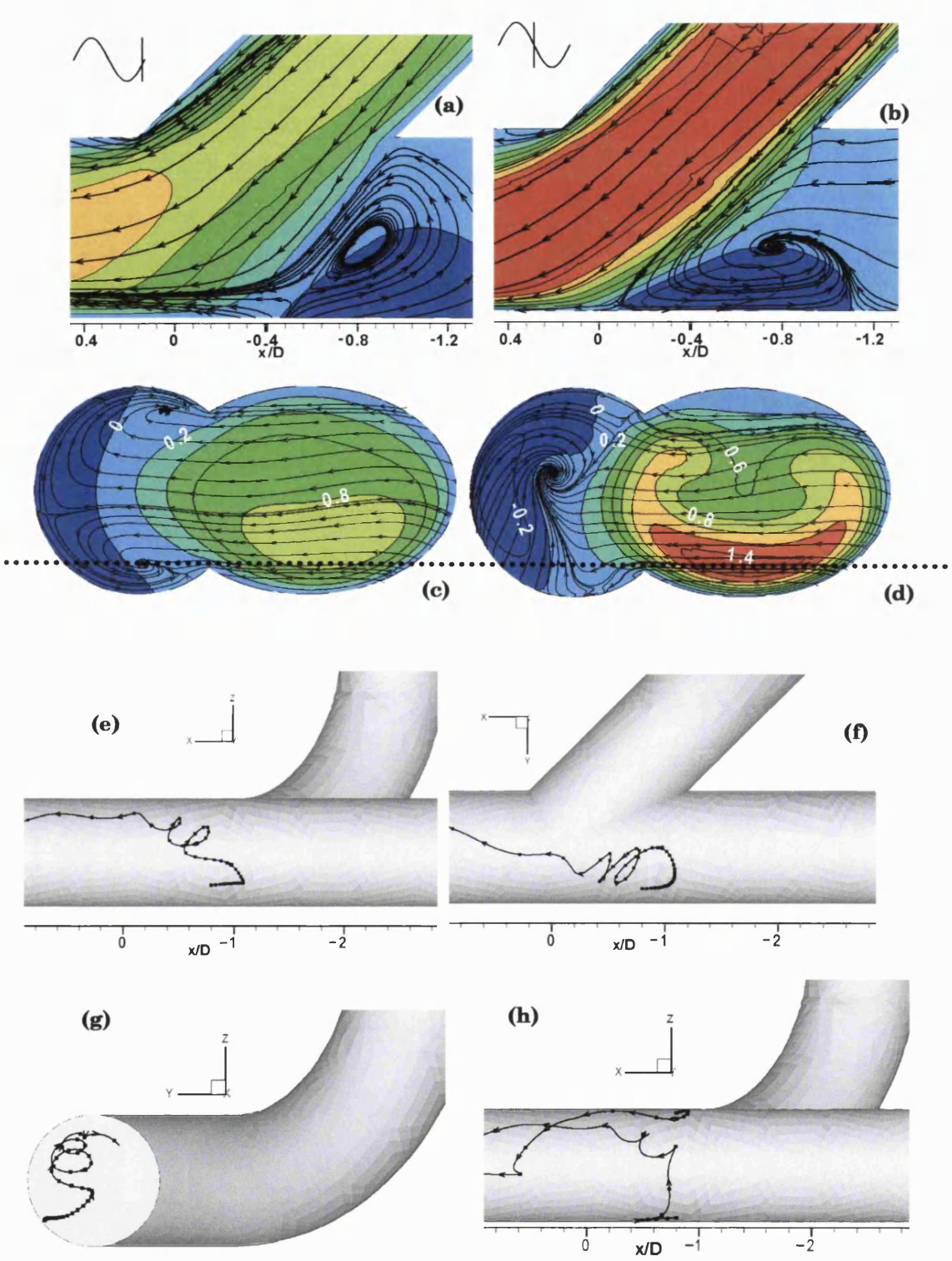

Figure 3.18 Flow patterns in the graft-host artery junction of the non-planar anastomosis. Streamtraces and vector plots at an x-y plane extracted at z=-0.3D at (a) approximately mid-acceleration and mid-deceleration (b). Streamtraces superimposed on axial velocity contours extracted at 1D proximal to the toe (c-d) at mid-acceleration (c) and mid-deceleration (d). Dotted line indicates level of slice extraction plane shown in panels (a) and (b). Also shown trajectories of fluid particles released at points within the elevated oscillatory shear region 1D proximal to the toe at mid-deceleration (e-h).

Figure 3.18 e-h shows different views of the trajectory of fluid particles released on the bed wall of the non-planar model at a flow separation point marked by converging wall shear streamlines and elevated oscillatory shear. Time integration markers are equally spaced in time and show the temporal evolution of the particles released. Released fluid particles initially move slowly along the wall and upstream towards the occluded section of the proximal host vessel. As these fluid particles reach the level of the heel they experience the strong in-plane force associated with the vortex located near the axis of the vessel and are drawn towards its core. As particles enter the vortex core they attain a swirling motion and are convected downstream where they rejoin the main flow stream and swiftly gain momentum. In Figure 3.18 g the convergence of fluid particles released upstream and downstream of the three-dimensional separation point (x/D=-0.8) is shown. Also shown is the trajectory of a particle released in the recirculation region (a region of elevated OSI) at the toe wall and just distal to the toe. Note the initial very slow upstream motion of the particle within the separation region and the swift change of direction as it negotiates the separation boundary.

3.3.4 Discussion

The aim of this investigation was to demonstrate the fundamental effects of flow pulsatility on the flow field in two geometric configurations of a distal end-to-side anastomosis. As discussed in the introduction, the flow conditions are somewhat idealized (Newtonian fluid assumed, rigid wall models used, single harmonic flow waveform applied) as the primary effect this study seeks to identify is that of the geometry.

The introduction of time-varying flow in the investigation on the effects of out-of plane graft curvature in a distal end-to-side anastomosis produced several interesting results. Although the gross features of the flow were similar to those found in the steady flow investigation of Sherwin et al. (2000), a number of important distinctive features are introduced. One such feature is the extensive flow separation observed on the toe wall just downstream of the toe in both model configurations. Low shear magnitude and long residence times associated with flow separation regions are hemodynamic conditions shown to promote the development of early vessel wall disease processes. In a detailed investigation of flow separation in the planar anastomosis for steady flow Ethier et al. (2000) reported no axial flow separation for Re<250, in

agreement with the result of Sherwin et al. (2000), and a single separation region on the toe wall and slightly downstream of the toe for Re between 250 and 450. Interestingly, for Re>450 they reported the formation of a second separation zone 1.3 diameters downstream of the toe. The unsteady flow results reported here where the Reynolds number varies between 62 and 437 show only a single axial flow separation region in both model configurations. The temporal and spatial evolution of this separation region is strongly influenced by the graft geometry and is coupled to the flow oscillation. The 10 % reduction in the peak magnitude of the time averaged wall shear stress in the non-planar model as compared to the planar configuration found here is in line with the steady flow result of Sherwin et al. (2000). The dynamic behaviour of the stagnation point on the bed of the anastomosis is of particular interest as it may assist in predicting the localization of vessel wall disease. While factors such as high shear magnitude and long exposure time may lead to platelet activation, forces acting in the direction of the vessel wall, as those found in the vicinity of a reattachment point, are necessary to carry activated platelets to the endothelium. The adhesion and aggregation process of activated platelets convected to the wall in the locality of the stagnation point is augmented by the low shear environment of the flow separation region (Wurzinger et al., 1983; Blasberg et al., 1983). It has been shown (Wurzinger et al. 1983; Karino and Goldsmith, 1984) in vitro that regions in the neighbourhood of the stagnation point are prone to thrombus formation, as platelets tend to strongly adhere to the wall at these sites. It has also been shown for steady flow in perfusion models (Pritchard et al., 1995) that blood monocyte adhesion to the vessel wall is inversely correlated to wall shear stress and is strongly influenced by the magnitude of in-plane flow and the presence of flow separation. In addition a recent investigation by Hinds et al. (2001) with both steady and pulsatile flow in a three dimensional perfusion model showed that blood monocyte adhesion was significantly higher in the locality of the flow separation region as compared to the post reattachment and pre-separation regions. They also found that flow pulsatility significantly altered monocyte adhesion patterns and introduced an overall more uniform adherent cell distribution. Therefore, the significant differences found in this study in the pattern of the oscillatory excursion of the stagnation point between the two model configurations suggests

a strong influence of out-of plane graft curvature in the distribution of sites on the vessel wall exposed to unfavourable hemodynamic conditions.

The significant changes in the spatial distribution of the separation zone associated with the introduction of out-of-plane curvature in the graft, highlights the strong influence of the three-dimensional character of the anastomosis on the flow behaviour in the native vessel. If blood monocytes tend to adhere more readily to the endothelium at regions of low shear stress and flow separation thus promoting the development of vessel wall disease, then based on the results of this study a reduction of the spatial extent of early wall lesions in the non-planar model as compared to the planar configuration might be expected. Furthermore, if a correlation between regions of elevated oscillatory shear and intimal thickening exists, as shown by Ku et al. (1985) in the carotid bifurcation, then the 16 % reduction in mean oscillatory shear found in the non-planar model as compared to the planar configuration would imply a corresponding reduction in the spatial extent of wall regions exposed to physiologically unfavourable flow conditions.

The flow behaviour in the occluded section of the host vessel is of considerable interest as it is associated with long residence times a flow condition known to promote clot formation. Thrombotic wall lesions initiated in the occluded part of the host vessel may proliferate distally penetrating the perianastomotic flow conduit and augment restenosis. Sherwin et al. (2000) found in steady flow an 80 % increase in the mass flux through the heel in the non-planar model as compared to the planar configuration. In pulsatile flow, an overall increase in the wall shear stress magnitude in the occluded section of the host vessel was found. This was a result of the introduction of upstream out-of-plane curvature in the geometry. This can be attributed to the development of a strong vortex at the heel directed downstream that sweeps particles, separated from the main flow on the bed, that enter the occluded section of the host vessel back into the main stream.

In the controlled conditions of an idealized anastomosis model it was possible to characterize flow features such as flow separation and stagnation and associate them with specific geometric parameters. It is shown that the introduction of out-of-plane curvature in the graft strongly influences perianastomotic flow and is thus expected to affect the localization of vessel wall disease. It would therefore be of interest

to extend this investigation to assess the sensitivity of the flow to the degree of out-of-plane curvature.

Although gross geometric features are considered as the most influential factors in vascular hemodynamics, it is the combined effect of gross and detailed features of geometry acting in conjunction with factors such as flow pulsatility and vessel wall mechanics that accounts for the variability in the localization and extent of lesions in revascularised vessels *in vivo*. Therefore, a series of studies incrementally incorporating flow and geometric features closer to the true *in vivo* hemodynamic conditions in arterial bypass grafts are necessary in order to assess the range and importance of the effects of natural geometric and flow waveform variability between individuals on perianastomotic flow patterns.

Chapter 4.

A Spline Based Modelling Technique for 2D Phase Velocity Encoded MRI Data

4.1 Introduction

By applying a data modelling process to an MRI phase velocity encoded data set, the following can be achieved: an analytical definition of the phase distribution in the region of interest can be obtained, the random noise in the data can be reduced and, flow related indices that require processing operations sensitive to noise (e.g. velocity gradients, vorticity) can be derived from the model without noise propagation penalties. Spline functions were selected as the basis of the proposed data modelling approach. The various algorithms for fitting surfaces based on bicubic spline functions proposed by Dierckx (1995) were adopted for the approximation of MRI phase data. The corresponding public domain Fortran routines developed by Dierckx (1995) and grouped in the FITPACK package were adapted for MRI phase velocity encoded data modelling.

A number of methods have been proposed to allow estimation of wall shear stress from MRI velocity measurements. Most methods use various types of post-processing algorithms to calculate wall shear stress from near wall velocity measurements (Oshinski et al., 1995; Oyre et al. 1997). Frayne and Rutt (1995 b) proposed a Fourier velocity encoding technique whereby one spatial dimension in the MRI image is used to encode velocity. With appropriate processing of the measurement the intra-

voxel velocity distribution and the exact wall location were obtained. The method was validated for steady flow in a straight tube yielding a mean error of - 15 % of the nominal wall shear stress.

Errors in the estimation of wall shear stress from MRI velocity measurements may arise from two separate sources. The first is locating the exact wall position at a subvoxel level, and the second is measuring or calculating the velocity gradient at the wall or very close to the wall. Due to the finite resolution of the MRI experiment, these processes will limit, to a greater or lesser extent, the accuracy of any method used to estimate wall shear.

Early methods of wall shear stress estimation from MRI phase velocity data used either linear or quadratic extrapolation of near wall velocity measurements to calculate the velocity gradient at the wall (Moore et al., 1994; Oshinski et al., 1995; Oyre et al. 1997; Oyre et al., 1998). Oshinski et al. (1995) proposed an algorithm whereby the wall shear stress estimate is obtained in three steps. Initially a user-defined threshold was applied to the magnitude image and the single pixel boundary was extracted. Then, the mean of the boundary voxel velocity and the first intraluminal voxel velocity was calculated. This mean velocity was used as an estimate of the true, partial volume corrected, boundary voxel velocity. Then the exact wall location within the boundary voxels was estimated using the corrected boundary velocities and applying conservation of mass. Finally the wall shear stress was calculated assuming a linear velocity profile within the boundary voxel. The influence of the voxel size on the accuracy of wall shear stress estimation was investigated by Strang et al. (1994) in fully developed steady axisymmetric flow. Shear stress was calculated by fitting a quadratic polynomial to the velocity profile. They concluded that even under the idealised conditions of their experiment (steady axisymmetric flow, sharp intensity gradient at the lumen wall boundary and no subject or vessel motion) large voxel size (pixel width > 0.5 mm or > 5% of vessel diameter) lead to significant underestimation of shear stress and subsequent overestimation of the vessel radius.

Lou et al. (1993) investigated the errors associated with curve fitting of velocity measurements to obtain wall shear stress estimates. Their theoretical analysis showed improved accuracy of the quadratic over the linear extrapolation method in both steady and time-varying well-defined flows. However they excluded from their analy-

sis the effects of measurement error. For time-varying flow they also showed that the wall shear stress estimation error using both linear and quadratic extrapolation increased as the thickness of the boundary layer decreased. Steinman et al. (1995) compared wall shear stress estimates based on linear and quadratic extrapolation of MRI phase contrast velocity measurements with numerical predictions for steady complex flow in an idealised planar anastomosis model. They reported a significant improvement in the match between results when quadratic instead of linear extrapolation was applied. Oyre et al. (1998) proposed a post processing technique to model the velocity distribution within a band near the wall by least squares fitting a number of surface patches in the form of two dimensional paraboloid functions to the MRI velocity data. This method works well when the velocity distribution can be modelled by parabolic functions. In fully developed steady axisymmetric flow they reported an error in the wall shear estimate of ± 4 % with respect to the theoretical value. However in cases of complex flows with skewed velocity profiles and strong in plane flow the accuracy of the wall shear estimates obtained from this method will be compromised. Such flow conditions are common near vessel bifurcations and in curved vessel sections. Furthermore this technique allows for discontinuities in the wall shear estimates to occur, since it does not enforce continuity of the velocity gradients across the boundaries of the surface patches. The method also relies on the assumptions that the boundary of the vessel lumen can be modelled by an ellipse and that the velocity distribution by a biquadratic function.

The accuracy of the three most common methods used to estimate wall shear stress from MRI velocity measurements was investigated by Masaryk et al. (1999). In their study they compared wall shear stress estimates obtained by linear extrapolation with and without correction for wall position as proposed by Oshinski et al. (1995), and quadratic extrapolation. Wall shear stress estimates were calculated from velocity measurements in a straight tube for steady and pulsatile flow and from velocity measurements acquired from the cervical segment of the internal carotid artery in healthy human subjects. They found a consistent underestimation of wall shear stress by the linear extrapolation method. They also reported, for pulsatile flow *in vitro*, root mean square differences between theoretically predicted and MRI extracted wall shear stress of 59%, 17%, and 22 % for the linear, corrected linear and quadratic extrapola-

tion methods respectively. These results however may not be representative of the merits of each method due to a limitation in the method used to calculate the reference wall shear stress values. Their results show a significant difference between the mean velocity waveform measured by the transit–time flow meter and that obtained from the MRI phase-velocity measurements. To overcome this problem the investigators derived their reference wall shear stress values from the linear summation of the Womersley solutions corresponding to the Fourier modes of the flow waveform reconstructed from the MRI measured mean velocities. However this approach does not yield the true accuracy of the three wall shear stress estimation methods they used, as it excludes systematic error due to temporal interpolation and waveform undersampling. The authors also report errors between 28 % and 98 % in the wall shear estimates calculated from *in vivo* MRI velocity measurements. However it should be noted that due to the various assumptions introduced (rigidity of the vessel wall, fully developed Womersley flow, Newtonian fluid) to obtain a reference solution for the *in vivo* results, the value of the error estimates was significantly compromised.

4.2 Method Description

The proposed method models the complete MRI measured velocity distribution in an arbitrarily shaped vessel lumen with bivariate B-spline functions. B-spline functions have two important properties: they impose derivative continuity constraints to the approximation solution and they provide local support which allows the approximation to easily adapt to local variations of the velocity distribution. Therefore, with this approach, derivative continuity across the whole of the approximation domain is ensured and the magnitude of the velocity gradients in the original velocity distribution is preserved in the model.

B-splines are piecewise polynomials. Their formulation is based on the concept of divided differences introduced by de Boor (1972). A set of knots distributed in the approximation domain defines the boundaries between local approximation functions. Bivariate spline functions can be used for fitting surfaces. A bivariate spline function $\mathbf{s}(r,\theta)$ in polar coordinates is given by the following expression:

$$s(r,\theta) = \sum_{i=-k}^{g} \sum_{j=-l}^{h} c_{i,j} N_{i,k+1}(r) M_{j,l+1}(\theta)\,, \tag{4.1}$$

where g and h are the number of knots in the radial and circumferential directions respectively, $c_{i,j}$ are the *B-spline* coefficients, and $N_{i,k+1}(r)$, $M_{j,l+1}(\theta)$ are the *B*-spline basis functions of degrees k and l defined on the knot sequences λ and μ respectively by the following expressions:

$$N_{i,k+1}(r) = (\lambda_{i+k+1} - \lambda_i) \sum_{j=0}^{k+1} \frac{(\lambda_{i+j} - r)_+^k}{\prod_{l \neq j, l=0}^{k+1} (\lambda_{i+j} - \lambda_{i+l})}, \tag{4.2}$$

$$M_{j,l+1}(\theta) = (\mu_{j+l+1} - \mu_j) \sum_{i=0}^{l+1} \frac{(\mu_{i+j} - \theta)_+^l}{\prod_{l \neq i, l=0}^{l+1} (\mu_{i+j} - \mu_{j+l})}. \tag{4.3}$$

Therefore, for a given set of knots defined in the radial and circumferential directions, a bivariate spline function can be used to fit a surface. Although two dimensional MRI phase velocity encoded data are typically reconstructed on a rectangular x y grid, the spline function is defined on a polar grid as it provides the most convenient parameterisation of the approximation domain. The process of fitting a spline function defined in cylindrical coordinates $\boldsymbol{s}(r,\theta)$ to the MRI velocity data requires a number of steps. The first step involves the definition of the boundary of the approximation domain. This is achieved by segmenting the MRI phase image based on the information in the modulus image. For the purposes of the current investigation, where only MRI flow measurements obtained *in vitro* will be considered, the application of a user specified threshold on the modulus image was sufficient to accurately extract a single pixel vessel – lumen boundary. A smooth closed parametric spline curve was then fit to this boundary by the following procedure. The extracted boundary points (x_r, y_r) describe an arbitrary curve in the MR slice extraction plane. For every point on the boundary, a value q_r of a parameter q is associated such that $q_r < q_{r+1}$. Then for an interval [a, b] two periodic spline functions $s_x(q)$ and $s_y(q)$ with common knots λ_i are determined such that the closed spline curve $\boldsymbol{s}(q)$ with parametric representation:

$$\begin{cases} x = s_x(q) \\ y = s_y(q) \end{cases}, \quad a \le q \le b \tag{4.4}$$

satisfies:

$$(s_x(q), s_y(q)) \simeq (x_r, y_r), \quad r = 1, \ldots, m \tag{4.5}$$

where m the number of points along the boundary extracted. The form of the approximating curve may be influenced by the choice of the curve parameterisation. Unless the boundary of the approximation domain presents severe indentations, a good choice for the parameter q is the angular coordinate of the original boundary data points. The smoothest curve that fits the data while maintaining a maximum Euclidian distance from the centre of the original boundary pixels of less than half the pixel width is calculated. The smoothness of the approximation is controlled by a user defined smoothing parameter (S) that is the upper limit of the residual approximation error ($\delta(\boldsymbol{c})$):

$$\delta(\boldsymbol{c}) = \sum_{r=1}^{m} (x_r - s_x(q_r))^2 + (y_r - s_y(q_r))^2 \leq S \tag{4.6}$$

where x_i, y_i are the x and y coordinates of the measured data point i and q_i is the angular coordinate of that point.

The solution to this approximation is based on the smoothing criterion, which uses the concept of the smoothing norm ($\eta(\boldsymbol{c})$):

$$\eta(\boldsymbol{c}) = \sum_{i=1}^{g} \left((s_x^{(k)}(\lambda_i+) - s_x^{(k)}(\lambda_i-))^2 + (s_y^{(k)}(\lambda_i+) - s_y^{(k)}(\lambda_i-))^2 \right) \tag{4.7}$$

where g is the number of knots and $s_x^{(k)}(\lambda_i+)$ and $s_x^{(k)}(\lambda_i-)$ are the right and left k^{th} order derivatives at knot λ_i of spline function $s_x(\,)$ of degree (k) calculated in the knot intervals $[\lambda_i, \lambda_{i+1}]$ and $[\lambda_{i-1}, \lambda_i]$ respectively and similarly for $s_y^{(k)}(\lambda_i+)$ and $s_y^{(k)}(\lambda_i-)$. A solution is sought that minimises $\eta(\boldsymbol{c})$ subject to the constraint expressed by equation (4.6).

In practice, the desired spline curve approximation is achieved iteratively. Initially a large smoothing factor is selected and the maximum Euclidian distance of the resulting closed spline curve from the original data on a point-to-point basis is calculated. The smoothing factor is then iteratively reduced by a small preset step value until the maximum Euclidian distance becomes less then half the pixel width (Figure 4.1).

To fit or model a two dimensional MRI phase velocity distribution by a spline function, an approximation criterion needs to be defined. A well-known example is the

least squares criterion, where the approximating spline function is calculated by minimising the approximation residual error ($\delta(\boldsymbol{c})$) defined as:

$$\delta(\boldsymbol{c}) = \sum_{i=1}^{N} w_i (u_i - s(r_i, \theta_i))^2 \tag{4.8}$$

where u_i is the value of the approximated velocity distribution at point i of the approximation domain and w_i the weight assigned to that value. The weights are used when there is a non-uniform distribution of uncertainty in the velocity measurements within the approximation domain. A relative estimate of the uncertainty for MRI velocity measurements on a pixel-by-pixel basis is given by the inverse of the standard deviation of the phase. By applying propagation of errors and assuming uncorrelated noise in the receiver channels, Contouro and Smith (1990) showed that phase noise on a pixel-by-pixel basis could be approximated by the SNR of the modulus image:

$$\sigma(\phi_i)^{-1} \propto \frac{I_i}{\sigma(I)} = SNR_i . \tag{4.9}$$

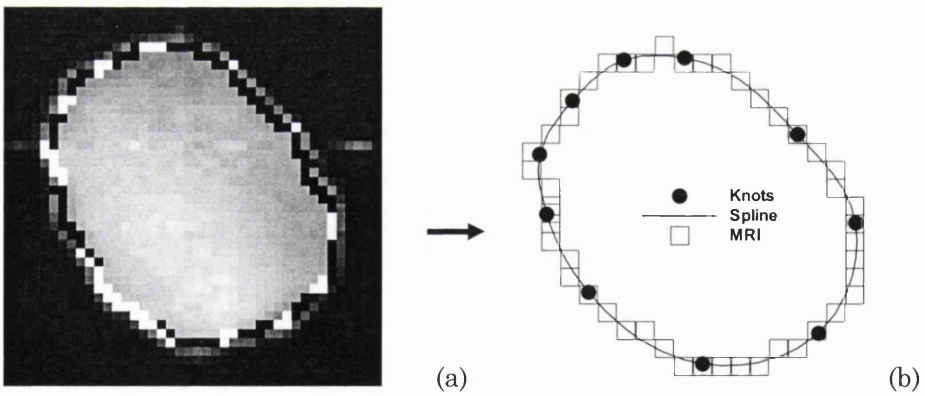

Figure 4.1 The single pixel boundary superimposed on the modulus image (a) and the approximation boundary (b) defined by the smoothest closed spline curve (solid line) fit through the boundary pixels (squares) maintaining a maximum Euclidian distance from the pixel centres of less then half the in-plane resolution of the MRI acquisition. The knots of the spline are also indicated (solid circles).

The least squares criterion however, does not impose any constraints on the solution with respect to the smoothness of the calculated spline function. Therefore the least squares splines approximation function, for an appropriately selected knot distribution, will pass through all the points of the original function and null the approximation residuals. However, such a solution would not serve the purpose of MRI

phase modelling as it would have included the random error of the original data. A more appropriate approximation would result by applying the smoothing criterion proposed by Dierckx (1981a). The approximation is based on minimising the smoothing norm ($\eta(\boldsymbol{c})$), which is derived by applying the derivative continuity constraints on the approximation polynomials at the knots subject to the additional constraint:

$$\delta(\boldsymbol{c}) = \sum_{i=1}^{N} w_i (u_i - s(r_i, \theta_i))^2 \leq S\,, \tag{4.10}$$

where $\delta(\boldsymbol{c})$ is the residual approximation error for a spline function defined by spline coefficients $\boldsymbol{c}$ and S is the smoothing factor. The smoothing norm ($\eta(\boldsymbol{c})$) is defined as:

$$\eta(\boldsymbol{c}) = \sum_{q=1}^{g}\sum_{j=-l}^{h}\left(\sum_{i=-k}^{g} c_{i,j} a_{i,q}\right)^2 + \sum_{r=1}^{h}\sum_{i=-k}^{g}\left(\sum_{i=-l}^{h} c_{i,j} b_{j,r}\right)^2, \tag{4.11}$$

where $c_{i,j}$ are the spline coefficients and $a_{i,q}$, $b_{j,r}$ are defined as:

$$a_{i,q} = N_{i,k+1}^{(k)}(\lambda_q +) - N_{i,k+1}^{(k)}(\lambda_q -) \tag{4.12}$$

$$b_{j,r} = M_{j,l+1}^{(l)}(\mu_r +) - M_{j,l+1}^{(l)}(\mu_r -)\,, \tag{4.13}$$

where $N_{i,k+1}^{(k)}(\lambda_q +)$ and $N_{i,k+1}^{(k)}(\lambda_q -)$ are the right and left k^{th} order derivatives at knot λ_q of the B-spline basis functions of degree (k) in the radial direction calculated in the knot intervals $[\lambda_q, \lambda_{q+1}]$ and $[\lambda_{q-1}, \lambda_q]$ respectively, and similarly $M_{j,l+1}^{(l)}(\mu_r +)$ and $M_{j,l+1}^{(l)}(\mu_r -)$ are the right and left l^{th} order derivatives at knot μ_r of the B-spline basis functions of degree (l) in the circumferential direction calculated in the knot intervals $[\mu_r, \mu_{r+1}]$ and $[\mu_{r-1}, \mu_r]$ respectively. Spline functions and their derivatives up to order k-1, where k the degree of the spline, are continuous by definition. However higher order derivatives may be discontinuous. The smoothing norm essentially controls the level of the spline k^{th} order derivative discontinuities at the knots.

The number and placement of the spline knots in the approximation domain is important for the quality of the spline fit calculated. The knot placing strategy proposed by Dierckx (1981b) initially seeks, for a given value of S, a set of knots that satisfies:

$$F_{g,h}(\infty) \leq S < F_{g,h}(0) \tag{4.14}$$

where $F_{g,h}(\infty)$ and $F_{g,h}(0)$ are the limiting values for the smoothing function $F_{g,h}(p)$ which depends on the smoothing spline representation s_p according to:

$$F_{g,h}(p) = \sum_{i=1}^{N} w_i (u_i - s_p(r_i, \theta_i))^2, \tag{4.15}$$

where N is the number of data points in the approximation domain. The solution of $F_{g,h}(p)$ when p tends to infinity:

$$F_{g,h}(\infty) = \sum_{i=1}^{N} w_i (u_i - S_{g,h}(r_i, \theta_i))^2, \tag{4.16}$$

is the weighted least squares spline $S_{g,h}(r_i, \theta_i)$ for a given set of knots. The solution of $F_{g,h}(p)$ when p tends to zero:

$$F_{g,h}(0) = \sum_{i=1}^{N} w_i (u_i - P_{k,l}(r_i, \theta_i))^2, \tag{4.17}$$

is the weighted least squares polynomial $P_{k,l}(r_i, \theta_i)$ of degrees k in r and l in θ. The knot insertion strategy involves the gradual insertion of knots (one at a time) in the approximation domain and the calculation of the sum of the approximation errors $F_{g,h}(\infty)$ based on the weighted least squares spline $S_{g,h}(r_i, \theta_i)$. Following each iteration, an additional knot is introduced within the knot interval where the largest approximation error is calculated. This process ends when condition (4.14) is satisfied.

This constrained optimisation problem is then solved using the method of Lagrange multipliers. This method searches for the critical points in the following function:

$$\xi(p, \boldsymbol{c}) = \eta(\boldsymbol{c}) + p(\delta(\boldsymbol{c}) - S) \tag{4.18}$$

The coefficients $(c_{i,j})$ of the bicubic smoothing spline are calculated by solving the following overdetermined system of equations:

$$\begin{aligned}
&w_r \sum_{i=-k}^{g} \sum_{j=-l}^{h} c_{i,j} N_{i,k+1}(r_r) M_{j,l+1}(\theta_r) = w_r u_r, \quad r = 1, \ldots, N \\
&\frac{1}{\sqrt{p}} \sum_{i=-k}^{g} c_{i,j} a_{i,q} = 0, \quad q = 1, \ldots, g; \quad j = -l, \ldots, h \\
&\frac{1}{\sqrt{p}} \sum_{j=-l}^{h} c_{i,j} b_{j,r} = 0, \quad r = 1, \ldots, h; \quad i = -k, \ldots, g
\end{aligned} \tag{4.19}$$

where p must be chosen as the root to the equation $F_{g,h}(p) = S$.

This unique parameter p^*, for a given set of knots that satisfies equation (4.14), for which $F_{g,h}(p^*) = S$, is iteratively determined by using a rational interpolation scheme (Dierckx, 1981a). For this a function $R(p)$:

$$R(p) = \frac{up + \upsilon}{p + w} \tag{4.20}$$

is used to reproduce the important properties of $F_{g,h}(p)$. By selecting three initial values for p:

$$p_1 = 0, \quad p_2 = p_0 = \frac{F(0) - S}{F_{g,h}(\infty) - S}, \quad p_3 = \infty,$$

the corresponding values of $F_{g,h}(p)$ (F_1, F_2, F_3) are then used to calculate the parameters u, υ, w from equation (4.20) so that $R(p_i) = F_i, \quad i = 1,2,3$. Then using the calculated values for u, υ, w and solving for $R(p) = S$, a new estimate $\tilde{p}$ for parameter p is calculated.

Following each iteration, the values of p_1, p_2, p_3 are adjusted as follows:

$$\text{if } F_2 < S : p_3 \leftarrow p_2, p_2 \leftarrow \tilde{p},$$
$$\text{if } F_2 > S : p_1 \leftarrow p_2, p_2 \leftarrow \tilde{p},$$

by this the interval $[p_1, p_3]$ is reduced with each iteration while:

$$p_1 < p_2 < p_3, \quad F_1 > S, \quad F_3 < S,$$

which makes the iteration convergent. The iteration ends when the following criterion is met:

$$\frac{\left| F_{g,h}(\tilde{p}) - S \right|}{S} \leq \tau, \tag{4.21}$$

where τ is approximation tolerance set to 0.001.

The approximation solution based on the smoothing criterion achieves the smoothest spline function for a given level of closeness of fit provided by the smoothing parameter S. Therefore, the selection of an appropriate value for S is important to the quality of the approximation. The mean uncertainty of the approximated data set can be used as an estimate of the smoothing factor. The approximation target in the case of the MRI phase velocity encoded data is to obtain the smoothest bivariate cubic

spline fit with an approximation residual error less than the mean standard deviation of the original data. This condition is expressed by the following merit function:

$$e_{rms} = \sqrt{\frac{1}{N-k-l-g-h}\sum_{i=1}^{N}(u_i - s(r_i,\theta_i))^2} < \frac{1}{N}\sum_{1}^{N}\sigma(\phi_i), \tag{4.22}$$

where as mentioned previously k and l are the degrees and g and h are the number of knots of the spline basis functions in the radial and circumferential directions respectively. When an approximation function with the desirable properties is calculated, flow indices such as wall shear or vorticity can be easily derived from the data model. The wall shear stress vector ($\boldsymbol{\tau}$) can be expressed as follows:

$$\boldsymbol{\tau} = -\mu \nabla \boldsymbol{U} \cdot \boldsymbol{n}_s, \tag{4.23}$$

where μ is the dynamic viscosity of the fluid, $\boldsymbol{n}_s$ is the surface unit normal and $\boldsymbol{U}$ the velocity vector. If the surface normal cannot be calculated from the MRI data the wall shear stress vector can be approximated, with a few necessary assumptions, by the inner product of the axial velocity component gradient at the wall with the boundary curve unit normal ($\boldsymbol{n}_c$):

$$\boldsymbol{\tau} \simeq -\mu \left.\frac{\partial \boldsymbol{u}}{\partial r}\right|_{r=R} \cdot \boldsymbol{n}_c = -\mu \left.\frac{\partial \boldsymbol{s}(r,\theta)}{\partial r}\right|_{r=R} \cdot \boldsymbol{n}_c. \tag{4.24}$$

The axial velocity gradient at the wall can be computed analytically by differentiating the spline function representation of the velocity distribution $\boldsymbol{s}(r,\theta)$.

4.3 Method Validation

4.3.1 Poiseuille Flow

As a first step in the validation of the proposed MRI phase modelling approach, the wall shear stress estimates based on measurements of Poiseuille flow are compared to the theoretically predicted values. Fully developed axisymmetric flow is established in a 1 m long straight precision bore (8 ± 0.02) mm glass tube (Schott Glass Gmbh) aligned with the scanner bore axis. Acquisition parameters used were: a 8 cm × 8 cm FOV, a 256 × 256 image matrix and the minimum TE of 6.8 ms, minimum TR of 18 ms and a FA of 50 degrees.

For Poiseuille flow the velocity $u(r)$ at any radial position r away from the axis in the tube is:

$$u(r) = 2\overline{u}\left(1 - \left(\frac{r}{R}\right)^2\right), \tag{4.25}$$

where R is the nominal inner tube radius and $\overline{u}$ is the mean velocity. The wall shear stress is:

$$\tau = \mu \left.\frac{du}{dr}\right|_{r=R} = -\mu\frac{4\overline{u}}{R} = -4\mu\frac{Q/\pi R^2}{R} = -\frac{4\mu Q}{\pi}\frac{1}{R^3}, \tag{4.26}$$

where Q the nominal flow rate.

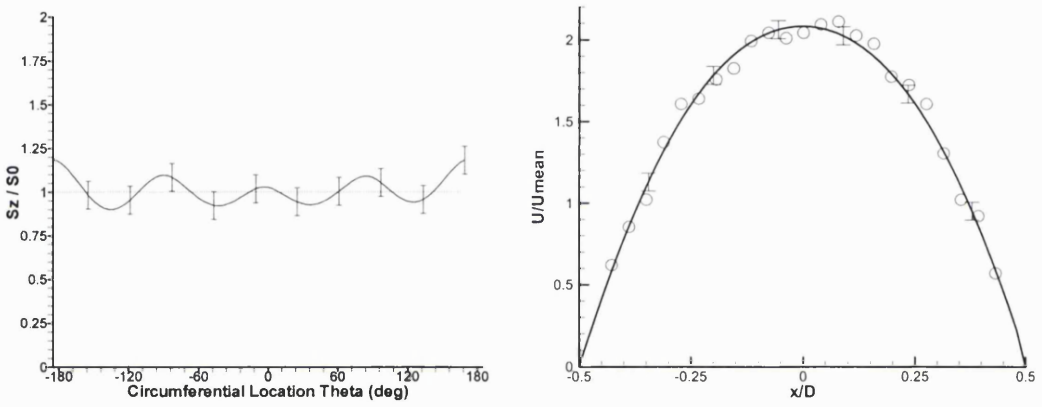

Figure 4.2 Comparison of normalised theoretical (dotted line) and estimated (solid line) wall shear stress along the circumference of a precision bore tube (a). Error bars correspond to ± 8 % of the theoretical wall shear. Also shown (b) a comparison of y constant centreline velocity profiles obtained from MRI measurements (symbols) and spline modelled data (line) in the straight tube model. Error bars placed on the spline model profile correspond to ± 5 % of the mean velocity.

The rms difference between the spline model wall shear estimates and the theoretical value was within ± 8 % (Figure 4.2a). This level of error is relatively small given that the precision of the velocity measurements was ± 5 % of $\overline{u}$ (Figure 4.2b). An estimate of the uncertainty in the theoretical wall shear stress value calculated from equation (4.26) can be obtained by applying propagation of error. Assuming all errors are independent and random, the formula for error propagation for the shear stress function is:

$$\frac{\delta\tau}{|\tau|} = \sqrt{\left(\frac{\partial\tau}{\partial Q}\frac{\delta Q}{|\tau|}\right)^2 + \left(\frac{\partial\tau}{\partial R}\frac{\delta R}{|\tau|}\right)^2 + \left(\frac{\partial\tau}{\partial\mu}\frac{\delta\mu}{|\tau|}\right)^2}$$
$$= \sqrt{\left(\frac{\delta Q}{Q}\right)^2 + \left(3\frac{\delta R}{R}\right)^2 + \left(\frac{\delta\mu}{\mu}\right)^2} \qquad (4.27)$$

Given that the fractional error, according to the manufacturer's specifications, in the flow rate Q is ± 1 % and in the tube radius R is ± 0.25 %, and that the fractional error in the viscosity estimate μ is 2.9 % the total fractional error in the wall shear stress τ is (Equation (4.27)):

$$\frac{\delta\tau}{|\tau|} = \sqrt{1\% + 0.6\% + 8.4\%} = 10\%.$$

Therefore the spline approximation wall shear stress estimate error is within the uncertainty of the nominal value.

4.3.2 Steady Complex Flow in a Planar Bypass Graft Model

The proposed method was also validated in steady complex flow. Flow measurements were obtained at two diameters downstream of a planar 45 degrees distal end-to-side anastomosis model and the circumferential wall shear stress distribution was estimated. Comparisons were then made with the numerically predicted wall shear stress for the same flow, using the results published by Sherwin et al. (2000).

Figure 4.3 shows a comparison of the raw MRI, the spline modelled MRI and the numerically computed axial velocity at two diameters downstream of the toe of the planar anastomosis model described in section 2.2.1. It is apparent that although the modelling process has removed most of the noise in the raw MRI data, the peak velocity and the steep velocity gradients have been largely preserved. This is attributed to the local support feature of the spline approximation functions. Although the overall agreement between the numerical predictions and the spline modelled MRI data is very good, some slight mismatch primarily in the vicinity of the vessel axis is apparent. This difference however, is also present in the raw MRI velocity distribution and is not therefore introduced by the approximation process. This can be clearly seen in the y-centreline velocity profiles shown in Figure 4.3. Although the spline fit to the original data is excellent, there is a difference between the numerical predictions and

the experimental results in a region near the tube axis (–0.2< x/D < 0.4). This mismatch may be due to imperfections in the construction of the physical model used in the experiments. This is exhibited in the MRI measurements as a slight asymmetry in the velocity distribution with respect to the y-centreline which should lie on the symmetry plane of the model.

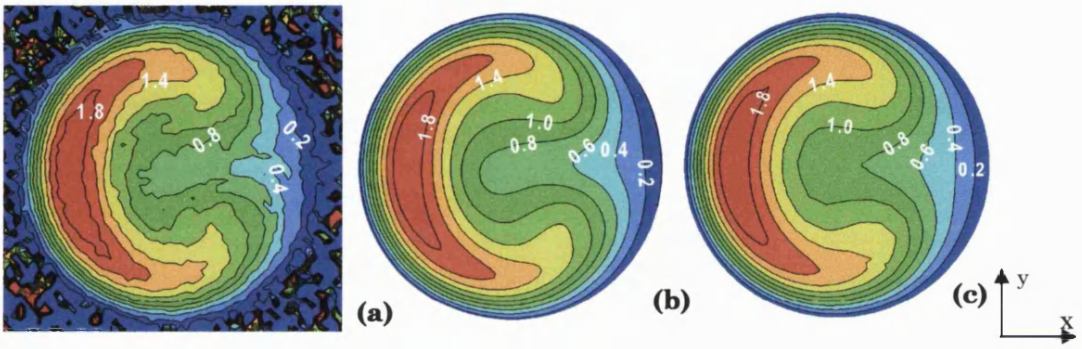

Figure 4.3 Comparison of the MRI measured (a) spline modelled (b) and numerically computed (c) normalised axial velocity extracted at 2D distal to the toe in the planar distal anastomosis model for steady flow (Re=250).

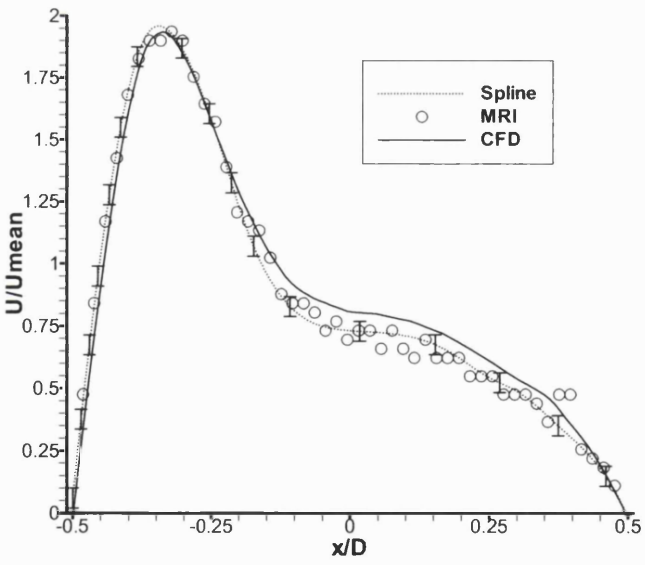

Figure 4.4 Comparison of the MRI measured (symbols) cubic spline modelled (dotted line) and numerically computed (solid line) normalised axial velocity y-centreline profiles extracted at 2D distal to the toe in the planar distal anastomosis model for steady flow (Re=250). Error bars corresponding to ±5 % of the mean axial velocity are placed for a number points on the spline fit curve.

A comparison of the numerically predicted and spline model MRI estimated circumferential wall shear stress distribution is shown in Figure 4.5. Also shown are the wall shear stress predictions based on a linear and a quadratic fit of the MRI measured velocity profiles. Using the numerical prediction as a reference solution, the spline model results tend to overestimate the wall shear magnitude in the high shear region (|theta|>100) and slightly underestimate it in the low shear region (-100<theta<100). To account for the uncertainty in the exact intravoxel wall location, the upper and lower bounds of the estimate are calculated by contracting and expanding respectively the boundary of the approximation domain by a distance equivalent to half the in plane resolution of the measurement. It should be noted that despite the high in plane resolution of the MRI velocity measurements, the error introduced in the wall shear estimate due to the uncertainty in the subpixel wall location can still be significant. The mean error in the location of the wall due to the spline fit is equal to half the pixel width, assuming that the boundary voxel is accurately located. This error is equivalent to 3 % of the tube radius based on the in plane resolution of the experiment and the nominal tube radius. This level of error alone would, assuming Poiseuille flow and as a result of error propagation, introduce an uncertainty of 9 % in wall shear stress calculated from equation (4.26).

Wall shear estimates obtained by applying the spline method are also compared to those obtained with the widely used methods of linear and quadratic extrapolation. Specifically three methods were examined: linear extrapolation using velocity measurements from the first two intraluminal voxels, least squares linear fit using velocity measurements from the first three intraluminal voxels and quadratic fit using velocity measurements from the first three intraluminal voxels. The results obtained at four angular equispaced locations along the circumference of the vessel are shown in Figure 4.5. These results show that overall the linear methods produce more accurate wall shear stress estimates as compared to the quadratic method. This is probably due to the fact that the velocity distribution investigated, based on the numerical predictions, is reasonably linear near the wall. However, overall these methods produced less accurate wall shear estimates compared to the spline model. Although spatial differences were found, the overall accuracy of the linear method wall shear rate esti-

mate was not significantly affected by the use of two or three intraluminal velocity data points.

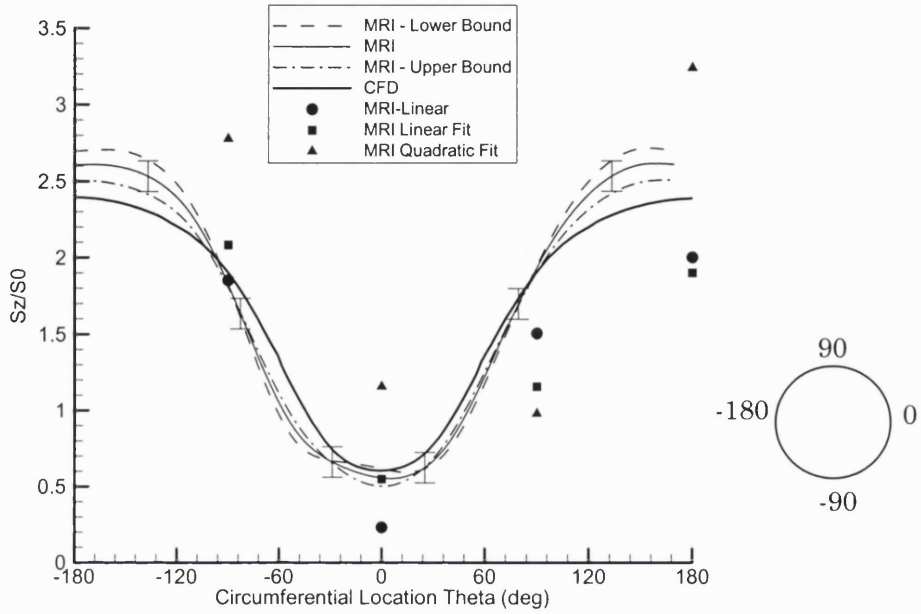

Figure 4.5 Comparison of numerically computed (thick solid line) and MRI spline model predicted (thin solid line) of wall shear stress magnitude along the circumference of the vessel wall extracted at 2 D downstream of a planar end-to-side distal anastomosis model in steady flow (Re=250). Wall shear stress is normalised by the Poiseuille wall shear stress at the graft inlet. Upper (dashed line) and lower (dashed-dot line) bounds of the estimate are also shown. Error bars correspond to +/- 10 % of the wall shear stress magnitude at the graft inlet. Symbols represent wall shear stress estimates based on the two-point linear method (circles) and the three-point least squares linear fit (squares) and quadratic fit (triangles) methods.

It should be noted however that for different flow (shape of velocity profile) and measurement conditions (VNR, spatial resolution) the quadratic method may yield more accurate results. Steinman et al. (1996) compared the two methods in complex flow and concluded that the quadratic method is superior to the linear method. However, a few comments on their study are warranted here. The setup of their experiment was such that offered minimum partial volume errors and very high wall-lumen contrast. They have also neglected the uncertainty of the velocity measurements in the calculation of the wall shear stress. They have only calculated shear rate for the peak shear location along the vessel circumference where the velocity profile is approximately linear and the velocity to noise ratio of the near wall pixels used in the polynomial fit process was significantly higher then the circumferential average. Fur-

thermore, to assess the effect of the voxel size on the accuracy of the wall shear estimate and compare the respective behaviour of the quadratic and linear methods, they used noise free numerically computed velocities. These results therefore can be rather misleading and not applicable to velocity measurements obtained *in vivo* with low VNR and spatial resolution thus significant partial volume error.

Method Limitations

These initial results show the potential of the proposed method. However, additional effort is required to address a number of outstanding issues. The method attempts to reach an optimum solution to a constraint optimisation problem with a number of control parameters as input. Given a phase velocity encoded image and its corresponding magnitude reconstructed image, the algorithm requires as user input the pixel intensity threshold used in the segmentation of the magnitude image. It also requires values for the upper limit of the smoothing factor used in the bicubic spline approximation of the velocity measurements that lie within the vessel lumen boundary.

If a strong edge at the vessel lumen boundary exists, the magnitude image can be easily segmented by a simple threshold method. An appropriate threshold can be selected as the minimum signal intensity threshold that excludes background noise in the vicinity of the boundary and maintains a relatively smooth and connected lumen outline. For velocity measurements in models, it was found that a threshold set to 95 % of the average peak background pixel intensity extracted from three background regions of interest in the vicinity of the lumen yielded satisfactory results.

The selection of the appropriate smoothing factor for the closed curve spline fit to the single pixel vessel lumen boundary definition, obtained by segmenting the magnitude image, is based on two rules. First, the boundary of the approximation domain should be as smooth as possible. This is important since the resulting spline surface fit and the wall shear estimate is sensitive to the smoothness of the boundary of the approximation domain. Second, the boundary should be constrained within the edge pixels. Therefore the optimum solution based on these rules is sought iteratively by start-

ing with a very high smoothing factor and gradually reducing its value until the second constraint is satisfied.

The selection of the smoothing factor for the surface bicubic spline fit is more complicated. A target for this optimisation process could be set with respect to the residual error of the fit computed as the rms difference between the measured velocity values (u_i) and the corresponding spline fit values $s(r_i,\theta_i)$ expressed by:

$$e_{rms} = \sqrt{\frac{1}{N}\sum_{i=1}^{N}(u_i - s(r_i,\theta_i))^2} < K, \tag{4.28}$$

where K is a user defined value and, N the number of experimental samples used in the approximation. Determining an appropriate value, or range of values, for K requires some information on the velocity measurement uncertainty. The mean velocity to noise ratio across the vessel lumen could be used as an estimate of the mean measurement uncertainty, assuming that systematic error in the velocity measurements is small. However the relationship between measurement uncertainty or precision and velocity to noise ratio has to be determined first. Then a formula or lookup table can be generated and used to set the range of values for K given the velocity to noise ratio of the measurements. Additional constraints in the approximation solution are required to determine the optimum approximation. For example constraints based on the spatial frequency spectrum of the spline approximation function and its derivatives could be introduced. By this, solutions containing spatial frequencies above a limit determined by the smallest flow features the measurement technique can resolve or are of interest can be excluded.

The effect of the smoothing factor on the shear estimate

The effects of the smoothing factor on the wall shear estimate calculated from the spline model of the MRI velocity distribution for complex steady flow (Re=250) at the toe of the non-planar distal anastomosis model were investigated. Two velocity measurements were obtained: one with a relatively low velocity to noise ratio (aliasing velocity of 1.2 u_{peak}) shown in Figure 4.6a and, one with a high velocity to noise ratio (aliasing velocity of 0.3 u_{peak}) shown, corrected for phase wrapping, in Figure 4.6b. A simple smoothing process was applied to the low VNR measurement whereby the ve-

locity at each point on the image grid is replaced by the average velocity of its neighbours with the condition that the second derivative of the velocity at the boundary is constant. The smoothed velocity distribution is shown in Figure 4.6c. It should be noted that only part of the noise in the original data has been removed by this simple smoothing approach. This process also reduced the size of the high velocity contours with subsequent effects on the velocity gradients (Figure 4.8). Therefore it is most likely that wall shear stress calculations based on data smoothed by this process will underestimate the true values.

The balance between the closeness of fit and the smoothness of the solution is critical to the quality of the spline approximation. One solution is to maximise the smoothness of the solution for a given level of residual approximation error determined by the measurement precision. However this approach does not necessarily yield either the optimum solution or the correct approximation. It is therefore necessary to establish an upper limit for the residual approximation error and determine the corresponding upper limit for the smoothness of the fit to meet the residual error target. Then, solutions obtained by progressively reducing the smoothness factor yielding closer fits to the original data should be inspected and the optimum solution selected. It should be noted that as the smoothing factor is reduced, thus a closer fit is requested, a new distribution of knots is calculated to meet the condition set by equation (4.14). The adaptive knot placement strategy ensures that there will be a larger number of knots with decreasing S and, a higher knot density in regions of the domain where the function underlying the data is more difficult to approximate than in regions where it is smoother. The spline fits and the corresponding knot distribution obtained by applying this process to the low VNR measurement shown in Figure 4.6a for three values of the smoothing factor S (8, 6.8 and 6.6) are shown in Figure 4.7 a-c respectively. It is not difficult to identify the preferred solution when the corresponding circumferential wall shear estimates shown in Figure 4.9 are considered. It is apparent that the approximation corresponding to a smoothing factor of S = 6.6 includes an unacceptable level of noise while the approximation corresponding to a smoothing factor of S = 8 has removed important features of the velocity distribution. A good compromise between closeness of fit and smoothness of the solution is achieved by selecting a smoothing parameter of S = 6.8.

A comparison of the y-centreline velocity profiles obtained from the low and high VNR MR velocity measurements, the spline fit on the low VNR data and the moving average smoothed low VNR data is shown in Figure 4.8. The moving average smoothing has retained the noise in the original data, which is more pronounced near the axis. Finally it should be noted that the spline fit to the low VNR data is very good and close to the high VNR profile.

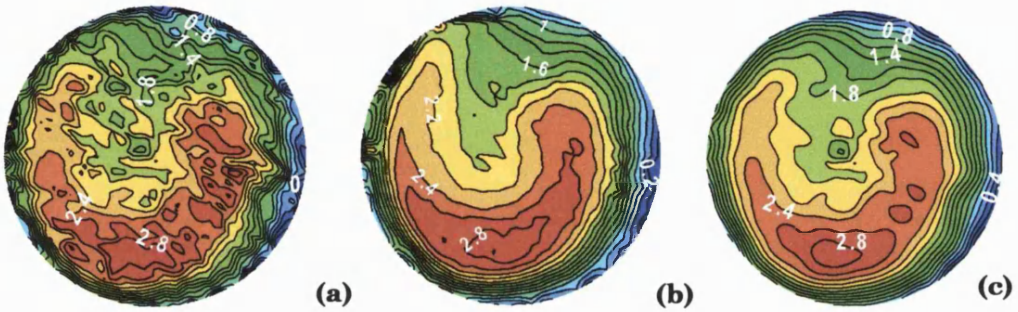

Figure 4.6 Raw MRI u-axial velocity contour maps extracted at the toe of the non-planar anastomosis model for steady flow (Re=437) using an aliasing velocity of 1.2 U_{peak} (a) and 0.3 U_{peak} (b). Also shown (c) is a smoothed version of the original measurement shown in A.

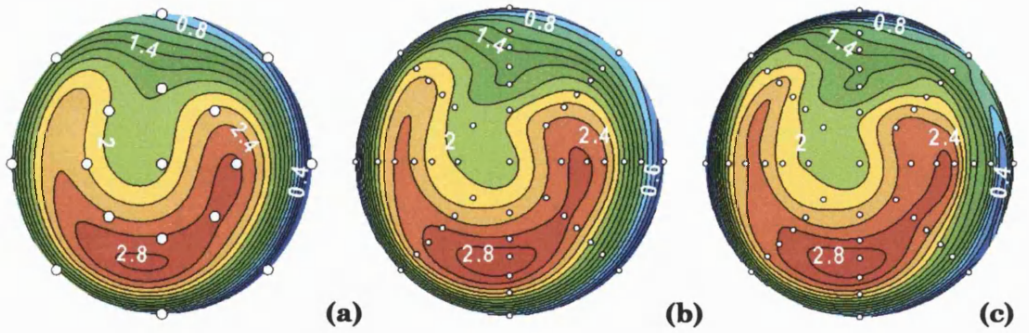

Figure 4.7 Spline modelled MRI data based on the velocity distribution shown in Figure 4.6a, obtained with different degrees of smoothness in the solution by altering the smoothing factor S. Results correspond to S = 8 (a), S = 6.8 (b) and S = 6.6 (c). Symbols indicate the knots used to calculate the spline fit.

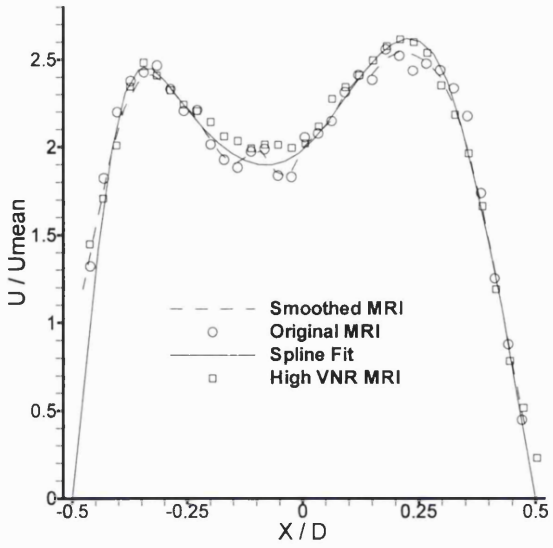

Figure 4.8 Comparison of y = 0 centreline velocity profiles extracted from the smoothed MRI (dashed line), the original low VNR MRI (circles), the spline fit (solid line) to the original MRI shown in Figure 4.7 b and the high VNR reference MRI data (squares).

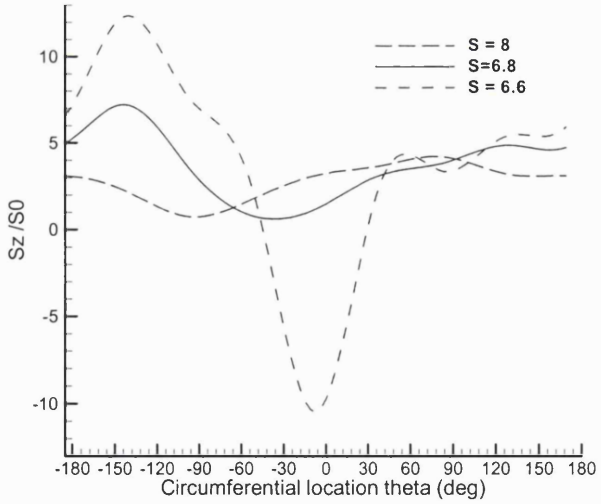

Figure 4.9 Circumferential wall shear stress distribution estimated from the spline modelled MRI phase velocity maps shown in Figure 4.7.

Chapter 5.

Flow in Realistic Geometry Bypass Graft Models

In previous chapters flow in idealised models of arterial anastomoses has been considered. Although such studies are important in understanding the fundamental effects of the various geometric and flow related parameters in a controlled environment, there is also the need to assess the flow field associated with more physiologically relevant flow conditions. Several studies have investigated the feasibility of non-invasive *in vivo* volume flow quantification in coronary arteries (Keegan et al., 1994; Hofman et al., 1996; Hundley et al., 1996; Sakuma et al., 1997) or coronary artery bypass grafts (Galjee et al., 1996) by MRI. These investigations demonstrated the possible applications of phase velocity mapping in small and difficult to image vessels or vascular reconstructions in the coronary circulation. However, there are still respiratory and heart motion related effects that have not been resolved and may compromise the accuracy of such measurements. With current MRI technology, highly resolved detailed *in vivo* studies of the complex local perianastomotic bypass graft flow field in the coronaries are not feasible. Although such studies are technically feasible for other small calibre arteries they may require long acquisitions and therefore increased patient tolerance.

To overcome these limitations, an alternative indirect approach to study the flow field in difficult to image vessels or vascular reconstructions, whereby the *in vivo* flow conditions could be transferred to *in vitro* models, was developed. This approach involves a number of steps. First the arterial geometry of interest is extracted *in vivo* by high spatial resolution MR angiography. The images obtained are then processed off-

line and the surface of the lumen is reconstructed. Finally, the digital representation of the surface is used to fabricate a hollow physical model of the flow conduit of interest. The velocity distribution at the inlet of the interrogated arterial segment can also be obtained *in vivo* either by MRI or pulsed Doppler ultrasound. For this investigation, due to access restrictions on the flow quantification pulse sequences available on the St' Mary's GE Signa scanner used for the *in vivo* acquisitions, the graft inlet flow waveform and the graft outflow division ratio were obtained from pulsed Doppler velocimetry.

The aim of this part of the investigation was to assess the effects of the detailed geometry on the local time varying flow field in realistic bypass graft models. For this, a femoro-tibial bypass graft geometry extracted *in vivo* and an aorto-coronary bypass graft geometry extracted *in vitro* from an arterial cast by MRI, are considered. Results from MRI velocity field measurements in the realistic bypass graft models fabricated based on the MR extracted geometric definitions are discussed. Parts of the material presented in this chapter formed the basis of a paper due to appear in Biorheology (Papaharilaou et al., 2002).

5.1 Aorto-coronary bypass graft model

5.1.1 Methods

5.1.1.1 Geometry measurements

Measurements were performed on a GE 1.5 Tesla MRI whole body scanner at St' Mary's Hospital and on a GE 1.5 Tesla 30 cm bore scanner at Imperial College.

Bypass grafts of the left anterior descending (LAD) coronary artery were constructed by an experienced heart surgeon using excised porcine hearts and human saphenous vein, surplus to requirements for coronary artery bypass grafting. The grafts were cast using an epoxy resin (Biresin G49, Cika Chemie) at a pressure equivalent to 74 mm Hg and extracted using hydrochloric acid (Figure 5.1a). The casts were then imaged immersed in a $CuSO_4$ doped water solution, using a standard three-dimensional gradient echo sequence with 0.19 mm in plane and 0.7 mm through plane resolution.

5.1.1.2 Surface reconstruction

The raw MRI images were segmented and single pixel edges defining the blood vessel boundaries were extracted. A closed spline was fitted through each edge and evaluated at a suitable number of sites to obtain a cloud of points representing the surface of the blood vessel. An implicit function which has minimum curvature and fits through these points and the centres of all closed splines is calculated (Peiro et al., 2001). The zero value contour of the implicit surface provides a good interpolation of the surface of the blood vessel (Figure 5.1b). By passing this geometry definition in terms of bicubic spline surfaces to the FELISA mesh generator (Peiro and Sayma, 1995), a computational mesh could be produced making it possible to use the extracted bypass graft geometry in numerical computations of the flow field.

5.1.1.3 Model Fabrication

A 1650 FDM rapid prototyping (RP) fused deposition modeller (Stratasys Inc., USA) using Acrylonitrile-Butadine-Styrene (ABS) thermoplastic applied in thin layers was used to produce the bypass graft replica. For the purposes of ensuring appropriate flow conditions for the MRI flow measurements circular cross section extensions were blended at the inlet and outlet of the bypass graft geometry definition that was then scaled by a factor of 1.5. This information was then input in stereolithography (STL) format to the RP manufacturer's processing software Quickslice™ to generate an output file defining the position of the RP head for physically creating the model, slice by slice every 0.25mm (Sanghera et al., 2001). The model was constructed in approximately 90 minutes (Figure 5.1).

A negative flexible transparent silicone model of the stereolithographic replica was fabricated and used for MRI flow measurements. The fabrication process of the physical model involved a number of stages. Initially a resin copy of the rapid prototype vascular replica was obtained. This was achieved by first constructing a silicone mold of the original model in two halves. A box was made from non silicone bonding material to enclose the replica. Silicone was then poured to create the lower half of the mold and was left to cure. A thin layer of non silicone bonding material is then applied

on the exposed surface of the cured lower half of the mold. By this, the upper half of the mold which is poured on top does not bond to the lower part and the two parts can be mechanically separated when cured. After allowing the upper half to cure the two halves are separated and the original rapid prototype model is removed. The mold was then used to produce a copy of the original rapid prototype model. The surface of the resin copy was then smoothed by applying a very thin layer of paint which was just enough to remove the surface roughness caused by approximately 0.1 mm deep grooves, characteristic of the model fabrication process used by the rapid prototyping system. A new silicone mold was then made from the smoothed version of the vascular model that was subsequently used to produce a wax copy of the smoothed resin model. The wax copy was then molded using a clear flexible silicone material (Elastosil 1450, Wacher Chemie) and was subsequently melted out leaving a clear negative silicone model that was used in the MRI flow experiments. The walls of the silicone model were made sufficiently thick to be assumed rigid for the range of pressures applied in the flow experiments.

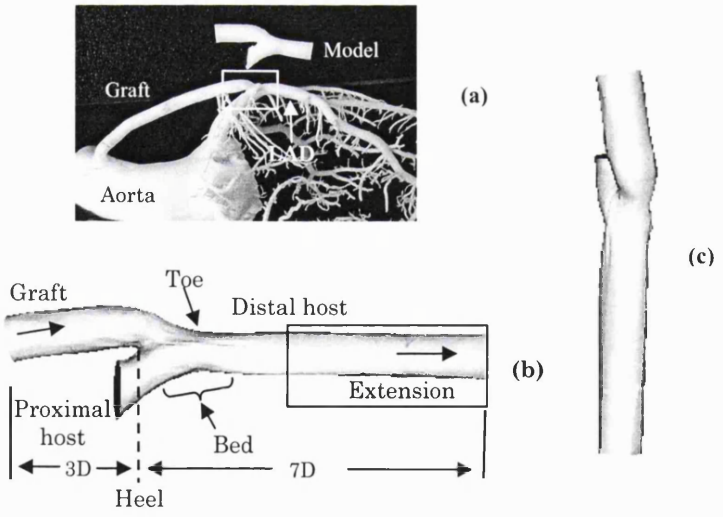

Figure 5.1 (a) Close-up view of the distal anastomosis cast and the scaled (1.5 × original) stereolithographic replica corresponding to the outlined cast region. Surface representation of the coronary artery bypass graft distal anastomosis in lateral view (b) and top view (epicardial surface) (c) with distal host section extended. Dimensions are normalised by the graft inlet diameter (D).

5.1.1.4 Flow measurements

Three inlet flow conditions were investigated. A fully developed steady and a set of time-varying axisymmetric flows were prescribed at the inlet. The pulsatile waveforms applied were: a single harmonic sinusoidal waveform with a superimposed steady flow component and, a multi-harmonic aorto-coronary bypass graft flow waveform. The physiological flow waveform used in this investigation was adapted from a blood flow velocity waveform obtained *in vivo* by Kajiya et al. (1986) using pulsed Doppler velocimetry. The flow measurements were conducted in a human during open-chest heart surgery. A blood flow velocity waveform obtained in the distal end of a vein coronary artery bypass graft of the left anterior descending (LAD) coronary artery of a patient with 99 % proximal stenosis of the LAD was selected for the purposes of this study. The original waveform was Fourier transformed and its power spectrum is plotted in Figure 5.2. The waveform signal was then low pass filtered with a cut-off frequency set at 13 Hz (Figure 5.3a). This cut-off frequency was selected so that the filtered signal retained 90 percent of the power in the original signal. The flow waveform low pass filtered with an 18 Hz cut-off frequency is shown in Figure 5.3b. As expected the additional frequency content does not significantly alter the information content already included in the waveform generated from the 13 Hz low pass filter process. To reduce the magnitude of retrograde flow, the filtered waveform was scaled down by a factor of two and a positive steady flow component was added (Figure 5.3c). A Womersley parameter of 2.7 and a Reynolds number that varied in the range of -10 to 225 with a mean value of 100 were specified at the graft inlet. The Womersley parameter and mean Reynolds numbers were within the physiological range for a heart at rest (Lou et al., 1992; Clarke et al., 1995).

To assess the effects of pulsatility on the flow field in the bypass graft, a second set of velocity measurements were acquired with the same scan parameters but for a simple single harmonic sinusoidal flow waveform with a superimposed steady flow component prescribed at the graft inlet. The Womersley number of the flow in this case was also 2.7 and the Reynolds number varied between 5 and 195 with a mean value of 100. A computer controlled flow simulator (Shelley Medical Imaging Inc.) was used to generate both flow waveforms. Steady flow measurements were also obtained at a Reynolds number of 100.

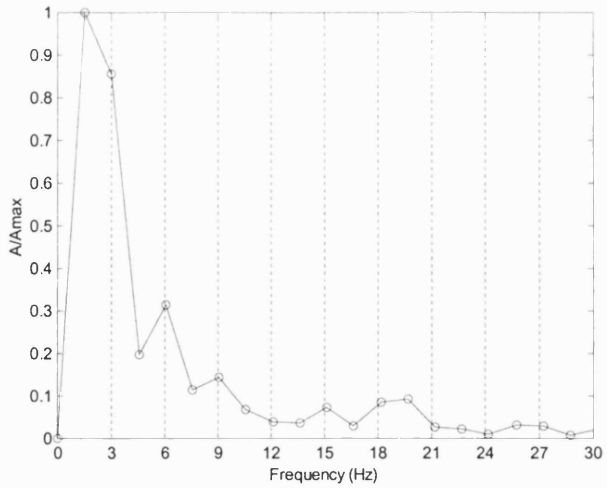

Figure 5.2 The power spectrum of a velocity waveform cycle recorded *in vivo* by pulsed Doppler velocimetry in a human subject just after aorto-coronary bypass graft surgery and before chest closure. Note that most of the signal power is contained in the first 8 harmonics (up to 13 Hz). The DC component (0Hz) has been subtracted from the signal. The fundamental frequency of the measured velocity waveform was 1.5 Hz.

A two dimensional phase contrast sequence was used to measure the velocity vector by exciting a 2 mm slice with a 50 degrees flip angle and a 256 × 256 image matrix with a 8 cm square FOV yielding a 0.31 mm in-plane resolution. The minimum echo and repetition times of 7.2 ms and 14.7 ms respectively were selected. The acquisition was gated to a pseudo ECG signal generated by the flow simulator. First order gradient moment nulling was applied to reduce flow pulsatility artefacts. To improve the signal to noise ratio of the measurement a contrast agent (Gd-DTPA) was introduced into the circulating fluid. Eight excitations were applied which combined with the 2 views per segment selected required a total acquisition time of 30 minutes per slice location.

Steady flow velocity vector measurements were also obtained by exciting a 2mm slice with a 50 degrees RF pulse and an 8 cm FOV on a 512×512 image matrix, yielding a 0.156 mm in-plane resolution. The minimum echo and repetition times of 7.4 ms and 18 ms respectively were selected. Thirty-two signal averages were prescribed resulting in a total acquisition time of 19 minutes per slice location. In order to extend the dynamic range of the velocity measurement to accommodate the differences in magnitude between the in-plane and axial velocity components, an aliasing velocity

significantly lower than the peak axial velocity was prescribed. An estimate of the peak axial velocity was obtained from a preliminary low-resolution short duration two-dimensional phase contrast acquisition. Based on this estimate, an aliasing velocity of 8 cm/s, approximately 60 % of the peak axial velocity, was selected. The aliased phase images were phase unwrapped to recover the correct phase distribution applying the technique described in section 2.3.2. A single pixel vessel wall lumen boundary was extracted from the magnitude image by applying an appropriate threshold level to exclude background pixels. Due to the high signal to noise ratio and spatial resolution of the velocity measurements a steep pixel intensity gradient outlined the boundary between background and lumen pixels, thus allowing for this simple segmentation method to give satisfactory results.

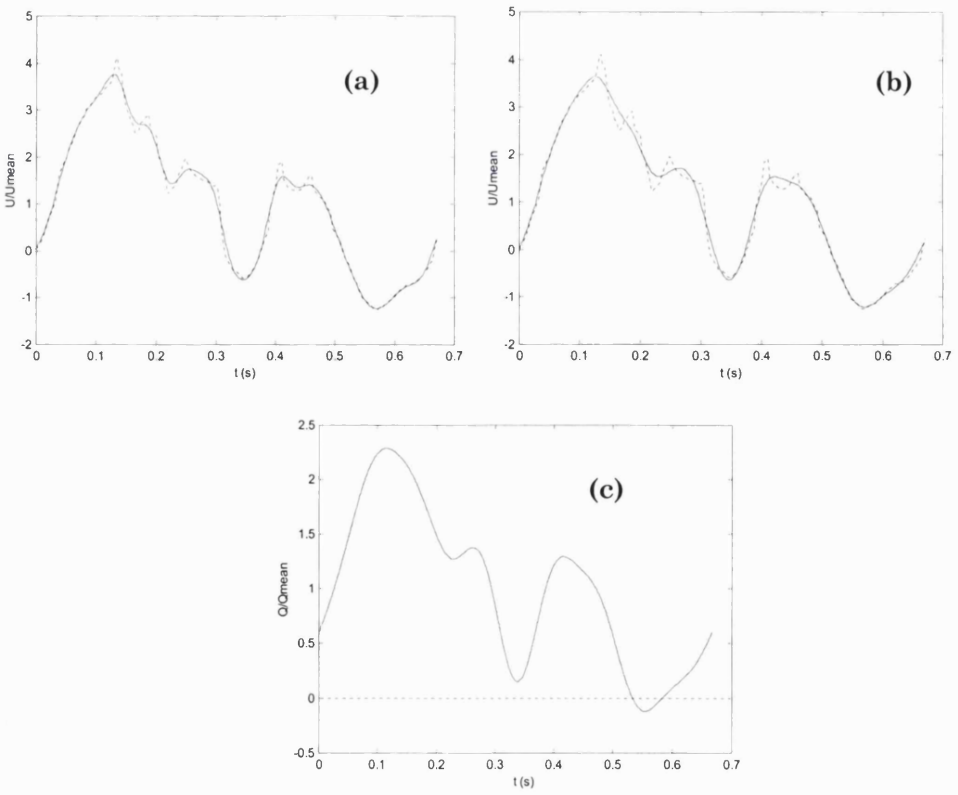

Figure 5.3 Comparison of the recorded (dotted line) and low pass filtered (solid line) flow waveform measured in the graft of a distal aorto-coronary anastomosis applying a cut-off frequency of 18 Hz (a) and 13 Hz (b). Waveform (c) was generated by scaling down by a factor of 2 and adding a DC offset to the filtered waveform shown in panel (a).

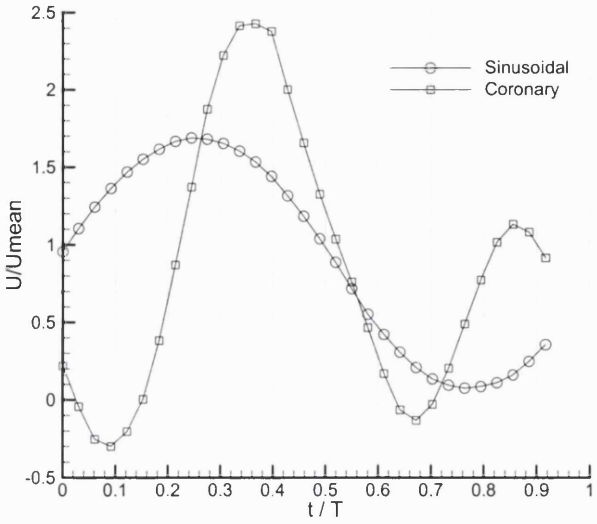

Figure 5.4 Coronary and sinusoidal flow waveforms at 1 D distal to the toe of the anastomosis of the aorto-coronary bypass graft model. Waveforms are derived from the evolution of the mean velocity calculated from the luminal pixels of the phase velocity images. Thirty one out of 33 phases, corresponding to a cycle period of 1.8 seconds and a phase spacing of 55 ms, were reconstructed.

Figure 5.4 shows the velocity waveforms reconstructed by calculating the instantaneous mean lumen velocity from the time resolved MRI phase velocity images. The bandwidth of the reconstructed coronary bypass graft appears to be reduced by a low pass filtering process compared to the prescribed flow waveform shown in Figure 5.3c. This difference could be attributed to errors in the physical reproduction of the waveform and also could be the result of under sampling. The frequency response of prospectively gated phase-velocity MR measurements has been investigated by Frayne and Rutt (1995a) and by Polzin et al. (1996). By applying a moving segment over contiguous views acquired to reconstruct all intermediate flow phases Polzin et al. (1996) found that the Nyquist sampling frequency becomes independent of the number of views. This result shows that view sharing improves the sampling rate of the measurement.

For the experiments reported here, care was taken to prevent under sampling. For this a long waveform cycle of 1.8 s was selected. As a result the maximum frequency in the prescribed filtered waveform was that of the eighth harmonic, or approximately 4.5 Hz. To satisfy the Nyquist criterion, a sampling frequency of at least 9 Hz should be used. The effective sampling frequency (f_{es}) for a segmented k-space se-

quential acquisition with viw sharing applied can be calculated by the following expression:

$$f_{es} = \left\{ (n_{flow} + 1) n_{rps}\ TR\ \right\}^{-1}, \tag{5.1}$$

where n_{flow} is the number of flow directions encoded, n_{rps} is the number of TR intervals between neighbouring reconstructed phases. The effective sampling rate for these measurements was approximately 18 Hz thus double the minimum requirement based on the Nyquist criterion. Although the acquisition of segments is sequential, the acquisition of the image pair corresponding to the normal and inverted flow encoding bipolar gradients is interleaved. For single velocity component measurements ($n_{flow} = 1$) four views per segment were acquired. When all three velocity components were encoded ($n_{flow} = 3$) two views per segment were selected to maintain the temporal resolution achieved for the single velocity encoding measurements. It should be noted that although through view sharing the true temporal resolution of the flow measurements remains unchanged and given by:

$$f_{ts} = \left\{ (n_{flow} + 1) n_{vps}\ TR \right\}^{-1} \tag{5.2}$$

where n_{vps} are the number of views or *k*-space lines grouped together in each segment of *k*-space sampled, however 2*n*-1 instead on *n* temporal phases are reconstructed and the effective sampling rate as determined by equation (5.1) is increased.

Data analysis for wall shear estimation

Wall shear stress estimates were calculated from the spline modelled MR velocity encoded phase by the following procedure. An estimate of the wall location within the boundary pixel was first obtained by fitting a smooth closed spline curve through the set of points determined by the centres of the boundary pixels. The selection of the smoothness parameter (*S*) for the closed spline curve was based on the assumption that the surface of the inner wall of the physical model used in these studies is smooth. Therefore the spline curve with the highest smoothness parameter that is contained within the boundaries of the edge pixels was selected as an initial estimate of the wall location.

Assuming that the wall location can be accurately determined at the pixel level, the maximum error in the wall location estimate will be equal to the in-plane resolution of the MRI experiment. The uncertainty in the wall shear stress estimate is also dependent on this error but is not directly proportional to it. Applying propagation or error to the wall shear stress function for Poiseuille flow as expressed by equation (4.26), assuming other parameters are exactly known, the fractional error in wall shear rate will be:

$$\frac{\delta\tau}{|\tau|} = \frac{1}{|\tau|}\left|\frac{\partial\tau}{\partial R}\right|\delta R = \frac{1}{R^{-3}} 3R^{-4}\delta R = 3\frac{\delta R}{R} \tag{5.3}$$

This result reveals the sensitivity of the wall shear stress estimate accuracy to errors in the detection of the exact wall location.

Once a spline definition of the boundary is obtained, the velocity at the spline boundary definition points could either be set to zero thus enforcing the no-slip condition at the wall, or left to be calculated as part of the spline approximation solution. The latter approach was selected, as it does not require *a priori* knowledge of the exact wall location. The calculation of the velocities at the boundary is based on the derivative continuity constraints enforced for the approximation solution. The approximation domain included all velocity data points contained by the closed spline boundary definition curve excluding boundary voxels.

5.1.2 Results and Discussion

5.1.2.1 Steady flow

A comparison of the steady flow (Re=100) axial velocity contours and cross flow streamlines extracted at the toe and at 1D distal to the toe are shown in Figure 5.5. There is a strong dominant vortex with its core at the upper part of the cross-section and a weaker counter-rotating vortex located towards the lower part of the cross section that can just be inferred. This weaker vortex is somewhat more developed at one diameter downstream of the toe. The asymmetry of this vortex structure differs from the Dean-type symmetric counter rotating vortices associated with flow in planar curves and demonstrates the influence of the out-of-plane graft curvature on the flow-field. Although the out-of-plane curvature (Figure 5.1c) appears low, there is a local

contraction at the anastomosis inlet which accelerates the flow thus increasing the asymmetry of its injection from the graft to the host artery. It should be noted that although at 1D distal to the toe cross flow streamlines converge and form a vortex core or sink in the primary vortex, they appear to diverge from a source point in the counter rotating secondary vortex. Streamline divergence or convergence occurs at points of cross flow stagnation where the magnitude of the cross flow vector is practically zero. A cross flow vortex will setup a helical pattern of fluid particle motion which may improve fluid mixing.

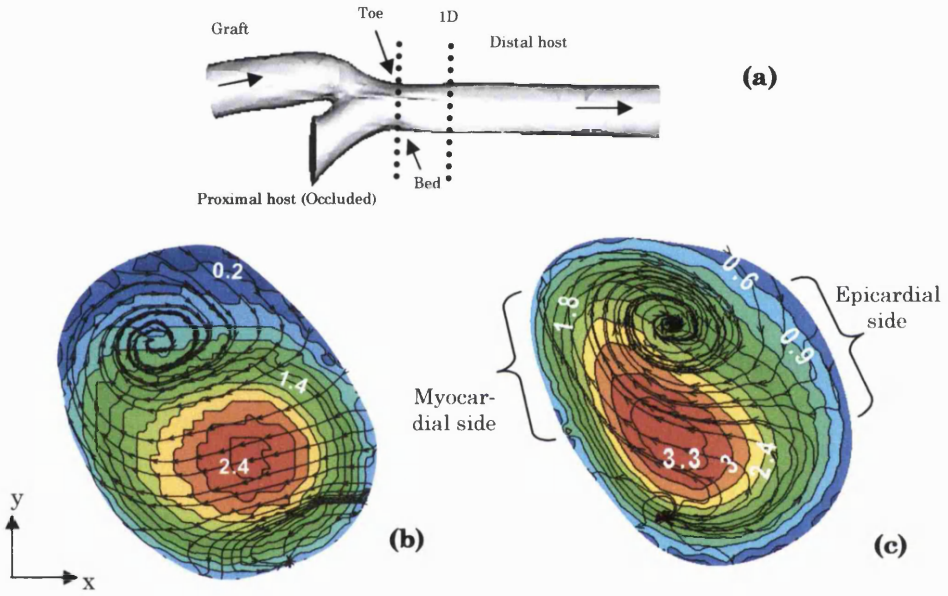

Figure 5.5 Surface representation of the coronary artery bypass graft distal anastomosis (a). Dotted lines indicate measurement stations for the MRI results shown in panels (b) and (c). Comparison of contours of the MRI measured normalised axial velocity and cross flow streamlines extracted at the toe (b) and at 1D distal to the toe (c) of the distal coronary bypass graft anastomosis in steady flow (Re=100).

Spline modelled data

Figure 5.6 shows a comparison of the raw and spline modelled axial velocity extracted just distal to the toe of the aorto-coronary anastomosis. Figure 5.7 and Figure 5.8 show similar comparisons for the horizontal in plane and vertical in plane velocity components respectively. It should be noted that the velocities calculated at the boundary of the approximation domain are in most cases significantly above zero due to phase averaging and partial volume errors in the MR data. However, if the spatial

resolution of the acquisition is high and the velocity gradient within the boundary voxel is assumed constant, the velocity gradient at the boundary of the approximation domain can be used as an estimate of the wall shear stress. It should be noted that although the absolute value of the pixel velocities near the wall may be inaccurate due to intravoxel phase averaging, the velocity gradient determined by these velocities can be correct if the intravoxel phase distribution is linear and symmetric. In contrast if the intravoxel phase distribution is non-linear, this assumption is not necessarily valid and the resulting estimate of the velocity gradient at the wall will be inaccurate.

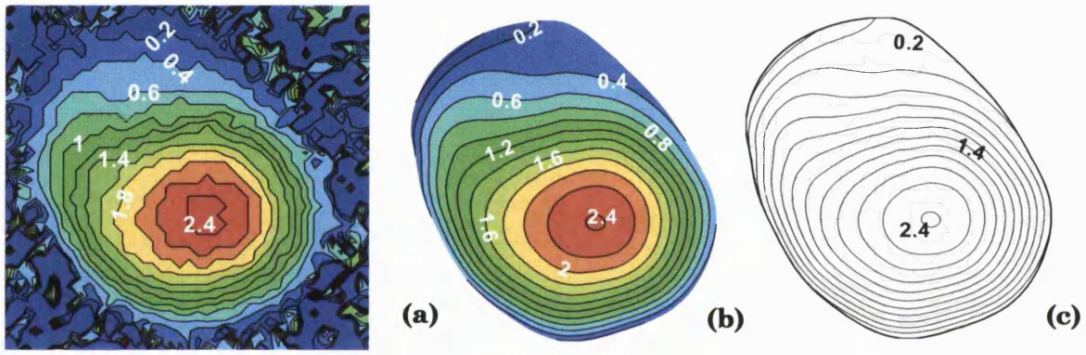

Figure 5.6 Comparison of the MRI measured (a) and spline modelled (b) axial-u velocity component normalised by the mean inlet velocity and extracted at the toe of the distal coronary bypass graft anastomosis model in steady flow (Re=100).(c) Comparison of MRI measured (dotted line) and spline modelled (solid line) axial velocity contours.

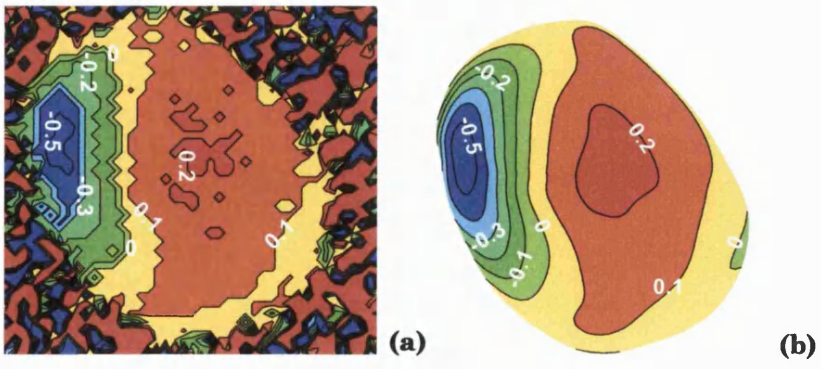

Figure 5.7 Comparison of the MRI measured (a) and spline modelled (b) vertical-w in-plane velocity component normalised by the mean velocity and extracted at the toe of the distal coronary bypass graft anastomosis model in steady flow (Re=100).

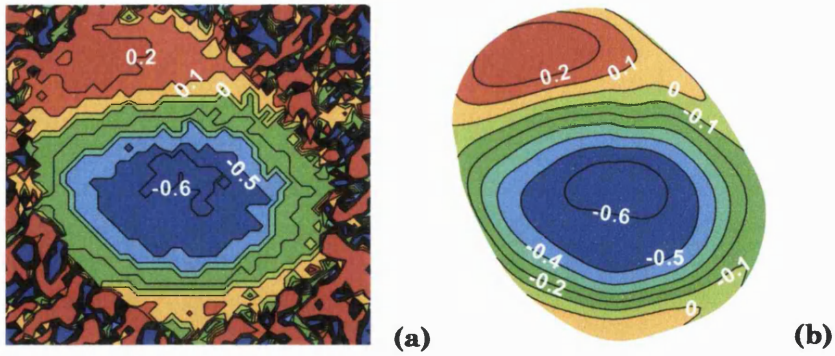

Figure 5.8 Comparison of the MRI measured (a) and spline modelled (b) horizontal-v in-plane velocity component normalised by the mean velocity and extracted at the toe of the distal coronary bypass graft anastomosis model in steady flow (Re=100).

Figure 5.9 shows a comparison of the contours of axial vorticity and cross flow streamlines calculated from the spline modelled MRI data extracted at the toe and at 1D distal to the toe of the aorto-coronary anastomosis model. As discussed in the introduction, vorticity is a measure of rotationality in the flow and can be used to asses the level of fluid mixing. The axial component of vorticity ω_z is given by:

$$\omega_z = \frac{\partial w}{\partial x} - \frac{\partial v}{\partial y} \tag{5.4}$$

There is a notable approximately factor of five reduction of the peak axial vorticity associated with the primary vortex between the toe and 1D downstream in the host vessel. This is associated with the sharp drop in cross flow magnitude occurring between the two locations. High vorticity at some distance away from the wall is usually associated with vortical features in the cross flow streamlines.

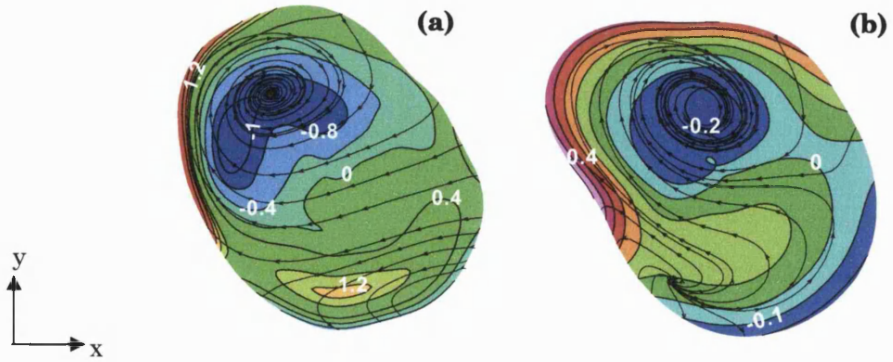

Figure 5.9 Spline modelled axial vorticity contours (b) with cross flow streamlines superimposed, from MRI measurements extracted at the toe (a) and at 1D distal to the toe (b) of the distal coronary bypass graft anastomosis model in steady flow (Re=100).

5.1.2.2 Time varying flow

Based on the temporal relationship between the flow waveforms depicted in Figure 5.4, a number of flow phases obtained at the toe and for each inlet flow condition, corresponding approximately (±5%) to the same Reynolds number, were processed and are shown in Figure 5.10. The results during early acceleration show a significant difference in the cross flow streamline patterns between the two flow regimes. The sinusoidal waveform result reveals the presence of two counter rotating vortices with well defined cores and, exhibits a less uniform velocity distribution as compared to that for the corresponding physiological waveform. Although the Womersley parameter is the same in both flow regimes there is a clear difference in the pressure-flow phase lag between the two cases. The flow field modulated by the physiological waveform appears to require additional time to accommodate the dynamics of the driving pressure gradient. This can be attributed to the steeper flow acceleration and deceleration gradients of the multi-harmonic coronary bypass graft waveform compared to the significantly smoother changes in flow rate forced by the single harmonic waveform. During early acceleration, in contrast to the sinusoidal flow case (Figure 5.10 b), the primary vortex can be just inferred and the secondary vortex is absent in the physiological waveform case (Figure 5.10 a). During mid deceleration, although the cross flow patterns are similar in both flow regimes (Figure 5.10 e & f), there is more pronounced axial flow separation in the physiological waveform case.

The velocity field in the aorto-coronary bypass graft was also interrogated at 1D distal to the toe of the anastomosis to investigate the effects of the change in the shape of the vessel lumen boundary on the velocity field and also the rate at which the effects of the anastomotic junction geometry on the flow field in the host vessel dissipate. Figure 5.11 shows three points in the flow cycle (peak flow (a&d), mid deceleration (b&e) and early acceleration (c&f)) for the physiological (top) and the sinusoidal (bottom) flow field. The strong influence of the flow waveform on the flow field found at the toe is also evident in these results.

Although panels (b) and (e) of Figure 5.11 correspond to only marginally different instantaneous Reynolds numbers, there is a clear separation region on the epicardial wall in the coronary waveform phase velocity map which is absent in the corre-

sponding sinusoidal waveform phase velocity map. Furthermore, by inspection of all MRI reconstructed phase velocity images in the sinusoidal flow cycle it was found that there is no boundary layer separation at any point in the cycle. It should be noted that unlike the sinusoidal flow waveform, the coronary flow waveform includes two short phases of bulk flow reversal. However, the results show boundary layer separation occuring during late deceleration but prior to bulk flow reversal.

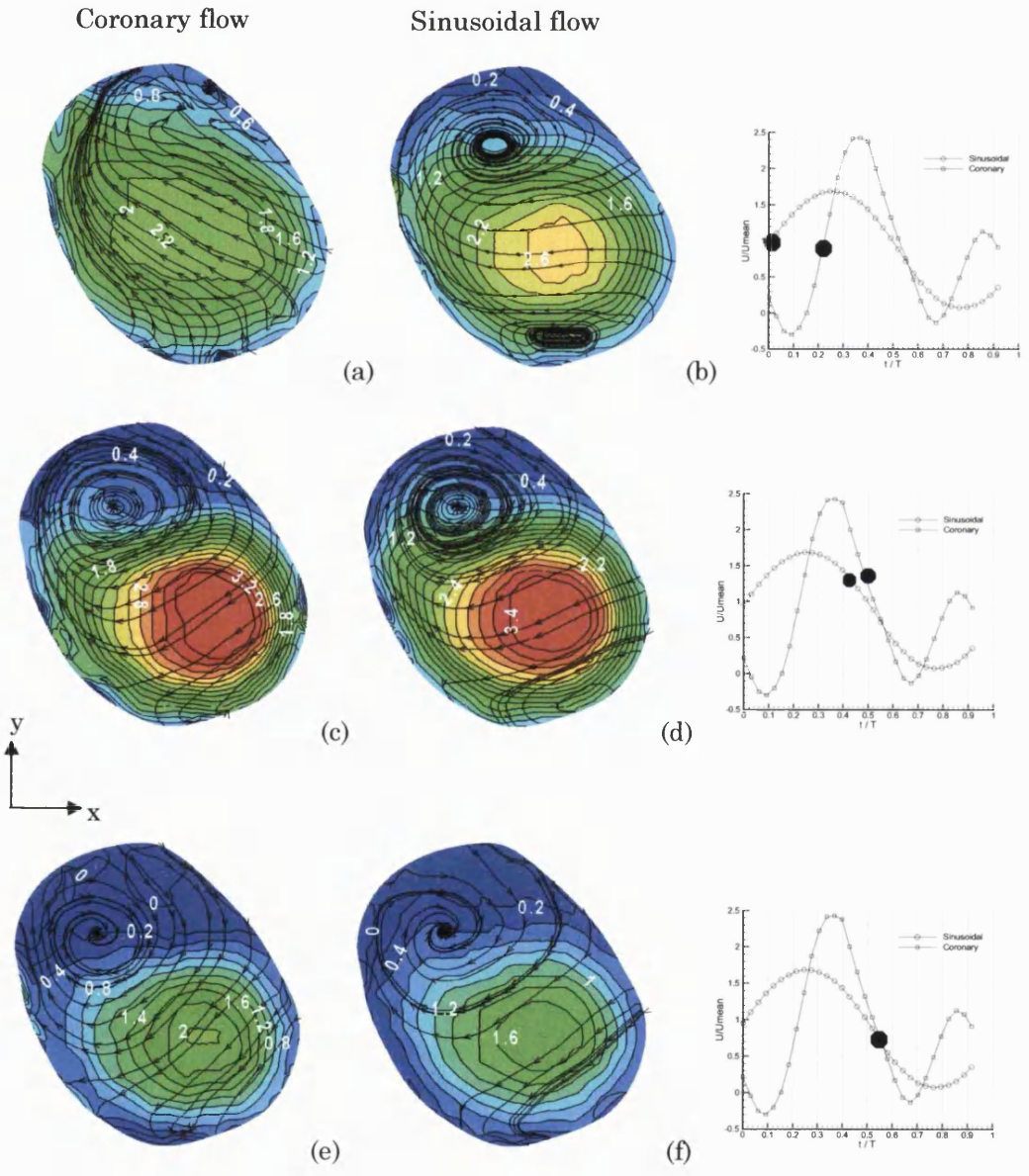

Figure 5.10 Contours of the MRI measured normalised axial velocity and cross flow streamlines extracted just distal to the toe of the aorto-coronary anastomosis at three points in the cycle. A coronary flow waveform was prescribed at the graft inlet for the figures on the left and a sinusoidal flow waveform for those on the right.

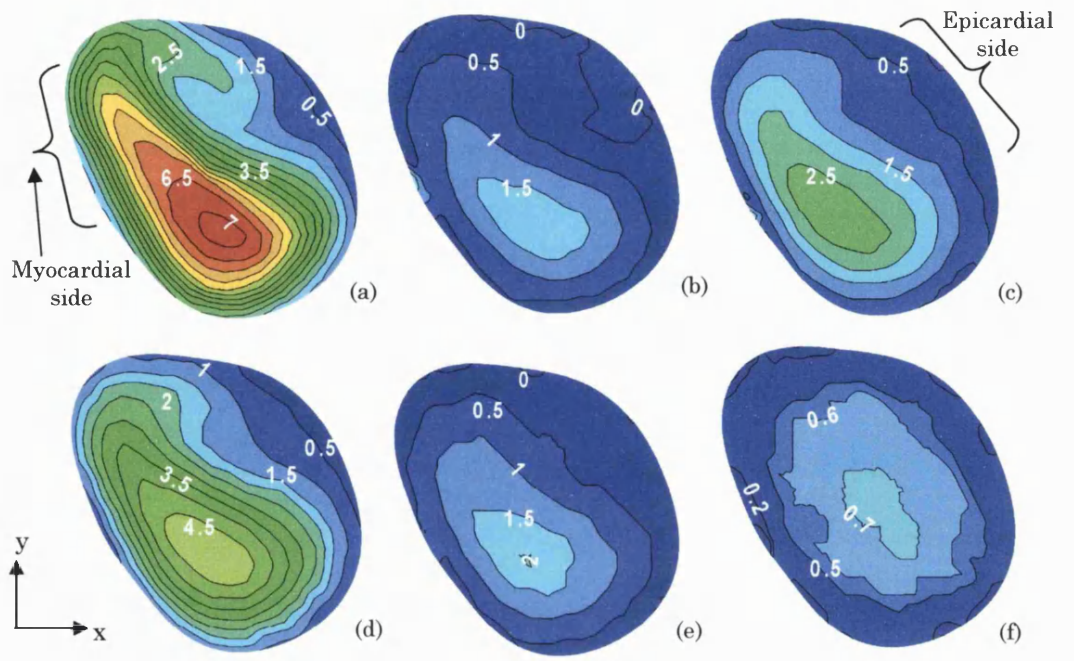

Figure 5.11 Axial velocity contour plots extracted at 1 D distal to the toe of the aorto-coronary anastomosis at peak flow (a&d), mid deceleration (b&e) and early acceleration (c&f). A coronary flow waveform was prescribed at the graft inlet for (a-c) and a sinusoidal flow waveform for (d-f).

Spline modelled data

Figure 5.12 shows the spline modelled axial velocity distribution extracted just distal to the toe of the aorto-coronary anastomosis at peak flow. There is (Figure 5.12a) a region of high shear on the lateral myocardial wall and a region of low shear on the epicardial wall. This asymmetry is introduced by the in plane pressure gradient that facilitates the change in the bulk flow direction as the flow negotiates the curvature of the graft-host artery junction. A comparison of raw MRI (symbols) and spline-modelled (solid line) axial velocity profiles extracted along the (y=0) horizontal centre-line, is shown in Figure 5.12b. The spline curve fit to the MRI velocity measurements data is excellent, with a residual approximation error of ±5 % of the mean axial velocity. During late deceleration (Figure 5.13), a region of axial flow separation develops on the epicardial wall. The near wall velocity gradients are significantly lower and more uniformly distributed along the vessel lumen boundary compared to those at peak flow and, near wall velocities are better resolved. This highlights the strong in-

fluence of the velocity distribution on the level of systematic error introduced by phase averaging and partial volume effects on near wall velocity measurements.

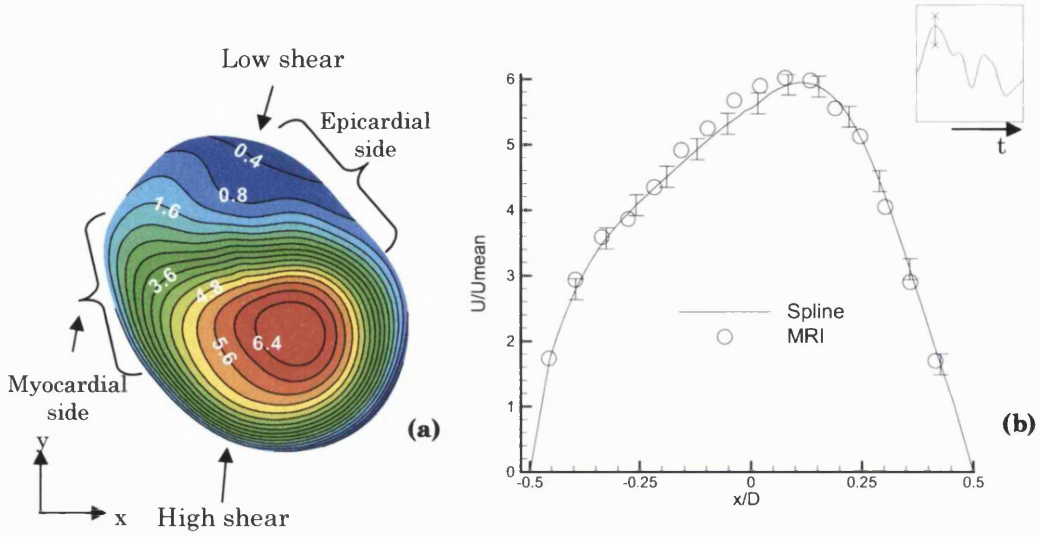

Figure 5.12 (a) Spline modelled MRI axial velocity contour plot extracted just distal to the toe of a distal end-to-side coronary artery anastomosis model at approximately peak flow. (b) Comparison of the corresponding MRI measured (symbols) and cubic spline modelled (line) normalised axial velocity y-centreline profiles. Error bars on the spline fit curve correspond to ±5 % of the mean axial velocity. Spline profile has been linearly extrapolated to the wall.

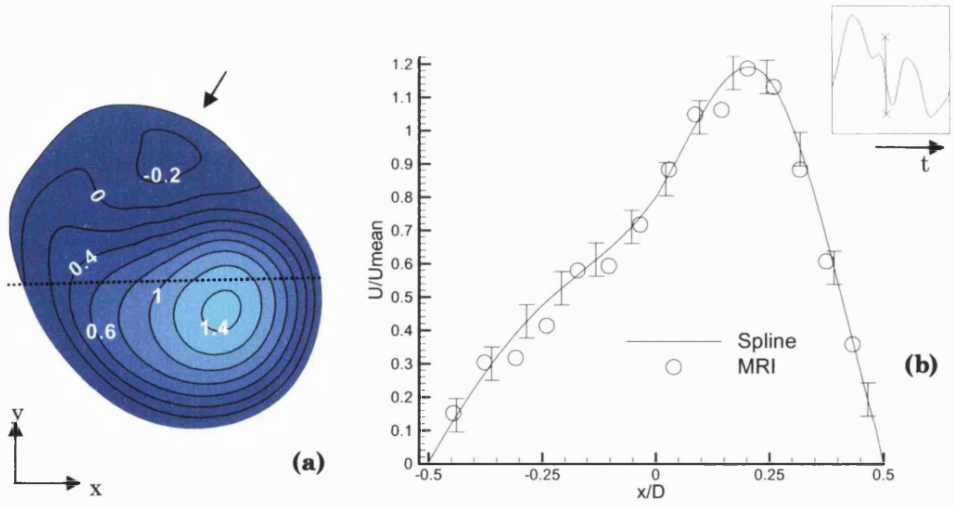

Figure 5.13 (a) Spline modelled MRI axial velocity contour plot extracted just distal to the toe of the distal end-to-side coronary artery anastomosis model at late deceleration. Note the significant flow separation region (arrow). (b) Comparison of the corresponding MRI measured (symbols) and cubic spline modelled (line) normalised axial velocity y-centreline profiles. Error bars on the spline fit curve correspond to ±5 % of the mean axial velocity.

Wall shear stress

The spline data modelling technique introduced in Chapter 4 can be applied to support the investigation of the complex flow regimes encountered in certain locations of the arterial system such as bends, bifurcations as well as in the perianastomotic region of surgically revascularised arteries. However, applying the proposed technique to estimate wall shear stress from data acquired *in vivo,* may be problematic. This is primarily due to the sensitivity of the wall shear rate to the accuracy by which the vessel-lumen boundary can be determined. This is less of a problem *in vitro*, as by careful selection of the wall material and the fluid magnetisation relaxation rates, a high contrast to noise ratio between the lumen and the wall, even at high spatial resolutions, can be achieved. Moreover, MR velocity measurements acquired *in vivo* are exposed to additional sources of error, due to patient or vessel motion and are typically obtained at lower spatio temporal resolutions compared to *in vitro* acquisitions, mainly due to limited subject tolerance.

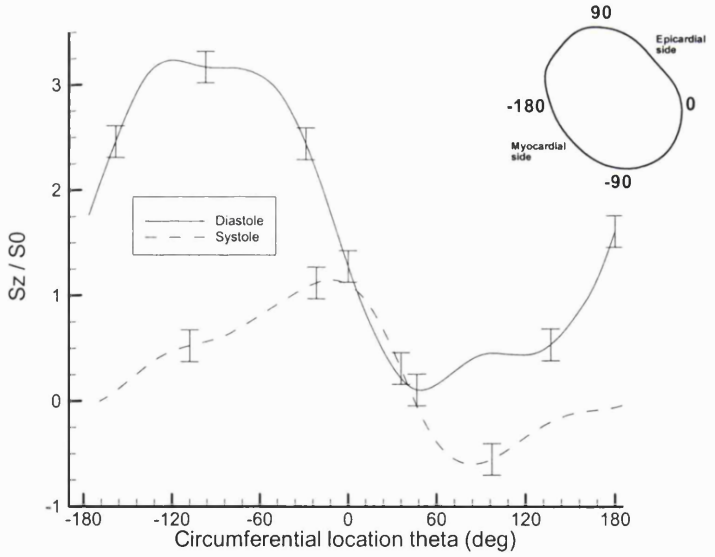

Figure 5.14 The temporal variation of the normalised circumferential axial wall shear stress distribution estimated from the MRI phase spline model data at late decceleration (dotted line) and at approximately peak flow (solid line). Shear stress is normalised by the mean inlet wall shear stress. Error bars correspond to ± 15 % of the mean inlet wall shear stress and indicate the upper and lower limits of the estimates based on the uncertainty in the location of the wall within the boundary pixel.

From the spline modelled MRI axial velocity data, the velocity gradient at the boundary of the approximation domain and an initial estimate of the axial wall shear stress was calculated. Upper and lower limits of this initial wall shear stress estimate were calculated by radially contracting and expanding respectively the boundary of the approximation domain by a distance equal to half the pixel width. Estimates of the normalised circumferential wall shear stress distribution for the peak flow and late deceleration phases of the cycle, with error bars denoting the upper and lower estimate limits, are shown in Figure 5.14. At peak flow and in the region between -60 and -140 degrees (myocardial wall), there is an approximately five-fold increase on average in axial wall shear stress as compared to the corresponding values during late deceleration. There is also, during late deceleration, a wall region (40<theta<180) with negative axial wall shear associated with axial flow separation.

To obtain an estimate of wall shear stress, the gradient of the velocity vector at the wall is calculated. For this, the exact wall location, the wall shear rate magnitude and direction and, the wall surface normal are required. However, knowledge of the vessel surface normal is not necessary if it is assumed that it lies approximately perpendicular to the slice plane normal. For the results reported in this section it was also assumed that the magnitude of the in-plane velocity components gradients at the wall is small compared to that of the axial velocity gradient and that there is a sufficiently high pixel intensity gradient across the edge of the boundary pixel to allow an accurate definition of the single pixel vessel wall boundary.

5.2 *Femoro-tibial bypass graft model*

Peripheral arterial disease

Peripheral arterial disease refers to disease processes obstructing blood flow in arteries other than those in the coronary and the cerebral circulation. Lumen narrowing results from atherosclerotic lesions or from thrombus formation due to underlying atherosclerosis. The focus of this investigation is disease within arteries of the lower leg. During the initial stages of the disease, patients suffer from intermittent pain in the muscles of the legs during exercise (intermittent claudication). As the disease progresses, ischemic tissue develops ulceration and gangrene which will eventually re-

quire major amputation in one third of all cases. Diagnosis of the disease currently relies on contrast arteriography which remains the gold standard. However, contrast enhanced magnetic resonance peripheral angiography is being increasingly used with promising results and may gradually replace contrast arteriography. Duplex ultrasound has also been used to detect patency of single arterial segments or bypass grafts.

Surgical revascularisation is the treatment of choice for patients with critical limb ischemia. Patency rates are quite satisfactory: 70-80 % at 5 years for bypass grafts to arteries even below knee when an un-diseased autologous vein graft of sufficient calibre is used. However, approximately 10 % of these surgical interventions fail and have to be repeated within the first year following surgery. Furthermore patency rates fall with a reduction in the calibre of the distal host vessel. Endovascular interventions are also used to treat limb arterial occlusive disease but with the long term patency of treated vessels remaining inferior to surgical revascularisation.

It should be noted that arterial stenosis resulting from atherosclerotic lesions is typically a long scale process that requires years to cause blockage. Often collateral circulation develops distal to stenotic lesions that can maintain blood flow, at least during rest, even at low perfusion pressures. Furthermore, by the process of autoregulation peripheral vascular resistance may be reduced and blood supply maintained distal to vascular stenosis. A good review of peripheral arterial disease is given by Ouriel (2000).

Patient Clinical Information

The subject of this investigation was an 88-year-old male. The graft was placed proximally at the superficial femoral artery with a side-to-end configuration. The distal anastomosis had an end-to-side configuration and was located at the distal section of the posterior tibial artery (Figure 5.15, Figure 5.16). An autologus reversed saphenous vein was used as the graft vessel. The graft diameter in the vicinity of the distal anastomosis was approximately 4 mm. The MRI measurement to extract the geometry of the distal anastomosis was conducted six days after surgery. Velocity measurements from the graft, the distal and, the proximal host vessels in the vicinity

of the anastomotic junction were also obtained by pulsed Doppler velocimetry on the day of the MRI acquisition. Although velocity measurements could have been acquired by MRI phase velocity mapping, practical limitations prevented this.

X-ray angiograms of the lower extremities, acquired prior to surgery, are shown in Figure 5.16. Although the flow in both legs appears compromised below the upper thigh (see arrows), only the flow problems in the right leg were surgically treated as the patient reported pain on the left leg only.

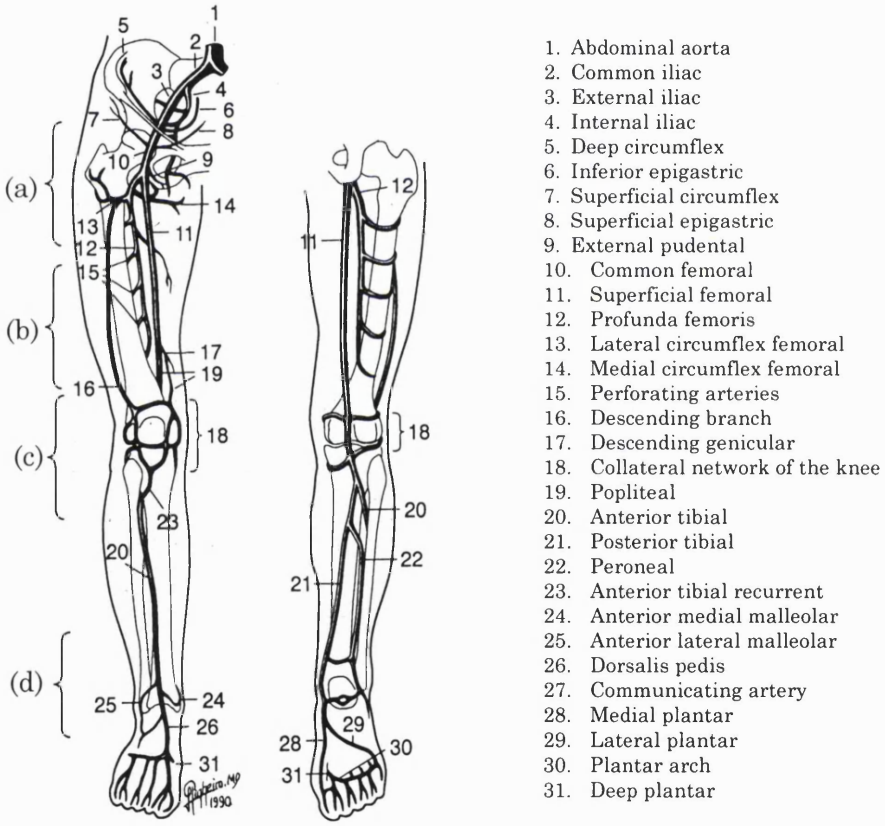

Figure 5.15 Schematic of the arterial anatomy of the lower extremities (Pinheiro, 1991). Regions (a-d) correspond to the approximate range of the respective planar angiograms shown in Figure 5.16.

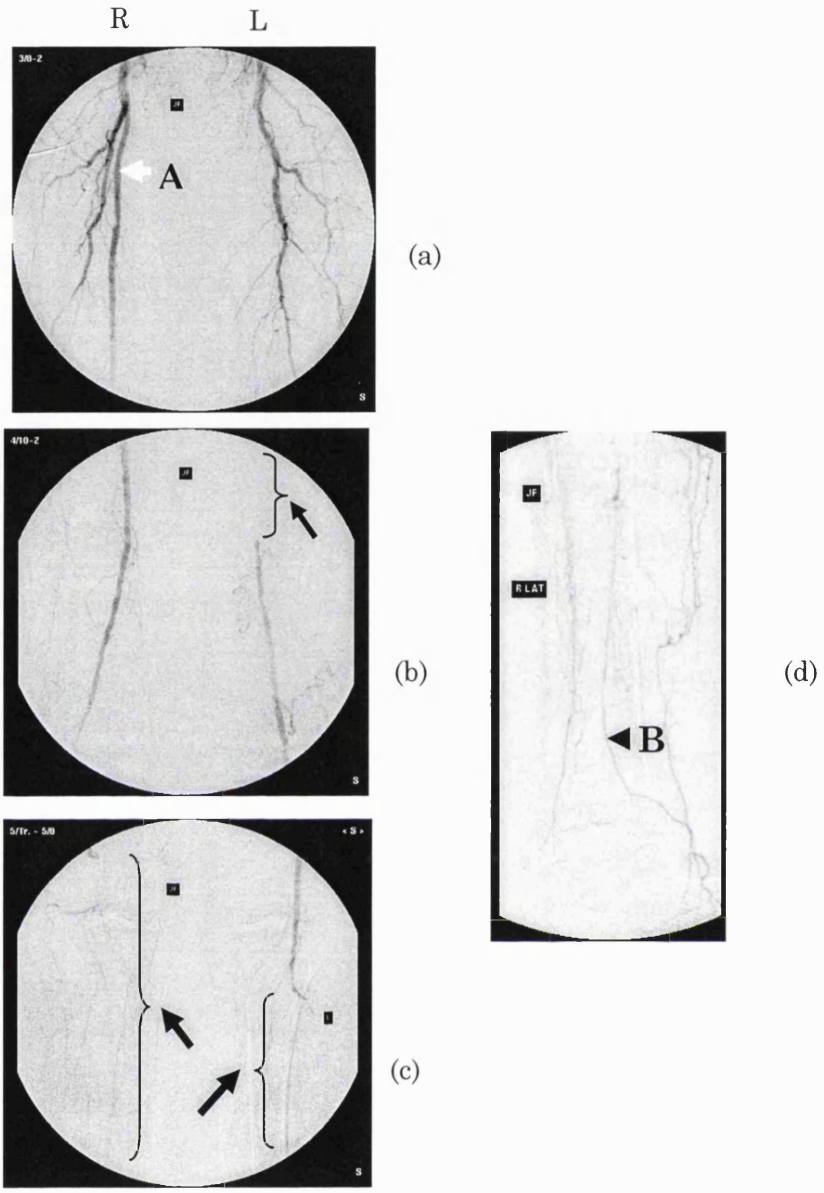

Figure 5.16 Pre-surgery planar angiograms of the lower extremity showing the arterial network of the upper thigh (a), the lower thigh (b), the knee joint (c), and at the lower calf of the right leg (d) as marked in Figure 5.15. Arrows indicate sites of compromised blood flow. The approximate locations of the proximal and distal anastomosis are indicated by letters A and B respectively.

5.2.1 Methods

5.2.1.1 Geometry measurements

Measurements were performed on a General Electric (GE) 1.5 T MRI whole body scanner at St' Mary's Hospital.

A three-dimensional time of flight gradient echo sequence was used to image the distal bypass graft anastomosis *in vivo*. A 1 mm through plane resolution and a 0.23

mm (interpolated at reconstruction from 0.46 mm) in-plane resolution was achieved during a 15 min acquisition. The MRI images were processed using the methods described in 5.1.1.2 and the lumen surface was reconstructed. This information was then used to fabricate a scaled up by a factor of 2 solid stereolithographic replica applying the methods described in 5.1.1.3 from which a silicone negative model was produced for use in the MRI flow study. A comparison of the surface representation and the stereolithographic replica is shown in Figure 5.17.

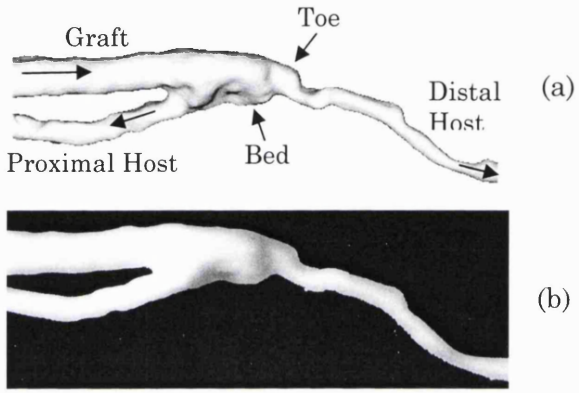

Figure 5.17 Surface representation (a) and solid stereolithographic replica (b) of a femorotibial distal end-to-side anastomosis extracted *in vivo* by MR angiography.

5.2.1.2 Flow measurements

Graft inlet flow conditions

The flow conditions specified at the graft inlet were based on measurements of the velocity waveform *in vivo* acquired by Dr. Mark Jackson at St' Mary's hospital using pulsed wave Doppler velocimetry. In brief, the technique utilises the Doppler principle which states that a wave transmitted by a stationary source and reflected by a moving target will undergo a frequency shift which is proportional to the velocity of the target. In blood flow measurement applications a sound wave is transmitted by the ultrasound transducer at an incident frequency (f_1) typically between 4 and 12 Mhz and at an insonation angle (θ) (i.e. the angle between the sound wave and the blood velocity vector). This wave is reflected by the red blood cells and received by the ultrasound transducer. The blood velocity (u) is then calculated by the following equation:

$$u = \frac{f_D c}{2 f_1 \cos\theta}, \tag{5.5}$$

where f_D is the Doppler frequency shift of the reflected wave and c is the speed of sound in the medium which is approximately 1540 m/s for tissue and blood. In the pulsed Doppler modality ultrasound bursts are transmitted periodically at a frequency termed the pulse repetition frequency. By transmitting bursts of ultrasound, waiting for a precise amount of time and then monitoring the reflected waves received, it is possible to calculate the depth at which the incident waves were reflected by the moving target. Pulsed Doppler thus allows a sampling volume (or gate) to be positioned in a vessel visualized on the grey-scale image, and displays a spectrum, of the full range of blood velocities within the gate plotted as a function of time. If the sampling volume spans across the interrogated vessel diameter the mean measured blood velocity can be used as an estimate of the mean vessel cross sectional velocity.

The frequency content of the pulsed Doppler velocity measurements was obtained by Fourier analysis of the sampled waveform. The power spectrum of the signal is shown in Figure 5.18. The mean Doppler frequency shift calculated from the reflected ultrasound wave originating from the sample volume was used as an estimate of the instantaneous mean velocity in the graft that was used to calculate the various flow indices. The flow waveform in the main arteries of the lower extremities is typically triphasic in nature. Most of the flow occurs within a short period of steep flow acceleration driven by a strong favourable pressure gradient followed by a steep deceleration period. This phase is followed by a short phase of retrograde flow caused by an adverse pressure gradient and then by a low flow phase which occupies most of the cycle period. From the Doppler ultrasound velocity measurements in the graft, a mean velocity of 11.4 cm/s was calculated by temporal averaging of the spatial mean instantaneous velocities over sixteen cycles. The cycle frequency was approximately 1.25 Hz and the vessel diameter was approximately 4 mm. Therefore assuming a kinematic viscosity of blood equal to 3.5×10^{-6} m^2s^{-1}, the mean Reynolds number was 145 and the Womersley parameter was 3. The peak to mean velocity ratio of the waveform was approximately 10. However, due to practical limitations in the physical reproduction of the flow waveform, a slightly higher Womersley parameter of 4 and a mean Reynolds number of 135 where specified. The normalised flow rate (Q/Q_{mean}) varied between -0.6 and 10.

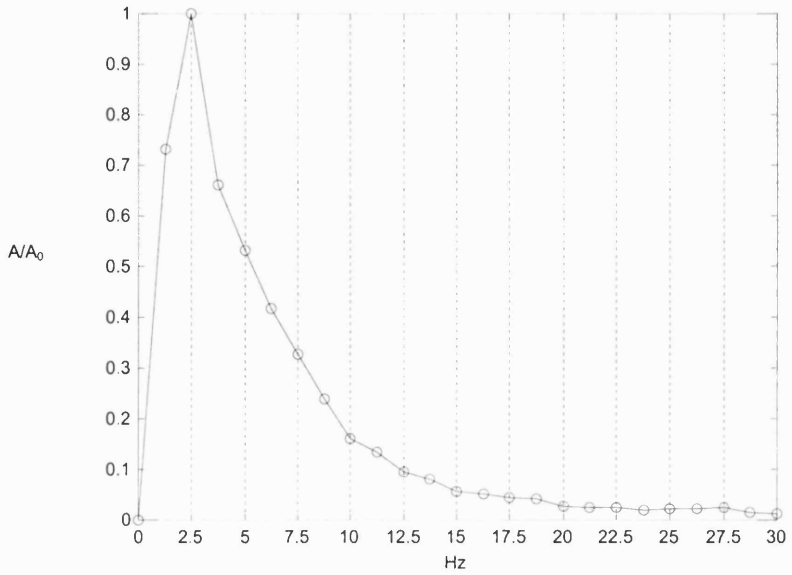

Figure 5.18 Power spectrum of the velocity waveform measured *in vivo* by pulsed Doppler velocimetry in the femoro-tibial bypass graft just proximal of the distal anastomosis. The sampling frequency was 100 Hz and the fundamental waveform frequency was 1.25 Hz. The power of the DC component has been subtracted from the data.

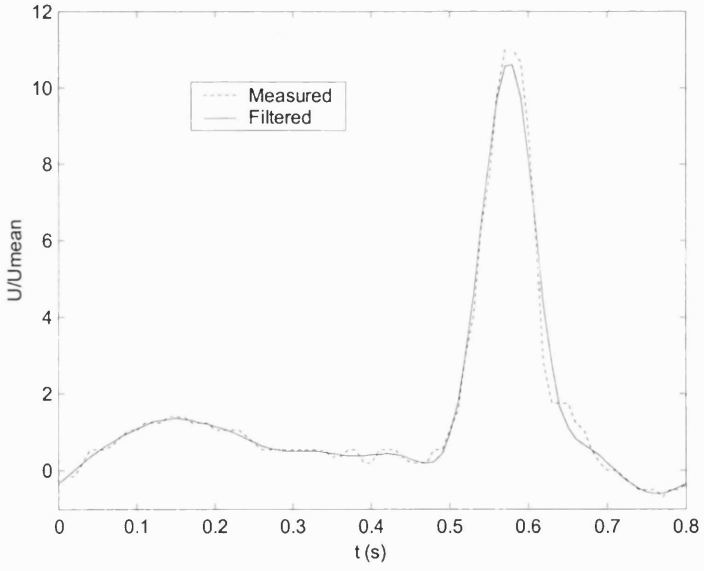

Figure 5.19 Measured (dotted line) and low pass filtered at a cut-off frequency of 11 Hz (solid line) velocity waveforms in the femoro-tibial bypass graft, normalised by the mean measured velocity.

Distal-proximal graft outflow division

Two flow regimes are investigated in the physical model fabricated based on the *in vivo* extracted femoro-tibial distal anastomosis geometry (Figure 5.20). In the first regime the proximal host artery was occluded yielding a 100:0 distal-proximal graft outflow division (DPGOD). In the second flow regime the proximal vessel was assumed patent, yielding a 60:40 DPGOD. The latter flow regime was based on the results of the Doppler velocity measurements acquired on the same day of the MR angiography and two weeks after bypass surgery. Color Doppler velocity measurements in the vicinity of the anastomotic junction indicated retrograde flow in the proximal host section during the major part of the flow cycle. This flow behaviour is due to the comparable flow resistance in the distal and proximal host artery flow conduits. As a result part of the blood flow in the graft travels upstream in the proximal host artery and is channelled through its branches, while the residual blood flow travels downstream in the distal host section. To replicate this flow regime in the physical model of the anastomosis used in the MR flow study, a tube with variable flow resistance was used to connect the proximal host with the extended outlet of the distal host section. The flow resistance was adjusted to create the desired graft outflow division between the distal and the proximal host vessels.

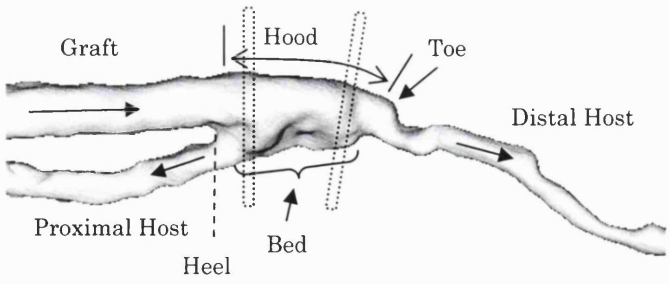

Figure 5.20 Surface representation of a femoro-tibial distal end-to-side anastomosis extracted *in vivo* by MR angiography. Dotted line rectangles indicate boundaries of slices excited for the MRI velocity measurements in the scaled silicone model of the geometry. Arrows indicate the temporal mean bulk flow direction and landmarks of the anastomosis.

A comparison of the cyclic variation in the MRI measured mean velocity extracted at a location just proximal to the toe of the anastomosis obtained with an 100:0 and a 60:40 distal to proximal graft outflow division is shown in Figure 5.21. It should

be note that the exact location of the toe in this complex flow bypass graft anastomosis is somewhat ambiguous. A site along the hood where a sharp change in surface curvature occurs was selected to represent the toe of the anastomosis. In contrast, the heel of the anastomosis can be unambiguously determined (Figure 5.20). Compared to the prescribed waveform shown in Figure 5.19, there is an apparent reduction in the peak to mean flow ratio by a factor of nearly two in the measured flow waveform. This difference was due to limitations associated with the physical reproduction of the flow waveform by the computer controlled flow pump, in combination with attenuation of the pressure wave in the tubes connecting the model to the pump. There is also a clear notch in the velocity waveform during the mid deceleration (t/T=0.5) phase of the cycle. This distortion is most likely the result of pressure wave reflections in the flow system.

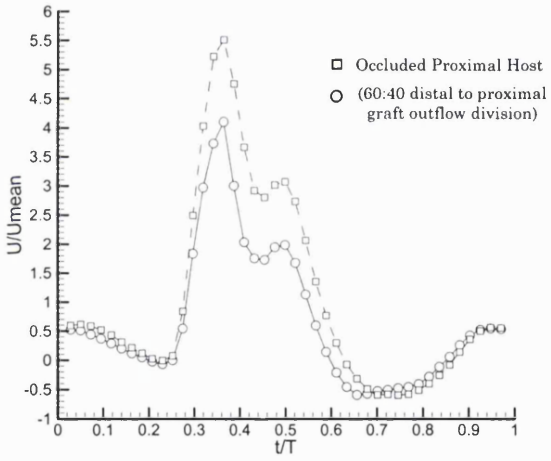

Figure 5.21 Velocity waveforms just proximal to the toe of the physiological femoro-tibial anastomosis model with an occluded proximal host vessel (squares) and a patent proximal host vessel (circles) yielding a 60:40 graft outflow division between the distal and the proximal host vessels. Waveforms are reconstructed from the temporal evolution of the mean velocity calculated from the lumen pixels in the phase velocity images.

Care was taken to ensure that the waveform was not under sampled. The sampling frequency was 18 Hz which was double that required by the Nyquist criterion (9 Hz). The frequency of the highest (9^{th}) harmonic included in the prescribed waveform was 4.5 Hz as a fundamental cycle frequency 0.55 Hz was selected. This was also experimentally verified by doubling the sampling rate and repeating the measurements. A comparison of the reconstructed flow waveforms measured with the two sampling

rates is shown in Figure 5.22. The small difference between the two waveforms suggests that the sampling rate of the original measurement was, as predicted, more than adequate.

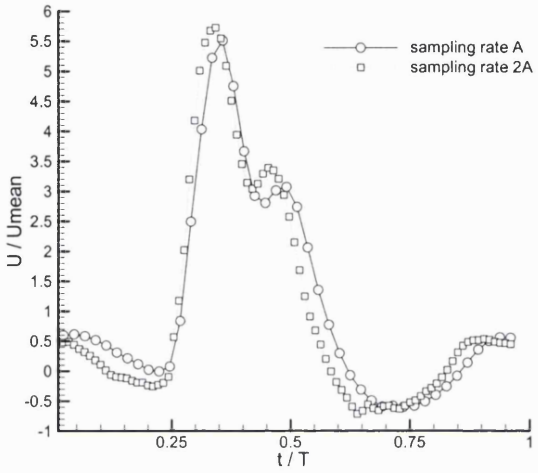

Figure 5.22 Velocity waveforms just proximal to the toe of the physiological femoro-tibial anastomosis model with an occluded proximal host vessel extracted from phase-velocity images acquired with two (squares) and four (circles) views per segment. Waveforms are reconstructed from the temporal evolution of the mean velocity calculated from the lumen pixels in the phase velocity images.

5.2.2 Results and Discussion

MRI velocity measurements were obtained in the anastomotic junction at approximately ½ D proximal to the toe and ½ D distal to the heel (Figure 5.20), with a physiological flow waveform shown in Figure 5.19 prescribed at the graft inlet. A series of axial velocity contour plots are shown in Figure 5.23 obtained at eight points in the flow cycle with the proximal host vessel occluded. There are several noteworthy points about the flow field dynamics. During mid systolic acceleration, as the instantaneous Reynolds number increases, the velocity crescent moves away from the bed and towards the hood wall of the anastomosis. The mushroom shaped pattern in the velocity contours is typically associated with entrance flows in curved vessels or Dean-type flows (Dean 1928). This pattern in the velocity field is somewhat unexpected as the graft provides a fairly straight flow conduit with very mild curvature primarily concentrated in the anastomotic sinus. However, the results show that above a certain Reynolds number the effects, even of this mild curvature, on the shape of the velocity

distribution are significant. An in plane pressure gradient accommodates the bulk change in direction of motion of the fluid particles in the graft as they negotiate the locally sharp curvature of the hood wall in the vicinity of the toe. This pressure gradient establishes a secondary in plane motion responsible for the redistribution of the velocities in the cross section. The pattern of this in plane motion is illustrated by the velocity vector map at peak flow shown in Figure 5.23i where two counter rotating vortices can be identified. As the magnitude of the pressure pulse generated by the contraction of the left heart ventricle is reduced, the adverse pressure gradient established decelerates the flow. This adverse pressure gradient will also cause low inertia fluid particles in the near wall region of the boundary layer to separate from the main stream. Separated fluid particles form a region of recirculating flow which is sustained by the shear forces acting on its boundary with the main flow stream. Kinetic energy is highly dissipated in the recirculation region by the dominant viscous forces. The size of the separation region grows as the instantaneous Reynolds number decreases during flow deceleration. Eventually as the adverse pressure gradient persists, the direction of the main stream reverses with high retrograde velocities emerge on the toe wall and forward moving fluid particles on the bed wall.

The femoro-tibial anastomosis investigated has several hemodynamically interesting geometric features. There is an extended hood, associated with the low anastomosis angle, and a large graft to host vessel calibre ratio. It has been shown (Crawshaw et al., 1980) that low anastomosis angles (<15 degrees) create a hemodynamic environment that is less favourable to the development of wall disease compared to acute anastomotic angles (>45 degrees). The hood length was also shown (White et al., 1993) to influence the flow behaviour in the sinus of the anastomosis with a longer hood length favouring flow separation along the distal end of the hood. The hood length is primarily determined by the anastomosis angle and the graft to host vessel calibre ratio. It should be noted that if the proximal host vessel is occluded, the transition from the graft to the distal host facilitated by the anastomotic sinus resembles fluid mechanically a flow contraction in a single vessel. Figure 5.24 shows axial velocity contours extracted at ½ D proximal to the toe with a 60:40 flow division ratio between distal and proximal host vessels. The results illustrate the strong influence of the flow division on the perianastomotic flow field. During early acceleration (Figure

5.24a) although the mean velocity is lower than for the corresponding phase in the 100:0 flow division regime (Figure 5.23a), the velocity distribution is fairly uniform in both cases suggesting the absence of significant cross flow. However, as the flow accelerates further, the Reynolds number is increased and certain differentiating flow features between the two flow regimes are established. For the 60:40 flow division ratio case, axial boundary layer separation occurs first on the toe wall during flow acceleration (Figure 5.24b) and is stronger and more spatially extensive throughout the cycle as compared to the occluded proximal host case. As the flow decelerates, the separation region gradually migrates clockwise towards the bed wall. This motion is reversed during bulk flow reversal and the separation region returns to the lateral toe wall. The velocity distribution shown in Figure 5.24c exhibits a combination of strong and spatially extensive flow separation and strong forward flow, resulting in elevated shear exposure of particles at the boundaries between the forward main flow stream and the separation region.

A sagital cross section of the steady flow (Re=400) velocity field of the anastomotic junction for the 60:40 and 100:0 graft outflow division cases is shown in Figure 5.25. Cross flow streamlines show the extent of the separation region in the 60:40 outflow regime. Extensive axial separation occurs both along the hood but also along the bed wall. Separation and reattachment points can be identified in these results. Axial flow separation along the hood develops as a result of a local adverse pressure gradient that decelerates the graft flow as it enters the anastomosis junction. This adverse pressure gradient is set-up to facilitate the change in the direction of fluid particles that enter the proximal host artery. In the vicinity of the distal host artery a strong, favourable pressure gradient is also present. This is required by the law of preservation of energy to balance the gain in the kinetic energy of the system as the flow enters the reduced cross section conduit of the distal host artery. Although this favourable pressure gradient stabilises the flow field in the vicinity of the toe, its effects are local and fails to counteract the destabilising effects of the non physiological flow regime created by the presence of retrograde flow in the patent proximal host artery. Although no separation occurs along the hood when the proximal host is occluded, flow along the bed appears slow or stagnant and reverses close to the heel.

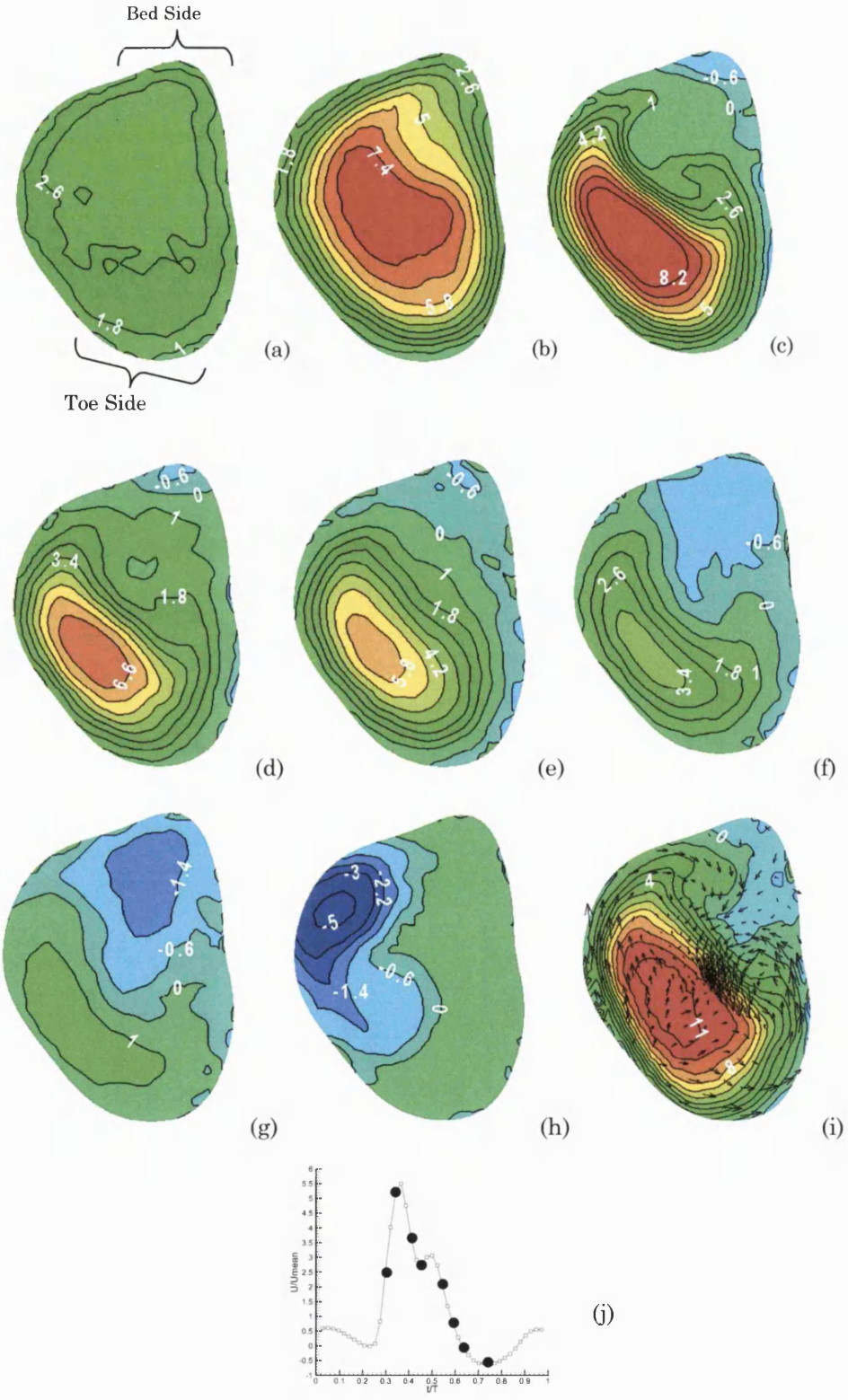

Figure 5.23 Axial velocity contour plots extracted at approximately one graft diameter proximal to the toe of the physiological femoro-tibial anastomosis model with a fully occluded proximal host vessel (100:0 DPGOD) at eight points in the cycle. An *in vivo* pulsed Doppler measured flow waveform was prescribed at the inlet of the graft. Panels a-h correspond to increasing time phases in the cycle indicated (solid circles) in panel (j). Axial velocity contours at peak flow with in plane vectors superimposed are shown in panel (i).

To identify the primary features of the complex steady flow field in the distal anastomotic junction, measurements of the steady cross sectional velocity field were also obtained at approximately ½ D distal to the heel (Figure 5.26) and ½ D proximal to the toe (Figure 5.27). The spline modelled results reveal the complexity of the flow field that can develop in the distal anastomosis of a surgically revascularized artery.

The cross flow streamlines at ½ D distal to the heel (Figure 5.27) reveal the critical points for each flow regime. As discussed previously, critical points occur at locations where the magnitude of the cross flow vector disappears and are points characterised from cross flow streamline convergence or divergence thus termed sinks or sources respectively. In the occluded proximal host flow field, a sink or vortex core is located at the upper part of the lumen and a source point at the lower. In the patent proximal host flow field, two sinks associated with two counter rotating vortices are established at the upper part and a source point can be identified at the lower part of the cross section. It should be noted that sinks are spatially associated with regions of elevated vorticity.

The lateral extent of flow separation can be assessed from the axial cross sections of the velocity field. At ½ D proximal to the toe (Figure 5.27), extensive separation occurs on both the toe and the bed wall in the 60:40 DPGOD case. At ½ D distal to the heel (Figure 5.26), flow separation occurs in both graft outflow division regimes. However it is stronger and more spatially extensive in the patent proximal host artery case.

Although the flow field in the distal host artery was of interest, it was very difficult to accurately measure by MRI even under the controlled conditions of a model study. The combination of a small lumen diameter and a highly tortuous vessel path generated flow conditions that introduced severe spatial displacement, intravoxel phase dispersion and phase averaging errors in flow measurements obtained with the imaging protocol used to acquire the velocity field in the anastomotic sinus. Although such errors could be significantly reduced by using a very fast (low TE) phase velocity mapping technique, an implementation of such a technique was not available on the MRI scanners used.

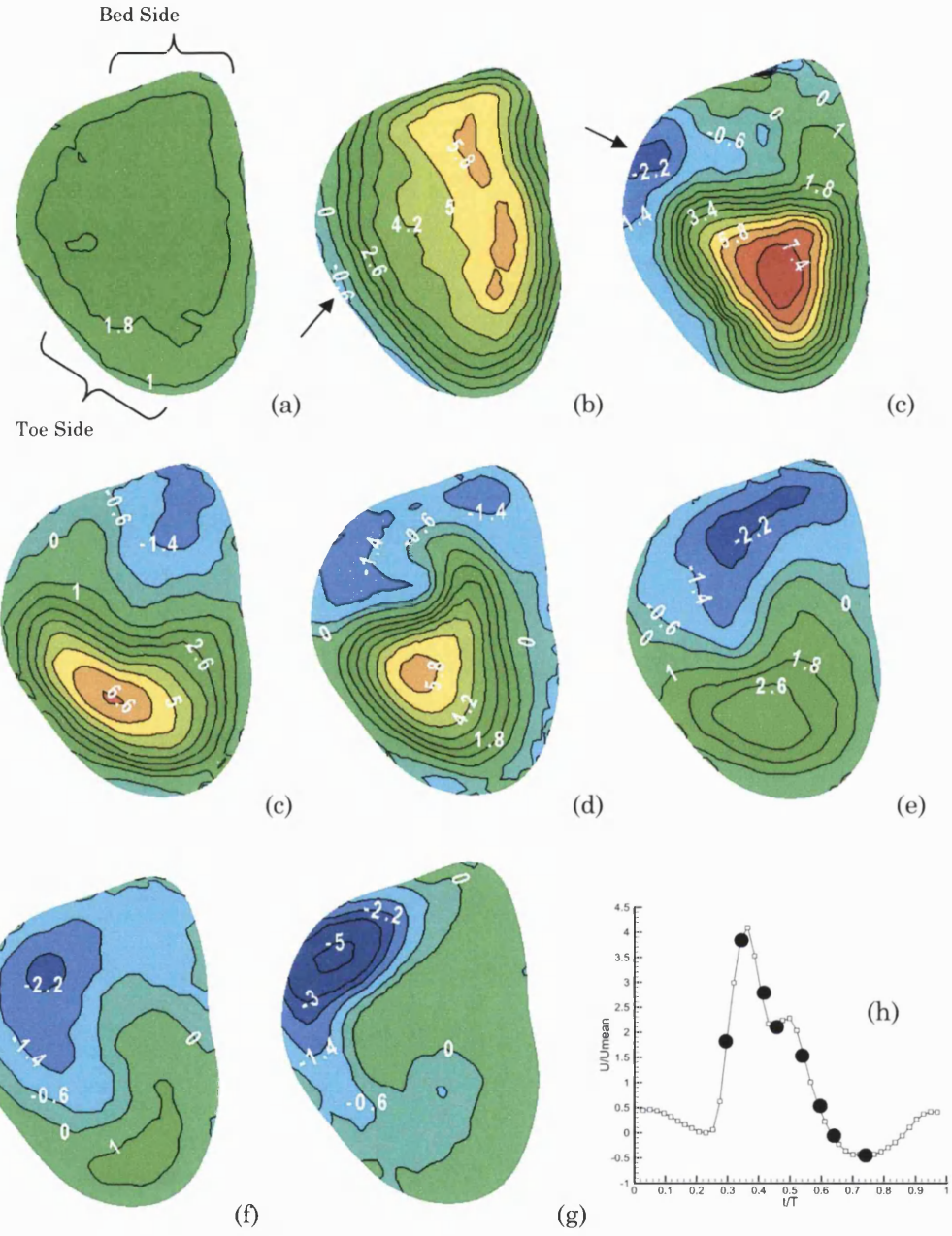

Figure 5.24 Axial velocity contour plots extracted at approximately one graft diameter proximal to the toe of the physiological femoro-tibial anastomosis model with a partly occluded proximal host vessel (60:40 DPGOD) at eight points in the cycle. An *in vivo* pulsed Doppler measured flow waveform was prescribed at graft inlet. Figures a-g correspond to the increasing time phases indicated (solid circles) in panel (h). Arrows indicate regions of early axial flow separation.

These results suggest that the presence of the additional flow conduit provided by the proximal host artery accentuates flow field complexity and generates potentially more unfavourable hemodynamic flow conditions within the anastomotic junction. However, it should be noted that at the same time it is likely that this additional flow conduit may augment blood supply to the distal ischemic leg and may prolong the life of the graft by acting as an alternative blood supply pathway if blood flow in the distal host vessel becomes compromised by disease.

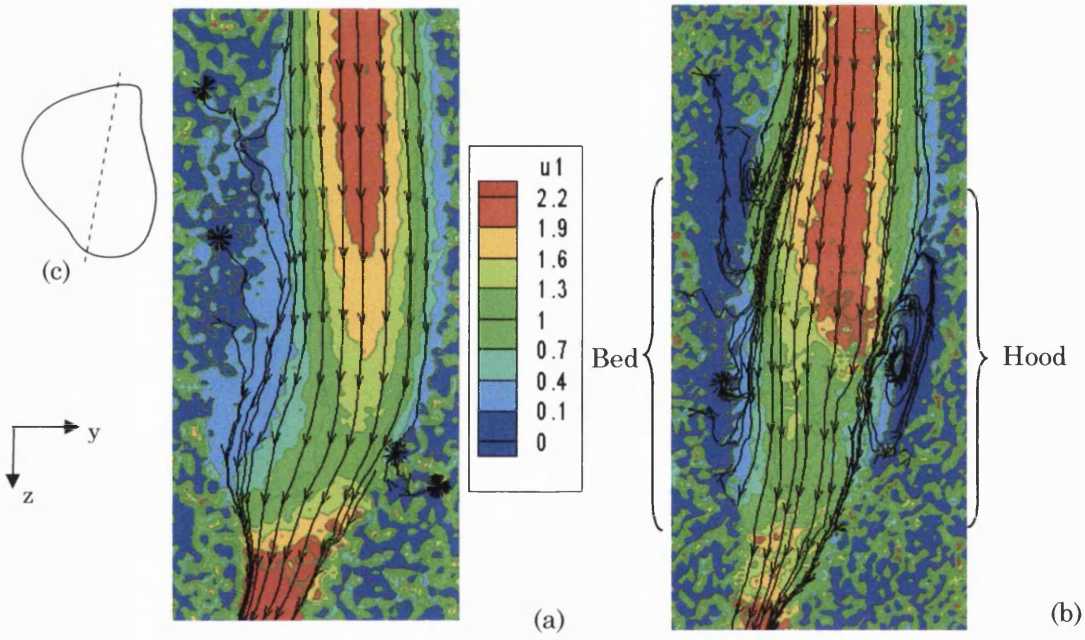

Figure 5.25 Oblique cross section of the physiological femoro-tibial anastomosis model. Steady flow (Re=400) axial velocity contours with cross flow streamlines superimposed for a 100:0 (a) and a 60:40 (b) distal-proximal host outflow division are shown. The location of the extracted plane (dashed line) with respect to the cross section of the model at ½ D proximal to the toe (solid line) is indicted in panel (c).

It should also be noted that in the patient studied, the proximal vessel was occluded at approximately halfway between the proximal and distal anastomoses. It augmented however the perfusion of the lower leg, by channelling through its branches, part of the blood flow supplied by the graft.

The strong influence of the proximal–distal host flow division ratio on the anastomotic junction flow field raises questions with respect to its clinical implications. Unfortunately these results can only provide some broad guideline as to what could be the effect on the *in vivo* perianastomotic hemodynamics from the flow division. A

study whereby the progress of the revascularisation is examined regularly after surgery in patients with various flow division ratios and where the development of disease is monitored is may assist in the identification of the preferable (if any) flow division ratio.

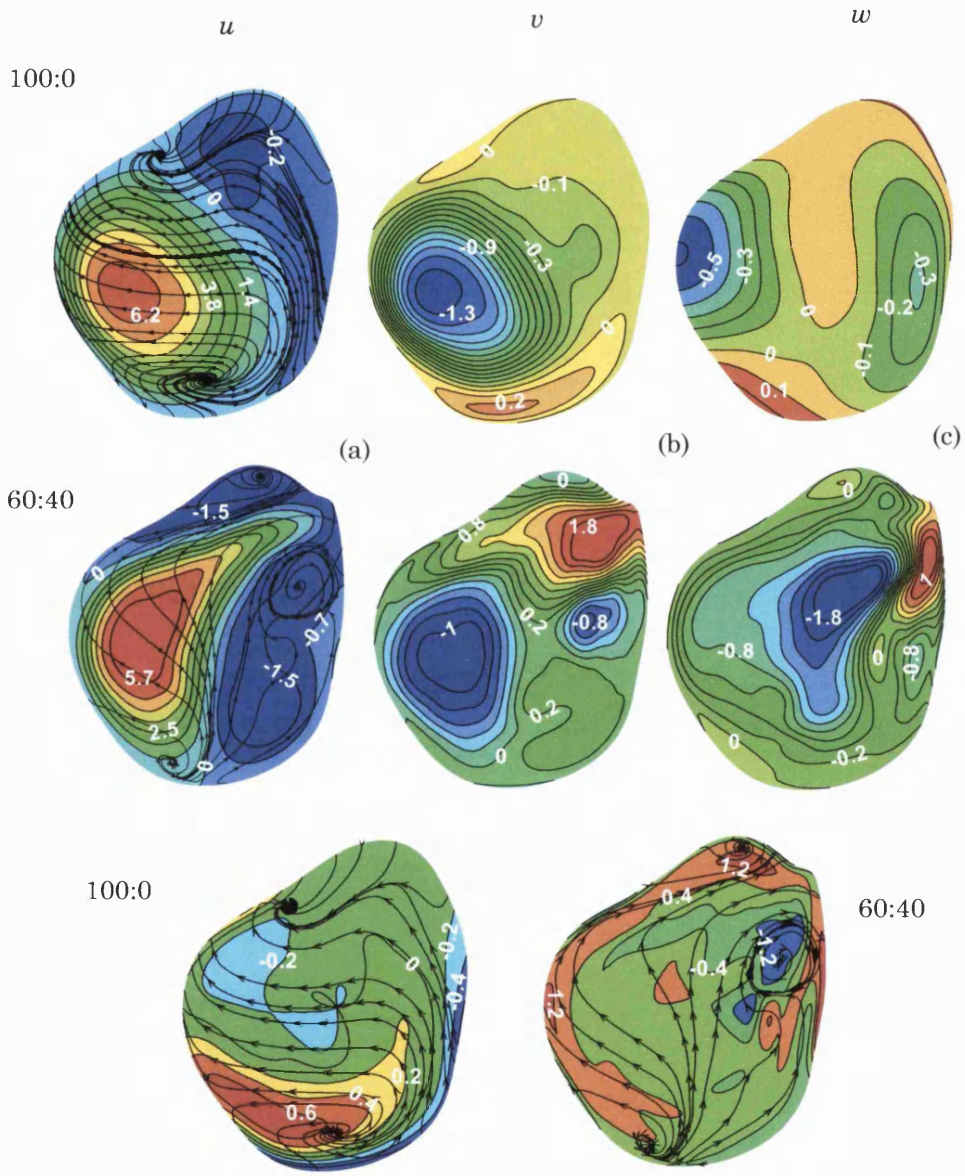

Figure 5.26 Spline modelled contour plot of axial u (a) and in plane v-horizontal (b) w-vertical (c) velocity components from MR data extracted just distal to the heel of the physiological femoro-tibial anastomosis model with an 100:0 (top) and a 60:40 (bottom) distal-proximal host outflow division in steady flow (Re=400). Cross flow streamlines superimposed for both outflow division cases. Also shown (bottom) are contours of axial vorticity with cross flow streamlines superimposed for both graft outflow division cases.

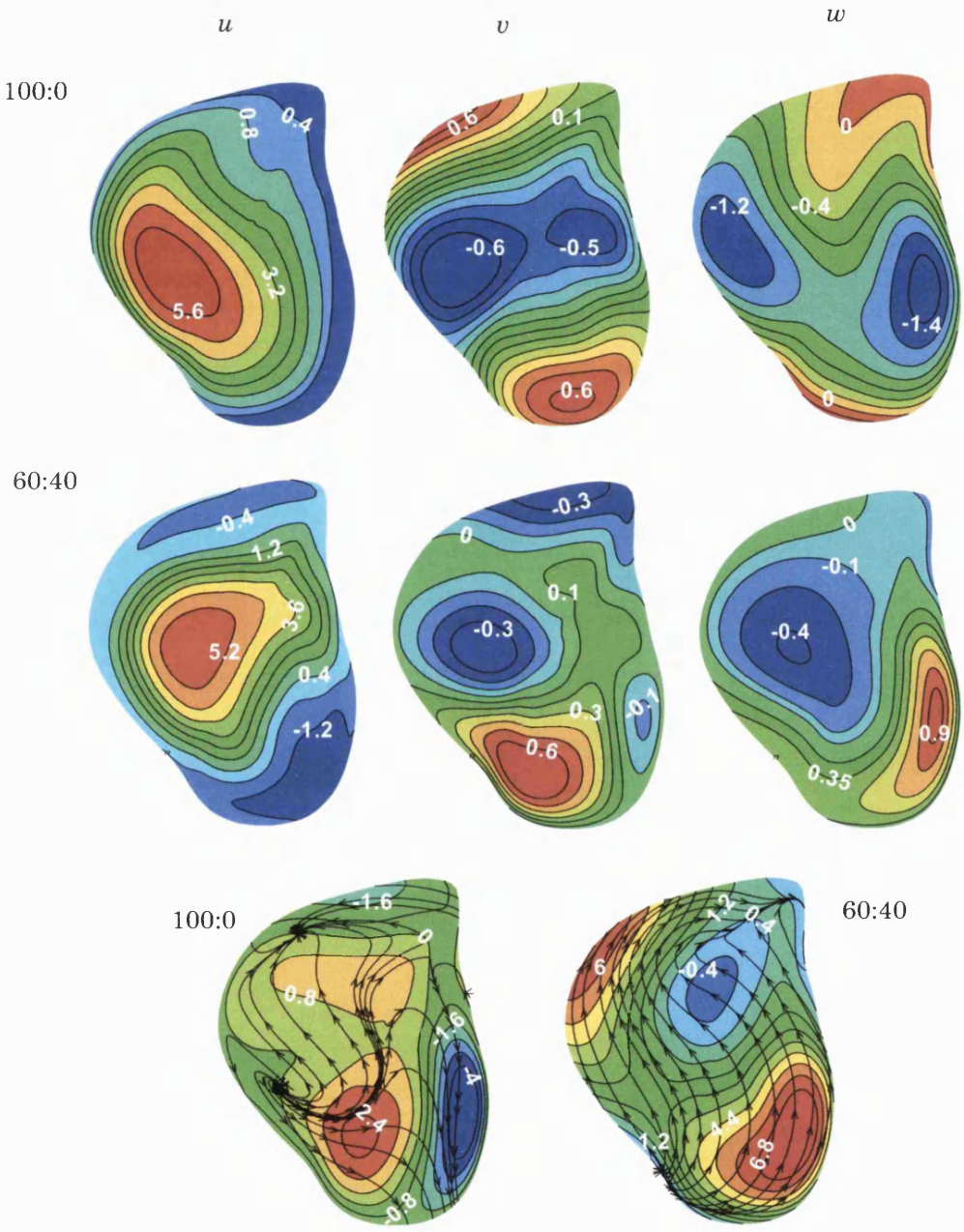

Figure 5.27 Spline modelled velocity vector from MR data extracted at ½ D proximal to the toe of the physiological femoro-tibial anastomosis model 100:0 (top) and a 60:40 (middle) distal-proximal graft outflow division in steady flow (Re=400). Also shown (bottom) are contours of axial vorticity with cross flow streamlines superimposed for both outflow division cases.

Chapter 6.

Conclusions and Further Work

This thesis elucidates the role of geometry and local hemodynamics in the development of wall disease in arterial bypass grafts. The detail distal anastomotic flow field was assessed, primarily, by magnetic resonance imaging. The application of numerical computations to predict the flow in bypass grafts was also examined.

Chapter 1 described the physiological problems and the motivation for this work, i.e. to use MRI to investigate the flow field in bypass grafts.

A key aspect of the use of MRI as a flow measurement device is its accuracy. Previous work has not systematically considered accuracy in complex flow fields as those expected to be found within *in vivo* geometries. Chapter 2 describes an investigation of the accuracy of MRI phase velocity encoded acquisitions for complex steady and time varying flow in idealised geometry models of distal end to side bypass graft anastomosis. Two measures were used to improve precision and reduce systematic errors: (i) a contrast agent was introduced to the circulating fluid and (ii) a low aliasing velocity was prescribed. A simple phase unwrapping technique was implemented to correct aliased velocities and improve the VNR of the measurement. Measurement error was estimated using results from numerical computations of the same flow as reference. The mean rms error found for MR velocity measurements of complex steady flows was 5.2 % of the mean inlet velocity, very close to the value of 5 % cited for well defined steady flows. Error was slightly higher near the toe of the planar anastomosis where cross flow was strongest. Wall shear stress estimates extracted by linear extrapolation from near wall MR velocity measurements consistently underestimated

the numerical predictions for the same flow. At the level of the toe and on the toe wall the numerically predicted near wall velocity profile was highly non-linear. In contrast the MR velocity profile was approximately linear. However the measurements suffered from severe localised signal loss at the level of the toe and on the toe wall primarily due to spin saturation (long residence times) and phase dispersion effects. Intravoxel phase averaging also contributed to the velocity profile shape mismatch at the toe. Consequently wall shear estimates calculated by the linear model were rather poor. Even under the controlled conditions of this model study, the mean error in the wall shear rate estimated by the linear method was 36 % with respect to the inlet wall shear rate. This error is expected to be significantly higher when this approach is applied to extract wall shear stress for MR velocity measurements acquired *in vivo*.

Two-dimensional phase-contrast MRI measurements of complex unsteady flows have also been assessed for accuracy together with procedures that can be used to improve measurement precision. The assessment used velocity measurements and accurate numerical solutions for a single harmonic sinusoidal flow in a rigid bypass graft model with a fully three-dimensional geometry. Comparisons of measured and numerically computed axial velocity profiles were made and instantaneous root mean square (rms) differences were calculated. Despite the complexity of the flow, with the aid of phase angle dynamic range extension, a spatially and temporally averaged rms error of between 7.8 % and 11.5 % with respect to the spatially and temporally averaged velocity was achieved. This result is close to the accuracy commonly cited for simple unsteady flow and it is concluded that with care, the method can be applied for measuring complex unsteady flows. Such flows are common around vessel bifurcations and in curved or tortuous vessels. Spin saturation primarily, and phase dispersion secondarily in complex transient recirculation zones were found to be significant contributors to overall error. Cross flow effects were also investigated but were of lesser significance. Limitations of the investigation are that it was performed using a rigid model and a single harmonic sinusoidal flow waveform. Therefore, the accuracy estimates presented may be considered as indicative of the upper limits of the procedure with reference to *in vivo* flow measurements.

The influence of out-of-plane curvature on the local distal anastomotic flow field was investigated in Chapter 3. The steady and time-varying flow fields in three idealised geometry bypass graft model configurations were examined experimentally by MRI and from the computational results. One planar and two non-planar model configurations, with thirty and ninety degrees of out-of-plane graft curvatures, were considered. The experimental results obtained in steady flow (Re=250) showed a rotation of the crescent shaped contours of the velocity field as the flow travels distally in the host artery section. This clockwise rotation of the 'velocity crescent' is indicative of a swirling or helical flow pattern imposed on the flow by the out-of-plane curvature of the graft. The significance of a helical flow pattern is that it may improve blood mixing and reduce residence times. Strong cross flow was found in the planar anastomosis model at the toe characterised by two symmetric counter rotating vortices. This vortical flow symmetry was broken by the introduction of out-of-plane graft curvature with the extent of flow assymetry dependent on the degree of out-of-plane graft curvature. Between the toe and five diameters downstream in the host vessel the rotation of the bulk velocity crescent was found to be approximately 90 degrees for the thirty degrees out-of-plane graft curvature and 180 degrees for the ninety degrees out-of-plane graft curvature. This result suggests that even a mild out-of-plane graft curvature angle can induce significant flow swirl downstream. Experimental results obtained with single harmonic unsteady flow showed separation on the toe wall during the deceleration phase of the cycle. The region of flow separation extended between the toe and two diameters downstream and was centred at one diameter distal to the toe where it was most spatially extensive. A reduction in the peak velocities of approximately 10 percent in the non-planar case as compared to the planar case was also found.

Results from numerical computations of the flow in the planar and the 90 degrees non-planar idealised end–to-side anastomosis models indicated a significant change in the spatial distribution of wall shear stress and a reduction of the time-averaged peak wall shear stress magnitude by 10 % in the non-planar model as compared to the planar configuration. The stagnation point oscillated in the single harmonic unsteady flow following a straight line path along the host artery bed of 0.8 diameters length in the planar configuration. By contrast in the non-planar case the

stagnation point oscillated about a centre that is located off the symmetry plane intersection with the host artery bed wall, and followed a parabolic path with a 0.7 diameter longitudinal and 0.5 diameter transverse excursion. The oscillatory shear index (OSI) has been defined previously as a measure of the unsteadiness in the direction of wall shear. However previous definitions failed to consider oscillations in shear stress of less than 90 degrees. Thus a new definition of OSI was introduced that varies between 0 and 0.5 and that accounts for a continuous range of wall shear stress vector angles. In both models, regions of elevated oscillatory shear were spatially associated with regions of separated or oscillating stagnation point flow. The mean oscillatory shear magnitude (considering sites were OSI>0.1) in the non-planar geometry was reduced by 22 % as compared to the planar configuration. These changes in the dynamic behaviour of the stagnation point and the oscillatory shear distribution introduced by out-of-plane graft curvature may influence the localisation of vessel wall sites exposed to physiologically unfavourable flow conditions.

A novel method to approximate MR phase velocity encoded data using spline functions was introduced in Chapter 4. The method generates a functional description of the two dimensional distribution of the MR measured velocity field that can be used to calculate flow indices such as vorticity and shear stress. The proposed method was applied to estimate the circumferential wall shear stress distribution from two dimensional MR velocity data obtained from measurements of both simple, well defined, and of complex steady flows. The technique was validated against theory for Poiseuille flow and against highly accurate numerical predictions for complex steady flow in an end-to-side anastomosis model. Accuracies of wall shear estimates of between 5 % and 15 % with respect to the mean wall shear rate were found for the proposed technique for steady well defined and for complex flows respectively. The accuracy of these estimates is superior to wall shear estimates obtained by the linear or quadratic extrapolation methods. With the proposed method no assumptions with respect to the shape of the velocity distribution are required. However the method was not fully automated and requires some degree of user intervention to achieve an optimum approximation of the underlying data. It was also found that the spline approximation was fairly sensitive to the selection of the parameter controlling the smoothness of the approxima-

tion. This problem however could be overcome by introducing additional constraints to the solution of this constraint optimisation problem.

A procedure whereby *in vivo* extracted arterial geometries can be transformed into physical and analytical models for experimental and numerical flow investigations is described in Chapter 5. MRI velocity field measurements were obtained in a realistic geometry models. The first model considered was fabricated via MR imaging of a cast of a porcine distal aorto-coronary (LAD) bypass graft anastomosis followed by CAD surface definition stereolithographic reproduction and creation of a silicone cast of its lumen using a dissolving wax. The measurement showed complex, swirling velocity fields to be present. In steady flow (Re=100) results at the toe of the anastomosis revealed a strong dominant vortex on the lateral myocardial wall and a weaker partly suppressed counter-rotating vortex on the lateral epicardial wall. The weaker vortex became more developed at one diameter downstream of the toe. A reduction of approximately a factor of five in the peak axial vorticity associated with the primary vortex between the toe and 1D distal to the toe was found. In time varying flow, wall shear stress on the myocardial wall calculated from spline modelled MR velocity measurements, was on average approximately five times higher during diastole than during systole. A region of negative axial wall shear associated with axial flow separation developed during systole on the lateral wall. The perianastomotic flow field was strongly influenced by the flow waveform prescribed at the graft inlet. Flow separation occurred on the epicardial wall during mid deceleration in the multi harmonic coronary waveform modulated flow field. In contrast there was no separation throughout the cycle in the sinusoidal flow case.

The second model considered was fabricated based on the geometric definition obtained by MR imaging of a femoro-tibial bypass graft *in vivo*. This model differed significantly from the aorto-coronary bypass model as it presented a severe graft artery area ratio mismatch resulting in an extended hood length and an enlarged anastomotic sinus. The recipient vessel was also highly tortuous and significant retrograde flow was measured in the proximal host section *in vivo*. The influence of the distal-proximal graft outflow division (DPGOD) on the perianastomotic flow field was investigated the femoro-tibial bypass graft model by considering the 60:40 and the 100:0 DPGOD cases. An extensive recirculation region along the hood and along the bed

wall, for steady flow (Re=400) and a 60:40 DPGOD, was found. Although no flow separation occurred along the hood when the proximal host was occluded (100:0 DPGOD), flow along the bed wall was very slow and reversed close to the heel. The axial vorticity distribution and the cross flow patterns in the anastomotic sinus were highly complex, especially when the proximal host was not occluded. In time–varying flow and for a 60:40 graft outflow division, separation first occurred during flow acceleration on the toe wall. During flow deceleration, the separation region gradually migrated clockwise towards the bed wall. During bulk flow reversal, peak retrograde velocities occurred near the lateral toe wall. In the 100:0 DPGOD case, flow separation first occurred during early deceleration on the bed wall. The footprint of the separation region expanded and contracted following the dynamics of the pressure wave but it did not migrate from the bed wall throughout the cycle. Overall flow separation was weaker and less spatially pronounced in the 100:0 DPGOD flow field as compared to the 60:40 DPGOD case.

General Discussion

A number of hemodynamic parameters have been identified to influence, to a larger or lesser extent, the development of vascular disease. It was confirmed that flow in the distal anastomosis of surgically revascularised arteries can be highly complex even at relatively low Reynolds numbers. Strong cross flow, axial flow separation, oscillating stagnation points and asymmetric shear stress distribution are some of the flow features identified in the anastomotic flow field. Changes in the peak to mean graft inlet Reynolds number, mean Reynolds number, Womersley parameter, graft outflow division ratio, or in the shape of the velocity profile injected in the distal anastomotic sinus were found to strongly influence the anastomotic flow field. It is therefore important to recognise the significance of these findings by considering the degree of change, at various time scales, of these hemodynamic parameters *in vivo*. Such changes occur due to the pathophysiological responses of the arterial wall to mechanical and chemical stimuli associated with the local flow environment and disease processes such as diabetes, heart disease or long-term hypertension. The time scale of these changes varies. Changes in blood pressure and flow can be continuous to meet

the physiological demands associated with the physical and psychological state of the individual. However, changes in the average flow conditions at rest occur over decades as part of the ageing process. Atherosclerosis is typically a long scale process that leads to intimal thickening and occurs over decades. Intimal thickening however can also occur over weeks or months in response to mechanical stimuli such as low mean and oscillating wall shear stress.

The surgical correction of an arterial occlusion typically introduces a non physiological flow environment. A vein becomes exposed to arterial flow with a mean transmural pressure of approximately 100mm Hg, when its wall structure has evolved to accommodate a mean pressure of approximately 10 mm Hg. Severe injury occurs in both the graft and the host artery along the suture lines at the graft artery anastomoses. The healing process triggered by these injuries and the resulting wound along the suture line, accentuate the graft artery compliance mismatch which has been suggested as implicated in the development of physiologically unfavourable hemodynamic conditions. In the distal anastomosis of arterial bypass grafts retrograde flow in the proximal host vessel, channelled distally through its branches, is commonly found during most of the flow cycle. This non physiological flow regime was shown to create highly unfavourable flow conditions in the anastomotic sinus. On the other hand if the proximal host is occluded in the vicinity of the distal anastomosis, flow conditions implicated with the development of vascular disease, such as very low mass flux and long residence times, will develop in the occluded artery. The host artery may also be stretched and become highly distorted at the anastomosis as a result of the forces applied by the surgically inserted graft. Furthermore, if a significant mismatch exists between the calibre of the graft and the recipient artery at the level of the anastomosis, a long incision in the host artery will be required to accommodate the larger circumference of the graft. This will tend to flatten the bed wall and locally distort the normal shape of the host artery lumen making it more elliptic, especially during the high pressure phase of the cardiac cycle. This calibre mismatch will also lead to a tapering of the graft near the anastomotic junction can be quite severe near the suture line. Although this reduction in cross sectional area has a stabilising effect on the flow it will also elevate wall shear stress at the mouth of the contraction in the vicinity of the suture line. If the product of shear stress and the corresponding shear exposure

time at the mouth of the contraction is above the threshold for shear-induced platelet activation, activated platelets convected downstream in the anastomotic sinus may adhere to the wall if trapped in regions of increased residence times (e.g. regions of flow recirculation). A contraction of the flow conduit may also occur at the toe of the distal anastomosis when a significant graft host artery calibre mismatch exists leading to a long hood and an enlarged anastomotic sinus.

Surgical interventions to relieve the symptoms of occlusive vascular disease significantly alter the hemodynamic conditions in the graft recipient vessel. The response of the endothelial cells to these changes will largely determine the outcome of the surgical revascularization. Endothelial cells may trigger a cascade of events leading to intimal hyperplasia and restenosis of the vessel lumen. A level of mean wall shear stress of approximately 15 dynes cm^{-2} has been proposed as the value that normal arteries strive to maintain (Zarins et al., 1988; Glagov et al., 1988; Giddens et al., 1990). This is achieved by changes in the arterial diameter through control of vascular tone and by wall remodelling. Low and oscillating shear stress have been linked to the development of wall disease. An inverse relationship between neointimal hyperplasia thickness and wall shear has been found (Friedman et al., 1981). However it is unclear below what level wall shear stress becomes detrimental to the health of the vessel wall and not simply a normal response to altered flow related mechanical stimuli. It is also unclear how sensitive the endothelial cell is to flow induced stimuli related to either absolute levels of shear stress or spatial and temporal gradients of shear stress and what the frequency response of the endothelial force sensor mechanism is. It is therefore still largely uncertain what constitutes a physiologically significant change in the hemodynamic parameters implicated in vascular wall disease. This information however is critical even from a flow measurement perspective as it will largely determine the minimum spatio-temporal resolution required to extract, *in vivo* or *in vitro,* hemodynamic features at physiologically relevant scales. If for example the higher frequency resolved by the endothelial cell is of the order of the flow cycle period, then temporal mean values of flow indices will be sufficient to convey most of the physiologically relevant information. In such case, the frequency response requirements for any measurement technique employed to extract a flow index such as wall shear stress *in vivo* may be relaxed.

The spatial scale of flow related effects on vascular wall biology is also important. If flow information is readily conveyed between cells through intercellular communication channels, then local flow disturbances may affect regions of the endothelial layer well beyond those directly exposed to these disturbances. The process of cell migration and proliferation triggered in response to flow induced stimuli over a longer time scale may also contribute to the spread of otherwise localised flow induced effects. This raises the question as to what level of spatial resolution is required to assess the physiological implications of the various flow induced forces affecting the arterial wall. Answers to such questions can be given by well controlled parametric studies of endothelial cell responses to flow related stimuli such as the recent study by White et al. (2001) on the effects of temporal and spatial gradients of shear on endothelial cell function in a flow expansion chamber lined with a cultured endothelial cell layer.

Suggestions for further work

The threshold based magnitude image segmentation technique employed to extract the single pixel boundary was rather simplistic and only works reasonably well for MRI magnitude images with a sharp vessel lumen edge. A more sophisticated segmentation method such as the level set method (Malladi and Sethian, 1995) to extract lumen boundaries at subpixel resolution would be more appropriate for magnitude images obtained *in vivo*.

The spline function MR velocity encoded phase approximation method proposed currently requires a certain degree of user intervention for an optimum solution to be achieved. The user criteria employed to select the optimum solution should be mathematically formulated and introduced as additional constraints in the constraint optimisation solution. By this a user-independent approximation routine that converges iteratively to an optimum solution could be achieved.

Further work is also required to assess the sensitivity of the local bypass grafts hemodynamics to the various geometric and flow pulsatility parameters implicated in the development of vascular disease. This effort could lead to the proposal of a prefer-

ential bypass grafts configuration that by design mitigates any adverse affects the hemodynamics can have on the vascular wall thus prolonging graft patency.

References

Altobelli SA, Nerem RM. An experimental study of coronary artery fluid mechanics. J Biomech. Eng., 1985; 107:16-23.

Andrew ER, Bottomley PA, Hinshaw WS, Holland GN, Moore WS, Siaroj C. NMR images by the multiple sensitive point method: application to larger biological specimens. Phys. Med. Biol., 1977; 22: 1971.

Asakura T, Karino T. Flow patterns and spatial distribution of atherosclerotic lesions in human coronary arteries. Circ. Res. 1990; 66: 1045-1066.

Axel L. Blood flow effects in magnetic resonance imaging. Am J Roentgenol, 1984; 143(6):1157-66.

Axel L, Summers RM, Kressel HY, Charles C. Respiratory effects in two-dimensional Fourier transform MR imaging. Radiology, 1986; 160:795-801.

Axel L, Shimakawa A, MacFall J. A time-of-flight method of measuring flow velocity by magnetic resonance imaging. Magn Reson Imaging, 1986; 4:199-205.

Axel L, Morton D. MR flow imaging by velocity compensated/uncompensated difference images. J Comput Assist Tomogr, 1987;11:31-34.

Axel L, Morton D. Correction of phase wrapping in magnetic resonance imaging. Med Phys, 1989; 16:284-7.

Bassiouny HS, White S, Glagov S, Choi E, Giddens DP, Zarins CK. Anastomotic intimal hyperplasia: mechanical injury or flow induced. J Vasc Surg , 1992; 15: 708-716.

Becker ED. High resolution NMR, theory and chemical applications. Academic Press, New York, 1980.

Berger SA, Talbot L, Yao LS. Flow in curved pipes. A Rev Fluid Mech, 1983; 15:461-512.

Berguer R, Higgins RF, Reddy DJ. Intimal hyperplasia. An experimental study. Arch Surg. 1980; 115:332-5.

Bernstein MA, Ikezaki Y. Comparison of phase difference and complex-difference processing in phase contrast angiography. J. Magn. Reson. Imaging, 1991; 1:725-729.

Bernstein MA, Zhou X, King KF, Ganin A, Pelc N, Glover G. Concomitant gradient terms in phase contrast MR: analysis and correction. Magn. Res. Med., 1998; 39:300-308.

Blasberg P, Wurzinger LJ, Scmhid-Schonbein H. Microrheology of thrombocyte deposition: effect of stimulation flow direction, and red cells. In Fluid dynamics as a localising factor for atherosclerosis. Edited by Schettler, G., Nerem, R.M., Schmid-Schonbein, H., Morl H., Diehm, C. pp. 91-101. Springer, Berlin, 1983.

Bloch F, Hansen WV, Packard ME. Nuclear induction Phys. Rev., 1946; 69:127.

Bohning DE. Basics of MR angiography. In: Vascular Imaging by color Doppler and magnetic resonance Lanzer P., Yoganathan A.P. editors. Springer-Verlag, Berlin, Heidelberg, 1991.

Botnar R, Rappitsch G, Scheidegger, MB, Liepsch D, Perktold K, Boesiger P. Hemodynamics in the carotid artery bifurcation: a comparison between numerical simulations an in vitro MRI measurements. J Biomech, 2000; 33:137-144.

Bryan, AJ, Angelini GD. The biology of saphenous vein graft occlusion: etiology and strategies for prevention. Curr. Opin. Cardiol, 1994; 9:641-649.

Bryant DJ, Payne JA, Firmin DN, Longmore DB. Measurement of flow with NMR imaging using a gradient pulse and phase difference technique. J. Comp. Assist. Tomogr., 1984; 8:588-593.

Buonocore MH. Visualizing blood flow patterns using streamlines, arrows, and particle paths. Magn Reson Med, 1998; 40:210-226.

Buonocore MH, Bogren H. Factors influencing the accuracy and precision of velocity-encoded phase imaging. Magn Reson Med, 1992; 26:141-154.

Caputo GR, Takayuki M, Gooding GAW, Chang J-M and Higgins CB. Popliteal and tibioperonal arteries: feasability of two-dimensional time-of-flight MR angiography and phase velocity mapping. Radiology, 1992; 182:387-392.

Caro CG. Transport of 14C-4-cholesterol between perfusing serum and dog common carotid artery: a shear dependent process. Cardiovasc Res, 1974; 8:194-203.

Caro CG, Doorly DJ, Tarnawski M, Scott KT, Long Q, Dumoulin CL. Fluid dynamics: basic concepts. Syllabus, Quantitative magnetic resonance flow imaging, 1995; 19-22.

Caro CG, Doorly DJ, Tarnawski M, Scott KT, Long Q, Dumoulin CL. Non-Planar curvature and branching of arteries and non-planar-type flow. Proc. R. Soc. Lond. A, 1996; 452:185-197.

Caro CG, Fitz-Gerald JM, Schroeter RC. Arterial wall shear stress and distribution of early atheroma in man. Nature, 1969; 223: 1159-1161.

Caro CG, Fitz-Gerald JM, Schroter RC. Atheroma and arterial wall shear: Observation, correlation and proposal of a shear dependent mass transfer mechanism for atherogenesis. Proc. Roy. Soc. Lond. B., 1971; 177:109-159.

Caro CG, Nerem RM. Transport of 14C-cholesterol between serum and wall in perfused dog common carotid artery. Circ Res, 1973; 32:187-194.

Caro CG, Pedley TJ, Schroter RC, Seed WA. The mechanics of the circulation. Oxford University Press, UK, 1978.

Carr HY, Purcell EM. Effects of diffusion on free precession in nuclear magnetic resonance experiments. Phys Rev, 1954; 94:630-638.

Cheshire NJ and Wolfe JH. Infrainguinal graft surveillance: a biased overview. Semin Vasc Surg, 1993; 6:143-149.

Clarke GD, Eckels R, Chaney C, Smith D, Dittrich J, Hundley WG, NessAiver M, Li HF, Parkey RW, Peshock RM. Measurement of absolute epicardial coronary artery flow and flow reserve with breath-hold cine phase-contrast magnetic resonance imaging. Circulation, 1995; 91:2627-34.

Conturo TE, Robinson BH. Analysis of encoding efficiency in MR imaging of velocity magnitude and direction. Magn Reson Med, 1992; 25:233-247.

Conturo TE, Smith GD. Signal-to-Noise in phase angle reconstruction: dynamic range extension using phase reference offsets. Magn Reson Med, 1990; 15:420-437.

Crawshaw H., Quist W., Serrallach E. Flow disturbance at the distal end-to-side anatomosis. Arch Sur, 1980; 115:1280-84.

Damadian R. Tumor detection by nuclear magnetic resonance. Science, 1971; 171:1151.

Davies P. Flow mediated endothelial mechanotransduction. Physiol Rev, 1995; 75:519-560.

de Boor C. On calculating with B-splines. Journal of Approximation Theory, 1972; 6:50-62.

Dean W.R. The stream-line motion of fluid in a curved pipe. Philos. Mag. Ser. 7, (1928); 5:673-95.

Deng X, Marois Y, How T, Merhi Y, King M, Guidoin R, Karino T. Luminal surface concentration of lipoprotein (LDL) and its effect on the wall uptake of cholesterol by canine carotid arteries. J Vasc Surg, 1995; 21:135-45.

Dierckx P. An algorithm for surface fitting with spline functions. *IMA Journal of Numerical Analysis*, 1981; 1:267-283.

Dierckx P. Curve and surface fitting with splines. Clarendon Press, Oxford. 1995.

Ding Z, Friedman M. Variability in planarity of the aortic bifurcation measured from Magnetic Resonance Images. In Proceedings of the Bioengineering Conference, ASME BED-Vol. 35, 1997.

Dobrin, PB. Mechanical factors associated with the development of intimal hyperplasia with respect to vascular grafts. In: Intimal Hyperplasia, Dobrin,PB (ed). R.G. Landes, 1994.

Dobrin, PB. Physiology and pathophysiology of blood vessels. In: The basic science of vascular disease. Sidawy AN, Sumpio BE, DePalma RG, Armonk NY (eds). Futura Publishing Company, 1997.

Doorly DJ, Peiro J, Sherwin SJ, et al. Helix and model graft flows: MRI measurement and CFD simulations. In Proc. of the ASME FED meeting, 1997. ASME paper FEDSM97-3423.

Doorly DJ, Sherwin SJ, Franke PT, Peiro J. Vortical flow structure identification and flow transport in arteries. Under review in Computer Methods in Biomechanics and BioMedical Engineering and Physics, 2001.

Dougherty L, Axel L. Real-time acquisition, reconstruction and display of blood velocity. In Proceedings of the 3rd ISMRM-ESMRMB, 1995, Nice-France, p. 589.

Dumoulin CL, Hart HR. Magnetic resonance angiography. Radiology, 1986; 161:717-720.

Dumoulin CL, Souza SP, Walker MF. Three-dimensional phase contrast angiography. Magn. Reson. Med., 1989; 9:139-149.

Dumoulin CL, Steinberg FL, Yucel EK, Darrow RD. Reduction of artifacts from breathing and peristalsis in phase-contrast MRA of the chest and abdomen. J. Comp. Assist. Tom., 1993; 17:328-332.

Dumoulin CL, Doorly DJ, Caro CG. Quantitative measurement of velocity at multiple positions using comb excitation and Fourier velocity encoding. Magn Reson Med, 1993; 29:44-52.

Dumoulin CL, Darrow RD, Eisner DR, Tarnawski M, Scott KT, Caro CG. Simultaneous detection of multiple components of motion with MRI. J Comput Assist Tomogr, 1994; 18:652-60.

Ernst RR, Anderson WA Application of Fourier Transform Spectroscopy to Magnetic Resonance. Rev Sci Instrum, 1966; 37:93-102.

Ethier CR, Prakash S, Steinman DA, Leask RL, Couch GG, Ojha M. Steady flow separation patterns in a 45 degree junction. J. Fluid Mech., 2000; 411:1-38.

Ethier CR, Steinman DA, Zhang X, Karpik SR, Ojha M. Flow waveform effects on end-to-side anastomotic flow-patterns. J. Biomech., 1998; 31:609-617.

Feinberg DA, Crooks LE, Hoenninger J, Arakawa M, et al. Pulsatile blood velocity in human arteries displayed by magnetic resonance. Radiology, 1984; 153:177-180.

Feinberg DA, Crooks LE, Sheldon P, Hoenninger J 3rd, Watts J, Arakawa M. Magnetic resonance imaging the velocity vector components of fluid flow. Magn Reson Med, 1985; 2:555-66.

Firmin DN, Nayler GL, Klipstein RH, Underwood SR, Rees RS, Longmore DB. In vivo validation of MR velocity imaging. J Comput Assist Tomogr. 1987; 11:751-6.

Firmin DN, Klipstein RH, Hounsfield GL, Paley MP, Longmore DB. Echo-planar high-resolution flow velocity mapping. Magn Reson Med. 1989; 12:316-27.

Firmin DN, Nayler GL, Kilner PJ, Longmore DB. The application of phase shifts in NMR for flow measurement. Magn Reson Med, 1990; 14:230-241.

Foo TK, Bernstein MA, Aisen AM, Hernandez RJ, Collick BD, Bernstein T. Improved ejection fraction and flow velocity estimates with use of view sharing and uniform repetition time excitation with fast cardiac techniques. Radiology, 1995; 195:471-478.

Fox B, James K, Morgan B, Seed A. Distribution of fatty and fibrous plaques in young human coronary arteries. Atherosclerosis, 1982; 41:337-347.

Frank LR, Buxton RB. Distortions from curved flow in magnetic resonance imaging. MRM, 1993; 29:84-93.

Frayne R, Holdsworth DW, Gowman LM, Rickey DW, Drangova M, Fenster A, Rutt BK. Computer-controlled flow simulator for MR flow studies. JMRI, 1992; 2:605-612.

Frayne R, Rutt BK. Frequency response of retrospectively gated phase-contrast MR imaging: effect of interpolation. J Magn Reson Imaging, 1993; 3:907-917.

Frayne R, Rutt BK. Frequency response of prospectively gated phase-contrast MR velocity measurements. J Magn Reson Imaging, 1995; 5:65-73.

Frayne R, Steinman AS, Ethier CR, Rutt BK. Accuracy of MR phase contrast velocity measurements for unsteady flow. J Magn Reson Imaging, 1995; 5:428-431.

Frayne R, Rutt BK. Measurement of fluid-shear rate by Fourier-encoded velocity imaging. Magn Reson Med, 1995; 34:378-87.

Friedman MH, Hutchins GM, Bargeron CB, Deters OJ, Mark FF. Correlation between intimal thickness and fluid shear in human arteries. Atherosclerosis 1981;39:425-436.

Friedman MH, Bargeron CB, Deters OJ, Hutchins GK, Mark FF. Correlation between wall shear and intimal thickness at a coronary artery branch. Atherosclerosis, 1987; 68:27-33.

Friedman MH, Bargeron CB, Duncan DD, Hutchins GK, Mark FF. Effects of arterial compliance and non-newtonian rheology on correlations between intimal thickness and wall shear. J. Biomech. Eng. , 1992; 114: 317-320.

Galjee MA, van Rossum AC, Doesburg T, Hofman MB, Falke TH, Visser CA. Quantification of coronary artery bypass graft flow by magnetic resonance phase velocity. Magn Reson Imaging, 1996; 14:485-93.

Garroway AN. Velocity measurements in flowing fluids by NMR. Letter to the editor. J. Phys. D, 1974; Appl. Phys. 7:L159-L163.

Gatehouse PD, Firmin DN, Collins S, Longmore DB. Real time blood flow imaging by spiral scan phase velocity mapping. Magn Reson Med, 1994; 31:504-12.

Germano M. On the effect of torsion on a helical pipe flow. J Fluid Mech, 1982; 125:1-8.

Glagov S, Zarins C, Giddens DP, Ku DN. Hemodynamics and atherosclerosis. Insights and perspectives gained from studies of human arteries. Arch Pathol Lab Med, 1988; 112:1018-31.

Gray, Henry. Anatomy of the Human Body. Lewis WH (ed). Philadelphia: Lea & Febiger, 2000.

Hahn EL. Detection of sea-water motion by nuclear precession. J Geophys Res, 1960; 65:776-7.

He X, Ku DN. Unsteady entrance flow development in a straight tube. J Biomech Eng, 1994; 116:355-360.

Henry FS, Collins MW, Hughes PE, How TV. Numerical investigation of steady flow in proximal and distal end-to-side anastomoses. J Biomec Eng, 1996; 118:302-310.

Hennig J, Muri M, Brunner P, Friedburg H. Quantitative flow measurement with the fast Fourier flow technique. Radiology, 1988; 166:237-40.

Herment A, Mousseaux E, Jolivet O, et al. Improved estimation of velocity and flow rate using regularized three-point phase-contrast velocimetry. Magn Reson Med, 2000; 44:122-128.

Hinds MT, Park YJ, Jones SA, Giddens DP, Avevriadou BR. Local hemodynamics affect monocytic cell adhesion to a three-dimensional flow model coated with E-selectin. J. Biomech., 2001; 34:95-103.

Hofer M., Rappitsch G, Perktold K, Trubel W, Schima H. Numerical study of wall mechanics and fluid dynamics in end-to-side anastomoses and correlation to intimal hyperplasia. J. Biomech., 1996; 29: 1297-1308.

Hofman MB, Visser FC, van Rossum AC, Vink QM, Sprenger M, Westerhof N. *In vivo* validation of magnetic resonance blood volume flow measurements with limited spatial resolution in small vessels. MRM, 1995; 33:778-784.

Hofman MB, van Rossum AC, Sprenger M, Westerhof N. Assessment of flow in the right human coronary artery by magnetic resonance phase contrast velocity measurement: effects of cardiac and respiratory motion. Magn Reson Med, 1996; 35:521-31.

Hughes TH, Taylor C, Zarins C. Finite element modelling of blood flow in arteries. Comp. Meth. Appl. Mech. Eng., 1998; 158:155-196.

Hundley WG, Lange RA, Clarke GD, Meshack BM, Payne J, Landau C, McColl R, Sayad DE, Willett DL, Willard JE, Hillis LD, Peshock RM. Assessment of coronary arterial flow and flow reserve in humans with magnetic resonance imaging. Circulation, 1996; 93:1502-8.

Hu BS, Pauly JM, Nishimura DG. Localized real-time velocity spectra determination. Magn Reson Med, 1993; 30:393-8.

Hutchison KJ, Karpinski E. In vivo demonstration of flow recirculation and turbulence downstream of graded stenoses in canine arteries. J Biomech, 1985; 18:285-96.

Hylton NM, Crooks LE. Principles of Magnetic Resonance Imaging. In : Lanzer P., Yogananthan A.P.(eds), Vascular imaging. Springer-Verlag, Berlin, 1991.

Jones SA, Giddens DP, Loth F, Zarins CK, Kajiya F, Morita I, Hiramatsu O, Ogasawara Y, Tsujioka K. In vivo measurements of blood flow velocity profiles in canine iliofemoral anastomotic bypass grafts. ASME J. Biomech. Eng., 1997; 119:30-38.

Jou LD, Berger S, van Tyen R, Saloner D. MRA image appearance for pulsatile and steady flow in 3D vessels with branches: a numerical simulation. In Proc. of the 4th ISMRM, 1996; 1268.

Kajiya F, Ogasawara Y, Tsujioka K, Nakai M, Goto M, Wada Y, Tadaoka S, Matsuoka S, Mito K, Fujiwara T. Evaluation of human coronary blood flow with an 80 channel 20 MHz pulsed Doppler velocimeter and zero-cross and Fourier transform methods during cardiac surgery. Circulation, 1986; 74:III53-60.

Kao HC. Torsion effect on fully developed flow in a helical pipe. J Fluid Mech, 1987; 184;335-356.

Karino T, Goldsmith HL. Role of blood cell-wall interactions in thrombogenesis and atherogenesis: a microrheological study. Biorheology, 1984; 21:587-601.

Keegan J, Firmin D, Gatehouse P, Longmore D. The application of breath hold phase velocity mapping techniques to the measurement of coronary artery blood flow velocity: phantom data and initial in vivo results. Magn Reson Med, 1994; 31:526-36.

Kilner PJ, Yang GZ, Mohiaddin RH, Firmin DN, Longmore DB. Helical and retrograde secondary flow patterns in the aortic arch studied by three-directional magnetic resonance velocity mapping. Circulation, 1993; 88:2235-47.

Ku DN, Biancheri CL, Pettigrew RI, Peifer JW, Markou CP, Engels H. Evaluation of Magnetic Resonance Velocimetry for Steady Flow. J Biomech Eng, 1990; 112:464-472.

Ku DN, Giddens D. Pulsatile flow in a model carotid bifurcation. Atherosclerosis, 1983; 3:31-39.

Laub GA, Kaiser WA. MR angiography with gradient motion refocusing. J. Comput. Assist. Tomogr., 1988; 12:377-382.

Lauterbur PC. Image formation by induced local interactions: examples employing nuclear magnetic resonance. Nature, 1973; 242:190.

Lauzon ML, Holdsworth DW, Frayne R, Rutt BK. Effects of physiologic waveform variability in triggered MR imaging: theoretical anlysis. J Magn Reson Imaging, 1994; 4:853-867.

Lee AT, Pike GB, Pelc NJ. Three-point phase-contrast velocity measurements with increased velocity-to-noise ratio. Magn Reson Med, 1995; 33:122-126.

Lei M, Giddens DP, Jones, SA, Loth F, Bassiouny H. Pulsatile flow in an end-to-side vascular model: comparison of computations with experimental data. J. Biomech. Eng. , 2001;123:80-87.

Lei M, Kleinstreuer C, Archie JP. Hemodynamic simulations and computer aided designs of graft-artery junctions. J. Biomech. Eng. , 1997; 119:343-348.

Leipsch D, Moravec S. Pulsatile flow of non-newtonian fluid in distensible models of human arteries. Biorheology, 1984; 21:571-586.

Lefebvre XP, Pedersen EM, Hjortdal JO, Yoganathan AP. Hemodynamics. In: *Vascular imaging by color Doppler and magnetic resonance*, Lanzer P, Yoganathan AP, eds. Springer-Verlag, 1991.

Li H, Clarke GD, NessAvier M, Liu H, Peshock R. Magnetic resonance imaging kappa-space segmentation using phase-encoding groups the accuracy of quantitative measurements of pulsatile flow. Med Phys. 1995; 22:391-9.

Lin W, Haacke EM, Smith AS, Clampitt ME. Gadolinium-enhanced high-resolution MR angiography with adaptive vessel tracking: preliminary results in the intracranial circulation. JMRI, 1992; 2:277-284.

Lou Z, Yang W. Biofluid dynamics at arterial bifurcations. Crit Rev Biomed Eng, 1992; 455-493.

Lou Z, Yang WJ, Stein PD. Errors in the estimation of arterial wall shear rates that result from curve fitting of velocity profiles. J Biomech, 1993; 26:383-90.

Malladi R, Sethian JA. Image processing via level set curvature flow. Proc Natl Acad Sci U S A., 1995; 92:7046-50.

Mansfield P, Maudsley AA. Planar and line-scan spin imaging by NMR. In Proc. XIXth Congress Ampere, Heidelberg, 1976; 247-252.

Masaryk AM In vitro and in vivo comparison of three MR measurement methods for calculating vascular shear stress in the internal carotid artery. AJNR, 1999; 20:237-245.

McKinnon GC, Debatin JF, Wetter DR, von Schulthess GK. Interleaved echo planar flow quantitation. Magn Reson Med, 1994; 32:263-7.

Meier D, Maier S, Boesinger P. Quantitative flow measurements on phantoms and on blood vessels with MR. Magn Reson Med, 1988; 8:25-34.

Milner JS, Moore JA, Rutt BK, Steinman DA. Hemodynamics of human carotid artery bifurcations: Computational studies with models reconstructed from magnetic resonance imaging of normal subjects. J Vasc Surg, 1998; 27:143-156.

Moore JA, Steinman DA, Prakash S, Johnston KW and Ethier CR. A numerical study of blood flow patterns in anatomically realistic and simplified end-to-side anastomoses. J. Biomech Eng., 1999; 121: 265-272.

Moore JE Jr, Maiser SE, Ku DN, Boesiger P. Haemodynamics in the abdominal aorta: a comparison of in vitro and *in vivo* measurements. J. Appl. Physiol., 1994; 76:1520-1527.

Moore JE Jr, Xu C, Glagov S, Zarins CK, Ku DN. Fluid wall shear stress measurements in a model of the human abdominal aorta: oscillatory behaviour and relationship to athrosclerosis. Atherosclerosis, 1994; 110:225-240.

Moran PR. A flow velocity zeugmatographic interlace for NMR imaging in humans. Magn. Reson. Imaging, 1982; 1:197-203.

Napel S, Lee DH, Frayne R, Rutt BK. Visualizing three-dimensional flow with simulated streamlines and three-dimensional phase-contrast MR Imaging. J Magn Reson Imaging, 1992; 2:143-153.

Nayler GL, Firmin DN, Longmore DB. Blood flow imaging by cine magnetic resonance. J Comput Assist Tomogr. 1986; 10:715-22.

Nerem RM, Seed WA. An in vivo study of aortic flow disturbances. Cardiovasc Res., 1972; 6:1-14.

Nichols WW, O'Rourke (Eds). McDonalds blood flow in arteries: theoretical, experimental and clinical principles, 3rd edition. Hodder and Stoughton, 1990.

Nishimura DG. Time-of-flight MR angiography. Magn. Reson. Med., 1990; 4:194-201.

Nishimura DG, Macovski A, Jackson JI, Hu RS, Stevick CA, Axel L. Magnetic resonance angiography by selective inversion recovery using a compact gradient echo sequence. Magn Reson Med, 1988; 8:96-103.

O'Donnell M. NMR blood flow imaging using multiecho phase contrast sequences. Med. Phys., 1985; 12:59-64.

Ojha M, Ethier CS, Johnston KW, Cobbold RS. Steady and pulsatile flow fields in an end-to-side arterial anastomosis model. J Vasc Surg, 1990; 12:747-753.

Ojha M. Spatial and temporal variations of wall shear stress within an end-to-side arterial anastomosis model. J Biomech, 1993; 26:1377-1388.

Ojha M. Wall shear stress temporal gradient and anastomotic intimal hyperplasia. Circ Res, 1994; 74:1227-31.

Ojha M, Cobbold RS, Johnston KW. Influence of angle on wall shear stress distribution for an end-to-side anastomosis. J Vasc Surg, 1994;19:1067-73.

Oshinski J.N., Ku D.N., Bohning D.E., Pettigrew R.I., Effects of acceleration on the accuracy of MR phase velocity measurements. JMRI, 1992; 2:665-670.

Oshinski JN, Ku DN, Mukundan Jr S, Loth F, Pettigrew RI. Determination of wall shear stress in the aorta using MR phase velocity mapping. J Magn Reson Imaging. 1995; 5:640-7.

Ouriel K. Peripheral arterial disease. Lancet, 2001; 358:1257-1264.

Oyre S, Pedersen EM, Ringgaard S, Boesiger P, Paaske WP. In vivo wall shear stress measured by magnetic resonance velocity mapping in the human abdominal aorta.Eur J Vasc Endovasc Surg, 1997; 13: 263-271.

Oyre S, Ringgaard S, Kozerske S, Paaske WP, Scheidegger MB, Boesiger P, Pedersen EM. Quantitation of circumferential subpixel vessel wall position and wall shear stress by multiple sectored three-dimensional paraboloid modelling of velocity encoded cine MR. Magn Reson Med, 1998; 40:645-655.

Papaharilaou Y, Doorly DJ, Sherwin SJ, Peiro J, Anderson J, Sanghera B, Watkins N, Caro CG. Combined MRI and computational fluid dynamics detailed investigation of flow in a realistic coronary artery bypass graft model. In Proceedings of the 9th ISMRM-ESMRMB, 2001, Glasgow, p. 379.

Papaharilaou Y, Doorly DJ, Sherwin. SJ. Assessing the accuracy of two-dimensional phase-contrast MRI measurements of complex unsteady flows. J Magn Reson Imaging, 2001; 14: 714-723.

Papaharilaou Y, Doorly DJ. Accuracy of MRI measurement of complex flows in bypass graft models. In Proc. of the ISMRM Flow and Motion Workshop, London. 1999;120.

Papaharilaou Y, Doorly DJ, Sherwin SJ, Peiro J, Griffith C, Chesire N, Zervas V, Anderson J, Sanghera B, Watkins N, Caro CG. Combined MR imaging and numerical simulation of flow in realistic arterial bypass graft models. Biorheology, 2002; In print.

Papaharilaou Y, Doorly DJ, Sherwin. SJ. The Influence of Out-of-Plane Geometry on Pulsatile Flow Within a Distal End-To-Side Anastomosis. J Biomech, 2002. In print.

Parker K, Caro CG. Flow in the macrocirculation: basic concepts from fluid mechanics. In: Magnetic resonance angiography, concepts and applications. Potchen EJ, Haacke EM, Siebert JE, Gotscalk A, eds. Mosby, St. Louis, 1993.

Peeters F, Jellus V, Sterckx J, Luypaert R, Eisendrath H, and Osteaux M. Eddy current effects in time resolved quantitative MR flow imaging. In Proc. of the 4th ISMRM, 1996; 596.

Peiro J and Sayma AI. In *Numerical Methods for Fluid Dynamics V*, Morton KW and Baines MJ, eds, Oxford University Press, 1995.

Peiro J, Giordana S, Grifith C, Sherwin SJ. High order algorithms for vascular modelling. Int. J. Numer. Method. Fluids, 2001, in print.

Perktold K, Hofer M, Rappitsch G, Loew M, Kuban BD, Friedman MH. Validated computation of physiologic flow in a realistic coronary artery branch. J. Biomech., 1998; 31:217-228.

Perktold K, Rappitsch G. Computer simulation of local blood flow and vessel mechanics in a compliant carotid artery bifurcation model. J. Biomech., 1995; 28:845-856.

Pernicone JR, Siebert JE, Potchen EJ, Pera A, Dumoulin CL and Souza SP. Three-dimensional phase-contrast angiography in the head and neck: preliminary report. American Journal of Neuroradiology, 1990; 11:457-466.

Pinheiro L. Vascular anatomy. In: *Vascular imaging by color Doppler and magnetic resonance*, Lanzer P, Yoganathan AP, eds. Springer-Verlag, 1991.

Polzin JA, Alley MT, Korosec FR, Grist TM, Wang Y, Mistretta CA. A complex-difference phase-contrast technique for measurement of volume flow rates. J Magn Reson Imaging. 1995; 5:129-37.

Polzin JA, Frayne R, Grist TM, Mistretta CA. Frequency response of multi-phase segmented k-space phase-contrast. Magn Reson Med., 1996;35:755-62.

Pritchard WF, Davies PF, Derafshi Z, Polacek DC, Tsao R, Dull RO, Jones SA, Giddens DP. Effects of wall shear stress and fluid recirculation on the localisation of circulating monocytes in a three-dimensional flow model. J. Biomech. , 1995; 28:1459-1469.

Purcell E.M., Torrey H.C., Pound R.V. Resonance absorption by nuclear magnetic moments in a solid. Phys. Rev., 1946; 69:37-8.

Redpath TW, Norris DG, Jones RA, Hutchison JM. A new method of NMR flow imaging. Phys Med Biol, 1984; 29:891-5.

Ringgaard S, Oyre S, Paaske WP, Kozerske S, Boesiger P, Pedersen EM. Accurate automatic determination of blood flow, vessel area and wall shear stress by modelling of magnetic resonance velocity data from the common carotid artery. Proc. ISMRM, 6, 1998; p. 2149.

Rood EP, Telionis DP. Editorial: Journal of fluids engineering policy on reporting uncertainties in experimental measurements and results. ASME Journal of Fluids Engineering, 1991; 113:313-314.

Sabbah HN, Khaja F, Brymer JF, Hawkins ET, Stein PD. Blood velocity in the right coronary artery: relation to the distribution of atherosclerotic lesions. Am J Cardiol, 1984; 53:1008-12.

Sabbah HN, Khaja F, Hawkins ET, Brymer JF, McFarland TM, Bel-Khan J van der, Doerger PT, Stein PD. Relation of atherosclerosis to arterial wall shear in the left anterior descending coronary artery of man. Am Heart J, 1986; 112:453-8.

Sabbah HN, Walburn FJ, Stein PD. Patterns of flow in the left coronary artery. J. Biomech. Eng., 1984;106: 272-279.

Sakuma H, Saeed M, Takeda K, Wendland MF, Schwitter J, Szolar DH, Derugin N, Shimakawa A, Foo TK, Higgins CB. Quantification of coronary artery volume flow rate using fast velocity-encoded cine MR imaging. AJR Am J Roentgenol, 1997; 168:1363-7.

Sanghera B., Naique S, Papaharilaou Y, Amis A. Preliminary study of rapid prototype medical models. Rapid Prototyping J, 2001; 7: 275-284.

Scheidegger MB, Maier SE, Boesiger P. FID-acquired-echoes (FAcE): a short echo time imaging method for flow artefact suppression. Magn Reson Imaging, 1991; 9:517-24.

Sherwin SJ, Karniadakis G. Tetrahedral *hp* finite elements: Algorithms and flow simulations. Journal of Computational Physics, 1996; 124:14-45.

Sherwin SJ, Shah O, Doorly DJ, Mc Lean M, Watkins N, Caro CG, Peiro J, Tarnawski M, Dumoulin CL. Visualisation and computational study of model planar and non-planar end-to-side arterial bypass grafts. Physiological Society Abstracts Plymouth, 1997.

Sherwin SJ, Shah O, Doorly DJ, Peiro J, Papaharilaou Y, Watkins N, Caro CG, Dumoulin CL. The influence of out-of-plane geometry on the flow within a distal end-to side anastomosis. J. Biomech. Eng., 2000; 122: 86-95.

Siegel Jr JM, Oshinski JN, Pettigrew RI, Ku DN. The accuracy of magnetic resonance phase velocity measurements in stenotic flow. J. Biomechanics, 1996; 29:1665-1672.

Singer JR. Blood flow rates by nuclear magnetic resonance measurements. Science, 1959; 130:1652-3.

Sottiurai VS, Yao JS, Flinn WR, Batson RC. Intimal hyperplasia and neointima: an ultrastructural analysis of thrombosed grafts in humans. Surgery, 1983; 93:809-817.

Sottiurai VS, Yao JS, Batson RC, Sue SL, Jones R, Nakamura YA. Distal anastomotic intimal hyperplasia: histopathologic character and biogenesis. Ann Vasc Surg, 1989; 3:26-33.

Spritzer CE, Pelc NJ, Lee JN, Evans AJ, Sostman HD and Riederer SJ. Rapid MR Imaging of blood flow with a phase-sensitive, limited-flip-angle, gradient recalled pulse sequence: Preliminary Experience. Radiology, 1990; 176:255-262.

Steinberg FL Yucel EK, Dumoulin, CL and Souza SP. Peripheral vascular and abdominal applicatons of MR flow imaging techniques. Magn. Reson. Med., 1990; 14:315-320.

Steinman DA, Frayne R, Zhang XD, Rutt BK, Ethier CR. MR measurement and numerical simulation of steady flow in an end-to-side anastomosis model. J Biomech, 1996; 29:537-542.

Steinman DA, Smith RF, Ethier CR, Rutt BK. Wall shear stress via MR: linear or quadratic extrapolation? In Proc. ISMRM, 4, 1996; p. 322.

Steinman DA, Ethier CR, Rutt BK. Combined analysis of spatial and velocity displacement artifacts in phase contrast measurements of complex flows. J Magn Reson Imaging, 1997; 7:339-46.

Strang JG, Herfkens RJ, Pelc NJ. Voxel size effects on vascular shear measurement. In Proc. SMR 2, 1994; p. 1002.

Sun Y, Hearshen DO, Rankin GW, Haggar AM. Comparison of velocity-encoded MR Imaging and fluid dynamic modelling of steady and disturbed flow. J Magn Reson Imaging, 1992; 2:443-452.

Suryan G. Nuclear resonance in flowing fluids, Proc. Indian Acad. Sci. [A], 1951; 33:107-111.

Tang C, Blatter DD, Parker DL. Accuracy of phase-contrast flow measurements in the presence of partial volume effects. J Magn Reson Imaging, 1993; 3:377-385.

Tardy Y, Resnick N, Nagel T, Gimbrone MA Jr, Dewey CF Jr. Shear stress gradients remodel endothelial monolayers in vitro via a cell proliferation-migration-loss cycle. Arterioscler Thromb Vasc Biol., 1997; 17:3102-6.

Traub O, Berk BC. Laminar shear stress: mechanisms by which endothelial cells transduce an atheroprotective force. Arterioscler Thromb Vasc Biol, 1998; 18:677-85.

Tritton DJ. Physical fluid dynamics. Van Nostrand Reinhold, 1977.

van Dijk P. Direct cardiac NMR imaging of heart wall and blood flow velocity. J Comput Assist Tomogr, 1984; 8:429-36.

Van Tyen R, Saloner D, Jou LD, Berger S. MR Imaging of flow through tortuous vessels: a numerical simulation. Magn Reson Med, 1994; 31:184-195.

Vock P, Terrier F, Wegmuller H, Mahler F, Gertsch P, Souza SP, Dumoulin CL. Magnetic resonance angiography of abdominal vessels: early experience using the three dimensional phase contrast technique. Br J Radiol, 1991; 64:10-16.

Wang Y, Christy PS, Korosec FR, Alley MT, Grist TM, Polzin JA, Mistretta CA. Coronary MRI with a respiratory feedback monitor: the 2D imaging case. Magn Reson Med. 1995; 33:116-21.

Wang Y, Rossman PJ, Grimm RC, Riederer SJ, Ehman RL. Navigator-echo-based real-time respiratory gating and triggering for reduction of respiration effects in three-dimensional coronary MR angiography. Radiology. 1996; 198:55-60.

Weston SJ, Wood NB, Tabor G, Gosman AD, Firmin DN. Combined MRI and CFD analysis of fully developed steady and pulsatile laminar flow through a bend. J Magn Reson Imaging, 1998; 8:1158-1171.

Wherli FW. Time-of-flight effects in MR imaging of flow. Magn. Res. Med., 1990; 14:187-193.

White SS, Zarins CK, Giddens DP, Bassiouny H, Loth F, Jones SA, Glagov S. Hemodynamics patterns in two models of end-to-side vascular graft anastomosis: effects of pulsatility, flow division, Reynolds numbers and hood length. J. Biomech. Eng., 1993; 115:104-111.

White CR, Haidekker M, Bao X, Frangos JA. Temporal gradients in shear, but not spatial gradients, stimulate endothelial cell proliferation. Circulation, 2001; 103:2508-13.

Wolf RL, Ehman RL, Riederer SJ, Rossman PJ. Analysis of systematic and random error in MR volumetric flow measurements. Magn. Reson. Med., 1993; 30:82-91.

Womersley JR. Method for the calculation of velocity, rate of flow and viscous drag in arteries when the pressure gradient is known. J Physiology 1955; 127:553-563.

Wurzinger LJ, Opitz R, Blasberg H, Eschweiler H, Schmid-Schonbein H. The role of hydrodynamic forces in platelet activation and thrombotic events: the effects of shear stress of short duration. In Fluid dynamics as a localising factor for atherosclerosis. Edited by Schettler, G., Nerem, R.M., Schmid-Schonbein, H., Morl H., Diehm, C., pp 91-101. Springer, Berlin, 1983.

Xiang QS. Temporal phase unwrapping for CINE velocity imaging. J Magn Reson Imaging, 1995; 5:529-34.

Xu XY, Long Q, Bourne M, Griffith TM. Effect of non-planarity on local blood flow patterns at human aortic bifurcations. In Proceedings of the Euromech, Coll 389, Graz, 1999.

Yamamoto T, Tanaka H, Jones CJ, Lever JM, Parker KH, Kimura A, Hiramatsu O, Ogasawara Y, Tsujioka K, Caro CG, Kajiya F. Blood velocity profiles in the origin of the canine renal artery and their relevance in the localisation and development of atherosclerosis. Atheroscler. Thromb., 1992; 12:626-632.

Yang GZ, Burger P, Kilner PJ, Karwatowski SP, Firmin DN. Dynamic range extension of cine velocity measurements using motion-registered spatiotemporal phase unwrapping. J Magn Reson Imaging, 1996; 6:495-502.

Yeung HN, Kormos DW. Separation of true fat and water images by correcting magnetic field inhomogeneity in situ. Radiology, 1986; 159:783-786.

Young IR, Bydder GM, Payne JA. Flow measurement by the development of phase differences during slice formation in MR imaging. Magn Reson Med, 1986; 3:175-9.

Zabielski L, Mestel A. Steady flow in a helically symmetric pipe. J Fluid Mech, 1998; 370: 297-320.

Zarins CK, Zatina MA, Giddens DP, Ku DN, Glagov S. Shear stress regulation of artery lumen diameter in experimental atherogenesis. J Vasc Surg, 1987; 5:413-20.

Zarins CK, Weisenberg E, Kolettis G, Stankunavicius R, Glagov S. Differential enlargement of artery segments in response to enlarging atherosclerotic plaques. J Vasc Surg, 1988; 7:386-94.

LIST OF FIGURES

List of Tables

List of Symbols

α	Womersley number
Re	Reynolds number
f	Frequency
f_1	Ultrasound beam incident frequency
f_D	Doppler frequency shift
θ	Insonation angle
θ_E	Ernst angle
c	Speed of sound in tissue
u	Axial velocity
υ	In-plane horizontal velocity
w	In-plane vertical velocity
R	Radius, Radius of curvature
a	Tube radius, Angle between $\boldsymbol{\tau}, \boldsymbol{n}_{mean}$
De	Dean number
μ	Dynamic viscosity, Sample mean
m	Sample mean
ρ	Density
σ	Standard deviation
ν	Kinematic viscosity
ω	Angular frequency
ω_0	Larmor frequency
$\hbar$	Planck's constant divided by 2π
k	Boltzmann's constant

τ	Shear stress vector
$\boldsymbol{n}_{mean}$	Mean direction of shear vector
w	Oscillatory Shear Index weighting factor, Spline weighting factor
t	Time
T	Flow waveform period
Q	Flow Rate
γ	Gyromagnetic ratio
S	Spline smoothness factor
χ	Magnetic susceptibility
B_0	Static magnetic field
B_1	RF magnetic induction field
G_x	Magnetic field gradient along the x-axis
G_y	Magnetic field gradient along the y-axis
G_z	Magnetic field gradient along the z-axis
ϕ	Phase angle
$\boldsymbol{M}$	Macroscopic magnetization vector
M_{xy}	Transverse magnetization
M_z	Longitudinal magnetization
I	Pixel intensity, Nuclear spin quantum number

List of Abbreviations

PC	Phase contrast
MRI	Magnetic Resonance Imaging
NMR	Nuclear Magnetic Resonance
SNR	Signal to noise ratio
VNR	Velocity to noise ratio
WSS	Wall Shear Stress
D	Diameter
DPGOD	Distal-Proximal Graft Outflow Division
CFD	Computational Fluid Dynamics
TE	Echo Time

TR	Repetition Time
FA	Flip angle
GRE	Gradient Recalled Echo
GE	General Electric
SE	Spin Echo
Venc	Velocity Encoding
NEX	Number of signal averages
ROI	Region of Interest
LAD	Left Anterior Descending
RF	Radio Frequency
RO	Read Out
PE	Phase Encoding
FID	Free Induction Decay
SS	Slice Select
FOV	Field of View
RMS	Root mean square
vps	Views per segment
Gd	Gadolinilum
OSI	Oscillatory Shear Index